



**HAL**  
open science

# Modélisation numérique et expérimentale des phénomènes de givrage par accrétion de neige collante

Alessandro Vigano

► **To cite this version:**

Alessandro Vigano. Modélisation numérique et expérimentale des phénomènes de givrage par accrétion de neige collante. Autre. ISAE-ENSMA Ecole Nationale Supérieure de Mécanique et d'Aérotechnique - Poitiers, 2012. Français. NNT : 2012ESMA0026 . tel-00786189

**HAL Id: tel-00786189**

**<https://theses.hal.science/tel-00786189v1>**

Submitted on 8 Feb 2013

**HAL** is a multi-disciplinary open access archive for the deposit and dissemination of scientific research documents, whether they are published or not. The documents may come from teaching and research institutions in France or abroad, or from public or private research centers.

L'archive ouverte pluridisciplinaire **HAL**, est destinée au dépôt et à la diffusion de documents scientifiques de niveau recherche, publiés ou non, émanant des établissements d'enseignement et de recherche français ou étrangers, des laboratoires publics ou privés.



# THESE

Pour l'obtention du Grade de  
DOCTEUR DE L'ECOLE NATIONALE SUPERIEURE DE MECANIQUE  
ET D'AEROTECHNIQUE  
(Diplôme National – Arrêté du 7 août 2006)

Ecole Doctorale :  
Sciences et Ingénierie en Matériaux, Mécanique, Energétique et Aéronautique

Secteur de Recherche : Mécanique des milieux fluides

Présentée par :  
Alessandro VIGANO

*Experimental and Numerical modeling of wet snow  
accretion on structures*

Directeur de thèse : M. Jacques BOREE  
Co-encadrant : M. Philippe DELPECH

Soutenue le 18 décembre 2012  
devant la Commission d'Examen

## JURY

Mr. Pascal PERSONNE  
Mr. Thomas Kringlebotn THIIIS  
Mr. Richard PERKINS  
Mr. Yves BERTIN  
Mr. Jacques BOREE  
Mr. Didier GUFFOND  
Mr. Philippe DELPECH

Président  
Rapporteur  
Rapporteur  
Examineur  
Examineur  
Examineur  
Examineur



*"vincit is qui putat se id facere"*

*Virgilio*



# *Acknowledgements*

The only part of my Ph.D thesis written in Italian...

In primo luogo vorrei ringraziare il mio direttore di tesi Jacques Borée per aver accettato di seguire e dirigere il lavoro di tesi durante questi tre anni. Il suo entusiasmo ed interesse verso argomenti lontani dal suo “quotidiano” sono stati per me un incoraggiamento continuo durante le fasi più difficili. La sua capacità d’analisi e di adattabilità ai più diversi temi sono stati motivo d’esempio durante tutta la tesi.

Un sentito ringraziamento va anche a Philippe Delpech per il suo ruolo come guida in seno al CSTB. Le sue infinite proposte per la parte sperimentale sono state fonte d’ispirazione continua, la sua “fantasia scientifica” è stata d’aiuto in svariate occasioni. Un grosso grazie va anche per la pazienza avuta per tutte le correzioni di francese fatte durante i lavori intermedi.

Ci tengo a ringraziare calorosamente tutto il mio jury di tesi: prof. Thiis, prof Perkins, prof. Personne, prof. Bertin, e l’ing. Guffond oltre al mio direttore di tesi e Philippe. Le loro analisi e spunti di riflessione sono stati un ulteriore aiuto per l’approfondimento scientifico delle problematiche

Un sentito grazie va anche a Sylvain per avermi proposto di fare una tesi al CSTB e per essersi prodigato in prima persona affinché un italiano venisse accettato senza remora. Alla fine hai vinto la tua scommessa, ho imparato il francese...Grazie anche per il sostegno e la pazienza dimostrata nello spiegarmi cose per me molto “sci-fi” come “croisement des trajectoires” o la turbolenza...

Grazie anche a tutte le persone incrociate durante questi tre anni di CSTB, nominarle tutte sarebbe impossibile ma ci tengo comunque a ricordare: Laetitia, Jaime, Nico, Adrien, Khaled, Armelle, Christophe x2, Sebastien, Hervé, Jérôme, Régis, Thierry, Patrick. Chiedo già scusa in anticipo per tutti quelli che mi sono dimenticato...

Un super grazie a tutta la truppa di sbandati extra-lavoro: Vale, Giggio, Mario, Vivi, Luca, Georges. Grazie a voi questi tre anni sono stati un po’ più leggeri, mi avete fatto sentire un po’ di più a casa ogni volta, grazie di tutto cuore.

Ma, Bi, Fazz, con relative donne: grazie. Grazie per aver sortito un “jutsu” che fermava il tempo ogni qualvolta tornavo a casa. Ad ogni mio ritorno è stato come se il tempo non fosse passato, è sempre stato come un semplice sabato sera tra noi, grazie di tutto cuore.

Grazie anche alla truppa “skype from the maison”: mamma papà e Chiara. Prima di tutto vi chiedo scusa per essere andato via tre anni, ma come promesso, sono di nuovo a casa. Il vostro sostegno e la vostra fiducia in me sono stati uno stimolo unico. Siete riusciti a starmi vicino anche a 1300km di distanza, grazie di tutto cuore. Grazie anche ai “nonni-skype”: i vostri consigli, così prima come durante questi tre anni, sono stati dogmi ai quali ispirarmi ogni giorno...Un sentito grazie anche ai miei cugini Sara e Davide per la citazione in latino.

Ti conosco, quindi so bene che leggendo queste righe ti sarà spuntato un punto di domanda in cima all’insalata...L’ultimo pensiero è proprio per te...Dirti grazie sarebbe scontato e superfluo così come penso che non ci siano parole per rendere giustizia a quello che hai rappresentato per me in questa esperienza francese: questo risultato senza di te, non sarebbe mai esistito.



# TABLE OF CONTENTS

|                  |   |           |
|------------------|---|-----------|
| <b>CHAPTER 1</b> | <b>INTRODUCTION.....</b>  | <b>1</b>  |
| 1.1              | PROBLEM STATEMENT.....  | 1         |
| 1.2              | METHODOLOGY.....  | 2         |
| 1.3              | OUTLINE OF THE THESIS.....  | 3         |
|                  | BIBLIOGRAPHY.....   | 5         |
| <b>CHAPTER 2</b> | <b>LITERATURE REVIEW ON WET SNOW ACCRETION PROCESS.....</b>   | <b>7</b>  |
| 2.1              | OVERVIEW OF THE SNOW INTERACTION ON STRUCTURES.....   | 8         |
| 2.1.1            | <i>Interactions with buildings.....</i>   | <i>8</i>  |
| 2.1.2            | <i>Interactions with cables.....</i>  | <i>9</i>  |
| 2.1.3            | <i>Interactions with terrestrial transports.....</i>  | <i>10</i> |
| 2.1.4            | <i>Interactions with wind turbines.....</i>   | <i>10</i> |
| 2.1.5            | <i>Overview conclusion.....</i>   | <i>10</i> |
| 2.2              | PHYSICAL CHARACTERIZATION OF SNOW PARTICLES RESPONSIBLE OF WET SNOW ACCRETIONS.....                                       | 11        |
| 2.2.1            | <i>An approach to reproduce wet snow: artificial snow produced by a snow gun.....</i>                                     | <i>13</i> |
| 2.2.2            | <i>Snow particles characterization conclusion.....</i>  | <i>14</i> |
| 2.3              | EFFECTS OF LWC ON IN CLOUD ICING ACCRETIONS.....  | 14        |
| 2.4              | MODELING WET SNOW ACCRETIONS: THE APPROACH CHOSEN.....  | 17        |
| 2.4.1            | <i>Aerodynamic aspect of accretion process: collision efficiency.....</i>   | <i>17</i> |
| 2.4.2            | <i>Mechanical aspect of accretion process: sticking efficiency.....</i>   | <i>18</i> |
| 2.4.3            | <i>Thermal aspect of accretion process: accretion efficiency.....</i>   | <i>19</i> |
| 2.4.4            | <i>Accretion modeling conclusion and synthesis of the accretion steps.....</i>  | <i>20</i> |
| 2.5              | THEORETICAL APPROACH TO CONTROL PARTICLE <i>LWC</i> : THE PARTICLE FREEZING THEORY.....                                   | 21        |
| 2.5.1            | <i>Particle freezing theory conclusion.....</i>   | <i>25</i> |
| 2.6              | THEORETICAL APPROACH TO MODEL SNOW PARTICLES DYNAMIC IN THE AIR FLOW.....   | 25        |
| 2.6.1            | <i>Forces acting on particles.....</i>  | <i>26</i> |
| 2.6.2            | <i>Stokes number definition.....</i>  | <i>29</i> |
| 2.6.3            | <i>Particle-flow interaction modeling.....</i>  | <i>30</i> |
| 2.6.4            | <i>Modeling of the turbulence fluctuation <math>u'_f</math>.....</i>  | <i>32</i> |
| 2.6.5            | <i><math>u'_f</math> modeling conclusions.....</i>  | <i>35</i> |
| 2.6.6            | <i>Inertia effect and Crossing trajectories effect.....</i>   | <i>35</i> |
| 2.7              | CONCLUSION.....   | 38        |
|                  | BIBLIOGRAPHY.....   | 39        |
| <b>CHAPTER 3</b> | <b>EXPERIMENTAL APPROACH TO INVESTIGATE WET SNOW ACCRETIONS.....</b>  | <b>43</b> |
| 3.1              | CLIMATIC CONDITIONS REPRODUCTION: CLIMATIC WIND TUNNEL.....   | 44        |
| 3.2              | WET SNOW PRODUCTION: SNOW GUN.....  | 45        |
| 3.3              | TEST CAMPAIGN DEVICES TO STUDY WET SNOW ACCRETIONS.....   | 47        |
| 3.3.1            | <i>Investigation of the aerodynamic aspect: test structure.....</i>   | <i>47</i> |
| 3.3.2            | <i>Estimation of the incoming snow flow rate: snow collectors.....</i>  | <i>49</i> |
| 3.3.3            | <i>Temperature monitoring: thermocouples, flow visualization: GoPro camera.....</i>                                       | <i>53</i> |
| 3.3.4            | <i>Characterization of the incoming flow: ultrasonic anemometer.....</i>  | <i>55</i> |
| 3.4              | EXPERIMENTAL PROCEDURE TO REPRODUCE WET SNOW ACCRETIONS.....  | 56        |
| 3.4.1            | <i>Wind tunnel setup.....</i>   | <i>56</i> |
| 3.4.2            | <i>Experimental principle to reproduce wet snow accretions.....</i>   | <i>58</i> |
| 3.4.3            | <i>Procedure undertaken during the experimental campaign.....</i>   | <i>59</i> |
| 3.4.4            | <i>Preliminary wind tunnel settings up: analysis of snow flow homogeneity and test reproducibility.....</i>               | <i>61</i> |
| 3.5              | THE EXPERIMENTAL RESULTS.....   | 64        |
| 3.5.1            | <i>Snow flow characterization through the ultrasonic anemometer.....</i>  | <i>64</i> |
| 3.5.2            | <i>Heat exchange blockage: estimation of the real flow speed.....</i>   | <i>68</i> |
| 3.5.3            | <i>Wet snow accretions quantification: coefficient <math>\beta</math>.....</i>  | <i>70</i> |
| 3.5.4            | <i>Experimental analysis of the <i>LWC</i> role of wet snow accretion through the coefficient <math>\beta</math>.....</i> | <i>71</i> |

|   |  |            |
|---|--|------------|
| 3.5.5   | <i>Experimental analysis of the thermal aspect of wet snow accretions: temperature profiles</i> .....  | 77         |
| 3.5.6   | <i>Experimental analysis of the aerodynamic aspect of wet snow accretions: cylinders role through a Stokes number and coefficient <math>\beta_{exp}</math></i> ..... | 78         |
| 3.6   | PHYSICAL MEASUREMENTS APPROACHED .....   | 80         |
| 3.7   | CONCLUSIONS .....  | 82         |
|   | BIBLIOGRAPHY .....   | 83         |
| <b>CHAPTER 4 PHYSICAL MODELS FOR THE DETERMINATION OF THE BOUNDARY CONDITIONS .....</b> |  | <b>85</b>  |
| 4.1   | MODEL IMPLEMENTATION: ESTIMATION OF PARTICLE <i>LWC</i> AT THE INSTANT OF IMPACT COUPLED WITH FLOW-PARTICLES INTERACTION. ....                                       | 86         |
| 4.1.1   | <i>Equations implementation in the coupled model: thermal and dynamic equations.</i> .....   | 87         |
| 4.1.2   | <i>Hypothesis introduced to represent the experimental conditions.</i> .....   | 93         |
| 4.1.3   | <i>Implementation in the model of the experimental conditions: thermal and flow parameters.</i> .....  | 95         |
| 4.1.4   | <i>Resolution procedure of the coupled model.</i> .....  | 97         |
| 4.1.5   | <i>Model implementation conclusions</i> .....  | 100        |
| 4.2   | MODELS RESULTS DISCUSSION .....  | 101        |
| 4.2.1   | <i>Boundary condition estimation: particle distribution “on” the cylinders.</i> .....  | 101        |
| 4.2.2   | <i>Particle size distribution on the cylinder</i> .....  | 104        |
| 4.2.3   | <i>The role of the gravity on particle distribution</i> .....  | 107        |
| 4.2.4   | <i>Particles <i>LWC</i> “on” the cylinder surface as a function of the ambient temperature.</i> .....  | 111        |
| 4.2.5   | <i>Physical parameters which can drive the particle <i>LWC</i>.</i> .....  | 119        |
| 4.2.6   | <i>Boundary condition estimation: <i>LWC</i> of the whole snow particle flow.</i> .....  | 122        |
| 4.3   | CONCLUSION.....  | 123        |
|   | BIBLIOGRAPHY .....   | 125        |
| <b>CHAPTER 5 ESTIMATION OF THE PARAMETERS TO MODEL WET SNOW ACCRETIONS .....</b>        |  | <b>127</b> |
| 5.1   | DETERMINATION OF THE AERODYNAMIC CONTRIBUTION TO WET SNOW ACCRETIONS: COLLISION EFFICIENCY. ....   | 128        |
| 5.1.1   | <i>Numerical modeling of the flowstream around the cylinders: setup</i> .....  | 129        |
| 5.1.2   | <i>Numerical modeling of the flowstream around the cylinders: results</i> .....  | 132        |
| 5.1.3   | <i>Lagrangian simulations of particle dispersion around the cylinders: setup</i> .....   | 134        |
| 5.1.4   | <i>Flowstream and lagrangian modeling setting up conclusions.</i> .....  | 137        |
| 5.2   | COLLISION EFFICIENCY EVALUATION OF THE EXPERIMENTAL CYLINDERS.....   | 137        |
| 5.2.1   | <i>Relation between Stokes number and collision efficiency.</i> .....  | 138        |
| 5.2.2   | <i>Particle size distribution on the cylinders and the resulting liquid water content</i> .....  | 141        |
| 5.2.3   | <i>Collision efficiency evaluation: conclusions.</i> .....   | 143        |
| 5.3   | QUANTIFICATION OF THE COLLISION EFFICIENCY IMPACT ON THE EXPERIMENTAL COEFFICIENT $\beta_{exp}$ .....  | 143        |
| 5.4   | QUANTIFICATION OF MODELED ACCRETION SHAPES.....  | 146        |
| 5.5   | STICKING EFFICIENCY AS A FUNCTION OF THE PARTICLE-SURFACE ANGLE OF IMPACT .....  | 150        |
| 5.5.1   | <i>Theoretical implementation of the angle criterion and application to the experimental cases.</i> .....  | 150        |
| 5.5.2   | <i>Accretion shape obtained with a threshold angle <math>\alpha_t = 45^\circ</math>.</i> .....   | 152        |
| 5.5.3   | <i>Accretion shape influence on the global collision efficiency <math>\eta_1</math>.</i> .....   | 153        |
| 5.5.4   | <i>Sticking efficiency evaluation for the experimental cases</i> .....   | 155        |
| 5.6   | ANALYSIS OF THE STICKING COEFFICIENT $\eta_2 = \mathcal{F}(\alpha_{imp})$ ON THE EXPERIMENTAL CASES. ....  | 158        |
| 5.6.1   | <i>Sticking efficiency analysis: conclusions.</i> .....  | 161        |
| 5.7   | CONCLUSION.....  | 161        |
|   | BIBLIOGRAPHY .....   | 164        |
| <b>CHAPTER 6 CONCLUSION.....</b>  |  | <b>165</b> |

# LIST OF FIGURES

|  |    |
|--|----|
| FIGURE 1. ACCRETION EXAMPLES: (A) AERIAL CABLE (B) TRAIN. ....   | 1  |
| FIGURE 2. EXAMPLES OF THE DAMAGES CAUSED BY SNOW ACCUMULATION: (A) A COLLAPSED ROOFS [3], (B) A MASSIVE SNOW FALL FROM A ROOF IN SCOTLAND [4]. ....  | 8  |
| FIGURE 3. (A) AN EXAMPLE OF ICICLES FORMATION ON A BUILDING [9]. (B) A SNOW SLIDING PHENOMENON [10] .....  | 9  |
| FIGURE 4. (A) EXAMPLE OF ACCRETION ON CABLES WHICH GIVES AN EXTRA LOAD OF 5KG/M [14]. (B) THE HIGHEST ACCRETION PHENOMENA DOCUMENTED [15] .....  | 9  |
| FIGURE 5. (A-B) WET-SNOW ACCRETIONS ON BOOGIES TRAIN [18] .....  | 10 |
| FIGURE 6. EXAMPLE SNOWFLAKES: (A) DRY SNOWFLAKES [24] (B) WET SNOWFLAKES [24] .....  | 11 |
| FIGURE 7. WET SNOW AGGREGATE: (A) CAPILLARY LIQUID WATER BETWEEN 5-15% AND AIR BUBBLE WHICH IS OFTEN >50% IN VOLUME [24] (B) AGGREGATE OF WET SNOW WHICH IS MELTING [24]. ....   | 12 |
| FIGURE 8. (A) AN ARTIFICIAL SNOWFLAKES. (B) A NATURAL SNOWFLAKE. [24]. ....  | 12 |
| FIGURE 9. ARTIFICIAL SNOW SYSTEMS PRODUCTION: (A) INTERNAL MIX SYSTEM. B) EXTERNAL MIX SYSTEM [26]. C) AIR/WATER/FAN SYSTEM [26]. ....   | 13 |
| FIGURE 10. SAMPLE ICE PARTICLES IMAGES FROM A SNOW GUN WITH INTERNAL MIX SYSTEM: (A) CAPTURED USING THE OAP (PARTICLE MEASURING SYSTEMS 2D-GREY OPTICAL ARRAY PROBE) SYSTEM [27]. (B) PHOTOGRAPHED WITH A MICROSCOPE [28]. ....  | 13 |
| FIGURE 11. EFFECTS OF $LWC$ ON AIRFOIL, EXPERIMENTAL TEST [29] .....   | 14 |
| FIGURE 12. IMPACT OF $LWC$ VARIATION ON IN CLOUD ICING OF AN AIRFOIL, EXPERIMENTAL TEST [32]. ....   | 15 |
| FIGURE 13. IMPACT OF $LWC$ AND $u_f$ VARIATION ON RESULTING ICE ACCRETION ON A CYLINDER (DIAMETER 2.54MM), EXPERIMENTAL TEST AT $Ta=-15^{\circ}C$ [33]. TEST DURATION FOR $u_f$ : $t \approx 5min$ ; FOR $2u_f$ WHEN $3LWC$ AND $LWC$ $t \approx 2.5min$ , WHEN $2LWC$ $t \approx 1min$ . .... | 15 |
| FIGURE 14. EFFECTS IN CLOUD ICING ON A CYLINDER(DIAMETER 2.54MM), EXPERIMENTAL TESTS AS A FUNCTION OF $T_a$ AND $LWC$ , MEAN WIND SPEED $u_f = 30m/s$ [33]. TEST DURATION $t \approx 5min$ . ....  | 16 |
| FIGURE 15. EFFECTS OF $LWC$ ON CYLINDER ACCRETIONS (DIAMETER 2.54MM), EXPERIMENTAL TESTS [33]. $u_f = 110m/s$ . TEST DURATION $LWC$ $t \approx 20min$ , $2LWC$ $t \approx 10min$ , $5LWC$ $t \approx 5min$ .....   | 16 |
| FIGURE 16. COLLISION EFFICIENCY $\eta_1$ . ....  | 18 |
| FIGURE 17. RIME ICE ACCRETION, $\eta_3 = 1$ : (A) SCHEMATIC REPRESENTATION [15]. (B) AN IMAGE [43]. ....   | 19 |
| FIGURE 18. GLAZE ICE ACCRETION, $0 < \eta_3 < 1$ : (A) SCHEMATIC REPRESENTATION [15]. (B) AN IMAGE [43] .....  | 20 |
| FIGURE 19. SYNTHESIS OF THE COEFFICIENTS TO MODEL THE ACCRETION. ....  | 20 |
| FIGURE 20. THE FOUR STAGES OF A PARTICLE FREEZING PROCESS .....  | 22 |
| FIGURE 21. THERMOCOUPLE TO MEASURE THE NUCLEATION TEMPERATURE [47] .....   | 24 |
| FIGURE 22. THE DRAG FORCE ACTING ON A PARTICLE .....   | 26 |
| FIGURE 23. COEFFICIENT OF DRAG AS A FUNCTION OF PARTICLE REYNOLDS NUMBER .....   | 27 |
| FIGURE 24. SCHEMES FOR LIFT FORCE (LEFT AND CENTER IMAGE) AND FOR BUOYANCY FORCE ON THE RIGHT. ....  | 28 |
| FIGURE 25. STOKES NUMBER: (A) PARTICLE CROSSES THE EDDY. (B) PARTICLE ACTS AS A TRACER .....   | 30 |
| FIGURE 26. METHODS TO MODEL THE TURBULENCE. ....   | 31 |
| FIGURE 27. THEORETICAL AUTOCORRELATION FUNCTION OF THE FLOW .....  | 32 |
| FIGURE 28. EIM MODEL: (A) AN EXAMPLE OF $u'_f$ , (B) THE AUTOCORRELATION $\mathcal{R}_L^E$ .....   | 33 |
| FIGURE 29. LANGEVIN MODEL: (A) AN EXAMPLE OF $u'_f$ , (B) THE AUTOCORRELATION $\mathcal{R}_L^E$ .....  | 34 |
| FIGURE 30. PARTICLE INERTIA AND CROSSING TRAJECTORY EFFECT. ....   | 35 |
| FIGURE 31. STOKES NUMBER: (A) $St \gg 1$ : HIGH PARTICLE INERTIA. (B) $St \ll 1$ : LOW PARTICLE INERTIA .....  | 36 |
| FIGURE 32. THE EVALUATION OF $t_{int}$ IN THE EIM APPROACH. ....   | 37 |
| FIGURE 33. JULES VERNE CLIMATIC WIND TUNNEL FACILITY. ....   | 44 |
| FIGURE 34. JULES VERNE CLIMATIC WIND TUNNEL: THERMAL CIRCUIT. ....   | 45 |
| FIGURE 35. SNOW GUN VOLUME PARTICLE DISTRIBUTION [2]. ....   | 45 |
| FIGURE 36. MALVERN POSITION [2] .....  | 46 |
| FIGURE 37. MEASUREMENT PRINCIPLE OF LASER DIFFRACTION. ....  | 46 |
| FIGURE 38. FUNCTION PRINCIPLE OF THE TRAPDOOR. ....  | 47 |
| FIGURE 39. AIR BOUNDARY LAYER AT THE STRUCTURE LOCATION: $16m$ FROM THE INLET. ....  | 48 |
| FIGURE 40. (A) A FRONT VIEW OF THE TEST STRUCTURE WITH ITS PRINCIPAL FEATURES AND DIMENSIONS. (B) THE COVER WHICH PROTECTS THE CYLINDER. ....  | 48 |
| FIGURE 41. (A) FRONT VIEW OF THE TEST STRUCTURE WITH THE FOUR SNOW COLLECTORS. (B) FIDE VIEW OF THE SNOW COLLECTORS. ....  | 49 |

|   |     |
|---|-----|
| FIGURE 42. ANALYSIS OF FILLING UP DRAWBACK OF SNOW COLLECTORS.....  | 51  |
| FIGURE 43. (A) SCHEMATIC VIEW OF SNOW COLLECTORS. (B) WIND TUNNEL SETUP. ....   | 51  |
| FIGURE 44. SNOW FLUX UNIFORMITY, $u_f \approx 10m/s$ . ....   | 52  |
| FIGURE 45. THERMOCOUPLES POSITION. ....   | 53  |
| FIGURE 46. (A) THERMOCOUPLE USED DURING THE EXPERIMENTAL CAMPAIGN. (B) MEASUREMENT PRINCIPLE OF THE THERMOCOUPLE. ....  | 53  |
| FIGURE 47. THERMOCOUPLE ON THE CYLINDER. ....   | 54  |
| FIGURE 48. GOPRO CAMERA. ....   | 54  |
| FIGURE 49. THE ULTRASONIC ANEMOMETER ON ITS SUPPORT. ....   | 55  |
| FIGURE 50. WIND TUNNEL SETTING UP FOR TEST. ....  | 56  |
| FIGURE 51. MEAN SNOW FLUX MEASURED DURING THE FIVE TESTS OF THE EXPERIMENTAL CAMPAIGN FOR THE EXETRNAL SNOW COLLECTORS.....   | 57  |
| FIGURE 52. $\tau_p$ EVALUATION LOOP. ....   | 58  |
| FIGURE 53. PARTICLE $LWC$ AS A FUNCTION OF THE AMBIENT TEMPERATURE FOR $d_{43} = 290\mu m$ . THE EVALUATION IS MADE THANKS TO THE DISPERSION NUMERICAL MODEL EXPLAINS LATER IN CHAPTER FOUR. ....   | 59  |
| FIGURE 54. TEMPERATURE DATA OF A TEST. ....   | 60  |
| FIGURE 55. (A) ACCRETION AT $T_a = -10^\circ C$ . (B) ACCRETION AT $T_a = -2^\circ C$ .....   | 61  |
| FIGURE 56. (A) SCHEME WITH TWO SNOW GUNS. (B) CONFIGURATION WITH ONE SNOW GUN. ....   | 61  |
| FIGURE 57. FLUX HOMOGENEITY IN CASE OF ONE OR TWO SNOW GUNS. ....   | 62  |
| FIGURE 58. (A) CONFIGURATION WITH ONE SIDE SNOW GUN. (B) $\delta\%_{\rho_S}$ DIFFERENCES. ....  | 62  |
| FIGURE 59. (A) CONFIGURATION WITH VERTICAL CYLINDERS. (B) A SCHEME OF THE ACCRETION DRAWBACK.....   | 63  |
| FIGURE 60. (A) CONFIGURATION WITH TWO HORIZONTAL CYLINDERS. (B) A SCHEME OF THE ACCRETION DRAWBACK IN WHICH $PSD^v$ IS THE VOLUME PARTICLE SIZE DISTRIBUTION. ....  | 63  |
| FIGURE 61. AIR FLOW ANALYSIS, COBRA PROBE: (A) FLOW SPEED . (B) CONVERGENCE ANALYSIS. ....  | 65  |
| FIGURE 62. SNOW FLOW ANALYSIS, ULTRASONIC ANEMOMETER: (A) FLOW SPEED. (B) CONVERGENCE ANALYSIS. ....  | 65  |
| FIGURE 63. AUTOCORRELATION FUNCTION FOR THE AIR STREAM. ....  | 66  |
| FIGURE 64. THE SUPPOSED EFFECT OF THE SNOW GUN ON THE EDDIES DIMENSION, TOP VIEW. ....  | 67  |
| FIGURE 65. AUTOCORRELATION FUNCTION FOR THE SNOW FLOW. ....   | 67  |
| FIGURE 66. THE AUTOCORRELATION COMPARISON. ....   | 68  |
| FIGURE 67. DECREASE OF THE MEAN FLOW SPEED DURING A TEST DAY.....   | 69  |
| FIGURE 68. (A) TRANSVERSAL FLOW UNIFORMITY. (B) TRANSVERSAL FLOW UNIFORMITY – CENTER ZOOM.....  | 69  |
| FIGURE 69. THE MEAN SNOW FLUX AND THE NORMALIZED ACCRETION ON THE CYLINDER, A LATER VIEW. ....  | 71  |
| FIGURE 70. IMPACTING FLOW UNIFORMITY ON THE CYLINDER CENTRAL PORTION. ....  | 71  |
| FIGURE 71. THE COEFFICIENT $\beta$ AS A FUNCTION OF THE AMBIENT TEMPERATURE. ....   | 72  |
| FIGURE 72. FOUR SIDE VIEWS OF THE ACCRETION ON THE CYLINDER $D_{50}$ . ....   | 73  |
| FIGURE 73. AUGMENTATION OF THE EFFECTIVE SECTION FOR $\beta$ AT $T_a = -3^\circ C$ .....  | 74  |
| FIGURE 74. TEMPERATURE PROFILES FOR THE SAME CYLINDER $D_{50}$ AT FOUR AMBIENT TEMPERATURES. ....   | 77  |
| FIGURE 75. THE $\beta_{exp}$ COEFFICIENT FOR ALL THE THREE CYLINDERS AS A FUNCTION OF THE AMBIENT TEMPERATURE. ....   | 78  |
| FIGURE 76. THE ACCRETION RATIO FOR THE THREE CYLINDERS.....   | 79  |
| FIGURE 77. (A) OTT PARSIVEL. (B) CAMPBELL SCIENTIFIC PRESENCE WEATHER SENSOR PWS100.....  | 80  |
| FIGURE 78. (A) TWC AND LWC PROBE. (B) SEA PROBE.....  | 81  |
| FIGURE 79.: (A) EXPERIMENTAL PROBE SENSOR HEAD. (B) CONTROL SYSTEM SET UP. ....   | 81  |
| FIGURE 80. COUPLING BETWEEN FREEZING AND TRACKING CODE.....   | 86  |
| FIGURE 81. PARTICLE FREEZING PROCESS SCHEME. ....   | 87  |
| FIGURE 82. FREEZING STAGE MODELING [2]: (A) ASSESSMENT OF THE MODELS REGARDING THE FREEZING DURATION (THE MODEL OUTPUTS ARE COMPARED TO EXPERIMENTAL RESULTS EXPRESSED IN TERM OF FREQUENCY OF OCCURRENCE), (B) TEMPORAL EVOLUTION OF PARTICLE TEMPERATURE ACCORDING TO THE HEAT BALANCE MODEL SUPERIMPOSED TO THE EXPERIMENTAL MEASUREMENT. .... | 89  |
| FIGURE 83. DYNAMIC AND THERMAL COUPLING MODEL.....  | 93  |
| FIGURE 84. (A) ACCRETION UNIFORMITY, (B) SNOW FLUX UNIFORMITY: $\delta err\%$ REPRESENTS THE PERCENTAGE DIFFERENCE BETWEEN THE SNOW FLUX MEASURED AT $x = 0$ AND $x = 0.5m$ OR $x = -0.5m$ .....  | 94  |
| FIGURE 85. PARTICLE INJECTION SCHEME.....   | 96  |
| FIGURE 86. PARTICLE TRAJECTORIES EXAMPLE: RED $d_p = 40\mu m$ , BLUE $d_p = 260\mu m$ , GREEN $d_p = 520\mu$ . ....   | 99  |
| FIGURE 87. INJECTIONS NUMBER CONVERGENCE ....   | 104 |
| FIGURE 88. THE PSD SUPPOSED AT THE EXIT OF THE SNOW GUN [9].....  | 104 |
| FIGURE 89. SNOW GUN PARTICLE SIZE DISTRIBUTION INTERPOLATION.....   | 105 |
| FIGURE 90. PARTICLE SIZE DISTRIBUTION WEIGHTING PROCESS.....  | 105 |

|   |     |
|---|-----|
| FIGURE 91. PARTICLE SIZE DISTRIBUTION “ON” THE CYLINDERS.....   | 106 |
| FIGURE 92. WIND TUNNEL GROUND DISCRETIZATION .....  | 107 |
| FIGURE 93. DEPOSITION ANALYSIS: (A) 0 – 2m, (B) 2 – 4m, (C) 4 – 6m, (D) 6 – 8m, (E) 8–10m, .....  | 108 |
| FIGURE 94. DEPOSITION ANALYSIS: (A) 0 – 2m, (B) 2 – 4m, (C) 4 – 6m, (D) 6 – 8m, (E) 8–10m, .....  | 109 |
| FIGURE 95. SNOW DEPOSITION ON WIND TUNNEL GROUND. ....  | 110 |
| FIGURE 96. GRAVITY EFFECT ON $PSD^v$ .....  | 110 |
| FIGURE 97. GRAVITY EFFECT ON $PSD^n$ .....  | 111 |
| FIGURE 98. STOCHASTIC AND THERMAL COUPLING IN THE MODEL.....  | 112 |
| FIGURE 99. (A) EFFECTS OF EIM MODEL ON $u_r$ AND $h$ , (B) $u_f'$ EXAMPLE.....  | 112 |
| FIGURE 100. (A) EFFECTS OF LANGEVIN MODEL ON $u_r$ AND $h$ , (B) $u_f'$ EXAMPLE. ....   | 113 |
| FIGURE 101. HEAT TRANSFERS RATIO.....   | 114 |
| FIGURE 102. PARTICLE TEMPERATURE EVOLUTION AS A FUNCTION OF $T_a$ .....   | 114 |
| FIGURE 103. PARTICLE TEMPERATURE PROFILE AS A FUNCTION OF $d_p$ .....   | 115 |
| FIGURE 104. PARTICLE LWC TEMPORAL EVOLUTION AS A FUNCTION OF THE AMBIENT TEMPERATURE $T_a$ .....  | 116 |
| FIGURE 105. $d_{cyl} = 50mm$ (A) $T_a = -3^\circ C$ , (B) $T_a = -6^\circ C$ , (C) $T_a = -9^\circ C$ .....   | 116 |
| FIGURE 106. PARTICLE LWC EVOLUTION AS A FUNCTION OF THE PARTICLE DIAMETER. ....   | 117 |
| FIGURE 107. LWC OF PARTICLES WITH RESPECT TO AMBIENT TEMPERATURE AND PARTICLE DIAMETER, 3D VIEW.....  | 117 |
| FIGURE 108. LWC OF PARTICLES WITH RESPECT TO PARTICLE DIAMETER FOR VARIOUS AMBIENT TEMPERATURE , 2D VIEW.<br>.....  | 118 |
| FIGURE 109. LWC TUNING AS A FUNCTION OF THE MEAN FLOW SPEED $u_f$ .....   | 119 |
| FIGURE 110. (A) LWC AS A FUNCTION OF $I_{\%}$ (B) $u_f'$ AS A FUNCTION OF $I_{\%}$ .....  | 120 |
| FIGURE 111. (A) LWC AS A FUNCTION OF CYLINDER – SNOW GUN DISTANCE: $\delta$ .....   | 120 |
| FIGURE 112. LWC AS A FUNCTION PARTICLE INITIAL TEMPERATURE. ....  | 121 |
| FIGURE 113. (A) LWC AS A FUNCTION OF HR (B) $q_m$ AS A FUNCTION OF HR. ....   | 121 |
| FIGURE 114. THE LWC OF THE WHOLE PARTICLE FLUX. ....  | 123 |
| FIGURE 115. A REPRESENTATION OF THE COLLISION COEFFICIENT $\eta_1$ .....  | 128 |
| FIGURE 116. COMPUTATIONAL DOMAIN FOR $d_{cyl} = 50mm$ .....   | 130 |
| FIGURE 117. (A) MESH REFINEMENT EVOLUTION, (B) SKEWNESS CONCEPT. ....   | 131 |
| FIGURE 118. CONVERGENCE ANALYSIS (A) $k - \varepsilon$ MODEL. (B) $k - \omega SST$ MODEL.....   | 132 |
| FIGURE 119. PRESSURE COEFFICIENT (A) $k - \varepsilon$ MODEL. (B) $k - \omega SST$ MODEL. ....  | 132 |
| FIGURE 120. OVERPRODUCTION OF $k$ (A) $k - \varepsilon$ MODEL. (B) $k - \omega SST$ MODEL. ....   | 133 |
| FIGURE 121. $k - \omega SST$ FLOWSTREAM COMPUTATIONAL RESULTS. ....   | 133 |
| FIGURE 122. VOLUME PSD AT THE CYLINDER LOCATION. ....   | 134 |
| FIGURE 123. (A) FLOW SPEED UNIFORMITY AT INJECTION POINT. (B) INJECTION POINT LOCATION.....   | 134 |
| FIGURE 124. PARTICLES INJECTION POINT IN THE COMPUTATIONAL DOMAIN.....  | 135 |
| FIGURE 125. PARTICLE BEHAVIOR IN THE BOUNDARY LAYER, $St_{BL}$ MEANING. ....  | 136 |
| FIGURE 126. SCHEME OF THE $\eta_1$ EVALUATION.....  | 137 |
| FIGURE 127. LOCATION OF THE CONTROL SURFACE, $d_{cyl} = 315mm$ .....  | 138 |
| FIGURE 128. $St_{cyl}$ CONCEPT (A) HIGH $St_{cyl}$ , (B) LOW $St_{cyl}$ .....   | 139 |
| FIGURE 129. COLLISION EFFICIENCY $\eta_1$ AS A FUNCTION OF $St_{cyl}$ . ....  | 140 |
| FIGURE 130. $PSD^v$ COMPARISON .....  | 141 |
| FIGURE 131. $LWC_g$ FOR THE THREE CYLINDERS: A COMPARISON. ....   | 143 |
| FIGURE 132. ACCRETION EFFICIENCY CONCEPT: (A) $\eta_3 = 1$ (B) $\eta_3 < 1$ ICING CASE, (C) $\eta_3 = 1$ WET SNOW CASE.....   | 145 |
| FIGURE 133. ACCRETIONS AT $T_a = -3^\circ C$ : (A) $d_{cyl} = 50mm$ (B) $d_{cyl} = 200mm$ , (C) $d_{cyl} = 315mm$ .....   | 145 |
| FIGURE 134. $\eta_2 = \mathcal{F}(LWC_g)$ . ....  | 146 |
| FIGURE 135. SCHEME OF THE $\eta_1$ LOCAL EVALUATION.....  | 147 |
| FIGURE 136. $acc_{shape} \varphi$ CONCEPT (A) A SCHEME, (B) AN EVALUATION EXAMPLE.....  | 148 |
| FIGURE 137. ACCRETION SHAPES: (A) $d_{cyl} = 50mm$ (B) $d_{cyl} = 200mm$ , (C) $d_{cyl} = 315mm$ . ....   | 148 |
| FIGURE 138. LOOP UNDERTAKEN TO COMPUTE THE ACCRETION SHAPE. ....  | 149 |
| FIGURE 139. ACCRETION SHAPE (A) MODEL RESULT, (B) EXPERIMENTAL RESULT. ....   | 150 |
| FIGURE 140. TRENKER PRINCIPLE (A) ANGLE OF IMPACT CONSTRAINT, (B) PARTICLE BEHAVIOR AFTER IMPACT. ....  | 151 |
| FIGURE 141. ACCRETION SHAPES AT DIFFERENT THRESHOLD ANGLES $\alpha_t$ . ....  | 151 |
| FIGURE 142. ACCRETION SHAPES OBTAINED. ....   | 153 |
| FIGURE 143. ACCRETION ANALYSIS OF THE UPPER AND LOWER PART OF THE CYLINDER $d_{cyl} = 50mm$ : (A) NUMERICAL<br>SIMULATION $\alpha_t = 45^\circ$ (B) EXPERIMENTAL RESULT, (C) $\alpha_t = 20^\circ, 30^\circ$ and $45^\circ$ ..... | 153 |
| FIGURE 144. FLOW FIELDS (A) CYLINDER SHAPE (B) ACCRETION SHAPE.....   | 154 |

|  |     |
|--|-----|
| FIGURE 145. GLOBAL COLLISION EFFICIENCY EVOLUTION (A) FOR THE THREE CYLINDERS, (B) $d_{cyl} = 50mm$ ZOOM. .... | 154 |
| FIGURE 146. (A) IMPACTED MASS, (B) STUCK MASS .....  | 155 |
| FIGURE 147. STICKING EFFICIENCY EVOLUTION AT EACH LOOP.....  | 156 |
| FIGURE 148. STICKING ANALYSIS (LEFT) IMPACTED MASS, (RIGHT) STUCK MASS. ....                                   | 157 |
| FIGURE 149. ACCRETION SHAPE EVOLUTION LINKED TO THE ANGLE CRITERION. ....                                      | 157 |
| FIGURE 150. RELATION BETWEEN $\eta_2$ AND $LWC_g$ .....  | 159 |
| FIGURE 151. ACCRETION SHAPES: (A) $d_{cyl} = 50mm$ (B) $d_{cyl} = 200mm$ , (C) $d_{cyl} = 315mm$ . ....        | 159 |
| FIGURE 152. PARTICLES IMPACT SPEED.....  | 160 |
| FIGURE 153. EXPERIMENTAL SETUP PROPOSED. ....  | 162 |

# LIST OF TABLES

|  |     |
|--|-----|
| TABLE 1. THE SNOW FLUX FOR EACH COLLECTORS FOR THREE PERIODS IN A TEST DAY. ....                       | 50  |
| TABLE 2. THE REPRODUCIBILITY OF THE TESTS .....  | 64  |
| TABLE 3. SCREENS OF SNOW ACCRETIONS AT THE SAME AMBIENT TEMPERATURE $T_a = -4^\circ\text{C}$ . ....    | 75  |
| TABLE 4. SCREENS OF SNOW ACCRETIONS FOR THE SAME CYLINDER. ....  | 76  |
| TABLE 5. VALUES OF $Stk_{cyl}$ .....   | 80  |
| TABLE 6. INFLUENCE ON PARTICLE $LWC$ , OF THE EVALUATION METHOD FOR THE THERMOPHYSICAL PROPERTIES..... | 95  |
| TABLE 7. ANALYSIS OF THE CHARACTERISTIC TIMES.....   | 100 |
| TABLE 8. ANALYSIS OF $\alpha_t$ INFLUENCE .....  | 100 |
| TABLE 9. DIFFERENCES BETWEEN $PSD^v$ AND $PSD^n$ .....   | 101 |
| TABLE 10. ANALYSIS OF LOW CUT-OFF FOR PARTICLE DIAMETER RANGE [9] .....                                | 102 |
| TABLE 11. ANALYSIS OF NUMBER OF PARTICLES TO INJECT .....  | 103 |
| TABLE 12. $PSD^v$ WITH ASSOCIATED $LWC$ FOR $LWC_g$ EVALUATION .....                                   | 122 |
| TABLE 13. $St_{cyl}$ AS A FUNCTION OF THE CYLINDER DIAMETER .....                                      | 129 |
| TABLE 14. ESTIMATION OF THE BLOCKAGE EFFECT .....  | 130 |
| TABLE 15. THE ANALYSIS OF THE MESHES. ....   | 131 |
| TABLE 16. COLLISION EFFICIENCY.....  | 138 |
| TABLE 17. THE EVALUATION OF $St_{cyl}$ AND THE ASSOCIATED $\eta_1$ . ....                              | 139 |
| TABLE 18. COLLISION EFFICIENCY EVALUATION WITH EQUATION (102). ....                                    | 140 |
| TABLE 19. EXAMPLE OF $PSD^v$ AND $LWC_i$ USED FOR $LWC_g$ EVALUATION.....                              | 142 |
| TABLE 20. COLLISION EFFICIENCY.....  | 144 |
| TABLE 21. $\Delta\eta_1$ AND $\Delta\eta_2$ EVALUATION.....  | 158 |

# NOMENCLATURE

| Symbol              | Concept  | Dimensions      | Value                |
|---------------------|--|-----------------|----------------------|
| $\alpha_p$          | Particle/air concentration ratio                           | dimensionless   | /                    |
| $\beta$             | accretion mass flux, incoming mass flux ratio              | dimensionless   | /                    |
| $\Delta p$          | Heat exchange pressure difference                          | $Pa$            | /                    |
| $\varepsilon$       | Turbulent dissipation                                      | $m^2/s^3$       | /                    |
| $\hat{\varepsilon}$ | Ice emissivity   | dimensionless   | 0.97                 |
| $\gamma$            | Particle surface tension                                   | $kg/s^2$        | $76 \cdot 10^{-3}$   |
| $\kappa$            | VonKarman constant   | dimensionless   | 0.41                 |
| $\lambda_f$         | Thermal conductivity of the air                            | $W/(m \cdot K)$ | 0.024                |
| $\lambda_l$         | Thermal conductivity of the water                          | $W/(m \cdot K)$ | 0.6                  |
| $\eta_1$            | Collision efficiency                                       | dimensionless   | /                    |
| $\eta_2$            | Sticking efficiency  | dimensionless   | /                    |
| $\eta_3$            | Accretion efficiency                                       | dimensionless   | /                    |
| $\xi$               | EIM random variable  | dimensionless   | /                    |
| $\rho_f$            | Air density  | $kg/m^3$        | 1.316                |
| $\rho_i$            | Ice density  | $kg/m^3$        | 910                  |
| $\rho_l$            | Water density  | $kg/m^3$        | 1000                 |
| $\rho_p$            | Particle density   | $kg/m^3$        | /                    |
| $\sigma$            | Fluctuating velocity variance                              | $m/s$           | /                    |
| $\hat{\sigma}$      | Stefan-Boltzmann constant                                  | $W/(m^2K^4)$    | $5.67 \cdot 10^{-8}$ |
| $\tau_{BL}$         | Characteristic time of the mean wall turbulence            | $s$             | /                    |
| $\tau_{cyl}$        | Characteristic time of the flow around the cylinder        | $s$             | /                    |
| $\tau_{col}$        | Characteristic time of the flow around the snow collectors | $s$             | /                    |
| $\tau_f$            | Characteristic time of the flow                            | $s$             | /                    |
| $\tau_{inj}$        | Particle flight time of the numerical simulation           | $s$             | /                    |
| $\tau_p$            | Particle relaxation time                                   | $s$             | /                    |
| $\tau_t$            | Particle thermal characteristic time                       | $s$             | /                    |
| $\mu_f$             | Flow dynamic viscosity                                     | $Pa \cdot s$    | $1.69 \cdot 10^{-5}$ |
| $\nu_f$             | Flow kinematic viscosity                                   | $m^2/s$         | $1.28 \cdot 10^{-5}$ |
| $\psi_a$            | Experimental snow accretion flux on the cylinder           | $kg/(m^2s)$     | /                    |
| $\varphi_s$         | Incoming snow flux   | $kg/(m^2s)$     | /                    |
| $\omega$            | Specific dissipation                                       | $Hz$            | /                    |
| $\Xi$               | $T_f^L/T_f^E$  | dimensionless   | /                    |

| ***               | ***   | ***              | ***               |
|-------------------|---|------------------|-------------------|
| $A_{col}$         | Snow collector area                                       | $m^2$            | /                 |
| $A_e$             | Cylinder reference area                                   | $m^2$            | /                 |
| $Bi$              | Biot number   | dimensionless    | /                 |
| $c_p^i$           | Specific heat of ice at constant pressure                 | $J/(kg \cdot K)$ | 2110              |
| $c_p^l$           | Specific heat of water at constant pressure               | $J/(kg \cdot K)$ | 4210              |
| $\dot{C}$         | Particle concentration of the ultrasonic anemometer       | $nb/m^3$         | /                 |
| $C_a$             | Water vapour mass concentration in the air                | $kg/m^3$         | /                 |
| $C_d$             | Drag coefficient  | dimensionless    | /                 |
| $C_p$             | Water vapour mass concentration at particle-air interface | $kg/m^3$         | /                 |
| $D_{w/f}$         | Water vapour diffusion in the air                         | $m^2/s$          | /                 |
| $d_{col}$         | Collector diameter  | $m$              | /                 |
| $d_{cyl}$         | Cylinder diameter   | $m$              | /                 |
| $d_p$             | Particle diameter   | $m$              | /                 |
| $dW(t)$           | Langevin random variable                                  | dimensionless    | /                 |
| $F_d$             | Drag force  | $kg \cdot m/s^2$ | /                 |
| $Fr$              | Froude number   | dimensionless    | /                 |
| $g$               | Gravitational acceleration                                | $m/s^2$          | 9.81              |
| $h$               | Heat transfer coefficient                                 | $W/(m^2K)$       | /                 |
| $I_{\%}$          | Turbulence intensity                                      | dimensionless    | /                 |
| $h_m$             | Mass transfer coefficient                                 | $m/s$            | /                 |
| $k$               | Turbulent kinetic energy                                  | $m^2/s^2$        | /                 |
| $k_f$             | Thermal conductivity                                      | $W/(m \cdot K)$  | 0.0243            |
| $l$               | Integral length scale                                     | $m$              | /                 |
| $l_{cyl}$         | Reference length of the cylinders                         | $m$              | 0.7               |
| $LWC$             | Liquid water content                                      | dimensionless    | /                 |
| $L_e$             | Latent heat of evaporation                                | $J/kg$           | $2.52 \cdot 10^6$ |
| $L_f$             | Latent heat of fusion                                     | $J/kg$           | $3.21 \cdot 10^5$ |
| $L_s$             | Latent heat of sublimation                                | $J/kg$           | $L_e + L_f$       |
| $m_{col}$         | Snow mass inside the collectors                           | $kg$             | /                 |
| $\dot{m}_{acc}$   | Accretion mass flux                                       | $kg/(m^2s)$      | /                 |
| $\dot{m}_{inc}$   | Incoming particle mass flux                               | $kg/(m^2s)$      | /                 |
| $\dot{m}_{imp}$   | Impacting particle mass flux                              | $kg/(m^2s)$      | /                 |
| $\dot{m}_{stick}$ | Sticking particle mass flux                               | $kg/(m^2s)$      | /                 |
| $m_p$             | Mass of a particle  | $kg$             | /                 |
| $m_p^l$           | Liquid mass of a particle                                 | $kg$             | /                 |
| $Nu$              | Nusselt number  | dimensionless    | /                 |
| $Pr$              | Prandtl number  | dimensionless    | /                 |

|                       |  |                  |        |
|-----------------------|--|------------------|--------|
| $PSD$                 | Particle size distribution                         | dimensionless    | /      |
| $p_p^{SAT}$           | Saturated vapour pressure                          | $Pa$             | /      |
| $q_h$                 | Convective heat flux                               | $W$              | /      |
| $q_m$                 | Convective mass transfer heat flux                 | $W$              | /      |
| $q_r$                 | Radiation heat flux                                | $W$              | /      |
| $\mathcal{R}_L(\tau)$ | Autocorrelation function                           | dimensionless    | /      |
| $Re_p$                | Particle Reynolds number                           | dimensionless    | /      |
| $RH$                  | Relative humidity                                  | dimensionless    | /      |
| $R_v$                 | Gas constant, water molar mass ratio               | $J/(kg \cdot K)$ | 461.53 |
| $S_p$                 | Particle surface                                   | $m^2$            | /      |
| $t_{cross}$           | Eddy cross time                                    | $s$              | /      |
| $t_{eddy}$            | Eddy life time                                     | $s$              | /      |
| $t_{int}$             | Turbulence eddy-particle interaction time          | $s$              | /      |
| $Sh$                  | Sherwood number                                    | dimensionless    | /      |
| $St$                  | Stokes number                                      | dimensionless    | /      |
| $T_a$                 | Ambient temperature                                | $^{\circ}C$      | /      |
| $T_{nuc}$             | Nucleation temperature                             | $^{\circ}C$      | /      |
| $T_f^L$               | Lagrangian integral time scale of the flow         | $s$              | /      |
| $T_f^E$               | Eulerian integral time scale of the flow           | $s$              | /      |
| $T_{f@p}^*$           | Integral time scale of the fluid seen by particles | $s$              | /      |
| $T_p^l$               | Particle temperature at liquid state               | $^{\circ}C$      | /      |
| $T_p^i$               | Particle temperature at solid state                | $^{\circ}C$      | /      |
| $u_f$                 | Flow speed   | $m/s$            | /      |
| $u_f'$                | Fluctuating velocity                               | $m/s$            | /      |
| $u_p$                 | Particle speed                                     | $m/s$            | /      |
| $u_r$                 | Particle-flow relative speed                       | $m/s$            | /      |
| $v_g$                 | Particle settling velocity                         | $m/s$            | /      |
| $\dot{V}_{air}$       | Air concentration                                  | $m^3$            | /      |
| $\dot{V}_p$           | Particle concentration                             | $m^3$            | /      |
| $V_p$                 | Particle volume                                    | $m^3$            | /      |
| $V_p^{evap}$          | Particle volume evaporated                         | $m^3$            | /      |
| $We$                  | Weber number                                       | dimensionless    | /      |
| $y^+$                 | Mean wall distance                                 | dimensionless    | /      |





# Chapter 1 Introduction

|     |                            |   |
|-----|----------------------------|---|
| 1.1 | PROBLEM STATEMENT.....     | 1 |
| 1.2 | METHODOLOGY.....           | 2 |
| 1.3 | OUTLINE OF THE THESIS..... | 3 |
|     | BIBLIOGRAPHY .....         | 5 |

## 1.1 Problem statement

**A**tmospheric phenomena have influenced many fields of engineering for a long time. The atmospheric phenomenon related to the present work is called atmospheric icing. Two forms of atmospheric icing are commonly distinguished: in-cloud icing and precipitation icing. The first one is due to liquid particles suspended in clouds which freeze when in contact with a cold surface forming the icing accretion. This type of icing is mainly related to aeronautics. For terrestrial structures as buildings, wind turbine, cables or ground vehicles, precipitation icing is a more important concern. Precipitation icing is addressed in this work. This type of icing is due to rain or snow precipitation that freezes when in contact with a surface. Both icing phenomena can be very hazardous under certain circumstances.

In-cloud icing has been extensively investigated in the last seventy years, but the domain of precipitation icing has not been examined with the same attention. A type of icing phenomenon not enough investigated is related to wet snow particles. These particles are characterized by a mixed phase. Wet-snow accretions concern several fields of engineering: buildings, cables, ground vehicles can be affected by this kind of accretion (Figure 1).

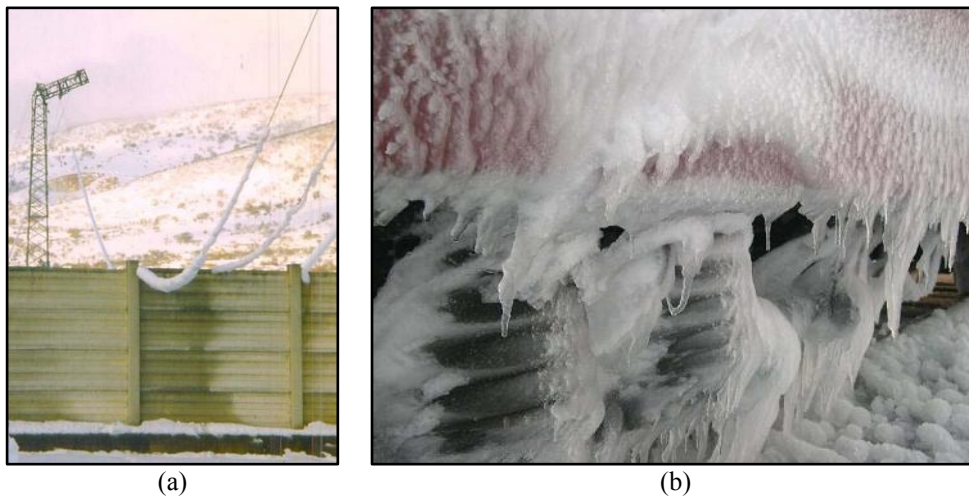


Figure 1. Accretion examples: (a) aerial cable (b) train.

The wet snow accretion process can be described as follow. A wet snow particle which reaches a structure may stick or not on the structure surface depending on

environmental parameters and particle characteristics. Once stuck to the structure, the liquid part of the particle can partially freeze and trap the solid part of the particle. If initiated, the process generates the accretion growth.

Wet snow accretion can be modeled according to different approaches based on empirical observations or physical modeling [1-2]. For a better comprehension of the physics of the phenomenon, an approach based on physical modeling has been undertaken in this work.

The modeling relies on the experimental approach undertaken in a climatic wind tunnel with artificial snow making capability. The base hypothesis is that wet snow accretions are reliably simulated by icing accretion due to artificial snow particle during the freezing stage.

The wet snow accretion phenomenon is quantified by three dimensionless coefficients.. The first coefficient is related to the efficiency of snow particles to reach a structure. The second coefficient quantifies the efficiency of particles to stick on the structure surface. The last coefficient quantifies the efficiency of stuck particles to contribute to the accretion.

Wet snow particles are characterized by a mixed phase. The dimensionless parameter which quantifies the mixed phase is the particle liquid water content  $LWC$ . It is defined as the ratio of the liquid mass of the particle to the whole particle mass. The purpose of this work is a better understanding of the link between the wet snow accretion and the  $LWC$  of the particles. An analysis of the physical parameters involved is done investigating each one of the three coefficients introduced above.

## 1.2 Methodology

The investigation is led using both an experimental and numerical approach. Experiments have been carried out in a climatic wind tunnel in order to link the wet snow mass accretion on horizontal cylinders to the  $LWC$  content of the particles. An important work has been done in order to control the physical parameters of the experimental simulation. The resulting experimental set-up allows keeping most of the physical parameters constant. The variation of the ambient temperature is used to modify the freezing process of the liquid particles exiting the snow gun and tune the liquid water content of the snow particles reaching the cylinders. The result of the simulations is the measurement of the coefficient  $\beta_{exp}$  (equal to the ratio of the mass of accretion to the incoming mass flow of snow) for different ambient temperatures:  $\beta_{exp} = \mathcal{F}(T_a)$ .

However it has been found to be complex to obtain some of the parameters of the simulations due to the lack of efficient measurement devices to characterize the wet snow incoming on the cylinders. It has then been chosen to model the turbulent dispersion and the freezing process of the particles in the wind tunnel using simple models. The goal is to obtain the missing physical parameters which could not be measured such as the particle size distribution and the liquid water content of the particle at the vicinity of the cylinders. The combination of those numerical models and the results of the measurements in the wind tunnel allows to link the evolution of the

accretion with the ambient temperature to the Liquid water content of the particle  $\beta_{exp} = \mathcal{F}(LWC)$ .

Finally those results are analyzed using a decomposition proposed by the literature which distinguishes the collision efficiency, the sticking efficiency and the accretions efficiency. A numerical modeling of the collision efficiency has been carried out using a CFD code coupled with a lagrangian computation. It allows then to distinguish the collision efficiency contribution to the coefficient  $\beta_{exp}$ . The final part of the work will show then that the sticking efficiency coefficient is difficult to model and the current models in the literature fail in reproducing the observations made in the wind tunnel.

### 1.3 Outline of the Thesis

The thesis has been developed in four parts.

Chapter two presents the literature review on wet snow accretions. A description of the particles which leads to wet snow accretion is presented. These particles are characterized by a mixed phase quantified by the liquid water content  $LWC$ . This dimensionless parameter is the ratio of the liquid particle mass to the whole particle mass. Moreover, a particle freezing model is presented. It validates that the  $LWC$  of the particles can be controlled by the ambient temperature. This is one of the leading principles of the experimental campaign. The modeling approach is presented via three different dimensionless coefficient:  $\eta_1$ ,  $\eta_2$  and  $\eta_3$ . Due to the two-phase nature of the snow flow, an approach to model particle-flow interactions is presented. The approach is based on the Lagrangian modeling. To model the turbulent feature of the flow, two approaches are presented: Eddy Life Time and Langevin approach. Both approaches are implemented in the numerical modeling.

Chapter three presents the experimental procedure undertaken to study the wet snow accretions. The accretions are analyzed on three cylinders of different diameter. This allows to study if the structure dimension plays a role on the accretion process. Wet snow particles are produced by a snow gun which injects liquid particles that freeze along their path before reaching the cylinders. Following the particle freezing theory the liquid water content is tuned as a function of the ambient temperature. The accretions obtained at different ambient temperature are analyzed by an experimental coefficient  $\beta_{exp}^{123}$ . This coefficient represents the ratio of the accretion rate to the mass flux of the incoming particles. Moreover,  $\beta_{exp}^{123}$  allows to take into account the three dimensionless coefficient:  $\eta_1$ ,  $\eta_2$  and  $\eta_3$ . During the experimental campaign the snow flow is characterized by mean flow speed, turbulence intensity and integral length scale.

Chapter four presents the physical model developed to estimate the boundary conditions of the model presented in chapter five. These boundary conditions are the particle size distribution  $PSD^v$  of particles upstream the cylinder with the associated liquid water content  $LWC_g$ . The physical model has been developed due to the difficulties to acquire the boundary conditions during the experimental campaign. It concerns the modeling of the particle trajectory coupled with the particle freezing process. The particle tracking part of the model estimates the  $PSD^v$  upstream the cylinders. This part is based on the Lagrangian approach and implements both

approaches to model the turbulent feature of the flow: EIM and Langevin. The particle freezing part evaluates the liquid water content associated to  $PSD^v$ .

Chapter five concerns the numerical modeling and the analysis of the accretions obtained during the experimental campaign. A series of numerical simulations allow to analyze the experimental coefficient  $\beta_{exp}^{123}$  as a function of the liquid water content and of the aerodynamic response of the particles to the flow around the test structures. Thus, the role of particle inertia and of the liquid water content on wet snow accretions is quantified. The accretion shapes are also investigated in the second part of the chapter. Two different approaches are presented and the results are compared to the experimental ones. The analysis is focused on the link between the angle of impact between the particle direction and the accretion surface and the accretion obtained. Suggestions for future works on wet snow accretions are discussed.

## Bibliography

- [1] L. Makkonen and B. Wichura, "Simulating wet snow loads on power line cables by a simple model," *Cold Regions Science and Technology*, vol. 61, pp. 73-81, 2010.
- [2] L. Makkonen, "Models for the growth of rime, glaze, icicles and wet snow on structures," *Philosophical Transactions: Mathematical, Physical and Engineering Sciences*, vol. 358, pp. 2913-2939, 2000.



## Chapter 2 Literature review on wet snow accretion process.

|       |  |    |
|-------|--|----|
| 2.1   | OVERVIEW OF THE SNOW INTERACTION ON STRUCTURES.....                                      | 8  |
| 2.1.1 | <i>Interactions with buildings.</i> .....  | 8  |
| 2.1.2 | <i>Interactions with cables.</i> .....   | 9  |
| 2.1.3 | <i>Interactions with terrestrial transports.</i> .....                                   | 10 |
| 2.1.4 | <i>Interactions with wind turbines.</i> .....  | 10 |
| 2.1.5 | <i>Overview conclusion.</i> .....  | 10 |
| 2.2   | PHYSICAL CHARACTERIZATION OF SNOW PARTICLES RESPONSIBLE OF WET SNOW ACCRETIONS.....      | 11 |
| 2.2.1 | <i>An approach to reproduce wet snow: artificial snow produced by a snow gun.</i> .....  | 13 |
| 2.2.2 | <i>Snow particles characterization conclusion.</i> .....                                 | 14 |
| 2.3   | EFFECTS OF LWC ON IN CLOUD ICING ACCRETIONS.....   | 14 |
| 2.4   | MODELING WET SNOW ACCRETIONS: THE APPROACH CHOSEN.....                                   | 17 |
| 2.4.1 | <i>Aerodynamic aspect of accretion process: collision efficiency.</i> .....              | 17 |
| 2.4.2 | <i>Mechanical aspect of accretion process: sticking efficiency.</i> .....                | 18 |
| 2.4.3 | <i>Thermal aspect of accretion process: accretion efficiency.</i> .....                  | 19 |
| 2.4.4 | <i>Accretion modeling conclusion and synthesis of the accretion steps</i> .....          | 20 |
| 2.5   | THEORETICAL APPROACH TO CONTROL PARTICLE <i>LWC</i> : THE PARTICLE FREEZING THEORY. .... | 21 |
| 2.5.1 | <i>Particle freezing theory conclusion</i> .....   | 25 |
| 2.6   | THEORETICAL APPROACH TO MODEL SNOW PARTICLES DYNAMIC IN THE AIR FLOW. ....               | 25 |
| 2.6.1 | <i>Forces acting on particles</i> .....  | 26 |
| 2.6.2 | <i>Stokes number definition</i> .....  | 29 |
| 2.6.3 | <i>Particle-flow interaction modeling</i> .....  | 30 |
| 2.6.4 | <i>Modeling of the turbulence fluctuation <math>u'_f</math></i> .....                    | 32 |
| 2.6.5 | <i><math>u'_f</math> modeling conclusions.</i> .....                                     | 35 |
| 2.6.6 | <i>Inertia effect and Crossing trajectories effect.</i> .....                            | 35 |
| 2.7   | CONCLUSION.....  | 38 |
|       | BIBLIOGRAPHY .....   | 39 |

This chapter presents the state of the art and a literature review of the wet snow accretion process. An overview on the possible interactions between snow and structures is first presented. The possible damages that may occur in case of accretion are also shown. The discussion continues with a description of the particles responsible for wet snow accretions. These particles are characterized by a liquid and a solid part. These two parts are quantified by a dimensionless parameter: the liquid water content *LWC*. The ambient conditions which generate these particles are also described. Finally the approach adopted to model this phenomenon is presented.

This approach can be divided into three different aspects. The first one mainly concerns the aerodynamic aspect. This means to evaluate if a snow particle approaching a structure hits the structure or not. The second aspect mainly concerns the mechanical aspect of the accretion. This one estimates, once the particle has hit the structure, if it

remains stuck on the structure. If the whole sticking part the contributes to the accretion concerns the third aspect.

Additionally a theoretical approach to estimate the particle *LWC* is also presented. This approach provides the basic principle of the whole experimental campaign as shown in chapter 3.

## **2.1 Overview of the snow interaction on structures.**

The icing of structures caused by wet snow may have several damaging effects on structures. This type of snow contains a certain amount of liquid and can be observed for temperature close to water fusion temperature. Wet snow can be classified as an icing precipitation with freezing rain [1]. The phenomena may affect several engineering domains as buildings, cables, wind turbine and transport.

### **2.1.1 Interactions with buildings.**

The problem of snow accumulation on buildings has interested scientists since 1800's, when roof slate tiles were used for pitched roofs and the overweight induced by snow could cause the breakup of tiles. Design and construction practices have changed in many ways. New trends like energy conservation, exclusive architecture, taller buildings and use of new materials and technologies have an impact on the performance of a building with respect to its environment. Facades are often tested for wind impact, thermal performance, water infiltration and structural capabilities. In specific cases, facades should also be tested regarding ice and snow accumulation risks [2]. As shown in Figure 2, large snow accumulation on building may lead to severe risks for people and structures.



Figure 2. Examples of the damages caused by snow accumulation: (a) a collapsed roofs [3], (b) a massive snow fall from a roof in Scotland [4].

The influence of winter conditions on buildings is far from controllable but could be inferred by review and analysis of historical meteorological data. This analysis is made by recording the frequency of the phenomena and the potential hazard associated [5-8]. Several climatic phenomena can affect buildings: wind drift, snow formations, sliding snow, snow loads, snow creep, melt water drainage issues, icicle formation, sliding ice sheets, etc.(Figure 3).



Figure 3. (a) An example of icicles formation on a building [9]. (b) A snow sliding phenomenon [10]

As seen above, the snow accretion may constitute a significant risk to people and structures. A better comprehension of parameters and physical processes which govern this phenomenon is necessary to foresee how and when snow accretions take place on building. An example of the necessity of a regulation to predict accretion phenomenon is the devastating icing event that took place in Quebec in January 1998. Two million people remained without electricity as the consequence of the collapse of 1300 high-power line towers due to accretion overload..

### 2.1.2 Interactions with cables.

As seen from the accident described above, wet snow accretions can occur on cables. As reported by Poots et al. [11, 12] the accretions on cables occur in a temperature range between  $0^{\circ}\text{C}$  and  $5^{\circ}\text{C}$ . Additionally Sakamoto [13] has shown how also in case of sub-freezing temperature, in conjunction with a wind speed less than  $2\text{m/s}$ , accretions on cable can occur. In the accretion process snowflakes collide with the snow/conductor surface: a part of the snowflakes will stick on the surface while another part rebound into the air flow. During the accretion process, snowflakes undertake a rapid thermodynamic process which permits snowflakes to bound together principally by capillary forces and forms a snow matrix [11]. In case of severe precipitation the accretion can grow rapidly and induce a serious overload problem. (Figure 4).

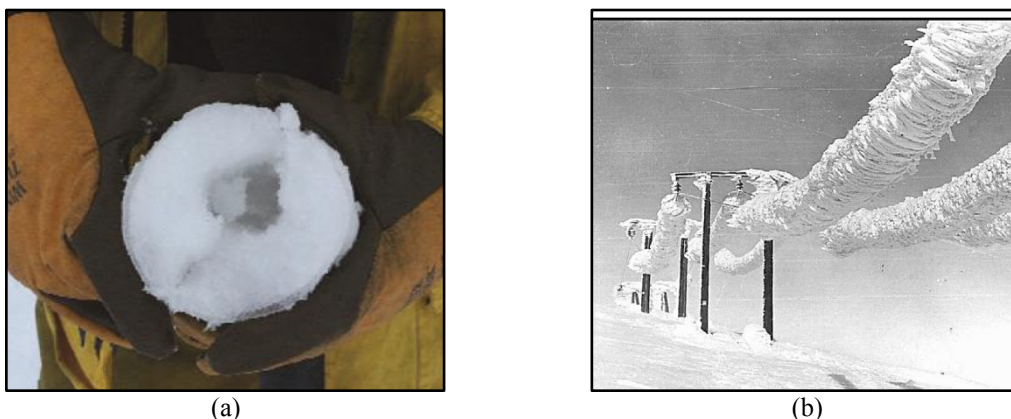


Figure 4. (a) example of accretion on cables which gives an extra load of  $5\text{kg/m}$  [14]. (b) the highest accretion phenomena documented [15]

Additionally it should be noted that in case of a temperature decreasing after wet-snow has formed on the cable, the accretion will freeze. In this case the adhesive

forces are strong, accretion becomes hard to shed. As a consequence a combination of snow and wind load takes place which can cause galloping [16]. Very few attempts have been made to study wet-snow accretion on cable in wind-tunnel. For this reason there is not a common procedure to reproduce and analysis the phenomenon in wind-tunnel. A method can be to collect fresh snow available outdoor and spread it in a cold chamber [13, 17].

### **2.1.3 Interactions with terrestrial transports.**

Terrestrial transports, focusing on the train case, may also be affected by wet-snow accretion problems. On trains the phenomenon occurs mainly in the bogies and the underframe. Snowpacking affects the bogie movements, movements within the bogie and all components placed underneath the carbody (Figure 5) [18].



(a) (b)  
Figure 5. (a-b) Wet-snow accretions on bogies train [18].

Snow accretions may block bogies movements, damage components and reduced accessibility for maintenance. It has been shown during a study in Japan how wet-snow accretion build up very fast in the underframe when average ambient temperature gets around  $-4^{\circ}\text{C}$  and the amount of snowfall exceeds  $3\text{cm}$  [18]. Like in wet-snow accretions on cables and buildings a universal modeling to prevent these hazards is not available, neither a regulation to design train against wet-snow accretion.

### **2.1.4 Interactions with wind turbines.**

The last branch which has been investigated for wet-snow accretion is the wind turbine case. Due to its low density, snow can be carried by the wind and ingested by wind turbine. In case of wind turbine nacelles, which are not necessary airtight, snow ingestion can be very fast. Snow accumulation inside the nacelle can damage electrical equipment and can also obstructs the ventilation openings and prevent the normal air circulation [19]. In case of accretion on blades, like reported by Bose [20], this accretion lead to vibration and power losses.

### **2.1.5 Overview conclusion.**

As seen from this concise overview, wet-snow accretion is a natural phenomenon which affects many engineering domains. Moreover, at the actual state, there is not a common and unique procedure to approach the problem seen its vastness. Once presented the principal engineering domains concerned by wet snow accretions, the work continues with a brief description of the particles which give origin to the phenomenon. This allows to present the characteristic parameters of wet snow particles on which will be based this work: the liquid water content *LWC*.

## 2.2 Physical characterization of snow particles responsible of wet snow accretions.

Snowflakes are constituted of two or three phases: ice, water vapor saturated and water. The presence at the same time of these phases shows that the formation of snowflakes is not far from water triple point [21]. As a consequence there are constant exchanges between phases; snowflakes are in constant evolution.

The formation of snow crystals begins in clouds in two main ways. The first way is related to nucleation of so-called “freezing nuclei” when the atmospheric temperature is below  $-12^{\circ}\text{C}$ . Freezing nuclei are solid particles suspended in clouds with a form similar to the ice crystal one. These freezing nuclei, when immersed in a supercooled water mass, permits the ice crystal growth. The second way is the freezing of droplets measuring  $20 - 50\mu\text{m}$  when ambient temperature is between  $-3^{\circ}\text{C}$  and  $-35^{\circ}\text{C}$  [22]. In both cases the initial shape is hexagonal and remains in continuous evolution according to the conditions of temperature and humidity of the environment. Once a droplet has frozen, it grows in the supersaturated environment: humid air is saturated with respect to ice when the temperature is below the freezing point. The droplets then grow by deposition of water molecules in the air (vapor) onto the ice crystal surface. This process is known as the Wegner-Bergeron-Findeison process [23]. Because water droplets are much more numerous than the ice crystals, the crystals are able to grow to hundreds of micrometers or millimeters in size at the expense of the water droplets. When snowflakes reach a millimetric size the growth continues by a mechanical bounding process with other ice crystals. As snowflakes reach a dimension around a centimeter they start to fall by gravity and may collide and stick together in clusters, or aggregates. In Figure 6.a is presented an example of this kind of crystals which are named dry snowflakes. However, precipitating snowflakes may pass through the isotherm  $0^{\circ}\text{C}$  and meet air at positive temperature. In this case, snowflakes growth stops due to a lack of thermal exchanges with the surrounding environment and a liquid film occurs on snowflakes surface (Figure 6.b). This liquid film assures a strong capillary bounding between snowflakes.

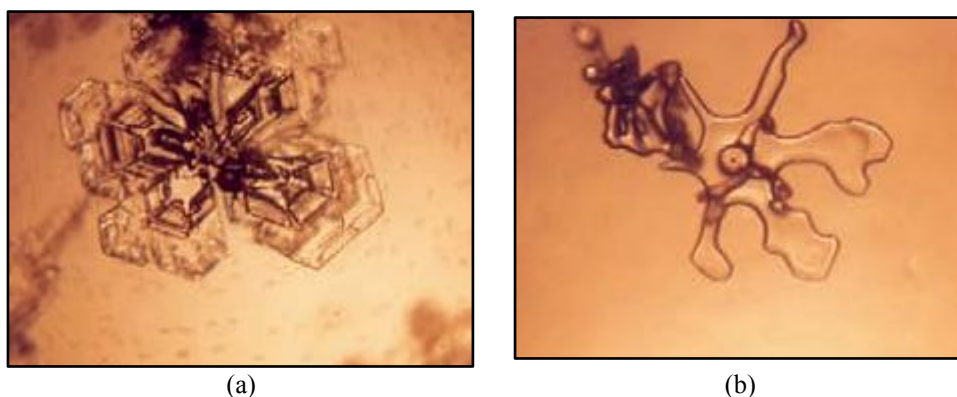


Figure 6. Example snowflakes: (a) dry snowflakes [24] (b) wet snowflakes [24].

When wet snowflakes, which contain an important quantity of water, strikes an obstacle the metamorphosis process is accelerated. Suddenly snowflakes lose their sharpness and turn into agglomerates of sub-millimetric ice granules with high inclusion of air bubbles. In these agglomerate ice granules (Figure 7.a), air bubbles and liquid water are jointed together by capillary forces [25]. In the case of an excessive heat

exchanges the liquid water can reach 40% and ice granules change into ice plates, just before they melt completely (Figure 7.b).

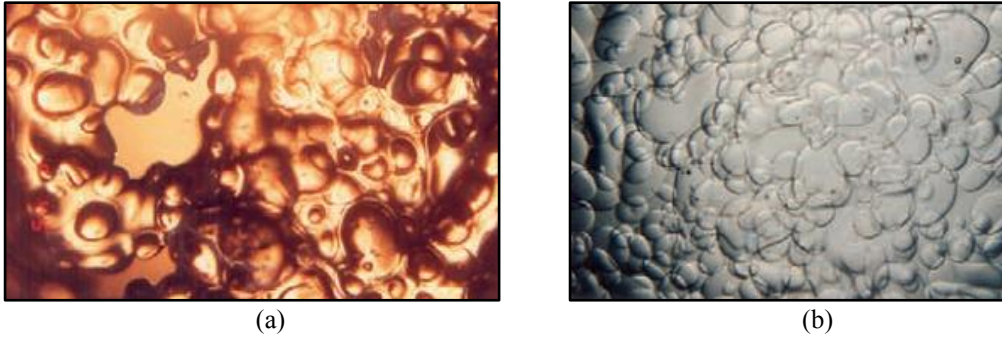


Figure 7. Wet snow aggregate: (a) capillary liquid water between 5-15% and air bubble which is often >50% in volume [24] (b) aggregate of wet snow which is melting [24].

The heat and mass exchange between the snowflakes and the environment lead to a ratio between ice, liquid water and air which is intimately related to ambient conditions as temperature and humidity. Wet-snow often falls for ambient temperature between  $1^{\circ}\text{C}$  and  $-5^{\circ}\text{C}$ . This snow can stick and accumulate on different structures like cable, wind turbine and buildings and can cause several damages as seen before. In this work, we assume that the accumulation is strictly dependent on snowflakes density and liquid water content ( $LWC$ ). The liquid water content of a snowflake indicates the quantity of water inside a snowflake.  $LWC$  can be expressed as the ratio between the liquid mass  $m_p^l$  and the total mass  $m_p$  of the snowflakes, and is dimensionless (1).

$$LWC = \frac{m_p^l}{m_p} \quad (1)$$

In this work the above definition is adopted as being more suitable to the building and civil engineering context instead of the aeronautic usual definition. In the aeronautic domain,  $LWC$  means the liquid content of a cloud with respect to a specific amount of dry air, in this case it is measured in  $\text{g}/\text{m}^3$ .

A snowflakes form strictly related to this study is a snow droplet produced by snow guns. Artificial snow is made by mixing water and air at high pressure and injecting this mixing out from a nozzle. Artificial snow is made of water droplets which freezes along their trajectory (Figure 8.a). The size and shape of artificial snow particles are different from natural fresh snow crystal structures (Figure 8.b). They are more comparable to eroded particles observed during wind driven snow events

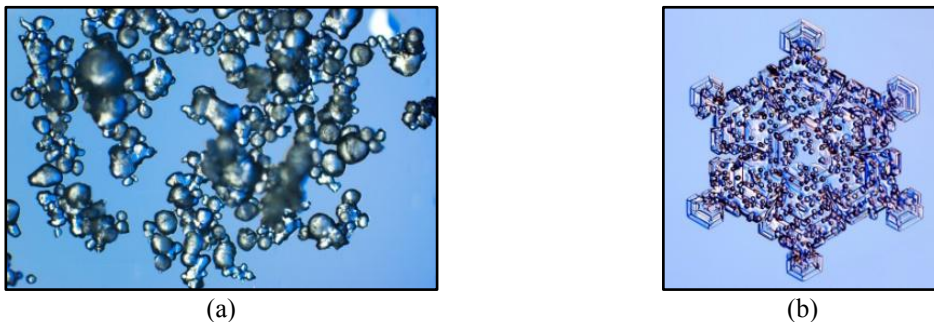


Figure 8. (a) an artificial snowflakes. (b) a natural snowflake. [24].

### 2.2.1 An approach to reproduce wet snow: artificial snow produced by a snow gun.

As exposed below, the experimental approach used in this work to study the wet snow accretion uses the capabilities of a large climatic facility including artificial-snow-making. The fully controllable environment of the test chamber allows to control the particle liquid water content  $LWC$  during the experimental campaign as explained in chapter 3. Artificial snow is made of water droplets which freeze when injected in the ambient air. A snow gun mixes compressed air and water. When this mixture exits the nozzle, it expands and produces a spray that cools down. Water droplets freeze into ice crystals, normally these kind of particles are smaller than natural snowflakes. Three systems are used in artificial snow production (Figure 9)

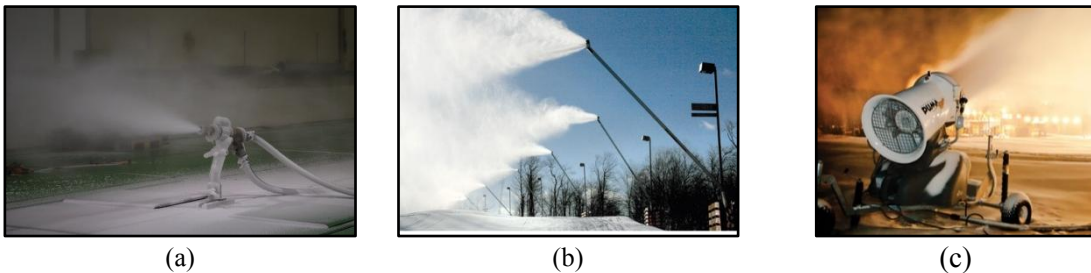


Figure 9. Artificial snow systems production: (a) internal mix system. b) external mix system [26]. c) air/water/fan system [26].

Moreover due to the physical atomization process, artificial snow particles are close to a spherical shape [27, 28].

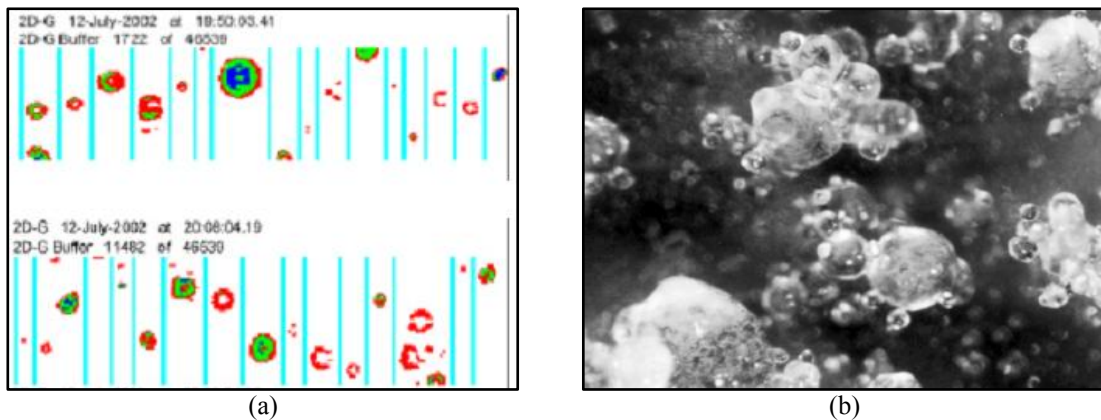


Figure 10. Sample ice particles images from a snow gun with internal mix system: (a) captured using the OAP (Particle Measuring Systems 2D-Grey Optical Array Probe) system [27]. (b) photographed with a microscope [28].

Whatever the method chosen to produce artificial snow with snow gun, this is made by mixing air and water and by pulverizing this mixture in the air. Once in the air, water cools and then starts to freeze along its path. As detailed in chapter three, this method is used during the experimental campaign to reproduce wet snow particles. Moreover, particles which have a mixed phase can be characterized by a parameter as seen before: the liquid water content  $LWC$ . A series of examples to better understand the influence of the  $LWC$  on the accretions in aeronautic domain are here presented.

### 2.2.2 Snow particles characterization conclusion.

The previous paragraph has introduced the different conditions under which a snowflake can have origin. Considering the context of this work, the most important feature of a snowflakes is its classification in a dry snowflakes and wet snowflakes. Moreover, wet snow accretions are relied to wet snowflakes which impacting a structure give origin to accretion. These wet snowflakes are characterized by a mixture of a solid and a liquid part. This mixture is synthetized by a parameter called *LWC* which represents the ratio between the liquid and the total mass of the particle.

### 2.3 Effects of LWC on in cloud icing accretions

As discussed before the liquid water content can be defined in two different ways. In case of wet snow accretions, the *LWC* characterizes the quantity of water of snowflake mixed phase. It quantifies the ratio between the liquid mass and the total mass of the particle. In case of aircraft icing it most often means the water concentration in the air.

Here after are reported some test results of the effect of the *LWC* in case of in cloud icing. The examples are extracted from aeronautical icing studies. Following the *LWC* definition in aircraft domain an increase of *LWC* means an increase of water concentration in the air. On the other hand, in case of wet snow accretion, an increase of *LWC* means an increase of the liquid part of particles with the same particle concentration.

Examples of the *LWC* effects in case of in cloud icing are reported by Lynch et al. [29]. In Figure 11 is reported the effect of the *LWC* on an airfoil. As one can note, the *LWC* increase has produced an important variation of the accretion on the front part of the airfoil. The accretion shape is also concerned by the *LWC* increase. The accretion on the rear part of the airfoil seems unchanged.

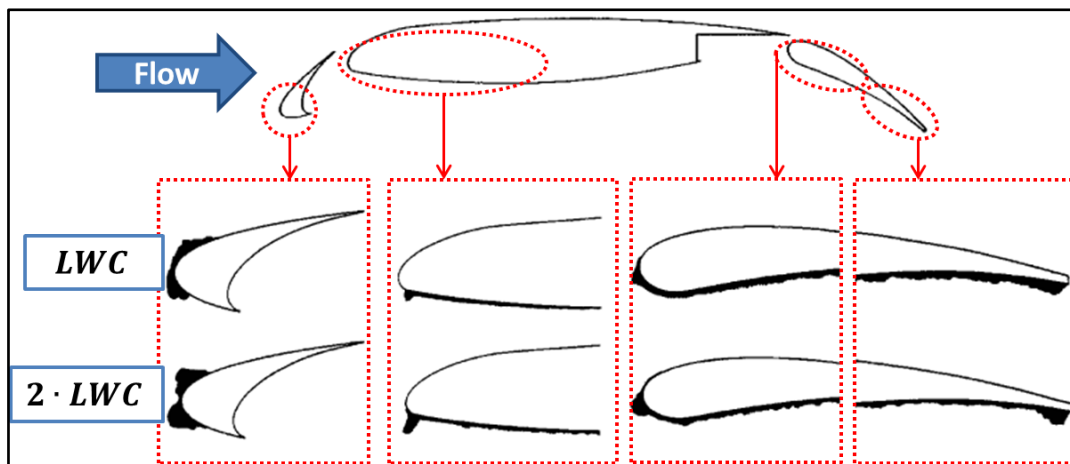


Figure 11. Effects of *LWC* on airfoil, experimental test [29].

The accretion leads to a reduction of the aerodynamic performance of the airfoil as shown by Bragg [30] which may induces risks for aircrafts, or in performance losses of wind turbines (Seifert et al. [31]).

Gent et al. [32] has shown how the augmentation of the  $LWC$  can lead to more accretion on an airfoil while the accretion pattern is the same (Figure 12)

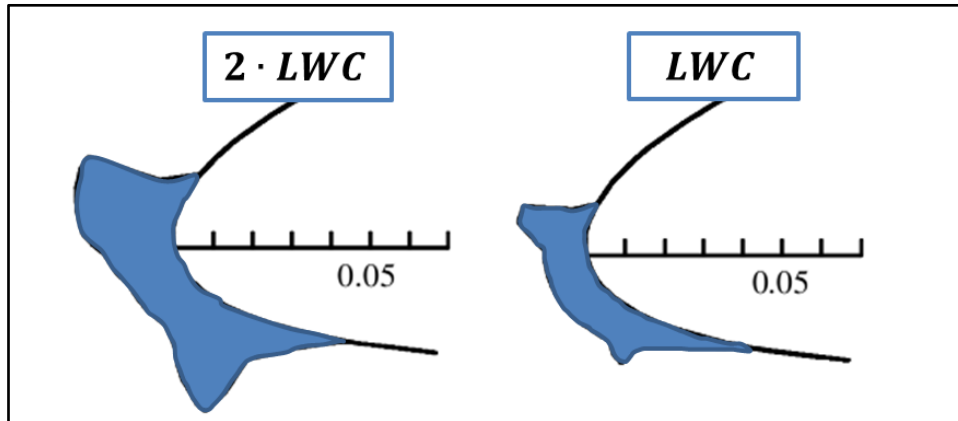


Figure 12. Impact of  $LWC$  variation on in cloud icing of an airfoil, experimental test [32].

One of the most relevant works on the  $LWC$  variation effects on the resulting accretions was presented by Lozowski et al. [33]. In this work the accretion phenomenon has been investigated on a horizontal cylinder for increasing values of  $LWC$ . Figure 13 shows how the accretion increases with the increase of the  $LWC$  and the mean speed of the flow  $\langle u_f \rangle$ .

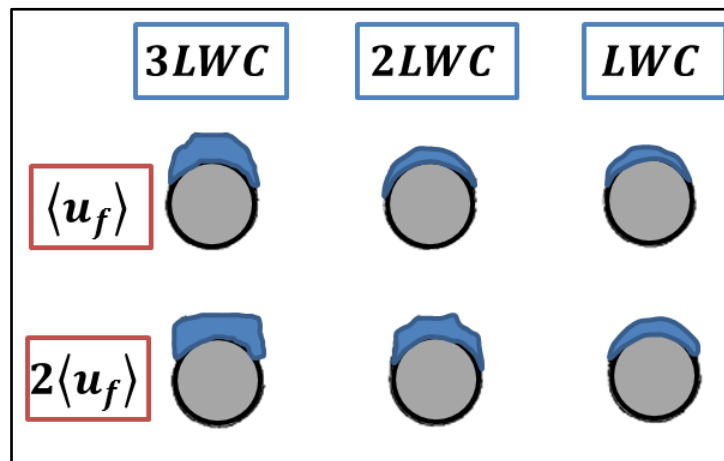


Figure 13. Impact of  $LWC$  and  $\langle u_f \rangle$  variation on resulting ice accretion on a cylinder (diameter 2.54mm), experimental test at  $T_a = -15^\circ\text{C}$  [33]. Test duration for  $\langle u_f \rangle$ :  $t \approx 5\text{min}$ ; for  $2\langle u_f \rangle$  when  $3LWC$  and  $LWC$   $t \approx 2.5\text{min}$ , when  $2LWC$   $t \approx 1\text{min}$ .

The work of Lozowski et al. [33] has also investigated the relation between the  $LWC$  and the ambient temperature  $T_a = -5^\circ\text{C}$ . As one can note from Figure 14 the accretion increases with the  $LWC$  whatever is the ambient temperature. Moreover, the ice accretion on the cylinder is less extended for the lowest ambient temperature.

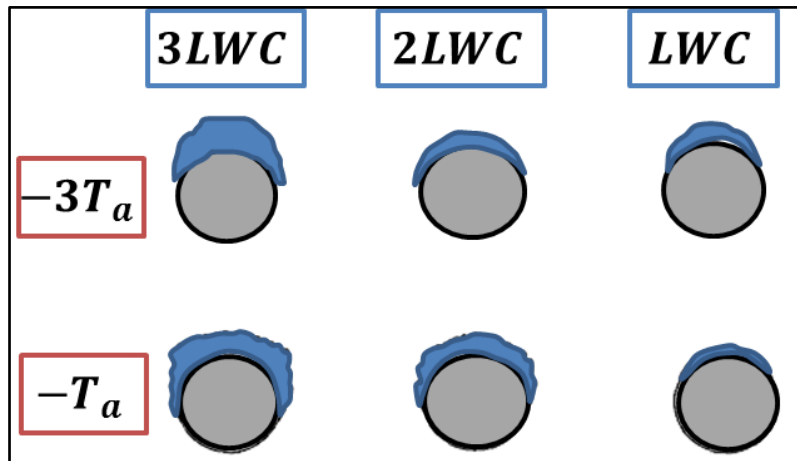


Figure 14. Effects in cloud icing on a cylinder(diameter 2.54mm), experimental tests as a function of  $T_a$  and  $LWC$ , mean wind speed  $\langle u_f \rangle = 30m/s$  [33]. Test duration  $t \approx 5min$ .

The works of Lozowski have also noted how the increase of the  $LWC$  can act on the accretion shape as also reported by Lynch et al.[29]. In Figure 15 is reported for an ambient temperature of  $T_a = -8^\circ C$  the three accretions obtained as a function of the  $LWC$  on the cylinder.

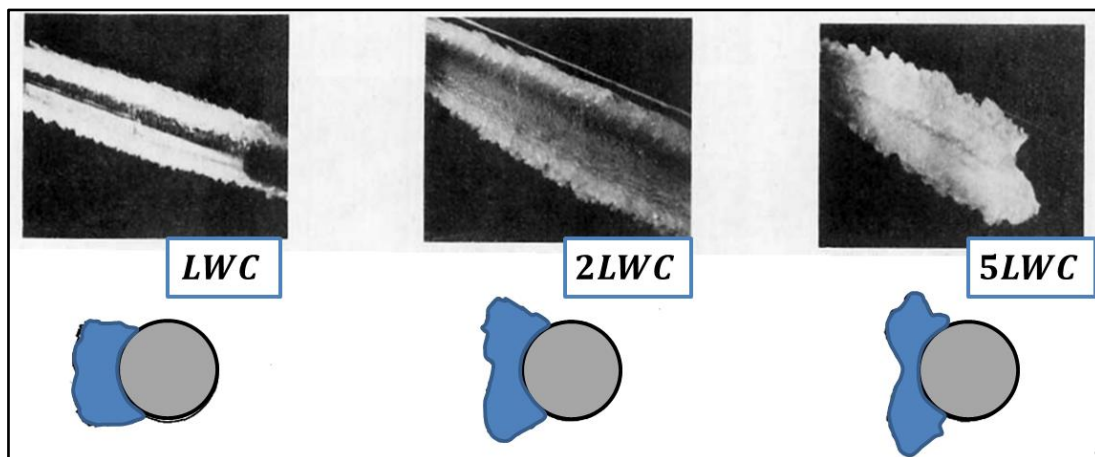


Figure 15. Effects of  $LWC$  on cylinder accretions (diameter 2.54mm), experimental tests [33].  $\langle u_f \rangle = 110m/s$ . Test duration  $LWC t \approx 20min$ ,  $2LWC t \approx 10min$ ,  $5LWC t \approx 5min$

As will be detailed later, the experiments made by Lozowski are very close to the one performed in this work. However, Lozowski's work is based on the aeronautical definition of  $LWC$  which is different from the definition adopted in this work to describe wet snow accretions. As a consequence, the results of Lozowski et al. cannot be directly compared to the one obtained during the experimental campaign of this work.

As one can note from the examples reported above, the liquid water content, that determines the dry or wet regime of the icing phenomena along with other ambient parameters, influences in an important way the accretion. Among the parameters which can influence the accretion process, during this work will be deepen the  $LWC$ . Here after will be introduced the numerical approach undertaken to study the accretions.

## 2.4 Modeling wet snow accretions: the approach chosen.

Following previous works by Makkonen [34, 35], Lozowski et al. [36], also summarized in the ISO 12494 standard [37], the accretion modeling considers three steps. According to these three steps, the accretion process will be analyzed, considering the aerodynamic, the mechanical and the thermal aspects. Before to proceed, it is important to remember how wet snow particles are characterized by a liquid and a solid part. The approach chosen will take into account these two parts.

The first step of the modeling concerns the analysis of the aerodynamic aspect. It concerns the evaluation of the probability for a snow particle approaching the structure, to strike or not the structure. The second step consists in estimating, once the particle has struck on the structure, whether it sticks or not on the surface structure. This step concerns the mechanical aspect of wet snow accretion. The last step concerns mainly the liquid part of the particle. It will be estimated the fraction of the liquid part which freezes once it has stuck on the structure. This last step concerns the thermal aspect of the accretion process.

The three steps of the modeling are summarized by three dimensionless coefficient presented below.

### 2.4.1 Aerodynamic aspect of accretion process: collision efficiency.

The aerodynamic aspect consists in establishing if the snow particles, which are approaching a structure, strike it or not. This aspect is modeled in this work by a parameter called collision efficiency  $\eta_1$  (2).

$$\eta_1 = \frac{\dot{m}_{imp}}{\dot{m}_{inc}} \quad (2)$$

This coefficient represents the mass of particles impacting the structure normalized by a reference surface:  $\dot{m}_{imp}$  divided by the incoming mass flux upstream the structure:  $\dot{m}_{inc}$ . Both the mass fluxes are quantified in  $\left[\frac{kg}{m^2s}\right]$ . As a consequence  $\eta_1$  is dimensionless and its values is between 0 and 1.

Let us consider as an example, a cylindrical object. The particles far upstream the cylinder are assumed to be moving at free stream velocity. While approaching the cylinder, a particle undergoes a deflecting force due to the diverging streamlines and a resistance due to its own inertia. Thus the particle motion relative to the airflow increases and the particle may not reach the cylinder surface before it is swept away by the airflow. The collision efficiency is reduced from one, because small particles tend to follow the air flow and can be deflected from their path towards the object (Figure 16). A collision efficiency  $\eta_1 = 0$  means that the incoming particle flux does not strike the structure surface while  $\eta_1 = 1$ , means that the whole incoming mass flux strikes the structure surface.

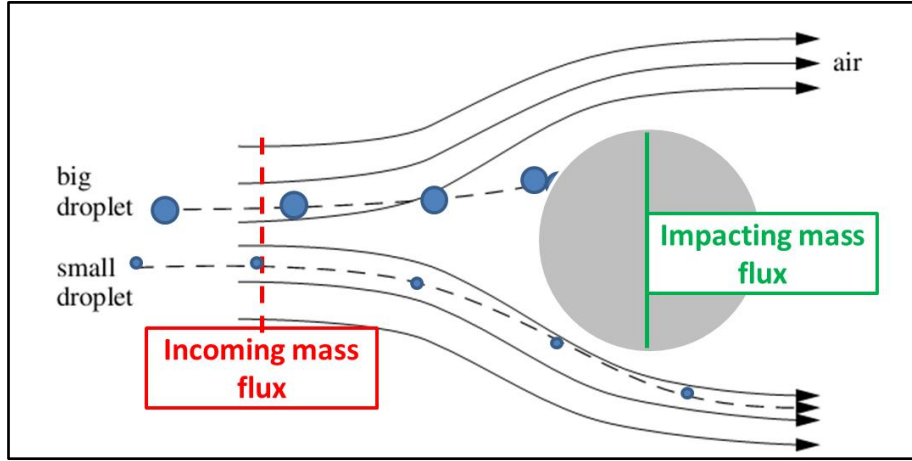


Figure 16. Collision efficiency  $\eta_1$ .

The collision efficiency evaluation will be deepened in chapter five where the numerical approach is presented.

#### 2.4.2 Mechanical aspect of accretion process: sticking efficiency.

Once a particle has struck the structure surface, the ratio between the sticking mass flux and the impacting mass flux is expressed by the sticking efficiency  $\eta_2$ (3). The sticking efficiency has a range between 0 and 1.

$$\eta_2 = \frac{\dot{m}_{stick}}{\dot{m}_{imp}} \quad (3)$$

According to the nature of particles the sticking efficiency may change. Water droplets can be generally considered not to bounce, so the  $\eta_2$  will be almost one as assumed in previous works (see for instance the ISO 12494 standard [34]). However, it is well known that liquid particle can splash when impacting a surface (Mundo et al. [35]). In case of frozen or partially frozen particles a fragmentation phenomenon may happen when striking a structure. In this case, Makkonen [15] reports how the volume of these fragments are very small and so the effect on the icing process can be negligible. For solid particles colliding a dry structure, the sticking coefficient is basically zero as noted by the ISO standard [34] which means  $\eta_2 \approx 0$ . Makkonen [15] points out how nowadays there is no universal theory about the sticking coefficient for wet snow particles.

The ISO 12494 standard [34] considers in case of wet snow particles the sticking coefficient for both the liquid and the solid part can be considered almost one at low impact speed. Moreover, the ISO 12494 standard suggests an empirical approach based on the mean flow speed  $\langle u_f \rangle$ :  $\eta_2 = 1/\langle u_f \rangle$ . Owing to this formulation the measurement unit should be  $\left[\frac{s}{m}\right]$ , but due to its empirical nature, the coefficient is considered dimensionless. Moreover no distinction between solid and liquid part is done in this case.

Another approach to evaluate the sticking coefficient has been presented by Trenker et al. [36, 37]. This work is related to wet snow particles and no distinction between liquid and solid part is made. Two conditions are imposed to assume particles

adherence. The first one concerns the particle angle of impact. The angle between the trajectory and the surface normal must be smaller than  $45^\circ$ . The second condition is a friction velocity smaller than  $0.21\text{m/s}$ . If one of these two conditions is not satisfied, the particle bounces. If this happens, the particle momentum is reduced to a fraction of the initial value, i.e. 1% in the normal direction and 20% in the tangential direction. This empirical approach has been applied to assess snow accretion on an airfoil and on train components. Due to the general characteristics, it might be applied in other cases. In this work, the Trenker's approach is adopted in chapter five to analyze the accretion shapes.

### 2.4.3 Thermal aspect of accretion process: accretion efficiency.

Once a snow particle sticks on a structure a thermal exchange arises between the surface and the particle as reported by Cansdale [38], Messinger [39] or Lozowski et al. [40]. Considering the liquid part of the impacting mass flux, the accretion efficiency can be expressed as (4).

$$\eta_3 = \frac{\dot{m}_{acc}}{\dot{m}_{stick}} \quad (4)$$

Where  $\dot{m}_{acc}$  represents the accretion mass flux related to the liquid and solid part of particles. This parameter represents the liquid mass flux which freezes and gives a contribution to the accretion with respect to the liquid mass flux which sticks to the structure. The most common models (Messinger [39], Guffond [41], Makkonen[42] or Lozowski et al. [40]) quantify the accretion efficiency with a mass balance and a thermal balance. As reported by Makkonen [15], to the value of  $\eta_3$  can be associated the form of the accretion and its definition. In case  $\eta_3 = 1$ , when all the sticking water freezes, the accretion is defined as rime. Figure 17.a shows a scheme of a rime ice while Figure 17.b an image of a rime ice accretion.

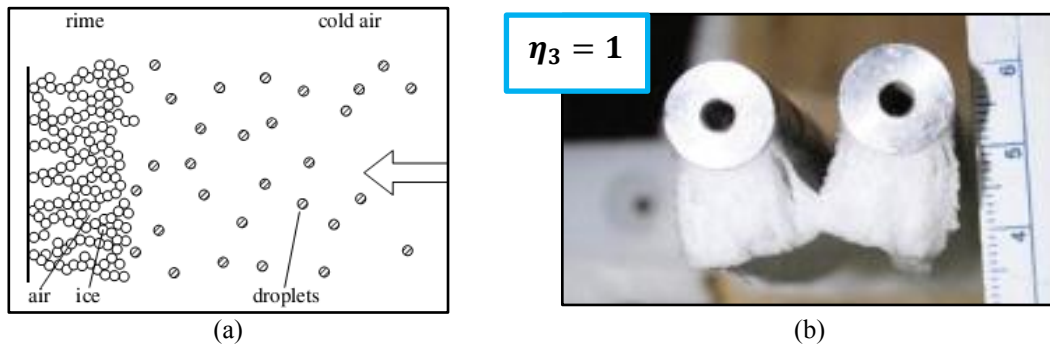


Figure 17. Rime ice accretion,  $\eta_3 = 1$ : (a) schematic representation [15]. (b) an image [43].

When not all the sticking water freezes, the accretion is called glaze ice and  $0 < \eta_3 < 1$ . In this case the accretion can trap the not-frozen water as reported by Makkonen [15] or Knight [44]. A representation of glaze ice accretion is reported in Figure 18.

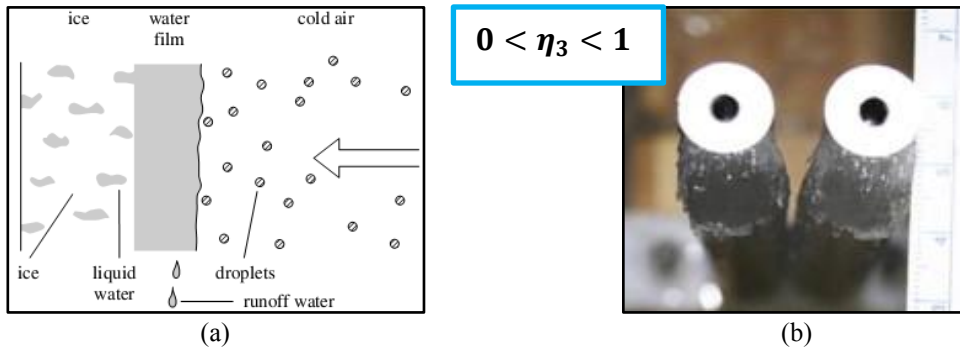


Figure 18. Glaze ice accretion,  $0 < \eta_3 < 1$ : (a) schematic representation [15]. (b) an image [43].

At the current state of knowledge the most common models estimate the accretion efficiency taking only into account the liquid part of the particle. These models have been developed for aircraft icing, where the solid part of particles is not considered or does not play a fundamental role in the accretion process (Brunet [45]).

Models which consider a theoretical approach to deal with the solid part of particle have been proposed by Cansdale et al. [38], Brunet [45] or Wright [46]. For the first two works mentioned, only the theoretical formulation is given without any application to real cases. Wright proposes a series of results without deepen in the theoretical background.

In this work the accretion efficiency is taken equal to one. A discussion about this assumption is undertaken on chapter five.

#### 2.4.4 Accretion modeling conclusion and synthesis of the accretion steps

In this work the approach to model the accretion process considers three steps which are synthesized by three dimensionless coefficients. The collision efficiency  $\eta_1$ , the sticking efficiency  $\eta_2$  and the accretion efficiency  $\eta_3$ . In Figure 19 is reported a synthesis of the three coefficient.

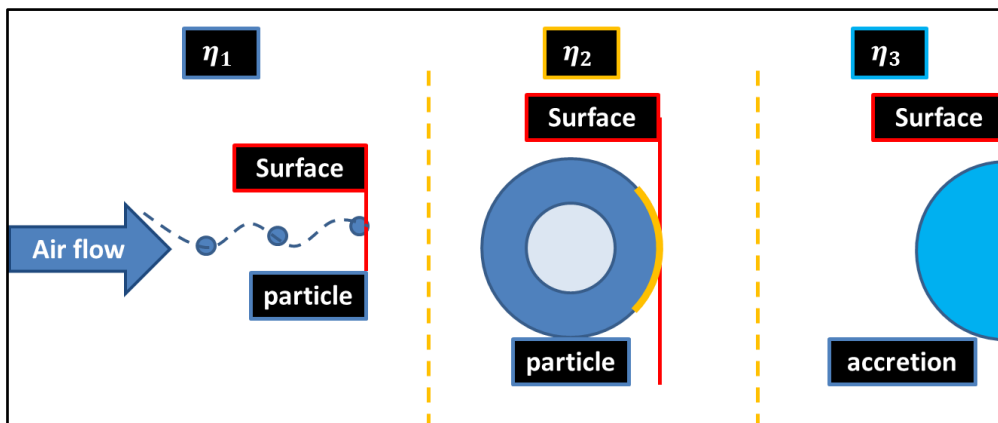


Figure 19. Synthesis of the coefficients to model the accretion.

If one takes into account the mass flux approaching a structure  $\dot{m}_{inc}$  through the three coefficients presented before: (2) (3) (4) it is possible to estimate the mass flux of the accretion  $\dot{m}_{acc}$  (5):

$$\dot{m}_{imp} = \dot{m}_{inc} \cdot \eta_1$$

$$\dot{m}_{stick} = \dot{m}_{inc} \cdot \eta_1 \cdot \eta_2 \tag{5}$$

$$\dot{m}_{acc} = \dot{m}_{inc} \cdot \eta_1 \cdot \eta_2 \cdot \eta_3$$

To synthesize the effects of the three steps of the approach a global dimensionless coefficient is proposed (6). It represents the ratio between the accretion mass flux  $\dot{m}_{acc}$  and the incoming mass flux  $\dot{m}_{inc}$ .

$$\beta^{123} = \frac{\dot{m}_{acc}}{\dot{m}_{inc}} = \eta_1 \cdot \eta_2 \cdot \eta_3 \tag{6}$$

The coefficient  $\beta$  will be the leading thread of the analysis presented in this work and it takes into account the three aspects of wet snow accretion: aerodynamic, mechanical and thermal aspect. The coefficient  $\beta$  will allow to characterize the accretion obtained during the experimental campaign. Furthermore it will allow the analysis between the experimental results and the numerical one.

## 2.5 Theoretical approach to control particle *LWC*: the particle freezing theory.

Artificial snow during the experimental campaign is produced by a snow gun which injects liquid particles that freeze in contact with the ambient air. This freezing process leads to particles characterized by a ratio of a solid and a liquid part. This ratio is quantified in this work by the *LWC*.

A part of the experimental campaign will be focused on the effect of the *LWC* on the accretions. As will be detailed during the experimental chapter the *LWC* will vary as a function of the ambient temperature  $T_a$ . Therefore, to explain the approach adopted during the experimental campaign, this part of the literature review concerns the presentation of the particle freezing theory.

The theoretical development is based on the works presented by Hindmarsh et al. [47] and Strub et al. [48] with the following hypothesis:

- a uniform particle temperature.
- during the entire freezing process the particle remains spherical.

The first assumption allows to assume that the transient heat transfer between the liquid particle and the environment can be modeled by a thermal balance that considers the heat flux at the particle surface and the particle internal energy. The second assumption allows to describe the process with a one dimensional model. The heat fluxes which characterize the evolution of the freezing particle are due to convection:  $q_h$  [W], mass transfer:  $q_m$  [W] and radiation:  $q_r$  [W] (7).

$$\begin{aligned}
 q_h &= -h_p(T_p - T_a)S_p \\
 q_m &= -Lh_m(C_p - C_a)S_p \\
 q_r &= -\sigma\hat{\varepsilon}(T_p^4 - T_a^4)S_p
 \end{aligned}
 \tag{7}$$

Analyzing the convection, the heat transfer coefficient of the particle is noted as  $h_p$ ,  $T_p$  is the particle temperature and  $S_p$  is the particle surface.

Considering the mass transfer,  $L$  is the latent heat of evaporation or sublimation in case the particle is respectively liquid or solid.  $h_m$  is the mass exchange coefficient and  $(C_p - C_a)$  is the difference between the water vapour mass concentration at the particle-air interface  $C_p$  and the ambient  $C_a$ .

The radiation is expressed as a function of  $\sigma$  which is the Stefan-Boltzmann constant,  $\hat{\varepsilon}$  which is the snow emissivity and the difference between the particle temperature at power four and the ambient temperature at power four.

The freezing process of a particle can be divided in four subsequent phases (Figure 20) [47-49]. In Figure 20 the evolution of the particle temperature during the freezing process is represented with a continuous black line.

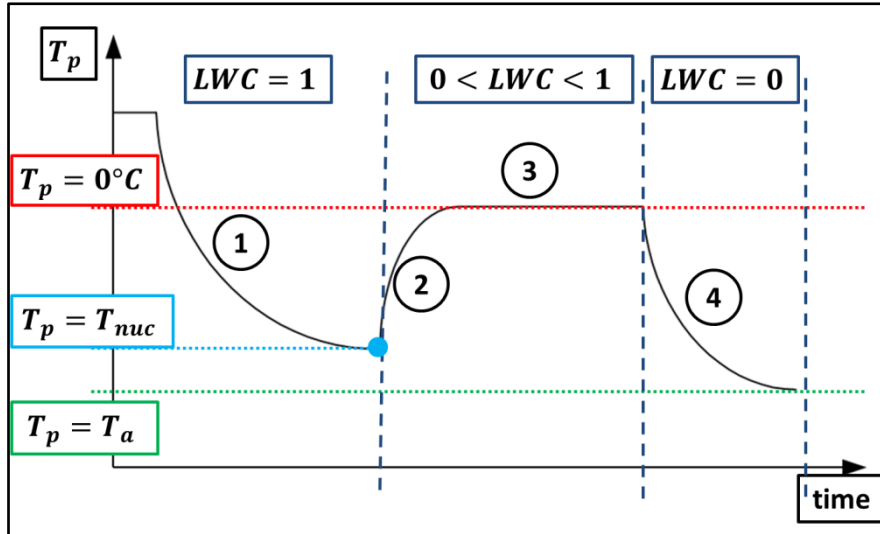


Figure 20. The four stages of a particle freezing process

The first phase of the process is represented by the so-called supercooling stage. During this stage the liquid particle may be cooled from the initial temperature to below the equilibrium freezing temperature (In Figure 20 represented by a red discontinuous line) until crystal nucleation occurs. The temperature at which starts the crystal nucleation is called the nucleation temperature from the work of Feuillebois [50]. Here convection and evaporation mainly drive the process. In the first stage the liquid water content of the particle is equal to one:  $LWC = 1$ .

The second phase is the recalescence stage, where supercooling drives rapidly the crystal growth [47]. The second stage ends when the particle temperature has

reached the equilibrium freezing temperature. This stage is the shortest one [48] among the four stages.

When the particle reaches the third phase the freezing process takes place driven mostly by convection, evaporation and sublimation. During this phase crystal grows at constant temperature till the particle is completely frozen. In the third phase the liquid water content is between zero and one:  $0 < LWC < 1$ . As will be shown later in chapter four, in this framework, this stage represents the longest among the four.

During the last phase the solid droplet temperature decreases close to the ambient temperature, a green discontinuous line in Figure 20, by convection and sublimation principally. In this case  $LWC = 0$ , the particle is completely frozen.

### ***The first phase (supercooling stage)***

This stage represents the first cooling part when the particle is entirely liquid:  $LWC = 1$ . The process involves a heat transfer by convection, a mass transfer by evaporation and a heat transfer by thermal radiation. The heat transfer by forced convection between the particle and the airflow is due to the temperature difference. For the same reason a heat transfer by thermal radiation takes place. Additionally the mass transfer by evaporation is due to the humidity difference between the drop-air interface and the ambient air.

The equation balance of this phase is obtained by balancing the internal energy with the heat flux from the droplet (8) for each time step  $dt$ . It allows to evaluate the temperature evolution of the particle. As indicated above, this is possible owing to the assumption of uniform temperature of the particle.

$$\rho_l V_p c_p^l \frac{dT_p^l}{dt} = -q_h - q_m - q_r W \quad (8)$$

In the equation  $\rho_l$  is the density of water,  $V_p$  is the particle volume and  $c_p^l$  the specific heat of water at constant pressure.  $T_p^l$  represents the temperature of the particle when it is in a liquid state. In this work this equation will be solved through a time discretization as function of the particle temperature  $T_p^l$ .

### ***The second phase (recalescence stage)***

The second stage of the particle freezing process is the so-called recalescence stage. Particle temperature increases rapidly after having reached the nucleation temperature ( $T_{nuc}$  in Figure 20). This stage represents, in the whole freezing process, the moment when the first ice layer appears. The most difficult part is the determination of the nucleation temperature. It can be measured using a thermocouple inside the water particle as reported by Strub et al. [48] or Hindmarsh et al. [47] as shown in Figure 21.

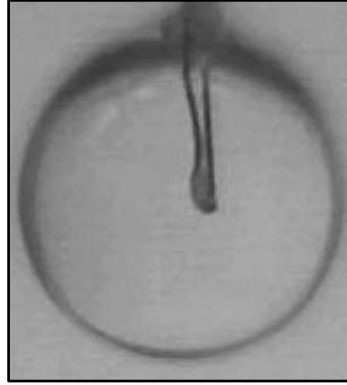


Figure 21. Thermocouple to measure the nucleation temperature [47]

Obviously, this approach can be only performed in case of a non-moving particle. The choice to record the nucleation temperature in this experimental approach is justified by the random characteristic of the nucleation process [48]. This means that the exact prediction of the crystallization is not possible. As explained by Dumas et al. [51] only the probability of crystallization can be determined. Additionally to the difficulties in its evaluation, the recalescence stage concerns a very short part of the freezing process as shown in this work. As a consequence, it will be considered negligible.

### **The third phase (freezing stage)**

After the recalescence stage the particle starts to freeze with the coexistence at the same time of a liquid and a solid part. That means that this phase is characterized by a  $0 < LWC < 1$ . With the hypothesis that the freezing process takes place uniformly in the whole particle, a *Heat balance model* is used in this work to evaluate the rate of frozen volume increase. The model has been presented by Hindmarsh et al. [47]. In this model the hypothesis of a constant freezing temperature is made. For each time step  $dt$  the heat balance is given by equation (9) which is solved as a function of the ice volume of particle  $V_p^i$ .

$$\rho_i L_f \frac{dV_p^i}{dt} = -q_h - q_m - q_r [W] \quad (9)$$

In this phase of the freezing process the particle temperature  $T_p$  is supposed equal to the equilibrium freezing temperature:  $T_p = 0^\circ C$ .  $\rho_i$  is the ice density,  $L_f$  the latent heat of fusion. The equation (9) is solved as a function of the ice volume  $V_p^i$ . Knowing the frozen particle volume it is possible to estimate the particle liquid water content as (10). In this work, equation (10), has been taken as a reference for the particles *LWC* estimation.

$$LWC = \frac{m_p^l}{m_p} = 1 - \frac{\rho_i V_p^i}{\rho_l V_p} \quad (10)$$

### **The fourth phase (tempering stage)**

Once the particle is completed frozen, which means  $LWC = 0$ , its temperature starts to fall down. As in the first stage the heat terms involved are convection:  $q_h$ , mass transfer:  $q_m$  and radiation:  $q_r$ .

As a consequence the heat balance is of the same form, the internal energy is balanced by the heat terms (11).

$$\rho_i V_p c_p^i \frac{dT_p^i}{dt} = -q_h - q_m - q_r [W] \quad (11)$$

Where  $c_p^i$  is the specific heat capacity at constant pressure of ice and  $T_p^i$  is the temperature of the frozen particle. Here the phase of the particles changed from liquid to solid then the mass transfer is due to sublimation instead of vaporization.

### 2.5.1 Particle freezing theory conclusion

The theoretical approach presented above will allow to justify the approach adopted during the experimental campaign. It will be shown how with the experimental physical parameters fixed the liquid water content can be tuned as a function of the ambient temperature:  $LWC = \mathcal{F}(T_a)$ . The particle freezing theory allows to estimate the particle  $LWC$  as a function of the ambient temperature  $T_a$ .

Due to the impossibility to measure the nucleation temperature  $T_{nuc}$  the implementation of this approach in this work will be constituted only by three phases:

- supercooling stage:  $LWC = 1$
- freezing stage:  $0 < LWC < 1$
- tempering stage:  $LWC = 0$

## 2.6 Theoretical approach to model snow particles dynamic in the air flow.

Snow particle dispersion in the air flow can be modeled as a two-phase flow. In this work the carrying phase is represented by the air flow and the second one is the discrete phase represented by snow particles. In the present work the evaluation of the particle dynamic in a flow concerns two parts. First a particle tracking model will be set up to estimate the particle size distribution at the experimental structure. Secondly, a numerical model to evaluate the collision efficiency will be presented in chapter five. Therefore, this part of the literature review is dedicated to an introduction of particle-flow interaction and modeling.

Two approaches have been developed to study the particles dispersion in flow: Eulerian approach and Lagrangian approach. In the first one the discrete phase is treated as a continuum. The conservation equations are developed in a control volume in a similar form as for the fluid phase. The Lagrangian approach considers particles as discrete phase and tracks the path of each particles distinctly. In this approach the fluid phase is treated as a continuum whereas the dispersed phase is solved computing the equation of motion of a large number of particles. Particles are modeled as spherical and smooth objects which can exchange mass, momentum and energy with the fluid phase. Two-way-coupling can be neglected if the dispersed phase does not influence the carrying phase [52, 53]. Lagrangian approach takes into consideration some aspects impossible or very hard to evaluate with Eulerian approach: particles rotation, particles wall interactions, particles-particles interaction an also large distributions of sizes. The

Lagrangian method [52], will be the one chosen to model particle-fluid interaction in this work.

### 2.6.1 Forces acting on particles

Particles are here assumed to be like solid spherical particles with a smooth surface. Moreover, they can be considered as points and momentum: heat and mass exchange can be modeled as a function of the local fluid properties if the particle diameter is smaller than the Kolmogorov scale in case of turbulent flow. Generally this last condition can be relaxed [52]. The equation governing particle motion is then the fundamental equation of mechanic (12).

$$\sum_i \vec{F}_i = m_p \cdot \vec{a}_p \quad (12)$$

where  $\vec{F}_i$  is any kind of forces acting on particle,  $m_p$  is the particle mass and  $\vec{a}_p$  is the particle acceleration.

#### The drag force.

The drag force is the net force in the direction of the flow due to pressure and shear stress forces on the surface of the object. It is in the opposite direction of particle relative velocity with respect to stream velocity (Figure 22).

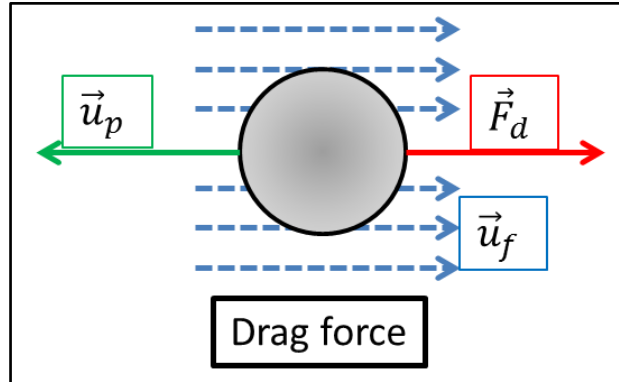


Figure 22. The drag force acting on a particle

The drag force is evaluated by using equation (13).

$$\vec{F}_d = \frac{1}{2} \rho_f S \vec{u}_r |\vec{u}_r| C_d \quad (13)$$

In this equation  $\rho_f$  is the density of flow,  $S$  the reference surface as  $\pi r^2$  where  $r$  is the particle radius. The relative velocity  $\vec{u}_r$  is defined as  $\vec{u}_r = \vec{u}_p - \vec{u}_f$  where  $\vec{u}_p$  is the velocity of the particle center of mass and  $\vec{u}_f$  is the velocity of the unperturbed stream. Practically the unperturbed stream velocity is the velocity of the stream in the hypothetic case of particle absence. As it can be seen from equation (13) the drag force depends on  $C_d$  which is the coefficient of drag. Drag coefficient is related to particle Reynolds number (14) and particle shape:

$$Re_p = \frac{d_p |\vec{u}_r|}{\nu_f} \quad (14)$$

here  $d_p$  is the diameter of the particle,  $|\vec{u}_r|$  is the absolute value of the particle-flow relative speed and  $\nu_f$  is the kinematic viscosity of the flow. In the present work, only particles of spherical shape are taken into account. This leads to consider values of  $C_d$  as given in equation (15) [54].

$$\begin{aligned} Re_p &\ll 1 & C_d &\approx 24/Re_p \\ 1 < Re_p < 1000 & & C_d &\approx \frac{24}{Re_p} (1 + 0.15 Re_p^{0.687}) \\ 1000 < Re_p & & C_d &\approx 0.44 \end{aligned} \quad (15)$$

Values of drag coefficient are valid under conditions that particle volume and shape remain unchanged during motion and particle surface can be assumed smooth. Three principal flow regimes for particles immersed in a stream can be analyzed. These differences in flow regime correspond to different formulation of  $C_d$ . In case of  $Re_p \ll 1$  the regime is called “*Stokes regime*” and viscous forces dominate. A “*transition regime*” is considered for  $1 < Re_p < 1000$  in which the flow in the wake of the sphere undergoes a series of transitions. In case of  $Re_p > 1000$ , the drag coefficient is constant after the boundary layer transition from laminar to turbulent. The wake of the sphere is characterized by a turbulent nature (Figure 23).

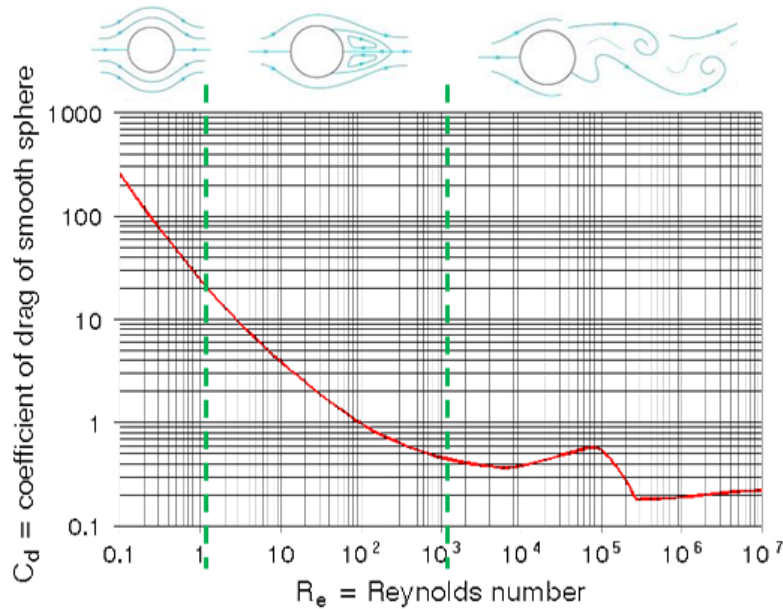


Figure 23. Coefficient of drag as a function of particle Reynolds number

For small solid particles having a density much larger than the carrying fluid, the drag force and the gravitational force are the two most significant forces acting on a particle. The gravitational force is evaluated as  $\vec{F}_g = m_p \vec{g}$  where  $m_p$  is the particle mass and  $\vec{g}$  the gravitational acceleration.

**Others forces.**

Besides drag and gravitational force there are others forces which may act on a particle. The **lift force** is the force applied to the particle by the fluid on the perpendicular direction of the particle motion. This force can be originated by particle rotation or by a shear field. When lift force is generated by particle rotation it is possible also to speak of “Magnus effect” [55] and it can be quantified by equation (16)

$$\vec{F}_{l_m} = C_{L_m} m_p \vec{u}_r \wedge \vec{\omega}_p \quad (16)$$

Where  $C_{L_m}$  is a specific coefficient in case of lift induced by rotation and  $\vec{\omega}_p$  is the particle angular velocity. In case of lift force induced by shear, the equation differs from the previous one only by the  $C_L$  coefficient (Figure 24).

The **buoyancy force** is associated to the density of the fluid surrounding the particle. It is independent from the flow around the particle. The force is equal to the Archimedes force (17) corresponding to and opposite to the mass of fluid  $m_f$  displaced by the particle.

$$\vec{F}_b = m_f \vec{g} \quad (17)$$

In case in which the fluid density is small respect to the particle density, the Archimedes force is negligible (Figure 24).

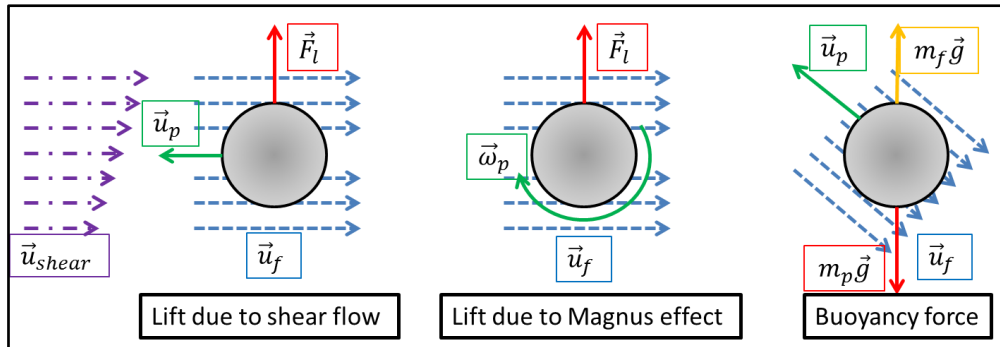


Figure 24. Schemes for lift force (left and center image) and for buoyancy force on the right.

The **added mass force** compensates the acceleration needed to get in motion the fluid mass which surrounds the particle. For particles with a density higher than the fluid one, the force can be considered negligible.

Finally the **Basset force** describes the force due to the lagging of the boundary layer development with acceleration of bodies moving through a fluid. The Basset force is hard to implement and its contribution on particle dynamics is negligible if  $\rho_f \ll \rho_p$ , for these reasons it is rarely implemented.

In the context of the study with particles considered solid and  $\rho_f \ll \rho_p$  only drag and gravitational will be considered as forces acting on a smooth, non-deformable, spherical particle. These assumptions lead to resolve the equation (18)

$$m_p \frac{d\vec{u}_p}{dt} = \vec{F}_d + m_p \vec{g} \quad (18)$$

### 2.6.2 Stokes number definition

Particles will react to a variation of the flow velocity as a function of their inertia and forces applied by the surrounding fluid. In our case  $\rho_f \ll \rho_p$ , as a consequence, inertia will drive principally the particle response to a flow velocity variation. The time with which the particle reacts to this variation is called relaxation time  $\tau_p$ . To understand what physically represents  $\tau_p$  one can image a non-moving particle ( $u_p = 0m/s$ ) immersed in a flow without velocity:  $u_f = 0m/s$  and no gravity:  $\vec{g} = 0m/s^2$ . When the flow velocity becomes different from zero, the particle starts to move. Supposing a constant flow velocity  $u_f = const$  the particle behavior in the flow can be expressed through equation (19).

$$m_p \frac{d\vec{u}_p}{dt} = \frac{1}{2} \rho_f S (\vec{u}_f - \vec{u}_p)^2 C_d \quad (19)$$

The solution of this equation can be expressed as

$$\vec{u}_p(t) = \vec{u}_f \left(1 - e^{-t/\tau_p}\right) \quad (20)$$

Where the particle relaxation time  $\tau_p$  is equal to (21) in case of Stokes regime: ( $Re_p \ll 1$ ).

$$\tau_p = \frac{\rho_p d_p^2}{18\mu_f} \quad (21)$$

As a consequence of equation (21), the momentum equation of a particle can be written as (22).

$$\frac{d\vec{u}_p}{dt} = \frac{(\vec{u}_f - \vec{u}_p)}{\tau_p} \quad (22)$$

In case the particle does not fall in a Stokes regime it can be applied a correction factor  $f = 1 + 0.15Re_p^{0.687}$  leading to a relaxation time  $\tau_p$  (23)

$$\tau_p = \frac{1}{f} \cdot \frac{\rho_p d_p^2}{18\mu_f} \quad (23)$$

In case of gravity, equation (22) can be written as (24) which is a differential equation of the first order. Its solution is an exponential curve with a characteristic time  $\tau_p$  which tends to a value  $\vec{u}_f + \tau_p \vec{g}$ .

$$\frac{d\vec{u}_p}{dt} = \frac{(\vec{u}_f - \vec{u}_p)}{\tau_p} + \vec{g} \quad (24)$$

The settling velocity  $\tau_p \vec{g}$  represents the particle speed only caused by the effect of gravity with a fluid velocity equal to zero in a Stokes regime ( $Re_p \ll 1$ ). The particle will reaches the 95% of its terminal speed in a time equal to  $3\tau_p$ . Therefore  $\tau_p$  indicates the time of the particle to react at the flow solicitations.

To characterize the capacity of a particle to react at a flow solicitation, a dimensionless number is introduced. The Stokes number is defined as (25) where  $\tau_f$  represents a characteristic time scale of the fluid. This number is used during this work to characterize the particles behavior in the flow or the particles behavior close to the experimental structure.

$$St = \frac{\tau_p}{\tau_f} \quad (25)$$

Moreover the Stokes number will be used in the modeling of the interactions between particle and flow. It will allow to characterize the particle behavior with respect to a turbulence eddy. In case  $St \gg 1$  the particle will cross the turbulence eddy (Figure 31.a), on the other hand, if  $St \ll 1$  the particle will follow the eddy in a tracer-like behavior (Figure 31.b).

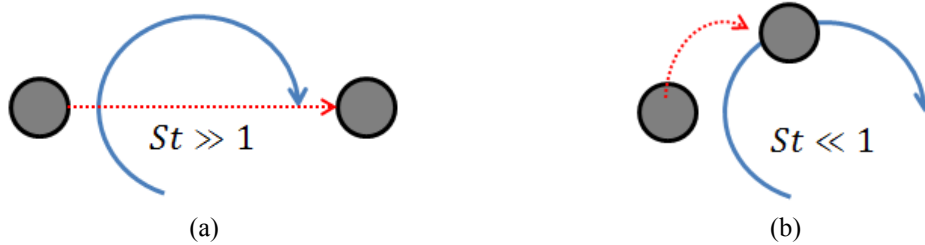


Figure 25. Stokes number: (a) particle crosses the eddy. (b) particle acts as a tracer.

### 2.6.3 Particle-flow interaction modeling

Particle movement is influenced by the surrounding flow. This flow, acting on particles, gives origin to forces as seen before. The way this flow, considered as turbulent, acts on particles, is one of the hardest challenge in particle-flow interaction modeling. Basically, turbulent flow is characterized by its random nature [56] and it is composed by a random superposition of eddies of various size. The random nature of a turbulent flow means that the prediction of the exacts value of its velocity field  $\vec{u}_f$  is impossible.

How to model particle-flow interaction is strictly related to the modeling of the carrying phase: DNS, LES or RANS are the three numerical approaches. The first one, Direct Numerical Simulation (DNS) permits to characterize the whole fluid phase by the resolution of all the spatial and temporal scale of the turbulence. This approach permits to fully describe the turbulent flow but the computational cost is tremendously high. This cost is related to the necessity to have a very refined mesh to “catch” all the turbulent structures (from the Kolmogorov scale  $\eta$  up to the integral one  $l$ ). In practical application DNS is unusable due to this computational cost and its utilization is restricted to “numerical experiments” with which investigate, for example, the nature of turbulence. LES and RANS approaches base the computation of the flow speed  $\vec{u}_f$  as a sum between a mean or filtered flow velocity  $\langle \vec{u}_f \rangle$  and a mean random velocity  $\vec{u}'_f$ .

$$\vec{u}_f = \langle \vec{u}_f \rangle + \vec{u}'_f \quad (26)$$

With the Large Eddy Simulation (LES) method, only the large eddies of turbulence are resolved. It acts as a low-pass filtering which models, instead to

calculate, the small scales of turbulence. In LES approach the computational cost is reduced with respect to DNS. Moreover it maintains a higher level of detail with respect to the RANS approach.

The Reynolds-Average Navier Stokes (RANS) approach is based on the full modeling of the turbulence through an on time averaged approach for all the turbulent structures. This modeling is performed by a series of scalars which represent statistically the whole turbulence and more particularly its main physical proprieties. Considering the RANS  $k - \varepsilon$  model these scalars are represented by  $k$ : the turbulent kinetic energy and  $\varepsilon$ : the turbulent dissipation. In case of RANS  $k - \omega$  model,  $\omega$  is the specific dissipation which determines the frequency scale of the turbulence and  $k$  assumes the same definition seen for  $k - \varepsilon$ . RANS approach is the faster one among the three but it is also the less detailed. A synthesis scheme of the three methods with the relative level of turbulence resolution is shown in Figure 26.

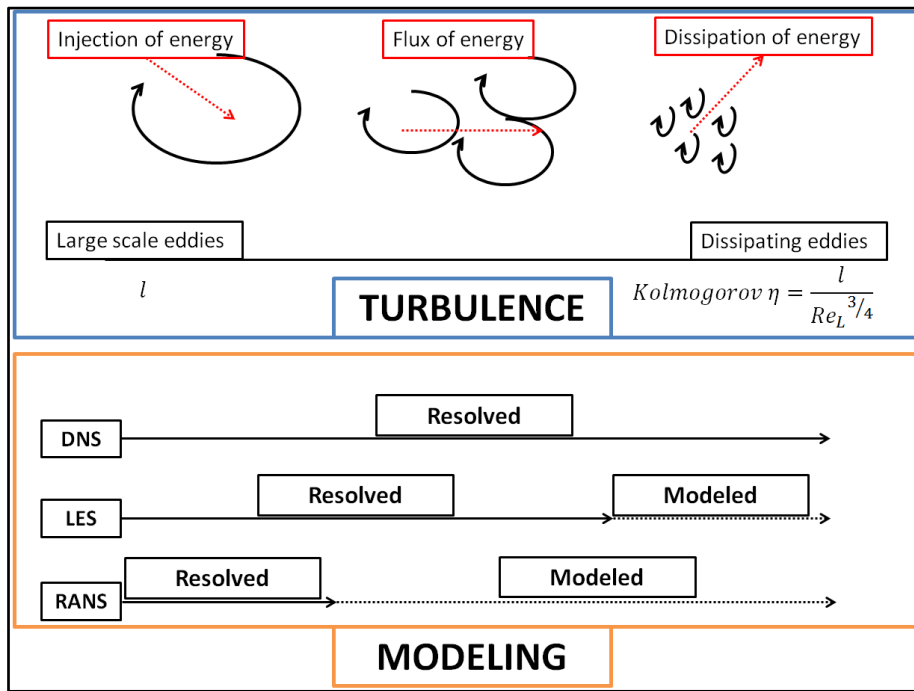


Figure 26. Methods to model the turbulence.

During this work a RANS approach will be adopted. The context of the study does not require to model turbulence in a more complex way. RANS gives an averaged information on turbulence. However, it is possible to reconstruct the randomness of the particle trajectories due to turbulence, by implementing a stochastic algorithm. To explain the stochastic approach, it is supposed here after, a condition of “*homogeneous isotropic turbulence*” for the flow. This means that the mean flow stationary velocity is zero and turbulence is equal and constant along the three spatial directions [56]. In this way it is sufficient to consider one component of the flow velocity (27) to describe particle-flow interactions:

$$\vec{u}_f = \langle \vec{u}_f \rangle + \vec{u}'_f \equiv u_f = u'_f \quad (27)$$

The stochastic approach permits to calculate  $u'_f$  which must respect two conditions:

1. The root mean square of  $u'_f$  is linked to the turbulent kinetic energy  $k$  of the modeled flow with:  $\langle u_f'^2 \rangle = \frac{2}{3}k$
2. The time scale of  $u'_f$  must correspond to the Lagrangian autocorrelation function of the flow, this means:  $\mathcal{R}_L(\tau) = \frac{\langle u'_f(t) \cdot u'_f(t+\tau) \rangle}{\langle u_f'^2 \rangle} \approx e^{-\tau/T_f^L}$  in case of homogeneous isotropic turbulence [52] (Figure 27).

where  $\tau$  represents the time shift and  $T_f^L$  is the Lagrangian integral time scale of the flow.

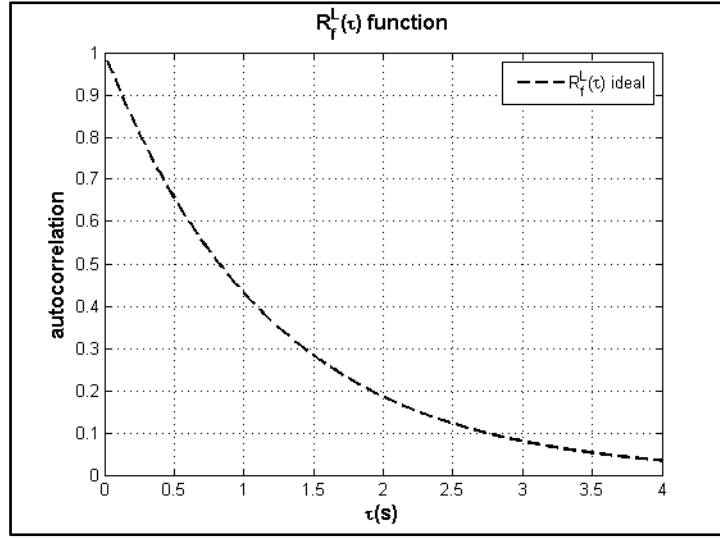


Figure 27. Theoretical autocorrelation function of the flow.

In Figure 27, while the time shift  $\tau$  increases the flow particle loses “memory” of its initial velocity and  $\mathcal{R}_L(\tau)$  decreases, so  $\mathcal{R}_L(\tau) \rightarrow 0$  when  $\tau \gg T_f^L$ . The modeling of  $T_f^L$  and associated autocorrelation function with stochastic models, has been the topics of several studies [57], and is described in what follows.

#### 2.6.4 Modeling of the turbulence fluctuation $u'_f$

Commonly the fluctuating velocity is modeled through the **Eddy-Interaction-Model (EIM)** also known as **Discrete-Random-Walk (DRW)** approach.

This model generates the fluctuating velocity  $u'_f$  starting from the local turbulence statistics. This fluctuating velocity acts on the mean velocity flow  $\langle u_f \rangle$  during a specific time  $t_{int}$  which represents the interaction time between the turbulence eddy and the particle. When  $t_{int}$  ends, a new value of  $u'_f$  is calculated as equation (28)

$$u'_f = \xi \sqrt{\frac{2}{3}k} \quad (28)$$

here  $\xi$  represents a random variable distributed as a normal with a zero mean and variance equal to one:  $\xi \sim \mathcal{N}(0,1)$ .

As noted by Oesterlé [52] the interaction time  $t_{int}$  must satisfy the autocorrelation function of the flow. With EIM approach it has a triangular shape: equation (29).

$$\mathcal{R}_L(\tau) \approx \begin{cases} 1 - \frac{\tau}{2T_f^L}, & \tau \leq 2T_f^L \\ 0, & \tau > 2T_f^L \end{cases} \quad (29)$$

This means that, to have an effective integral time scale equal to  $T_f^L$ , the interaction time must be  $t_{int} = 2T_f^L$ .

An example of the fluctuating velocity modeled with the EIM method is shown in Figure 28.a. This example is extrapolated from a flow speed computation of one hour. As shown, the simplest EIM model is unable to reproduce the continuity of  $u'_f$  as also reported by Oesterlé [52] or Pozorski et al. [53].

Figure 28.b shows with a black line the autocorrelation of the carrying phase. The blue one reproduces a computation example of EIM autocorrelation function on a window for  $\tau = 4s$ . As shown the autocorrelation has a triangular form which is far from the ideal one. EMI model can be implemented easily and it requests less computational time.

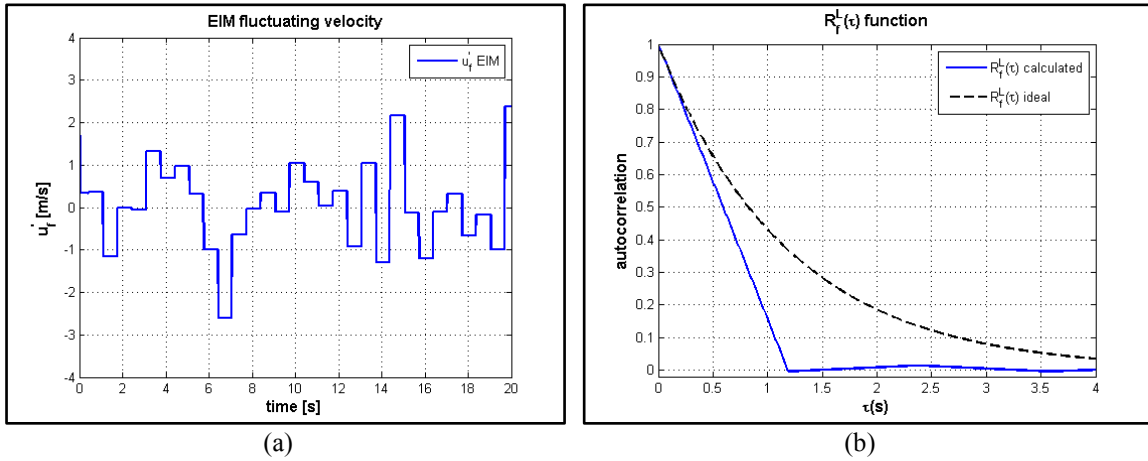


Figure 28. EIM model: (a) an example of  $u'_f$ , (b) the autocorrelation  $\mathcal{R}_L(\tau)$

Several improvements have been proposed to compensate the drawbacks of the EIM approach. Oesterlé in [52] proposed to generate a new  $t_{eddy}$  and  $t_{cross}$  by an exponential law with mean  $T_f^L$  and  $l$  respectively. Also Graham in [58] proposes a new version of EIM with random length and time scale. The aim is to obtain an exponential decreasing shape for the autocorrelation function which is more realistic.

The turbulence fluctuation velocity  $u'_f$  can be also reproduced by the **Langevin** approach (Pozorski [53]) which is also known as **Continuous Random Walk (CRW)**: equation (30).

$$du'_f(t) = -u'_f(t) \frac{\delta t}{T_f^L} + \sqrt{\frac{2\sigma^2}{T_f^L}} dW(t) \quad (30)$$

Where  $\delta t$  is the time step,  $\sigma$  the fluctuating velocity variance equal to  $\frac{2}{3}k$  and  $dW(t)$  is a random variable. This last one is distributed as a Gaussian, independent from position and velocity  $u'_f$ , with a zero mean and a variance  $\langle dW(t) \rangle$  equal to  $dt$ . It is called Wiener process. The equation (30) can be rewritten through the finite-difference equation (31) thank to Hito's integral (Oesterlé [52]).

$$u'_f(t + dt) = u'_f(t) - u'_f(t) \frac{dt}{T_f^L} + \sqrt{\frac{2\sigma^2 dt}{T_f^L}} dW(t) \quad (31)$$

Where  $u'_f(t + dt)$  is the fluctuation velocity at time  $(t + dt)$ ,  $-u'_f(t) \frac{dt}{T_f^L}$  is the deterministic drift and  $\sqrt{\frac{2\sigma^2 dt}{T_f^L}} dW(t)$  is the diffusion term. This approach assures a continuity of  $u'_f$ : the fluctuating velocity  $u'_f(t + dt)$  has a “memory” of the precedent one  $u'_f(t)$ . Moreover the Langevin approach (30) presents the autocorrelation function reported in (32).

$$\mathcal{R}_L(\tau) \approx e^{-\tau/T_f^L} \quad (32)$$

which leads to evaluate the Lagrangian integral time scale as (33):

$$T_f^L \equiv \int_0^\infty \mathcal{R}_L(\tau) d\tau \quad (33)$$

Hence this approach permits to compute a Lagrangian theoretical integral time scale consistent with the one of the carrying phase: Oesterlé [52], Pope [56]. In Figure 29.a is shown the trend of  $u'_f$  extrapolated from a flow speed computation of one hour. In Figure 29.b is shown a comparison between the theoretical autocorrelation function of  $u'_f$  and the one obtained with Langevin approach on a window of four seconds. As one can note, the autocorrelation function with the Langevin approach is closer to the ideal one.

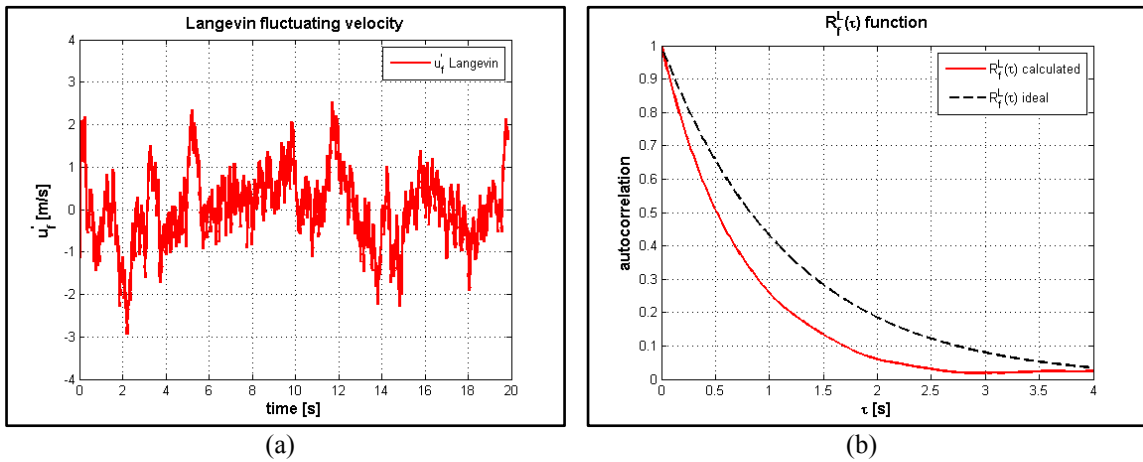


Figure 29. Langevin model: (a) an example of  $u'_f$ , (b) the autocorrelation  $\mathcal{R}_L(\tau)$

### 2.6.5 $u'_f$ modeling conclusions.

In this work both the modeling will be used. The EIM approach will be exploited during the numerical modeling to evaluate the collision efficiency. On the other hand, the Langevin approach will be employed to model the particle-flow interaction during the particle freezing process. As will be shown later, the particle heat transfer coefficient  $h_p$  of the particle freezing process is related to the relative velocity  $\vec{u}_r = \vec{u}_f - \vec{u}_p$  through  $Re_p$ . As a consequence the modeling of the flow speed  $\vec{u}_f$  will influence the coefficient  $h_p$ . The choice to model  $u'_f$  with a Langevin approach in the particle freezing model will ensure a more physical behavior of the coefficient  $h_p$ . This aspect and the coupling between the particle dynamic and the particle freezing process will be deepened in chapter four.

### 2.6.6 Inertia effect and Crossing trajectories effect

#### *Inertia effect*

As seen in the precedent paragraph, the Langevin approach and the EIM approach allow to reproduce a fluctuating velocity with an autocorrelation function consistent with the one of the flow. While modeling  $u'_f$  also the inertia effect and the crossing trajectory effect must be considered. These two effects cause the fluid element and particle trajectories to differ (Figure 30). Particle inertia induces a relatively instantaneous motion of particles with respect to the fluid neighborhood. Crossing trajectory effect induces a mean particle drift due to gravity: Lain [59].

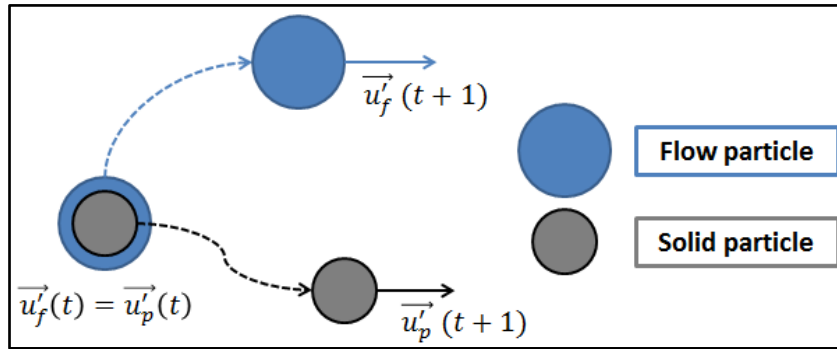


Figure 30. Particle inertia and crossing trajectory effect.

Analyzing first the inertia effect and supposing that solid particles are immersed in a system without external forces, Wang and Stock [60] have proposed an integral time scale which depends on the inertia of particles (34). This integral time scale allows to take into account the inertia of a solid particle with respect to a fluid particle.

$$T_{f@p}^* = T_f^E \cdot [(1 - (1 - \Xi)(1 + \Xi St)^{-0.4(1+0.01\Xi St)}] \quad (34)$$

Where  $T_{f@p}^*$  is the integral time scale of the fluid seen by particles as a consequence of the inertia effect.  $T_f^E$  represents the Eulerian integral time scale and it is defined in a reference frame moving with mean flow velocity  $\langle u_f \rangle$ .  $T_f^L$ , as seen before,

is the Lagrangian integral time scale. The parameter  $\Xi$  is defined as the ratio between  $T_f^L$  and  $T_f^E$ .

The Stokes number  $St = \tau_p/\tau_f$  in equation (34) allows to take into account the inertia of particles with respect to the carrying phase inertia.

This means that  $St \gg 1$  particles are characterized with a high inertia with respect to the fluid. As a consequence particle will slightly interact with turbulence and  $T_{f@p}^* \rightarrow T_f^E$  (Figure 31.a). When  $St \gg 1$  the particle is close to moving at the same mean velocity of the flow. Vice versa, when particle inertia is low,  $St \ll 1$  and  $T_{f@p}^* \rightarrow T_f^L$ : particle is “trapped” by the eddy (Figure 31.b).

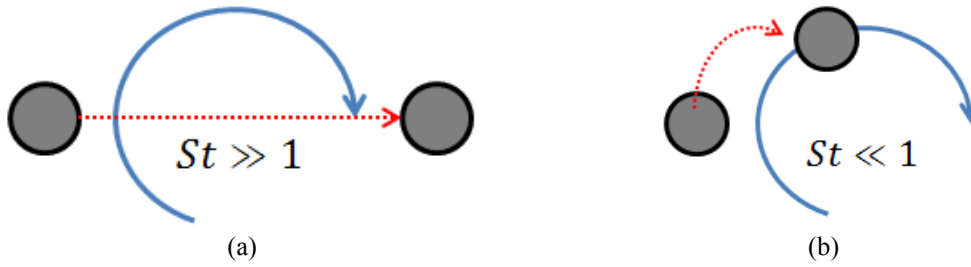


Figure 31. Stokes number: (a)  $St \gg 1$ : high particle inertia. (b)  $St \ll 1$ : low particle inertia.

The inertia effect can be taken into account in the Langevin approach by substituting  $T_f^L$  with  $T_{f@p}^*$ : equation (35).

$$u_f'(t + dt) = u_f'(t) - u_f'(t) \frac{dt}{T_{f@p}^*} + \sqrt{\frac{2\sigma^2 \Delta t}{T_{f@p}^*}} dW(t) \quad (35)$$

As reported by Oesterlé [52] the EIM is not able to reproduce inertia effect with its simplest formulation. Graham in [61] proposes a modified EIM which takes into account the inertia effect. Anyway, as underlined by Oesterlé [52], the implementation of these modifications is far to be fully accomplished and will not be implemented during this work.

### **Crossing trajectories effect**

When an external force acts on a particle-flow system an extra drift between flow particle and solid particle takes place. This extra shift leads to a mean relative velocity  $\langle u_r \rangle$  between the carrying phase and the discrete phase. Due to this mean relative velocity the integral time scale seen by particles is reduced along  $\langle u_r \rangle$  direction. Moreover a further reduction occurs in the transversal direction due to the so-called continuity effect. To take into account these reduction Csanady proposed two formulations for the integral time scale seen by particle. In equation (36) the implementation for a Langevin approach:

$$T_{f@p \parallel}^* = T_{f@p}^* \cdot \frac{1}{\sqrt{\left(1 + \frac{T_{f@p}^{*2} u_r^2}{l^2}\right)}}, T_{f@p \perp}^* = T_{f@p}^* \cdot \frac{1}{\sqrt{\left(1 + 4 \frac{T_{f@p}^{*2} u_r^2}{l^2}\right)}} \quad (36)$$

where  $\parallel$  and  $\perp$  represents respectively the parallel direction and the perpendicular direction to the mean relative velocity. Oesterlé [52] reported also an improvement to  $T_{f@p\perp}^*$ :

$T_{f@p\perp}^* = T_{f@p}^* \cdot \frac{1}{\sqrt{1+\Psi}} \left(1 - \frac{\Psi}{2(1+\Psi)}\right)$  with  $\Psi = \frac{T_{f@p}^{*2} u_r^2}{l^2}$  and it permits a better agreement with several numerical simulations. The present work will integrate the Csanady formulations with the improvement to  $T_{f@p\perp}^*$ .

In its simplest implementation, the crossing trajectory effect can be implemented in the EIM taking the interaction time  $t_{int}$  as the minimum between the eddy life time  $t_{eddy}$  and the time necessary to particle to cross the eddy  $t_{cross}$ : equation (37).

$$t_{int} = \min(t_{eddy}, t_{cross}) \quad (37)$$

The eddy life time must be  $t_{eddy} = 2T_f^L$  and the eddy crossing time  $t_{cross} = \frac{2l}{|u_r|}$  with  $l$  the integral length scale. These two formulations ensure a consistent EIM autocorrelation function with respect to the flow one. Thus the evaluation of  $t_{int}$  compares the life time of the eddy  $t_{eddy}$  with the time necessary to the particle to cross the eddy  $t_{cross}$ .

The Csanady correction can be introduced also in EIM approach, taking the interaction time  $t_{int} = \frac{T_f^L}{\sqrt{1+\Psi}}$  with  $\Psi = \frac{T_f^2 u_r^2}{l^2}$

By introducing the crossing trajectory effect in EIM it is assured the continuity of the interaction time  $t_{int}$  (Figure 32 – blue line). Red line in Figure 32 shows how the evaluation of the interaction time with the minimum formulation (equation (37)) the continuity is not ensured.

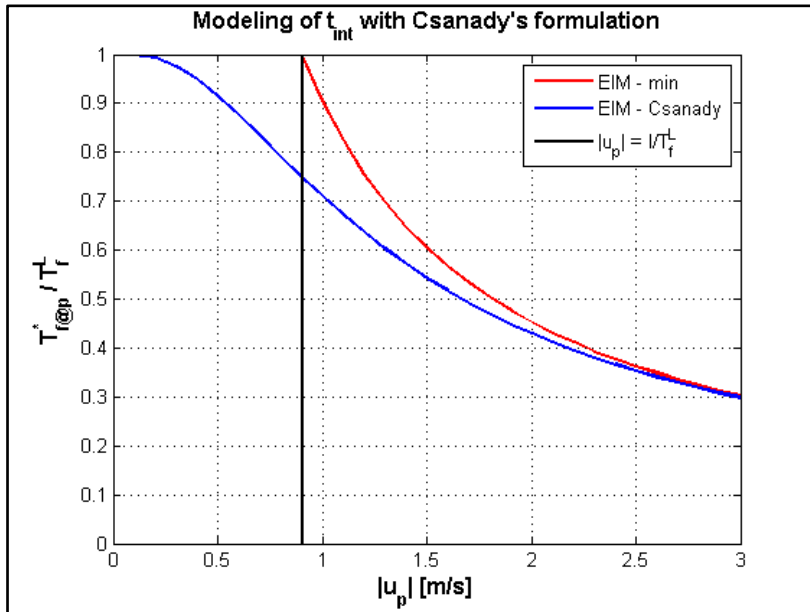


Figure 32. The evaluation of  $t_{int}$  in the EIM approach.

In Figure 32 the black vertical line represents the limit velocity for the minimum formulation after which  $t_{int}$  is evaluated as  $\frac{2l}{|vr|}$  instead of  $2T_f^L$ . To assure a consistent EIM autocorrelation function with respect to the flow one  $t_{int}$  must be twice the value  $\frac{T_f^L}{\sqrt{1+\Psi}}$ .

## 2.7 Conclusion

The review on the effects of wet snow accretions on structures has shown how the risks associated can be extremely sever. Wet snow accretion concerns several fields of engineering as buildings, cable, trains or wind turbine. As seen, particles responsible of wet snow accretion are characterized by a mixed phase of a liquid part and a solid part. This mixed phase is synthetized by a dimensionless coefficient: the liquid water content  $LWC$ . This one is defined as the ratio between the liquid mass of a particle and the particle mass. The  $LWC$  will be the leading thread of the work.

A brief review on  $LWC$  effect on in cloud icing has been presented. As reported, the liquid water content plays a crucial role on the accretion. It drives both the accretion forms and the accretion mass. Hence to model the accretion process, an approach which takes into account the  $LWC$  is imperative.

The approach undertaken to model wet snow accretion is based on the separation of the aerodynamic, the mechanical and thermal influence: Makkonen [15], ISO 12494 standard [34]. This separation is synthetized in this work by three dimensionless coefficient. The aerodynamic effect is taken into account by the collision efficiency  $\eta_1$ , the mechanical effect by the sticking efficiency  $\eta_2$  and the thermal effect by the accretion efficiency  $\eta_3$ .

Due to the system chosen during the experimental campaign to reproduce the wet snow accretion, the freezing process of a particle has been summarized: particle  $LWC$  can be adjusted as a function of the ambient temperature.

In the last part the Lagrangian approach chosen to model the interactions between snow particle and the fluid flow has been presented. Both the Eddy-Interaction-Model and the Langevin model have been presented. Both models will be applied in the present work.

## Bibliography

- [1] M. C. Homola, "Impacts and Causes of Icing on Wind Turbines," Narvik University College, Narvik, Norway 2005.
- [2] M. Carter and R. Stangl, "Beware of Falling Ice and Snow," in *Construction Canada*, ed, 2012, pp. 8-14.
- [3] K. Andersen. (2012). *Near Record Snowfall in Anchorage Challenges Residents and Roofs!* Available: <http://reidmiddleton.wordpress.com/2012/03/27/near-record-snowfall-in-anchorage-challenges-residentsand-roofs/>
- [4] A. Brown. (2010). *Warning over dangerous roof snow in Edinburgh*. Available: <http://www.bbc.co.uk/news/uk-scotland-edinburgh-east-fife-11911326>
- [5] W. Henson and R. Stewart, "Severity and return periods of icing events in the Montréal area," *Atmospheric Research*, vol. 84, pp. 242-249, 2007.
- [6] J. N. Laflamme and G. Périard, "The climate of freezing rain over the province of Québec in Canada: a preliminary analysis," *Atmospheric Research*, vol. 46, pp. 99-111, 1998.
- [7] L. Makkonen and K. Ahti, "Climatic mapping of ice loads based on airport weather observations," *Atmospheric Research*, vol. 36, pp. 185-193, 1995.
- [8] B. Tammelin and K. Santti, "Icing in Europe," presented at the BOREAS IV, Hetta, Finland, 1998.
- [9] D. Shemanske. (2010). *Winter descends on Village*. Available: [http://www.fnal.gov/pub/today/archive\\_2010/today10-01-15.html](http://www.fnal.gov/pub/today/archive_2010/today10-01-15.html)
- [10] K. Klavin. (2010). *Snow sliding off the roof of our apartment complex in Salmo, B.C.* Available: <http://www.cbc.ca/news/yourcommunity/2010/01/photo-of-the-day-jan11-2010.html>
- [11] G. Poots and P. L. I. Skelton, "Simple models for wet-snow accretion on transmission lines: snow load and liquid water content," *International Journal of Heat and Fluid Flow*, vol. 15, pp. 411-417, 1994.
- [12] G. Poots and P. L. I. Skelton, "Simulation of wet-snow accretion by axial growth on a transmission line conductor," *Applied Mathematical Modelling*, vol. 19, pp. 514-518, 1995.
- [13] Y. Sakamoto, "Snow accretion on overhead wires," *Philosophical Transactions: Mathematical, Physical and Engineering Sciences*, vol. 358, pp. 2941-2970, 2000.
- [14] C. Klinger, M. Mehdiانpour, D. Klingbeil, D. Bettge, R. Häcker, and W. Baer, "Failure analysis on collapsed towers of overhead electrical lines in the region Münsterland (Germany) 2005," *Engineering Failure Analysis*, vol. 18, pp. 1873-1883, 2011.
- [15] L. Makkonen, "Models for the growth of rime, glaze, icicles and wet snow on structures," *Philosophical Transactions: Mathematical, Physical and Engineering Sciences*, vol. 358, pp. 2913-2939, 2000.
- [16] P. McComber and A. Paradis, "A cable galloping model for thin ice accretions," *Atmospheric Research*, vol. 46, pp. 13-25, 1998.
- [17] L. E. Kollár, O. Olqma, and M. Farzaneh, "Natural wet-snow shedding from overhead cables," *Cold Regions Science and Technology*, vol. 60, pp. 40-50, 2010.
- [18] L. Kloow, "High-speed train operation in winter climate," Royal Institute of Technology (KTH), KTH Railway Group, Stockholm, Sweden 2011.
- [19] T. Laakso, I. Baring-Gould, M. Durestewitz, R. Horbaty, A. Lacroix, E. Peltola, G. Ronsten, L. Tallhaug, and T. Wallenius, "State-of-the-art of wind energy in cold climates," Finland 2010.
- [20] N. Bose, "Icing on a small horizontal-axis wind turbine — Part 2: Three dimensional ice and wet snow formations," *Journal of Wind Engineering and Industrial Aerodynamics*, vol. 45, pp. 87-96, 1992.
- [21] S. Boisson-Kouznetzoff, "Qualification de la neige produite dans la soufflerie climatique Jules Verne: mise au point du dispositif expérimental et modélisation numérique du procédé," Docteur, Dynamique des Fluides et des Transerts, Ecole Doctorale Sciences Pour l'ingénieur De Nantes, Nantes, 1997.
- [22] M. Farzaneh, "Wet Snow Accretion on Overhead Lines," in *Atmospheric Icing of Power Networks*, C. Université du Québec à Chicoutimi, Ed., ed: Springer, 2008, pp. 119-169.
- [23] A. Korolev, "Limitations of the Wegener–Bergeron–Findeisen Mechanism in the Evolution of Mixed-Phase Clouds," *Journal of the Atmospheric Sciences*, vol. 64, pp. 3372-3375, 2007/09/01 2007.
- [24] K. G. Libbrecht. (1999). *Snowflakes and Snow Crystals*. Available: <http://www.its.caltech.edu/~atomic/snowcrystals/>
- [25] S. C. Colbeck, "Grain clusters in wet snow," *Journal of Colloid and Interface Science*, vol. 72, pp. 371-384, 1979.

- [26] I. SMI Snow Machines. (2012). *Snow Machines, INC.* Available: <http://www.snowmakers.com/english/index.html>
- [27] K. Al-Khalil, "Assessment of Effects of Mixed-Phase icing Conditions on Thermal Ice Protection Systems," U.S. Department of Transportation 2003.
- [28] S. Boisson-Kouznetzoff and P. Palier, "Caractérisation de la neige produite en soufflerie climatique," *International Journal of Refrigeration*, vol. 24, pp. 302-324, 2001.
- [29] F. T. Lynch and A. Khodadoust, "Effects of ice accretions on aircraft aerodynamics," *Progress in Aerospace Sciences*, vol. 37, pp. 669-767, 2001.
- [30] M. B. Bragg, A. P. Broeren, and L. A. Blumenthal, "Iced-airfoil aerodynamics," *Progress in Aerospace Sciences*, vol. 41, pp. 323-362, 2005.
- [31] H. Seifert and F. Richert, "Aerodynamics of Iced Airfoils and their Influence on Loads and Power Production," presented at the EWEC '97, Dublin, Ireland, 1997.
- [32] R. W. Gent, N. P. Dart, and J. T. Cansdale, "Aircraft icing," *Philosophical Transactions Royal Society London*, vol. 325, pp. 2873-2911, 2000.
- [33] E. P. Lozowski, J. R. Stallabrass, and P. F. Hearty, "The Icing of an Unheated, Nonrotating Cylinder. Part II. Icing Wind Tunnel Experiments," *Journal of Climate and Applied Meteorology*, vol. 22, pp. 2063-2074, 1983/12/01 1983.
- [34] ISO, "Atmospheric icing of structure," vol. 12494, ed. Geneva: ISO copyright office, 2001, p. 58.
- [35] C. Mundo, M. Sommerfeld, and C. Tropea, "Droplet-wall collisions: Experimental studies of the deformation and breakup process," *International Journal of Multiphase Flow*, vol. 21, pp. 151-173, 1995.
- [36] M. Trenker and W. Payer, "Investigation of snow particle transportation and accretion on vehicles," presented at the 24th Applied Aerodynamics Conference, San Francisco, 2006.
- [37] M. Trenker, W. Payer, C. Krenn, G. Haider, and M. Mann, "Numerical Simulation of Snow Entrainment with Application to Train Undercarriage Design," presented at the NAFEMS, World Congress, Malta, 2005.
- [38] J. T. Cansdale and I. I. McNaughtan, "Calculation of surface temperature and ice accretion rate in a mixed water droplet ice/crystal cloud," 1977.
- [39] B. L. Messinger, "Equilibrium temperature of an unheated icing surface as a function of air speed," *Journal of Aeronautical Science*, vol. 20, pp. 91-104, 1953.
- [40] E. P. Lozowski, J. R. Stallabrass, and P. F. Hearty, "The Icing of an Unheated, Nonrotating Cylinder. Part I: A Simulation Model," *Journal of Climate and Applied Meteorology*, vol. 22, pp. 2053-2062, 1983/12/01 1983.
- [41] D. Guffond, "Aspects Thermiques du givre atmosphérique des aéronefs," O.N.E.R.A., Meudon.
- [42] L. Makkonen, "Modeling of Ice Accretion on Wires," *Journal of Climate and Applied Meteorology*, vol. 23, pp. 929-939, 1984/06/01 1984.
- [43] K. P. Owusu, D. C. S. Kuhn, and E. L. Bibeau, "Capacitive probe for ice detection and accretion rate measurement: Proof of concept," *Renewable Energy*, vol. 50, pp. 196-205, 2013.
- [44] C. A. Knight, "On the Mechanism of Spongy Hailstone Growth," *Journal of the Atmospheric Sciences*, vol. 25, pp. 440-444, 1968/05/01 1968.
- [45] L. Brunet, "Conception et discussion d'un Modele de Formation du Givre sur des Obstacles Varies," Doctorat Université de Clermont II, U.E.R. de Recherche Scientifique et Technique, 1986.
- [46] W. B. Wright, P. C. E. Jorgenson, and J. P. Veres, "Mixed Phase Modeling in GlennICE with Application to Engine Icing," presented at the AIAA Guidance, Navigation and Control Conference, Toronto, Ontario Canada, 2010.
- [47] J. P. Hindmarsh, A. B. Russell, and X. D. Chen, "Experimental and numerical analysis of the temperature transition of a suspended freezing water droplet," *International Journal of Heat and Mass Transfer*, vol. 46, pp. 1199-1213, 2003.
- [48] M. Strub, O. Jabbour, F. Strub, and J. P. Bédécarrats, "Experimental study and modelling of the crystallization of a water droplet," *International Journal of Refrigeration*, vol. 26, pp. 59-68, 2003.
- [49] M. Epstein and H. K. Fauske, "Kinetic and heat transfer-controlled solidification of highly supercooled droplets," *International Journal of Heat and Mass Transfer*, vol. 36, pp. 2987-2995, 1993.
- [50] F. Feuillebois, A. Lasek, P. Creismas, F. Pigeonneau, and A. Szaniawski, "Freezing of a Subcooled Liquid Droplet," *Journal of Colloid and Interface Science*, vol. 169, pp. 90-102, 1995.

- [51] J. P. Dumas, M. Krichi, M. Strub, and Y. Zeraoui, "Models for the heat transfers during the transformations inside an emulsion—I. Crystallizations of the undercooled droplets," *International Journal of Heat and Mass Transfer*, vol. 37, pp. 737-746, 1994.
- [52] B. Oesterlé, *Ecoulements multiphasiques*. Paris: Lavoisier, 2006.
- [53] J. Pozorski and J.-P. Minier, "On the Lagrangian turbulent dispersion models based on the Langevin equation," *International Journal of Multiphase Flow*, vol. 24, pp. 913-945, 1998.
- [54] C. Marchioli, A. Giusti, M. Vittoria Salvetti, and A. Soldati, "Direct numerical simulation of particle wall transfer and deposition in upward turbulent pipe flow," *International Journal of Multiphase Flow*, vol. 29, pp. 1017-1038, 2003.
- [55] C. K. K. Lun and H. S. Liu, "Numerical simulation of dilute turbulent gas-solid flows in horizontal channels," *International Journal of Multiphase Flow*, vol. 23, pp. 575-605, 1997.
- [56] S. B. Pope, *Turbulent Flows*, VII ed. Cambridge, United Kingdom: Cambridge University Press, 2010.
- [57] B. Oesterlé and L. I. Zaichik, "Time scales for predicting dispersion of arbitrary-density particles in isotropic turbulence," *International Journal of Multiphase Flow*, vol. 32, pp. 838-849, 2006.
- [58] D. I. Graham, "Improved Eddy Interaction Models with Random Length and Time Scales," *International Journal of Multiphase Flow*, vol. 24, pp. 335-345, 1998.
- [59] S. Lain and C. A. Grillo, "Comparison of turbulent particle dispersion models in turbulent shear flows," *Brazilian Journal of Chemical Engineering*, vol. 24, pp. 351-363, 2007.
- [60] L.-P. Wang and D. E. Stock, "Dispersion of Heavy Particles by Turbulent Motion," *Journal of the Atmospheric Sciences*, vol. 50, pp. 1897-1913, 1993/07/01 1993.
- [61] D. I. Graham, "On the inertia effect in eddy interaction models," *International Journal of Multiphase Flow*, vol. 22, pp. 177-184, 1996.



## Chapter 3 Experimental approach to investigate wet snow accretions.

|       |   |    |
|-------|---|----|
| 3.1   | CLIMATIC CONDITIONS REPRODUCTION: CLIMATIC WIND TUNNEL.....   | 44 |
| 3.2   | WET SNOW PRODUCTION: SNOW GUN .....   | 45 |
| 3.3   | TEST CAMPAIGN DEVICES TO STUDY WET SNOW ACCRETIONS.....   | 47 |
| 3.3.1 | <i>Investigation of the aerodynamic aspect: test structure.....</i>   | 47 |
| 3.3.2 | <i>Estimation of the incoming snow flow rate: snow collectors.....</i>  | 49 |
| 3.3.3 | <i>Temperature monitoring: thermocouples, flow visualization: GoPro camera.....</i>   | 53 |
| 3.3.4 | <i>Characterization of the incoming flow: ultrasonic anemometer.....</i>  | 55 |
| 3.4   | EXPERIMENTAL PROCEDURE TO REPRODUCE WET SNOW ACCRETIONS .....   | 56 |
| 3.4.1 | <i>Wind tunnel setup.....</i>   | 56 |
| 3.4.2 | <i>Experimental principle to reproduce wet snow accretions.....</i>   | 58 |
| 3.4.3 | <i>Procedure undertaken during the experimental campaign.....</i>   | 59 |
| 3.4.4 | <i>Preliminary wind tunnel settings up: analysis of snow flow homogeneity and test reproducibility.....</i>   | 61 |
| 3.5   | THE EXPERIMENTAL RESULTS.....   | 64 |
| 3.5.1 | <i>Snow flow characterization through the ultrasonic anemometer.....</i>  | 64 |
| 3.5.2 | <i>Heat exchange blockage: estimation of the real flow speed.....</i>   | 68 |
| 3.5.3 | <i>Wet snow accretions quantification: coefficient <math>\beta</math>.....</i>  | 70 |
| 3.5.4 | <i>Experimental analysis of the LWC role of wet snow accretion through the coefficient <math>\beta</math>.....</i>  | 71 |
| 3.5.5 | <i>Experimental analysis of the thermal aspect of wet snow accretions: temperature profiles.....</i>  | 77 |
| 3.5.6 | <i>Experimental analysis of the aerodynamic aspect of wet snow accretions: cylinders role through a Stokes number and coefficient <math>\beta_{exp}</math>.....</i> | 78 |
| 3.6   | PHYSICAL MEASUREMENTS APPROACHED .....  | 80 |
| 3.7   | CONCLUSIONS .....   | 82 |
|       | BIBLIOGRAPHY .....  | 83 |

This chapter is dedicated to the experimental approach undertaken in the climatic wind tunnel to study the wet-snow accretion process. As presented in the literature review, wet snow accretions are characterized by three aspects: aerodynamic, mechanical and thermal one. To synthesize the influence of the three aspects, a dimensionless coefficient  $\beta_{exp}$  is here presented and discussed. The influence on the accretions of particle *LWC* is investigated. The liquid water content of particles is tuned by varying the ambient temperature  $T_a$  in the wind tunnel as seen in chapter 2. The aerodynamic aspect is investigated by analyzing the coefficient  $\beta_{exp}$  for three cylinders of different diameters.

Moreover, a set of boundary conditions are measured for further analysis and numerical modeling: mean flow speed  $\langle u_f \rangle$ , turbulent intensity  $I_\%$  and integral length scale  $l$  of the snow flow. The data acquired on accretion forms give also a database with which validate the accretion model presented in chapter five.

An important part of our work has been to set up an experimental procedure to study the wet-snow accretion due to the lack of a universal procedure in the climatic wind tunnel. In such a large wind tunnel, it was very important to build a procedure leading to reliable results. Moreover an important work has been done to ensure the reproducibility of the results. To achieve this goal all the parameters of the experimental setup have to be understood and controlled.

### 3.1 Climatic conditions reproduction: climatic wind tunnel.

The wind tunnel facility of C.S.T.B. was built to conduct tests at full scale. It is possible to investigate the wind effects on many kinds of structures in conjunction with different climatic conditions: rain, snow, dust, sun, icing. Moreover the facility is adapted to study the aerodynamic of vehicles, the ventilation of building and the performances of materials subjected to extreme climatic conditions. The wind tunnel is constituted of two parts. The first one is called the “dynamic circuit”. It is operated since 1990 (the green ring in Figure 33). The second part, called “thermal circuit” is operated since 1995 (the purple ring in Figure 33). The latter unit permits to reproduce warm and cold environment from  $50^{\circ}\text{C}$  down to  $-25^{\circ}\text{C}$ . This large range of temperature allows to reproduce several climatic conditions among which wet-snow storms.

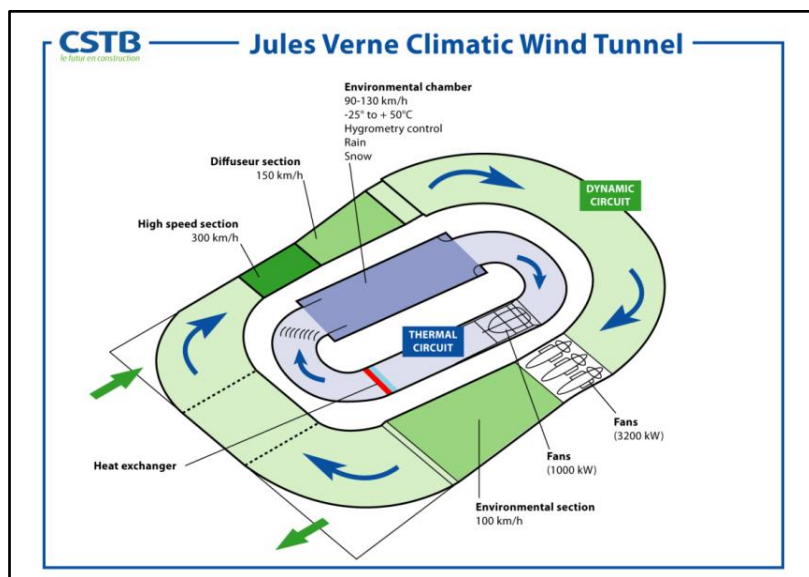


Figure 33. Jules Verne Climatic Wind Tunnel facility.

The thermal circuit includes a six blades fan of  $1\text{MW}$ . The fan can reach  $350\text{rpm}$  limited to  $285\text{rpm}$  when the temperature inside the chamber is less than  $-15^{\circ}\text{C}$ . The test chamber is  $22\text{m}$  long,  $10\text{m}$  wide and  $7\text{m}$  high. Previous tests, conducted with only air flow, have characterized the chamber with a turbulence intensity of  $I_0 = 5\%$  and an integral length scale of  $l = 0.8\text{m}$  using air as a fluid. The flow inlet has a variable section: from  $30$  to  $18\text{m}^2$ . The maximum reachable speed depends on the inlet section. For  $30\text{m}^2$  flow speed can go up to  $100\text{km/h}$ , when test section is  $18\text{m}^2$  the flow speed can reach  $145\text{km/h}$ . The heat exchanger allows to adjust temperature from  $-25^{\circ}\text{C}$  to  $50^{\circ}\text{C}$  with a temporal gradient of  $15^{\circ}\text{C}/\text{hour}$ . The hygrometry can be adjusted from  $30\%$  to  $99\%$ . A completed description of the cooling systems can be

found in [1]. A set of turning vanes are installed upstream the flow inlet to assure a straight flow in the test chamber (Figure 34).

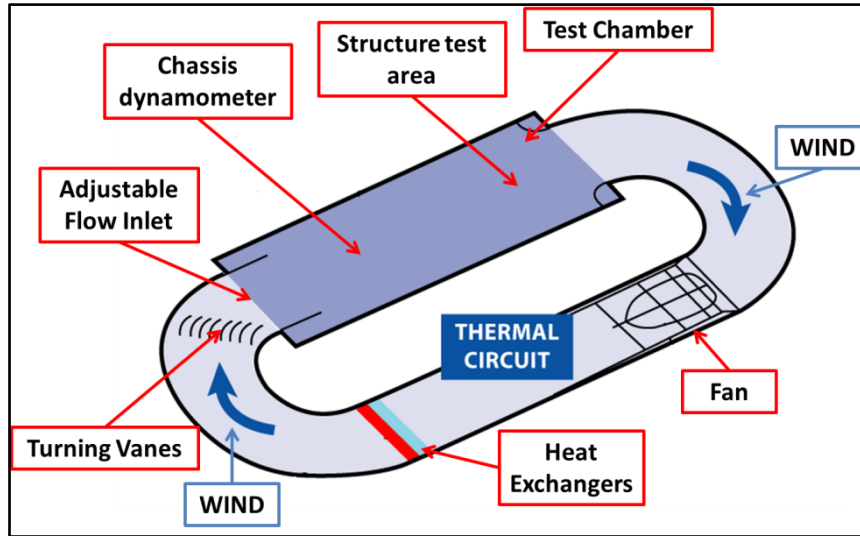


Figure 34. Jules Verne Climatic Wind Tunnel: thermal circuit.

### 3.2 Wet snow production: snow gun

As seen in literature review there are three types of snow guns, the one utilized here to produce artificial snow presents an internal mixing chamber. This means that water and air are mixed inside a chamber and then expelled at high pressure: from 6 to 10bar which means approximately 100m/s [1]. The gun air/water ratio can be adjusted to obtain a more or less wet snow [1], as a consequence, tuning this ratio is another approach to adjust the *LWC* of particles. However the gun air/water ratio influences the particle distribution of the snow gun [1]. Therefore, to ensure the same snow gun particles distribution for all tests (Figure 35) and, due to the difficulties to adjust the *LWC* precisely through the gun air/water ratio, the air/water ratio was kept unchanged during all the tests. The flux of air/water mixture has been set-up to 1.7m<sup>3</sup>/hour.

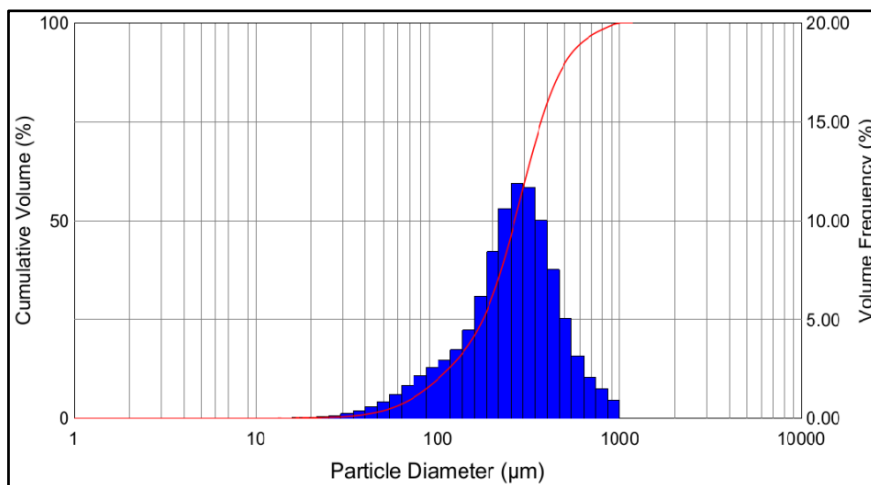


Figure 35. Snow gun volume particle distribution [2].

The particles distribution (Figure 35) was measured during a precedent test campaign held in C.S.T.B. in 2007 with a MALVERN Spraytec [2]. The measurements have been taken as Figure 36 with the snow gun placed on a side of the wind tunnel. The snow gun was placed one meter ahead of the MALVERN. One is aware that the distribution of Figure 35 does not correspond exactly the distribution at the exit of the snow gun. Nevertheless, due to the high particles concentration it was impossible to approach more the MALVERN to the snow gun.

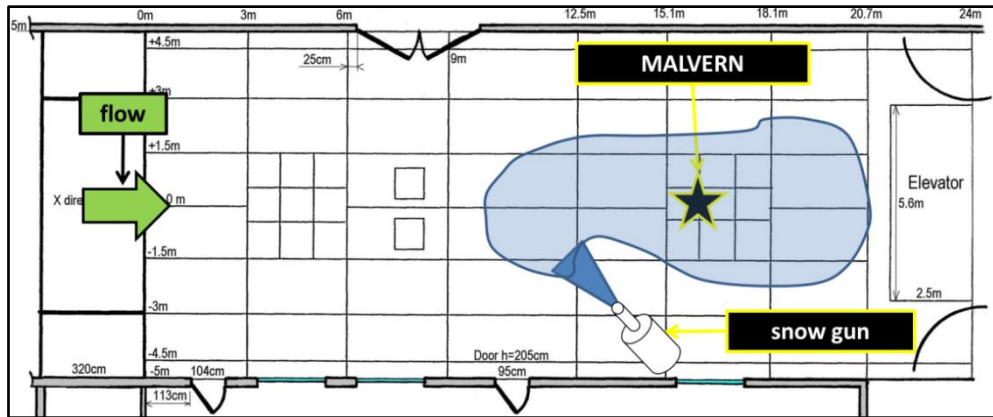


Figure 36. MALVERN position [2].

The measurement principle is based on laser diffraction. This means that the particles size distribution is evaluated by measuring the angular scatter of a laser beam which passes through the dispersed phase (Figure 37). The angular scattering intensity is then analyzed to calculate the size of the particles.

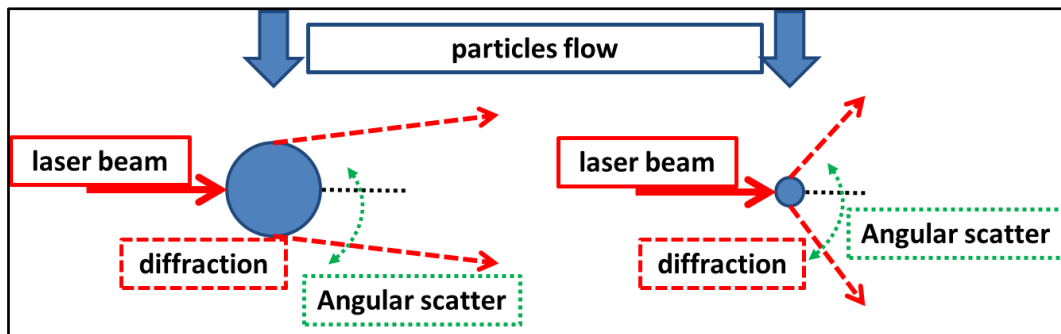


Figure 37. Measurement principle of laser diffraction.

As shown in Figure 37 the angular scatter is a function of the particles diameter: small particles scatter the laser beam more than larger particles.

To characterize a distribution of the dispersed phase the Sauter diameter  $d_{32} = \frac{\sum d_p^3}{\sum d_p^2}$  and De Brouckere diameter  $d_{43} = \frac{\sum d_p^4}{\sum d_p^3}$  are often utilized. The

first one is the surface area moment mean, the second one is the volume moment mean and it is also called the mean volume diameter ( $M_{\text{ean}}VD$ ). These diameters indicate around which particle diameter the (surface area or volume) distribution is centered. In our case the particle distribution of the snow gun is characterized by a  $d_{32} \approx 190\mu\text{m}$  and  $d_{43} \approx 290\mu\text{m}$ . Due the fact that our studies are focused on the mass of the snow accreted, the diameter  $d_{43}$  is most appropriated to deal with. The particles distribution

of Figure 35 will be taken into account in chapter four while modeling the particles stochastic dispersion model, it will also be used to characterize the particle distribution close to the cylinder.

Due to the fact that the snow gun has a transition time during startup before the water flux becomes stable, a trapdoor was installed facing the snow gun during the whole test campaign (Figure 38). This expedient has allowed to reduce noticeably the quantity of snow spread in the test chamber before the actual beginning of the tests which can accumulate and perturb the flow. Moreover it limited the quantity of snow in the vicinity of the temperature and humidity sensor of the wind tunnel which can perturb the regulation system during the test. Thanks to the trapdoor a good part of the mixture flowed away under the test section ground. When the stability of the water flux was reached, the trapdoor was then lowered to permit a fully diffusion of the flow.

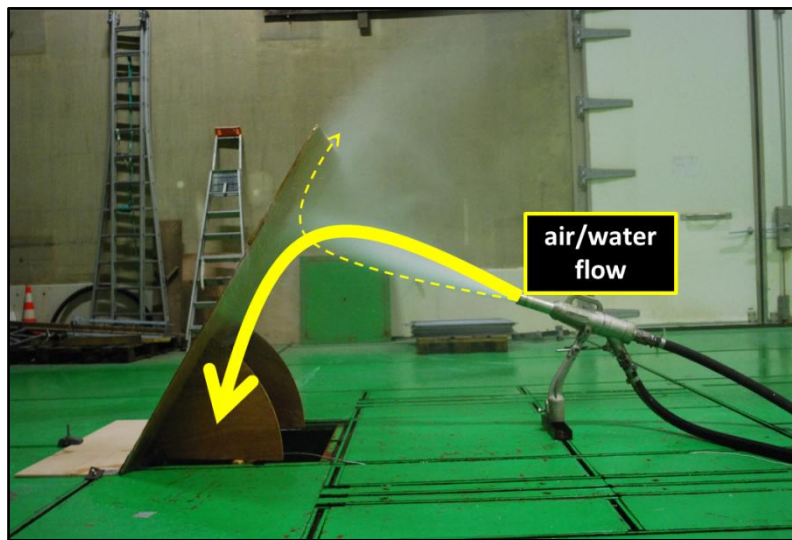


Figure 38. Function principle of the trapdoor.

### 3.3 Test campaign devices to study wet snow accretions.

#### 3.3.1 Investigation of the aerodynamic aspect: test structure.

The test structure was built in the C.S.T.B. workshop. It consists in a main part made of two vertical bars that hold horizontally one PVC cylinder 1.5m long. To investigate the aerodynamic aspect of the accretion three cylinders of various diameter were tested:  $d_{50} = 50mm$ ,  $d_{200} = 200mm$  and  $d_{315} = 315mm$ . The cylinder was placed 1.3m above the ground to ensure a uniform snow flow outside the boundary layer (Figure 39).

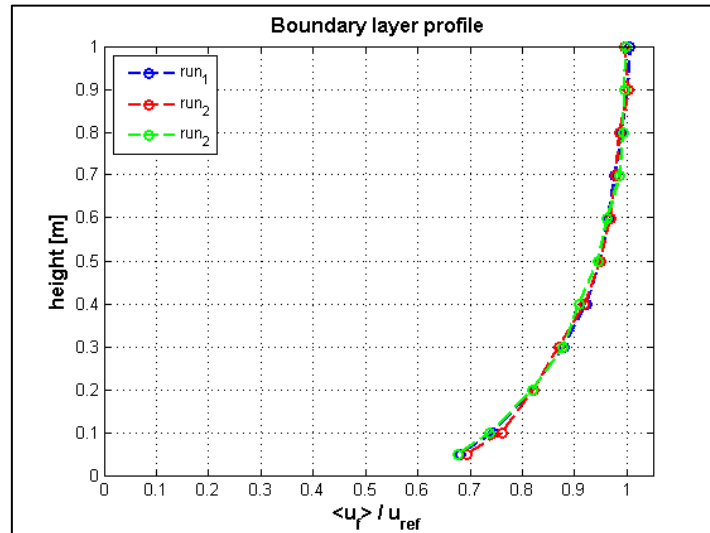


Figure 39. Air boundary layer at the structure location: 16m from the inlet.

The boundary layer measured without snow particles into air was evaluated using a “*Turbulent flow instruments*” cobra probe at a data output frequency of 256Hz. The measurements have been made in a configuration without snow gun to avoid flow perturbations. Considering the homogeneity of the speed values at 0.9m and 1m of height, the flow speed reference  $u_{ref}$  to evaluate the profile is the average between the speeds at these heights. Three runs guaranteed the reproducibility of the test. Measurements above 1.0m are not available, but analyzing the boundary layer profile obtained, one can suppose that at 1.3m above ground the flow can be considered uniform.

The cylinder was protected (Figure 40.a) by a removable cover to safeguard the cylinder during the startup of the snow gun (Figure 40.b).

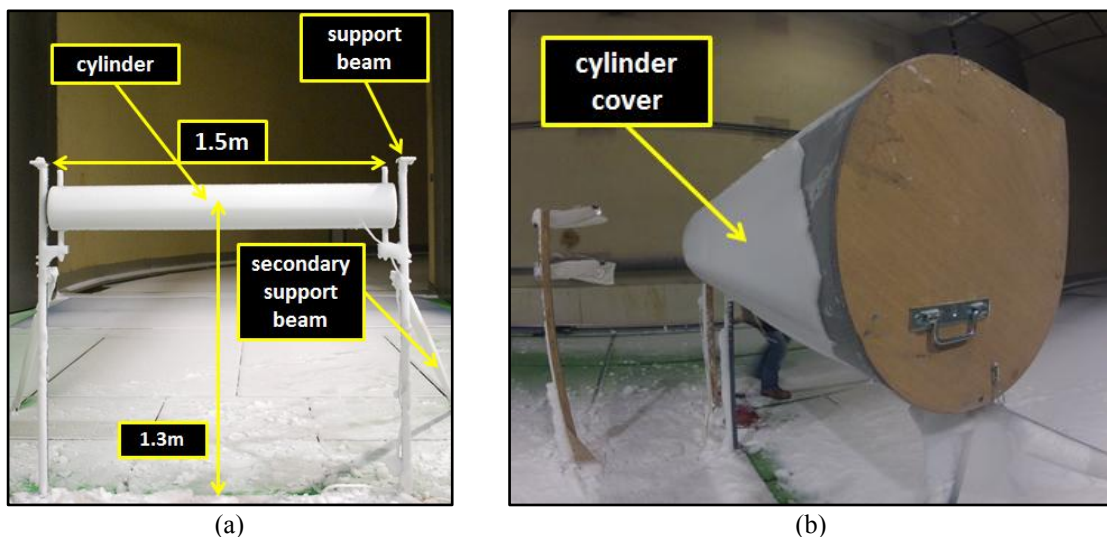


Figure 40. (a) A front view of the test structure with its principal features and dimensions. (b) The cover which protects the cylinder.

### 3.3.2 Estimation of the incoming snow flow rate: snow collectors.

A couple of snow collectors with a diameter of  $8\text{cm}$  were installed on both sides of the test structure. One collector placed at  $1.10\text{m}$  from the ground and the other one at  $1.50\text{m}$  to ensure a full coverage of the impacting area of the cylinder (Figure 41.a). Snow collectors permitted to measure the mean incoming snow flux  $\langle\varphi_s\rangle$  (38). The mean incoming flux will be a part of the evaluation of the experimental coefficient  $\beta$  and of the accretion model presented in chapter five.

$$\langle\varphi_s\rangle = \frac{\langle m_{col} \rangle}{(A_{col} \cdot t)} = \frac{kg}{m^2 \cdot s} \quad (38)$$

Where  $\langle m_{col} \rangle$  is the mean snow mass accumulated inside the four snow collectors,  $A_{col}$  the snow collector area and  $t$  the duration of the test. A similar approach to measure the snow flux was also undertaken by Font et al.[3]. This device is made of tissue characterized by a porosity of  $60\mu\text{m}$ : the air pass through the tissue while the snow remains collected inside. The snow collectors were mounted on two vertical poles placed 1 meter ahead from the structure. The collectors were equipped with a pincer and a horizontal rod to maintain the collectors horizontal and straight (Figure 41.b high) during the tests. This approach guarantees that the snow accumulated inside the collector did not obstruct the inlet by closing down the porous tissue (Figure 41.b low).

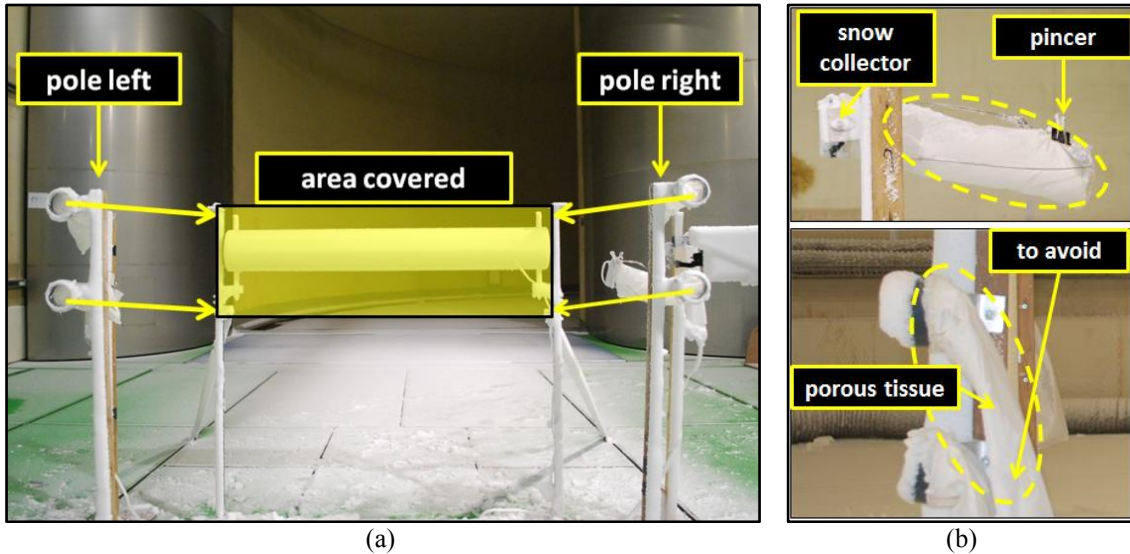


Figure 41. (a) Front view of the test structure with the four snow collectors. (b) Side view of the snow collectors.

This configuration ensures an acceptable homogeneity of snow flux for each collector during all a test day as shown in Table 1. Here is reported, for each flux  $\varphi_s$  of the four collectors, the percentage difference with respect to the mean flux of the day  $\langle\varphi_s\rangle_{day}$ . This means:  $\delta\varphi_{s\%} = \frac{(\varphi_s - \langle\varphi_s\rangle_{day})}{\langle\varphi_s\rangle_{day}}$ . The duration of the test was

$10\text{min}$ . In the evaluation of the snow flux, one has to consider the errors committed during the sampling of the snow and while weighting the snow. In this case an error analysis has evaluated at about  $\sim 10\%$  the uncertainty committed while sampling the snow mass. One can suppose that this uncertainty is mainly related to the difficulties to completely empty the snow collectors and to the difficulties to have exactly the same

flow uniformity during all the tests. The uncertainty associated to the balance used to weight the snow is  $0.1g$ . Tests have shown that the mean snow mass gathered by the snow collectors is about  $\langle m_{col} \rangle \approx 140g$  which means a mean uncertainty of snow sampling of  $\approx 14g$ . Seeing the error associated to the balance, one can suppose that the most important error contribution to  $\delta\varphi_{s\%}$  is given by the sampling process and the flow homogeneity.

Table 1. The snow flux for each collectors for three periods in a test day.

|            | $\delta\varphi_{s\%}$<br>beginning | $\delta\varphi_{s\%}$<br>middle | $\delta\varphi_{s\%}$<br>end |
|------------|------------------------------------|---------------------------------|------------------------------|
| high left  | -0.58%                             | 2.98%                           | -5.48%                       |
| low left   | -7.59%                             | 12.49%                          | -0.58%                       |
| high right | -4.08%                             | 11.32%                          | -5.02%                       |
| low right  | 4.32%                              | -4.78%                          | 12.02%                       |

Moreover one can wonder if the snow particles, while approaching the snow collectors, can be deviated by the flow close to the snow collectors increasing the measurement error. Taking as a reference particle the  $d_{43} = 290\mu m$  of Figure 35 distribution, it is possible to estimate the behavior of the particle close to the snow collector through a Stokes number. As will be shown later in this chapter the  $d_{43}$  is characterized by a  $\tau_p \approx 100ms$ . The evaluation of characteristic time of the flow which surrounds the collector  $\tau_{col} = \frac{d_{col}}{\langle u_f \rangle}$  leads to a Stokes number  $\tau_p / \tau_{col} \approx 11$ . With

$d_{col} = 0.08m$ , the diameter of the collectors and  $\langle u_f \rangle = 10m/s$  the mean flow speed. This value of Stokes number, as seen in chapter two, means an inertial behavior of particles: therefore one can preliminary suppose that particles are not so much deviated by the flow close to snow collectors. As a consequence of this analysis, one can suppose excludable the influence of the flow around the snow collectors on snow particles which could perturb the snow collector filling.

***Test duration analysis.***

Being aware that a flow blockage of the collectors can happen when measuring the snow flux with this simple system, a series of pre-tests to study the optimal test duration was performed. Three tests of 5,10 and 15 minutes showed how the flow blockage can arise above 10min (Figure 42 - black circle).

The test is based on the evaluation of the mean snow flux between the four collectors:  $\langle \varphi_s \rangle$ , defined in equation (38).

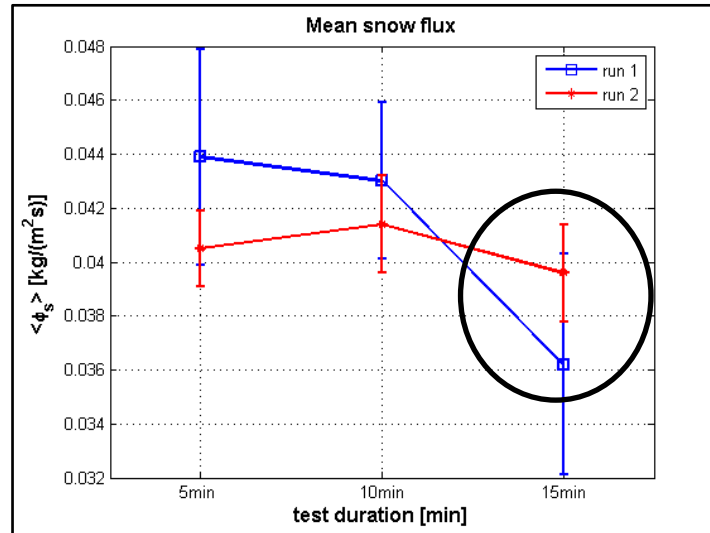


Figure 42. Analysis of filling up drawback of snow collectors.

The whole experimental campaign was based on 10min tests, that permitted to avoid snow collectors filling-up. Two runs assured reproducibility of the filling-up tests.

#### ***The transversal uniformity of the snow flow.***

An important part of the experimental campaign has been dedicated to study the transversal homogeneity of the snow flow. This means to check if the snow flow measured with the snow collectors placed aside the test structure well-represent the snow flux at the center of the test structure. To investigate this problematic, a series of measurements of the snow flow distribution have been performed. Five snow collectors placed on a row have allowed to study the transversal homogeneity of the incoming flux (Figure 43). The snow collectors have been placed in the same place of the test structure. The height of the collectors was the same of the cylinders: 1.3m. The two lateral collectors have been placed in the same position of the test configuration (Figure 41).

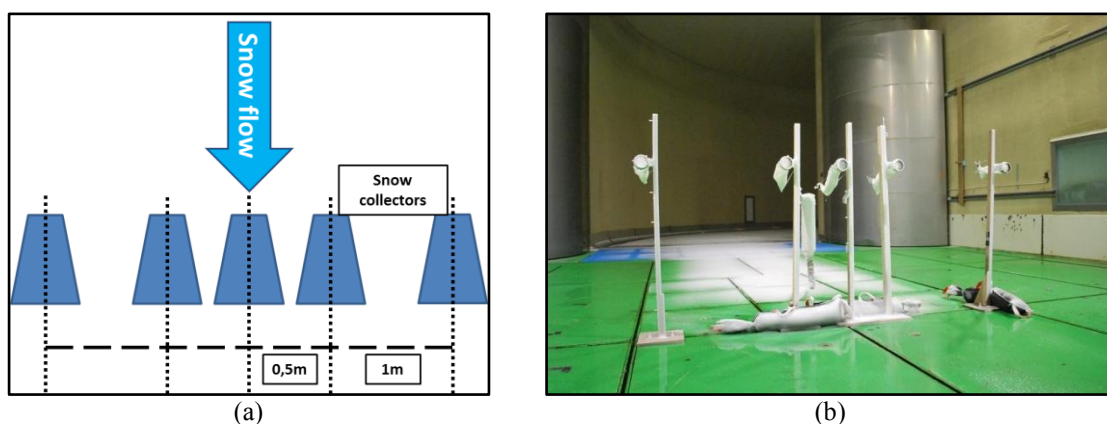


Figure 43. (a) Schematic view of snow collectors. (b) Wind tunnel setup.

The measurements of concentration along five different points have shown how the snow flux uniformity is assured only on the central part: only the three collectors at the center have shown a flow homogeneity (Figure 44). It is important to underline how the three central collectors cover well the central part of the cylinder on which has been done the analysis of the accretion.

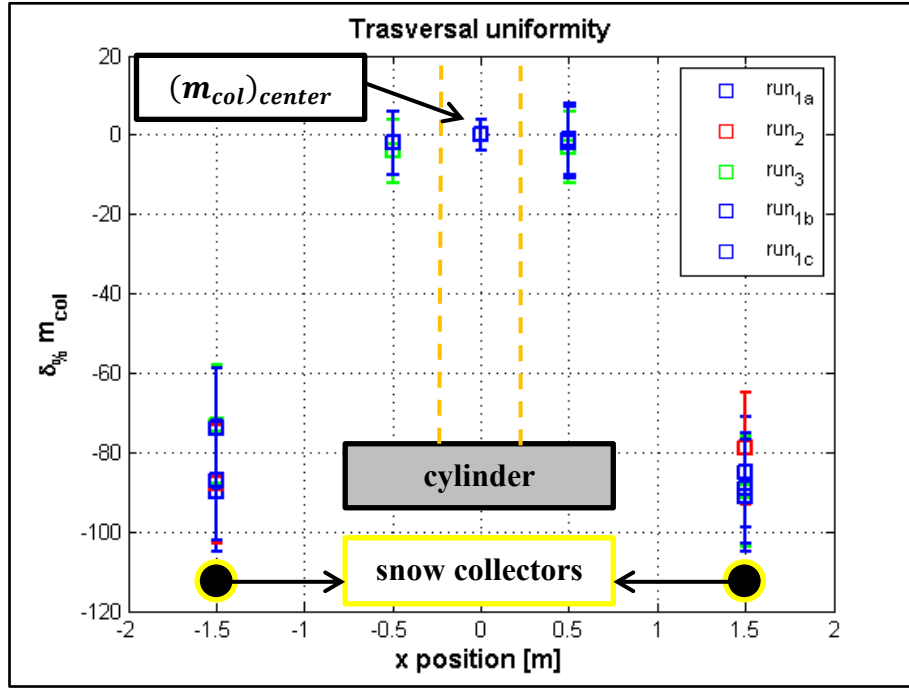


Figure 44. Snow flux uniformity,  $\langle u_f \rangle \approx 10m/s$ .

In Figure 44, run<sub>1a</sub>, run<sub>1b</sub> and run<sub>1c</sub> are characterized by an ambient temperature  $T_a = -10^\circ C$  and a test duration equal to 10min. run<sub>2</sub> has been performed at  $T_a = -5^\circ C$  with a test duration of 10min, while for run<sub>3</sub> the test duration was 6min at  $T_a = -10^\circ C$ . The choice to vary the ambient temperature and the test duration has shown how these parameters do not influence considerably the transversal uniformity of the flow. The percentage differences between the snow mass inside each collectors is evaluated as (39).

$$\delta_{\%} m_{col} = \frac{((m_{col})_{center} - (m_{col}))}{(m_{col})} \quad (39)$$

Where  $(m_{col})_{center}$  represents the snow mass collected from the central collector and  $(m_{col})$  the mass collected from the other four collectors of Figure 43. The error bars are based on the standard deviation evaluated for each collector.

As one can note from Figure 44, the flux can be considered homogeneous only in the central part. The cylinders are 1.5m long and, as will be explained later, the analysis of the accretion is focused on their central part which is 0.7m long. As a consequence, analyzing Figure 44, one can suppose that the incoming flux on the central part of the cylinders is homogeneous (Figure 44 - orange lines).

It is important to note how the configuration with a snow collector placed at the center was impossible to use at the same time of the accretion tests on the cylinders. For this reason, all the tests have been undertaken with the four lateral collectors as seen in Figure 41.

Considering the fact that the incoming snow flux during the tests is measured aside the test structure, it is necessary to recalibrate the snow mass gathered inside the snow collectors by a coefficient to have the real snow flux which impacts the cylinders.

This coefficient is taken equal to the mean difference between the snow mass collected at the center and aside of the flow. The mean difference has been estimated as  $\approx 85\%$ . As a consequence, all the snow flux measured with the lateral snow collectors have been recalibrated with a coefficient  $k_s = 1.85$  to obtain the supposed snow flux at the center. Moreover one can suppose how  $\delta_{err}\%$  of Figure 44 does not change as a function of the ambient temperature  $T_a$ . Therefore it has been supposed that the coefficient of 1.85 was acceptable for all the temperatures tested in the experimental campaign.

### 3.3.3 Temperature monitoring: thermocouples, flow visualization: GoPro camera.

A total of four k-type thermocouples (chromel-alumel Figure 46.a) were installed during the tests. One for each side of the structure (Figure 45), one on a wall of the wind inlet and the last one on the cylinder surface facing the snow flow at the stagnation point.

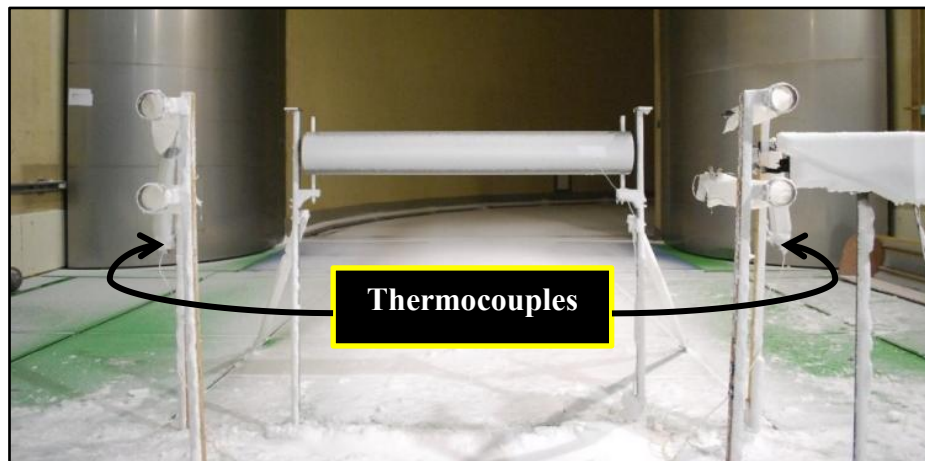
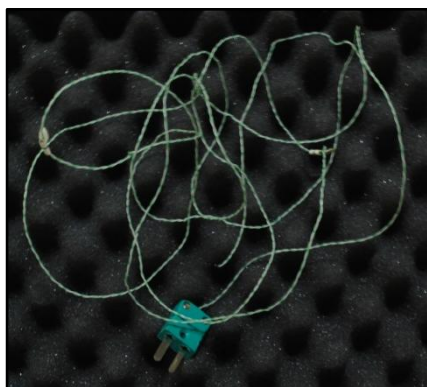
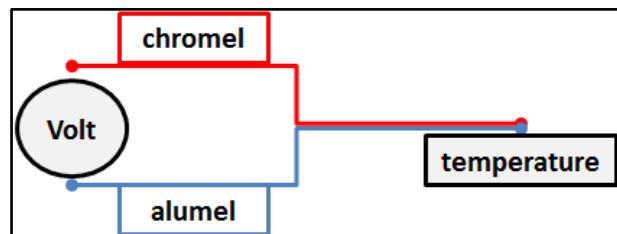


Figure 45. Thermocouples position.

The principle of measurement is based on the difference of voltage generated when two different conductors are subjected to a temperature gradient. By measuring this voltage difference it is possible to determine the temperature (Figure 46.b). This kind of thermocouples has a temperature range between  $-270$  and  $1370^\circ\text{C}$  with a temperature accuracy of  $0.2^\circ\text{C}$  and a sensitivity of  $41\mu\text{V}/^\circ\text{C}$ .



(a)



(b)

Figure 46. (a) Thermocouple used during the experimental campaign. (b) Measurement principle of the thermocouple.

Acquiring the temperature at  $1\text{Hz}$  allowed to control precisely its trend for each test. The aim was to survey the temperature in the wind tunnel and begin the test when temperature stability was reached. This control was necessary to take into account the thermal inertia of the whole facility and of the flow. To protect from icing, the two thermocouples on the side were protected with the same porous tissue as the snow collectors. The contact thermocouple on the cylinder allows an analysis of the temperature evolution in the first instants of the accretion (Figure 47). It is placed facing the incoming snow at the stagnation point. Its side position on the cylinder avoids to perturb the accretion at the center.

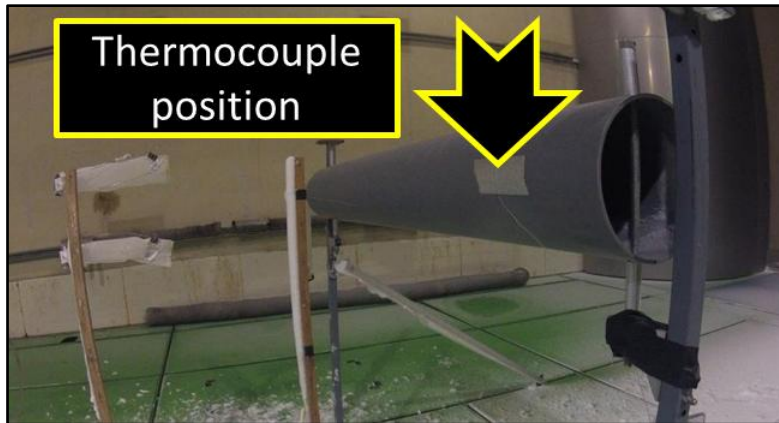


Figure 47. Thermocouple on the cylinder.

The thermocouple on the right wall of the flow inlet allowed, via a comparison with the twos on the sides of the structure, a control on the general uniformity of the temperature inside the chamber.

With its design for climatic extreme conditions the GoPro camera (Figure 48) was suitable during our tests. The camera was placed on one side of the setup so as to not perturb the flow.



Figure 48. GoPro camera.

With this device a series of photos at a frequency of  $0.5\text{Hz}$  were taken, to visualize afterwards, a qualitative analysis of the accretion evolution.

### 3.3.4 Characterization of the incoming flow: ultrasonic anemometer

Due to the fact that the snow flow presents a water content which makes impossible the use of a cobra probe or a hotwire anemometer, a METEK USA-1 ultrasonic anemometer was employed to obtain the flow speed data. The device was placed at the same level of the structure (Figure 49).



Figure 49. The ultrasonic anemometer on its support.

It permitted to measure flow speed along the three spatial direction up to a speed of  $50\text{m/s}$  with a resolution of  $0.01\text{m/s}$  at a maximum sampling rate of  $25\text{Hz}$ . The accuracy of the instrument is  $\pm 2\%$ . The six heads are heated to prevent icing which can perturb the measuring process. An ultrasonic anemometer uses sound to measure wind speed. It sends a sound wave from a fixed transmitter to a fixed receiver. By measuring the time that the sound wave takes to reach the receiver, the ultrasonic anemometer computes the speed of flow. It must be underlined how the presence of the dispersed phase in the air can modify the sound wave speed and reducing the accuracy. Nevertheless previously applications in Chritin et al.[4], Lehning et al.[5] or Cierco et al.[6] justify the use of the ultrasonic anemometer to measure the speed of the air with the presence of snow. However it is important to underline how these experiments have been conducted in open field where snow concentration is less important than during our tests. Moreover, in none of the previous cited studies is presented an estimation of the error committed by using the ultrasonic anemometer with two-phase flow. Here after, a simple estimation of the number of particles which pass through the measurement volume of the ultrasonic anemometer is made. This provides a preliminary estimate of the particle influence on the flow speed measurements.

The reference values are: a particle diameter  $d_{43} = 290\mu\text{m}$ , a measurements volume of the ultrasonic anemometer  $V_{us} \approx 5 \cdot 10^{-7}\text{m}^3$  and the mean snow flux at the center  $\langle \varphi_s \rangle \approx 0.088 \text{ kg/m}^2\text{s}$ . The mean snow flux is taken equal to the mean value of the whole experimental campaign weighted for the coefficient. With the mean wind

speed  $\langle u_f \rangle = 10m/s$  and the ice density of  $910kg/m^3$  it is possible to evaluate the particles concentration as (40).  $m_p$  is the particle mass.

$$\dot{C} = \frac{\langle \varphi_s \rangle / \langle u_f \rangle}{m_p} \approx 1.7 \cdot 10^6 \frac{nb}{m^3} \quad (40)$$

With the particles concentration and  $V_{us}$  it is possible now to estimate the number of particles through the measurement volume as  $n_p \approx \dot{C} \cdot V_{us} \approx 8 \cdot 10^{-1}$ . This preliminary estimation shows how the number of particles, passing through the measurement volume for a given instant, is less than one. As a consequence, one can suppose that the flow speed measurements are slightly affected by particles.

If the presence of particles is important, then additionally, it is interesting to consider the particle state (liquid and/or solid) influence as a function of the ambient temperature. During our tests the particle state has been tuned by adjusting the ambient temperature. Hence, the measurement of the flow speed at an ambient temperature  $T_a = -3^\circ C$  could be different from another one at  $T_a = -9^\circ C$ . The influence of the particle state on the measurement is not well documented in the literature. Moreover, no clear discrepancy was observed during our own measurements at various ambient temperature. As a consequence, it will be not be taken into account during the analysis.

### 3.4 Experimental procedure to reproduce wet snow accretions

#### 3.4.1 Wind tunnel setup

The wind tunnel setting up of the tests follows the scheme of Figure 50

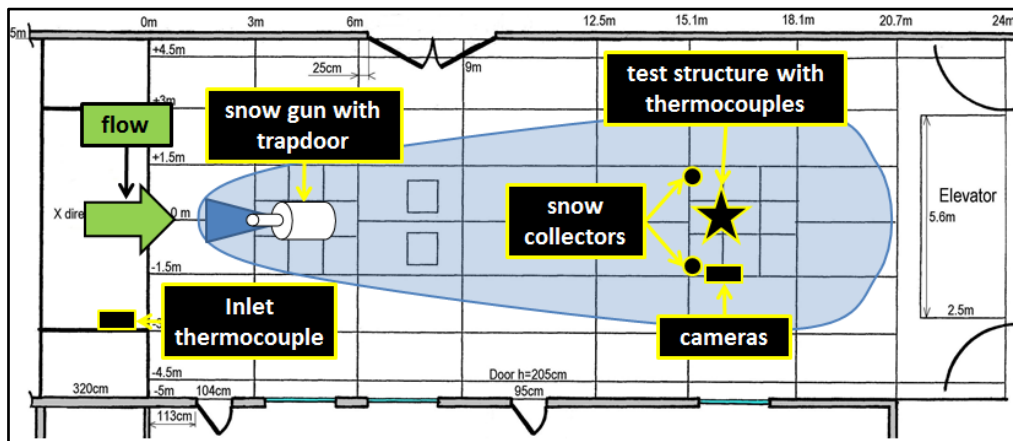


Figure 50. Wind tunnel setting up for test.

The test structure was placed at  $16m$  from the inlet, with the snow collectors  $1m$  ahead. The snow gun, after several optimization tests, was positioned in a counter-current configuration with an inclination of  $20^\circ$ . Moreover, it has been analyzed if the mean snow flux, during a test day, measured with the lateral snow collectors, was constant along the five test days. One can note how, with this configuration, the mean snow flux of a day was close to the mean lateral snow flux of the whole campaign

(Figure 51). The errors bars have been evaluated taking into account the standard deviation for all the measurements during the test days.

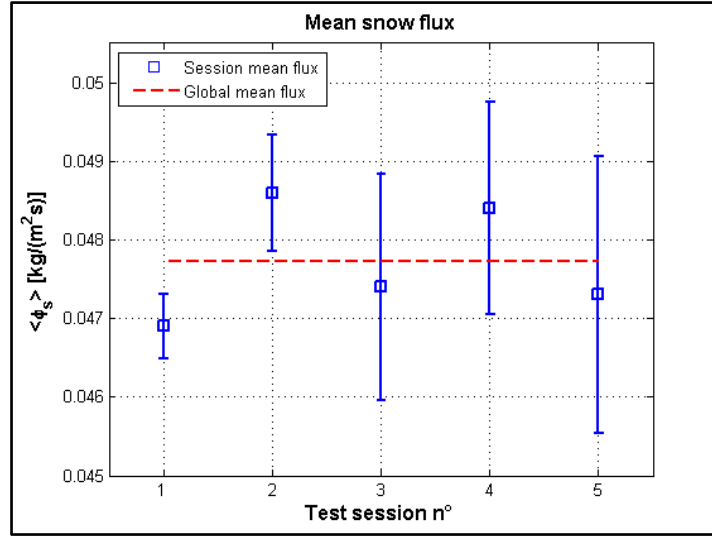


Figure 51. Mean snow flux measured during the five tests of the experimental campaign for the external snow collectors.

With the aim to characterize the snow flow which impacts the test structure a preliminary evaluation of the particle concentration  $\alpha_p$  was performed. The estimation was performed taking the mean snow flux impacting the test structure  $\langle \phi_s \rangle \approx 0.088 \text{ kg}/\text{m}^2\text{s}$ , a mean flow speed of  $\langle u_f \rangle = 10 \text{ m/s}$  and the snow collector area

$A_{col} = 0.005 \text{ m}^2$ . The results of  $\alpha_p = \frac{\dot{V}_p}{\dot{V}_{air}} \approx 9 \cdot 10^{-6}$  has shown how the particle

concentration is between the threshold of consider the influence of particles on the carrier phase (one-way or two-way coupling).  $\dot{V}_p$  is the particle concentration and  $\dot{V}_{air}$  the concentration of the air. One-way coupling means that interactions between particles can be neglected as well as the influence of the dispersed phase on the carrier phase [7]. Two-way coupling means that the dispersed phase acts on the carrier phase through a modulation of the carrier fluid. In this case, due to the qualitative nature of the  $\alpha_p$  evaluation and due to the proximity of one-way coupling limit ( $\alpha_p \approx 6 \cdot 10^{-6}$ ) it has been considered anyway a condition of one-way coupling. This assumption will be also taken into account during the modeling of the dispersion model in chapter four. Moreover the snow flux can be characterized by a set of characteristic parameters as follow.

As a first approximation for the evaluation of  $\tau_p$  can the mean volume diameter  $d_{43} = 290 \mu\text{m}$  be taken in consideration as a reference diameter. As a consequence one can assume that the settling velocity  $v_g = \tau_p g$  gives the most important contribution to the relative velocity  $|u_r| = |u_p - u_f|$ . Furthermore one can perform an iterative evaluation (Figure 52) of the relaxation time and the Reynolds number[8] supposing a Stokes regime for the first iteration:

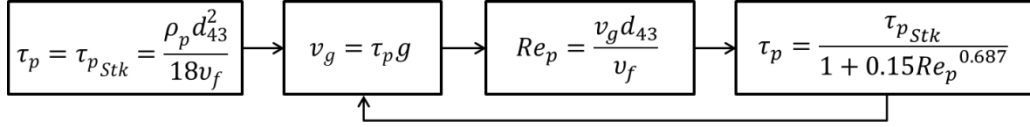


Figure 52.  $\tau_p$  evaluation loop.

Taking a particle density  $\rho_p = 910 \text{ kg/m}^3$  and a kinematic viscosity  $\nu_f = 1.25 \cdot 10^{-5} \text{ kg/ms}$  the loop reaches the convergence at  $\tau_p \approx 100 \text{ ms}$  which differs from the supposition of Stokes regime of  $\approx 58\%$ .

Moreover an estimate of the characteristic time of the turbulent flow can be performed as  $\tau_f = l/u'_f$ . The integral length scale of the fluid  $l$  is estimated as  $l \approx 0.86 \text{ m}$  and  $u'_f = I_{\%} \langle u_f \rangle \approx 0.8 \text{ m/s}$ . The values of  $l$  and  $I_{\%}$  will be detailed later in this chapter. This leads to a characteristic time of the flow  $\tau_f = \frac{l}{\langle u'_f \rangle} \approx 1.1 \text{ s}$ . To give an estimation of the particle behavior with respect to the turbulence a Stokes number is proposed as:  $St_p = \tau_p/\tau_f \approx 0.1$ . One can note that particles will follow the large scale turbulence eddies but gravity effect will have an important role on particles trajectories with  $v_g = \tau_p g \approx 1 \text{ m/s}$ .

### 3.4.2 Experimental principle to reproduce wet snow accretions.

The main goal of the test campaign was to study the thermal and aerodynamic aspect of the accretion. The thermal aspect was investigated varying the  $LWC$  as a function of the ambient temperature  $T_a$ . Let us take as an example a particle with diameter equal to  $d_{43}$  of the snow gun distribution, the trend of  $LWC$  evolution is shown in Figure 53. For the set-up of the test campaign this particle has a flying time of  $\approx 1.2 \text{ s}$  (the purple line of Figure 53).

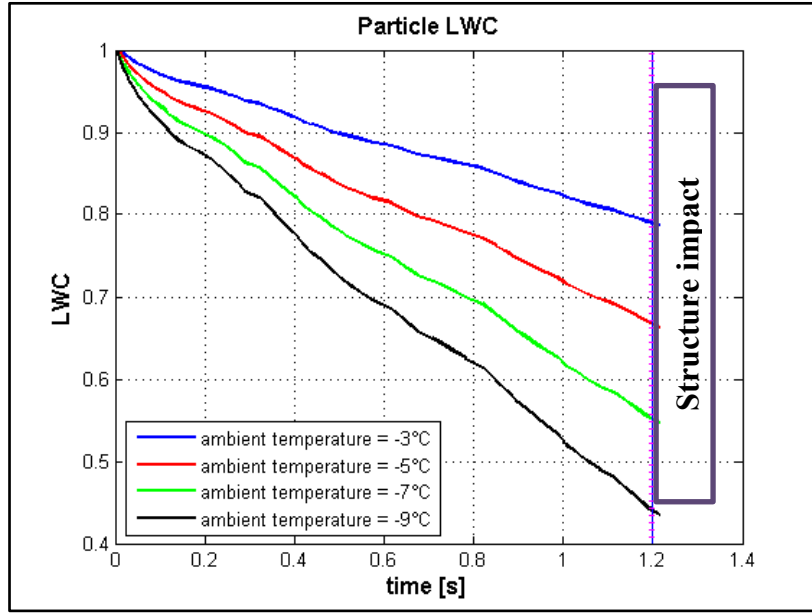


Figure 53. Particle *LWC* as a function of the ambient temperature for  $d_{43} = 290\mu\text{m}$ . The evaluation is made thanks to the dispersion numerical model explained later in chapter four.

The graph above shows how, when the particles flying time is fixed, the particles reach the test structure with a *LWC* which depends only on the ambient temperature. As seen in chapter 2 the accretion depends strongly on the particles *LWC*, as a consequence, the thermal aspect is investigated by changing the ambient temperature to adjust the particle *LWC*.

The aerodynamic aspect is examined by changing the diameter of the cylinder placed on the test structure. The particles behavior with respect to the flow can be characterized with the Stokes number  $St_p$  as explained in literature review. In the same way the behavior of particles close to the cylinder can be investigated with a Stokes number (43)

$$St_{cyl} = \frac{\tau_p}{\tau_{cyl}} \quad (41)$$

where  $\tau_p$  is the particles relaxation time as seen in chapter 2 and  $\tau_{cyl} = d_{cyl} / \langle u_f \rangle$  is the time scale of the flow around the cylinder. This means that changing the diameter of the cylinder leads to change the time scale  $\tau_{cyl}$  and, as a consequence, the behavior of particles close to the cylinder. The larger is  $St_{cyl}$  the more particles have an inertial behavior close to the cylinders, this parameter will be helpful in paragraph 3.5.3 to explain partially the aerodynamic aspect of the accretion.

### 3.4.3 Procedure undertaken during the experimental campaign.

At the beginning of a test, the cylinder was shielded by the cover, snow collectors were empty and protected with a plastic bag to avoid unwanted filling during snow gun start-up. A test starts when of a constant desired wind speed of  $10\text{m/s}$  is obtained. A fixed wind speed implies that, with the distance between the test structure and the flow inlet fixed, the mean particle flying time is fixed. As a consequence of a

fixed mean particle flying time the *LWC* of the impacting particles varies only as a function of the ambient temperature. Thus the tuning parameter of the campaign is the ambient temperature. With a stable wind speed, thermocouples data acquisition started to control the temperature stability inside the climatic chamber (green circle - Figure 54). When also the temperature in the climatic wind tunnel was stable (blue arrow - Figure 54) the snow-gun was started. After the snow gun startup period was completed (light blue circle - Figure 54), plastic bags as well as the cylinder cover was removed. At the same time the trapdoor was lowered. Starting from this moment (yellow arrow - Figure 54), a test of 10 minutes is performed (yellow circle - Figure 54).

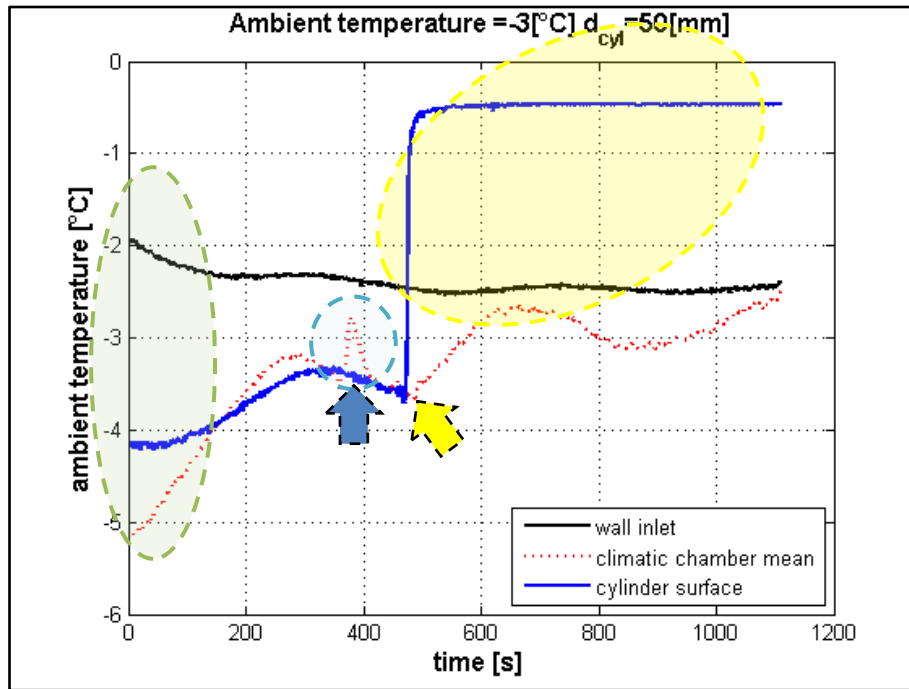


Figure 54. Temperature data of a test.

At  $t = 10min$ , the wind speed and then the snow gun was stopped as well as thermocouples acquisition and also the GoPro video. Afterwards the central portion,  $0.7m$  long, of the snow accretion on the cylinder was weighed with a precision balance as well as the snow mass inside the four collectors. Additionally the thickness of the accretion was noted down. Before starting a new test, the cylinder surface was cleaned from the residual accretion with hot water and then dried to assure the same cylinder surface condition for each test.

This procedure was performed for the three cylinders and for a temperature range between  $-3^{\circ}C$  and  $-9^{\circ}C$ . The results obtained at  $-10^{\circ}C$  and  $-2^{\circ}C$  from a previous campaign test have provided the limiting cases of the study (Figure 55).

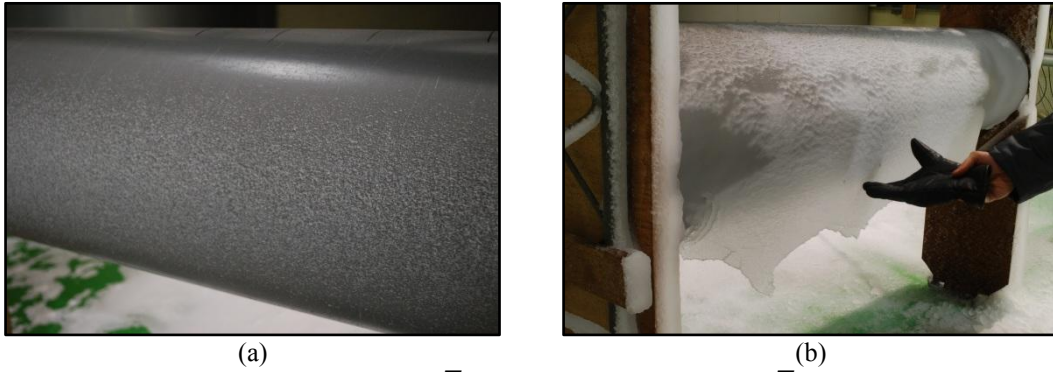


Figure 55. (a) Accretion at  $T_a = -10^\circ\text{C}$ . (b) Accretion at  $T_a = -2^\circ\text{C}$ .

In the first case the accretion was very thin and could not be weighted with sufficient accuracy. When ambient temperature was  $-2^\circ\text{C}$  the accretion was too humid and could no longer be considered as actual snow.

### 3.4.4 Preliminary wind tunnel settings up: analysis of snow flow homogeneity and test reproducibility.

The accuracy of the results presented in this chapter are the consequence of a long period of work to study a configuration which could ensure the homogeneous of the snow flux and the repeatability of the tests.

#### *The snow gun position*

Two principal configurations were tested. The first one was characterized by two snow guns placed on both sides of the climatic chamber (Figure 56). The second one presents one snow gun placed at the center of the climatic wind tunnel, has presented in Figure 50.

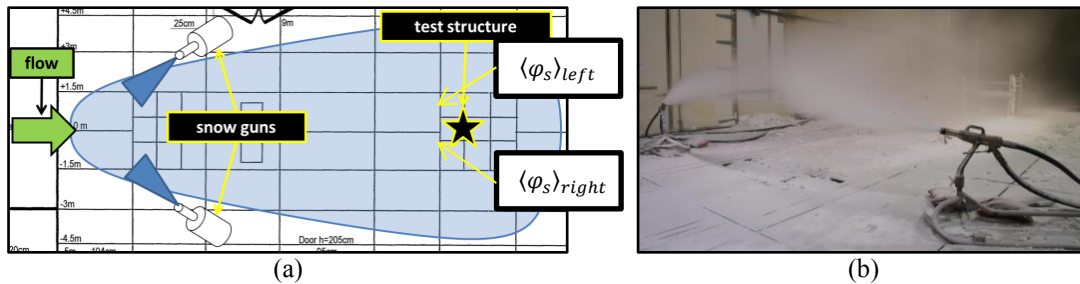


Figure 56. (a) Scheme with two snow guns. (b) Configuration with one snow gun.

The test session with two snow guns aimed to obtain the snow flux as homogeneous as possible. In our case the two snow guns did not have exactly the same air/water flux which can lead to a different flux of snow injected during the tests. Moreover another difficulty was to place the two guns exactly in the same position at the same inclination. These drawbacks led to a spatial inhomogeneity of the snow flux (Figure 57).

The spatial homogeneity has been evaluated as

$$\delta_{\%}\langle\varphi_s\rangle = \frac{(\langle\varphi_s\rangle_{left} - \langle\varphi_s\rangle_{right})}{\langle\varphi_s\rangle_{right}} \quad (42)$$

where  $\langle \varphi_s \rangle_{left}$  indicates the mean snow flux of the two collectors on the left side and  $\langle \varphi_s \rangle_{right}$  the mean snow flux on the two collectors on the right side. Two data sets have been analyzed to ensure the reproducibility (Figure 57).

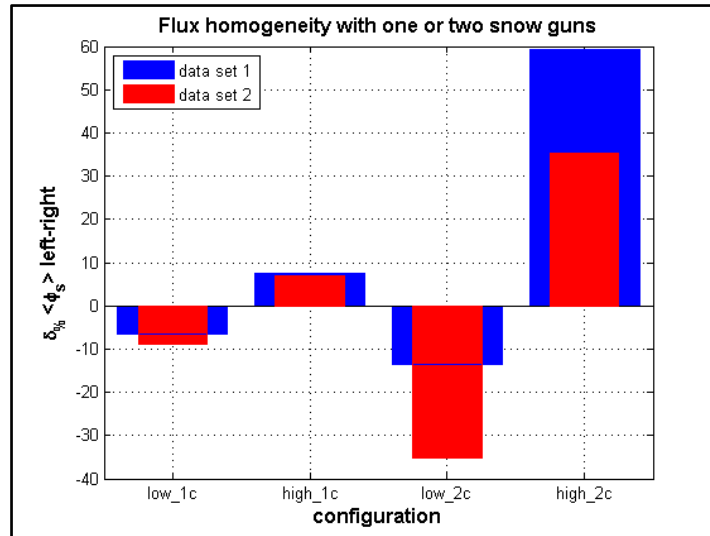


Figure 57. Flux homogeneity in case of one or two snow guns.

In Figure 57 the position of the snow collectors is the same of Figure 41, with “1c” is indicated the  $\delta_{0\%} \langle \varphi_s \rangle$  obtained for a configuration with one snow gun, and with “2c”, is reported  $\delta_{0\%} \langle \varphi_s \rangle$  in case of two snow guns placed both sides of the climatic wind tunnel. Low and high are referred to the snow collectors height: low means at 1.10m and high means 1.50m.

A third configuration was also tested by placing one snow gun on a side of the climatic chamber. This solution was undertaken to reduce as much as possible the perturbation of the snow gun jet on the air stream. However, the results have shown important flux inhomogeneity between the mean snow flux on left side  $\langle \varphi_s \rangle_{left}$  and on the right side  $\langle \varphi_s \rangle_{right}$  (Figure 58).

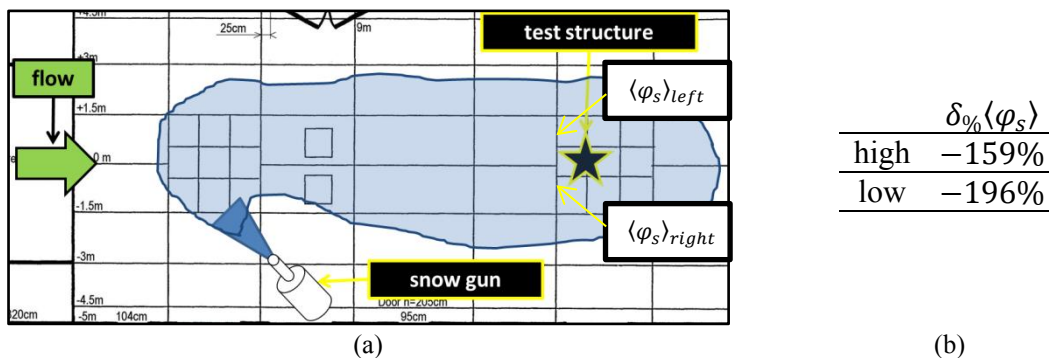


Figure 58. (a) Configuration with one side snow gun. (b)  $\delta_{0\%} \langle \varphi_s \rangle$  differences.

This paragraph has shown how the configuration with one snow gun placed at the center of the climatic chamber allows a better control on the spatial homogeneity of snow flux.

### The position of the test cylinders

The final position of the test cylinders was the result of a long work dedicated to establish the best position which could guarantee the uniformity of the accretion. The first one, presented a series of vertical cylinder of different diameter placed at the center of the climatic wind tunnel (Figure 59.a). This configuration was abandoned due to the vertical non-homogeneity of the accretions obtained (Figure 59.b). This non-homogeneity was supposed to be linked to a water film originated on the upper part of the cylinder, that afterwards froze in the lower part of the cylinder. The accretion here obtained had a triangular shape.

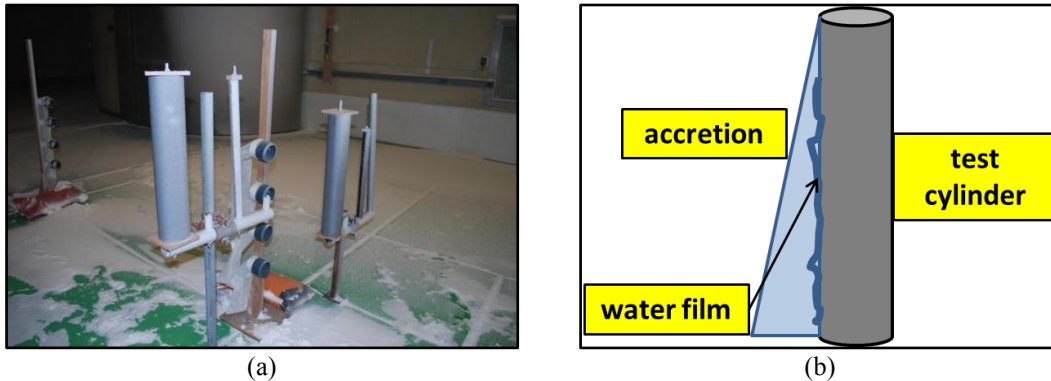


Figure 59. (a) Configuration with vertical cylinders. (b) A scheme of the accretion drawback.

The second configuration undertaken was characterized by two horizontal cylinders (Figure 60.a). This was an improvement to the previous solution which permitted to obtain a uniform accretion. This configuration was used several times but, after having developed the stochastic dispersion model, one has realized that the two cylinders were impacted by a different volume particle distribution  $PSD^v$  (Figure 60.b). These differences were supposed to be due to gravity and boundary layer influence.

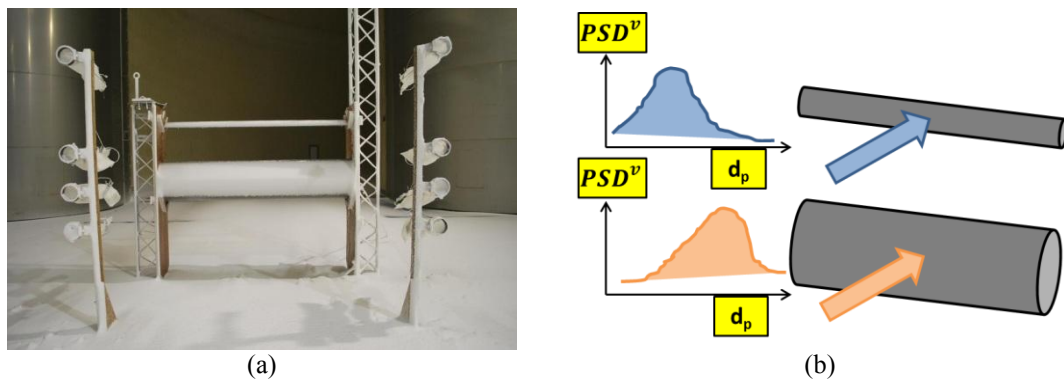


Figure 60. (a) Configuration with two horizontal cylinders. (b) A scheme of the accretion drawback in which  $PSD^v$  is the volume particle size distribution.

As a consequence, the final test structure was designed with one horizontal cylinder. The structure had a practical system to change rapidly the cylinders. The same height for all the cylinders had ensured the same volume particle size distribution impacting the cylinders.

### The reproducibility with the final setup

The reproducibility of the final setup (presented in paragraph 3.4.1) was ensured with a second run of measurements. This second run was performed for all the three

cylinders in an ambient temperature range between  $-6^{\circ}C$  and  $-4^{\circ}C$ . The Table 2 shows the results as a  $\delta_{\%}\beta = (\beta_{run1} - \beta_{run2}) / \beta_{run2}$  where  $\beta_{run1}$  represents the  $\beta$  coefficient of the first run and  $\beta_{run2}$  the one of the second run.

Table 2. The reproducibility of the tests

|                     | $\delta_{\%}\beta d_{50}$ | $\delta_{\%}\beta d_{200}$ | $\delta_{\%}\beta d_{315}$ |
|---------------------|---------------------------|----------------------------|----------------------------|
| $T_a = -4^{\circ}C$ | $\approx -5\%$            | $\approx -4\%$             | $\approx -1\%$             |
| $T_a = -5^{\circ}C$ | $\approx -15\%$           | $\approx 28\%$             | $\approx 6\%$              |
| $T_a = -6^{\circ}C$ | $\approx 23\%$            |                            | $\approx 7\%$              |

The table above shows how control scrupulously all the boundary conditions of the test campaign was difficult. Nevertheless, the results of  $\delta_{\%}\beta$  obtain at  $\hat{T}_a = -4^{\circ}C$  and  $T_a = -5^{\circ}C$  give a confirmation of the progress in the setting up of the experimental structure and procedure. Moreover one does not forget the large dimension of the wind tunnel and its industrial characteristics. Looking at the previous test configurations described in this chapter one can consider the actual setting up and procedure are suitable to study the accretion process.

Additionally one can notice  $\delta_{\%}\beta$  increase while the temperature decrease. This could be imputable to the fact that collecting snow from the cylinders was more difficult at low temperature due to the harder texture of the accretion.

Lastly it is possible to note, how the experimental errors decrease when the diameter of the cylinder increase. One can suppose, that the error committed during the collection of snow from the cylinder  $d_{315}$  are less important on the collected mass  $m_{cyl}$  with respect to the small cylinder  $d_{50}$ . This leads the errors between the first and the second run to be more important for the small cylinder.

### 3.5 The experimental results.

Here after the results of the experimental campaign are exposed. First the evaluation of the turbulence intensity and integral length scale of the flow are presented. After a procedure to recalibrate the values of mass inside the snow collectors and on the cylinder is explained. This recalibration is necessary to take into account the filling-up of the heat exchanger and, as a consequence, the time evolution of the flow velocity during the tests. Finally to investigate the accretion process, a new dimensionless coefficient  $\beta$  is presented.

#### 3.5.1 Snow flow characterization through the ultrasonic anemometer.

To measure the mean speed  $\langle u_f \rangle$ , the integral length scale  $l$  and the associated turbulence intensity  $I_{\%}$  of the flow, a series of measurements with the cobra probe and the sonic anemometer were performed at the beginning and at the end of two test days. To characterize precisely the incoming flow on the cylinders, the measurements were done  $0.5m$  ahead of the cylinders. Moreover, the maximum sampling rate of the ultrasonic anemometer is  $25Hz$ . In case of the cobra probe the data output rate was  $256Hz$ . The cobra probe has been used in case of air stream. With the snow flow the ultrasonic anemometer has been employed. Here after an analysis on the data acquired

is proposed. First the statistical convergence of the data is investigated for a case with only the air stream and a case with the snow flow. The statistical convergence is examined by checking if the second order moments of speed data are stationary: the running average of the flow speed and the flow speed variance must converge toward their mean values. This analysis is performed to control the suitability of the data acquired for a flow characterization in terms of turbulence intensity and integral length scale. Figure 62 shows how the stability of the signal around its mean is verified (Figure 62.a) and how the running average of the mean flow velocity  $\langle u_f \rangle$  and of the flow variance  $\langle u_f^2 \rangle$  converge towards their mean values.

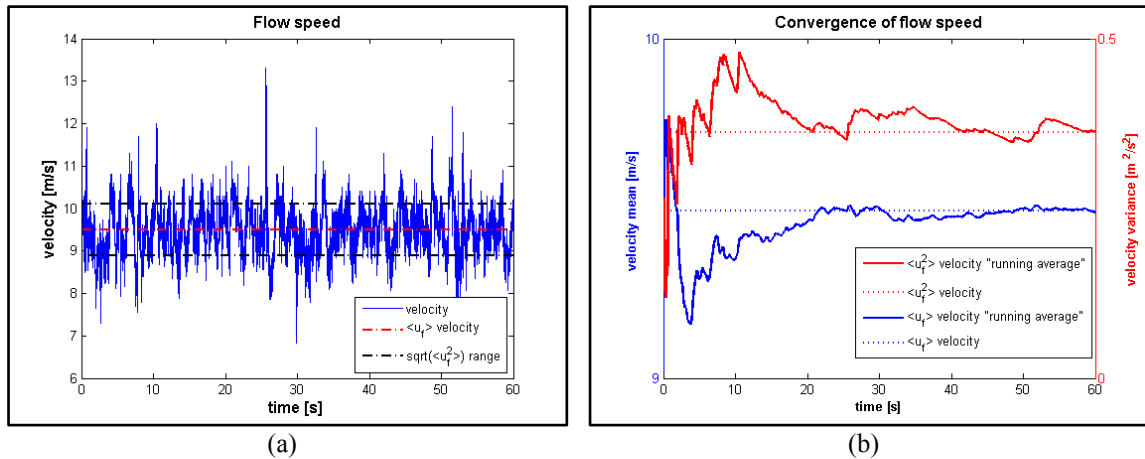


Figure 61. Air flow analysis, cobra probe: (a) flow speed . (b) convergence analysis.

In the same way the analysis of the data convergence is performed in case of flow with snow particles dispersed. Figure 62 shows how, even in case of the snow flow, the stability of the flow speed is verified (Figure 62.a) as well as the convergence of the second order moments (Figure 62.b).

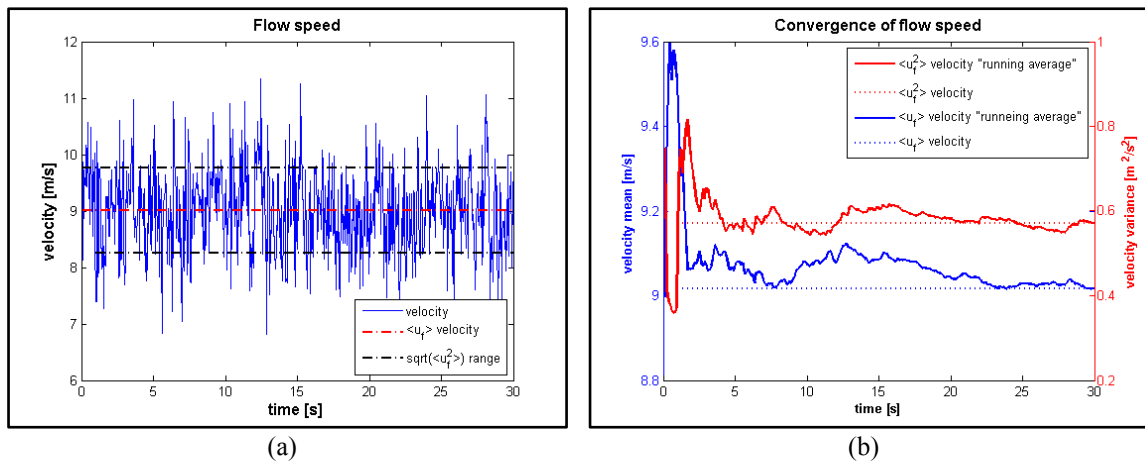


Figure 62. Snow flow analysis, ultrasonic anemometer: (a) flow speed. (b) convergence analysis.

This check is performed to all the flow speed data acquired. The data file which respects better the stationariness of  $\langle u_f \rangle$  and  $\langle u_f^2 \rangle$  is taken as a reference for the evaluation of  $I_{0\%}$  and  $l$ . The intensity of turbulence is evaluated as (43).

$$I_{\%} = \frac{\sqrt{\langle u_f'^2 \rangle}}{\langle u_f \rangle} \quad (43)$$

$\sqrt{\langle u_f'^2 \rangle}$  represents the root mean square of the fluctuation speed of flow where  $u_f' = u_f - \langle u_f \rangle$ . This approximately gives a turbulence intensity of  $\approx 6\%$  for the air stream and  $\approx 8\%$  in case of snow flow. Then the evaluation of the integral length scale  $l$  for the air stream is proposed through the analysis of the autocorrelation function. As seen in chapter two, the autocorrelation function follows the equation  $\mathcal{R}_{\mathcal{L}}(\tau) = \frac{\langle u_f'(t) \cdot u_f'(t+\tau) \rangle}{\langle u_f'^2 \rangle}$  and it is characterized by a value at  $\tau = 0$  of  $\mathcal{R}_{\mathcal{L}}(\tau) = 1$ .

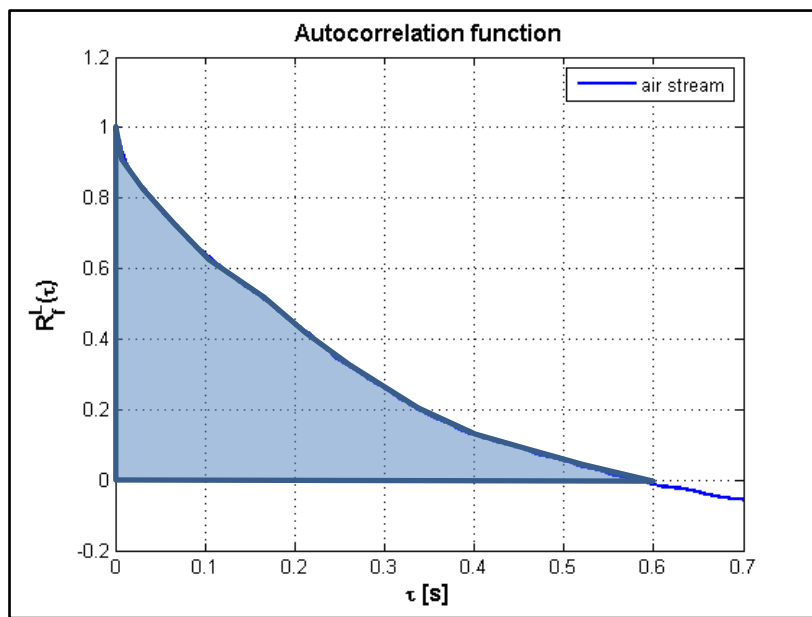


Figure 63. Autocorrelation function for the air stream.

To evaluate the integral length scale one has to evaluate the integral time scale of the flow by an integration of the area under the curve between  $\tau = 0$  and the first  $\tau$  at which  $\mathcal{R}_{\mathcal{L}}(\tau) = 0$ . In this case  $\mathcal{R}_{\mathcal{L}}(0.582) = 0$  (Figure 63 – blue area). The area evaluation leads to an integral time scale of  $\approx 0.2s$ . Taking as a reference a mean flow speed  $\langle u_f \rangle \approx 9.38m/s$ , this leads to an integral length scale for the air stream  $l \approx 1.9m$ .

### **The estimation of the integral length scale in case of snow flow**

The snow gun jet emerging against the main flow is responsible for a new turbulent flow structure. Indeed, the counter-current jet induces high level of shear and therefore, turbulence production. Moreover, turbulent length scales are influenced by the wake of the jet. (Figure 64).

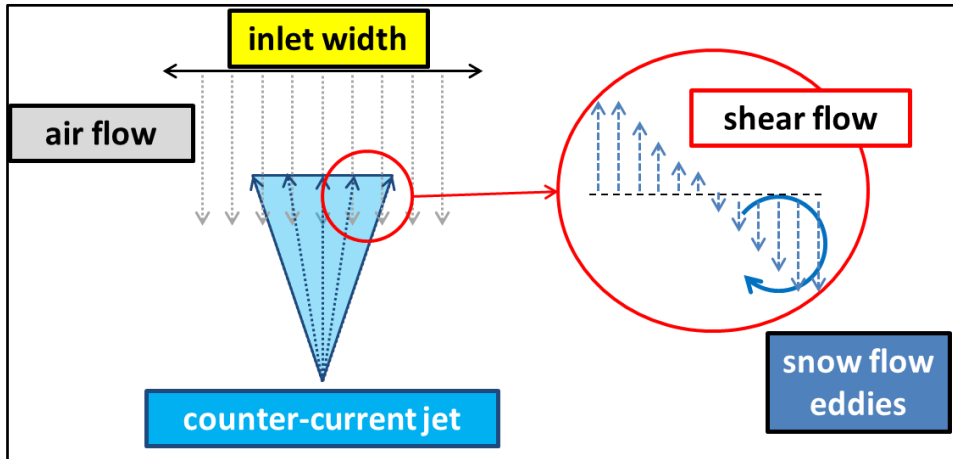


Figure 64. The supposed effect of the snow gun on the eddies dimension, top view.

Moreover, taking into account the fact that the cylinder is placed in the wake region of the counter-current jet, one has to estimate the integral length scale for the snow flow with care. The autocorrelation function is again used (Figure 65).

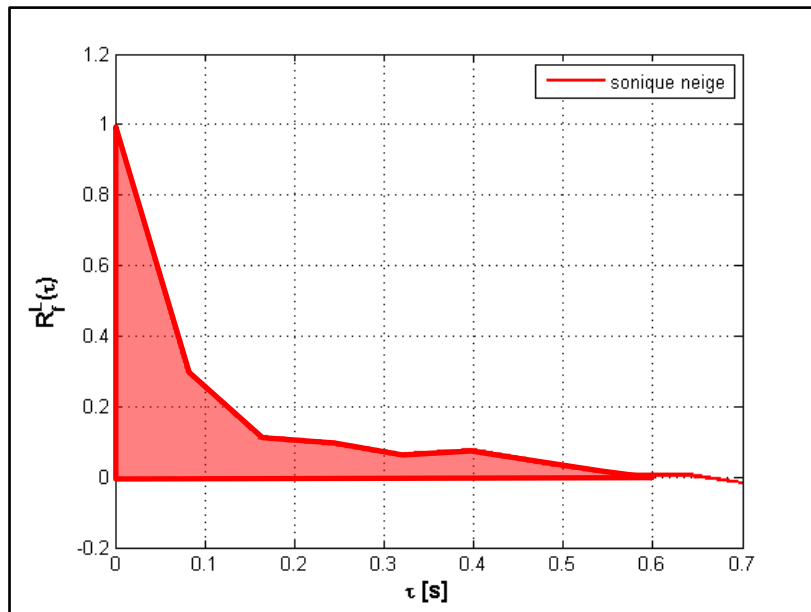


Figure 65. Autocorrelation function for the snow flow.

Figure 65 shows that the frequency response of the ultrasonic probe is not sufficient to provide an accurate value. However, it is very hard to measure turbulence in presence of snow. This evaluation is kept in the following.

In case of snow flow, the estimation of the integral length scale leads to an approximate values of  $l \approx 0.9m$ . More precisely the cylinder as well as the ultrasonic anemometer is placed in the wake region of the counter-current jet. This can explain how the turbulent intensity of the snow flow is larger than in case of air stream and also how the integral length scale is smaller for the snow flow. By overlapping the two autocorrelations one can have a confirmation of the fact that the integral length scale of the snow flow is smaller than the one for the air stream (Figure 66).

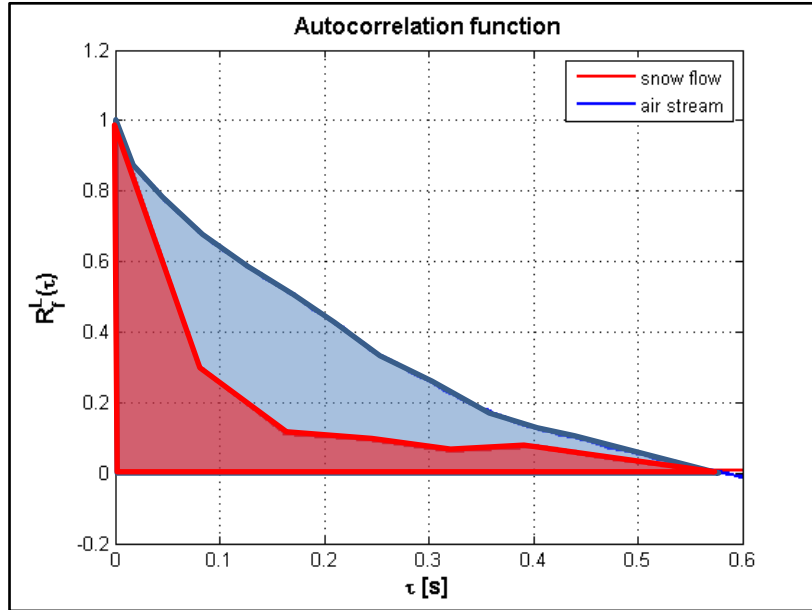


Figure 66. The autocorrelation comparison.

### 3.5.2 Heat exchange blockage: estimation of the real flow speed.

It has been observed during the tests that snow can stick and pack on the wind tunnel heat exchanger causing an obstruction which can lead to a decrease of the mean flow speed  $\langle u_f \rangle$ . As a consequence the mean snow flux  $\langle \varphi_s \rangle$  and the snow mass gathered on the cylinder  $m_{cyl}$  decrease as well. Therefore it is important to recalibrate  $\langle \varphi_s \rangle$  and  $m_{cyl}$  with respect to a dimensionless coefficient  $\chi_n = \frac{\langle u_f \rangle_1}{\langle u_f \rangle_n}$  which takes into account the heat exchange obstruction.  $\langle u_f \rangle_1$  is the mean flow speed at the beginning of a test day supposed to be not affected by the heat exchanger obstruction.  $\langle u_f \rangle_n$  is the mean flow speed of the “*n*-th” test of the day.

The pressure difference  $\Delta p$  measured between upstream and downstream the heat exchanger is the warning parameter: when it grows the heat exchanger starts to be obstructed. To control when obstruction arises the pressure difference  $\Delta p_n$  of each test is noted.

Seen the practical impossibility to measure the mean flow speed of each test  $\langle u_f \rangle_n$  with the ultrasonic anemometer, an empirical law is here presented to rely the  $\Delta p$  of a test to the correspondent mean flow speed. The mean flow speed employed for the data fitting is taken from the data analyzed in paragraph 3.5.1 with the associated  $\Delta p$  (Figure 67). As one can observe from the figure below, during a test day, the snow flow speed can decrease up to  $\approx 13\%$  from  $\approx 9m/s$  to  $\approx 7.8m/s$ .

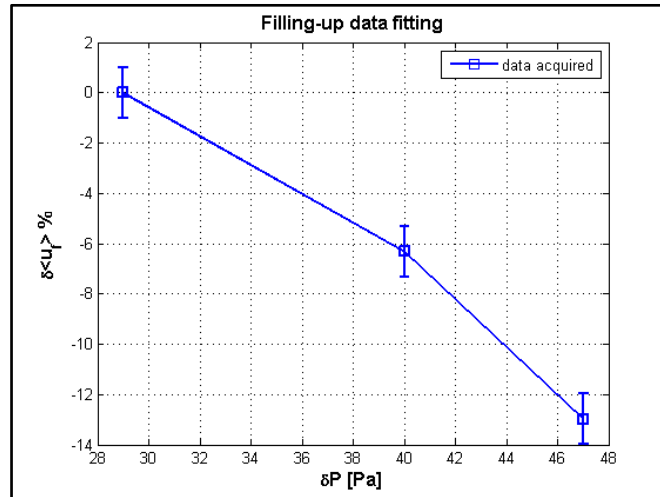


Figure 67. Decrease of the mean flow speed during a test day.

Hence the data presented above are interpolated with a second order polynomial fit to obtain an empirical law (44) which, for a given  $\Delta p_n$ , estimates the mean flow speed  $\langle u_f \rangle_n$ . The mean decrease of the flow speed during a test day has been evaluated in  $\approx 10\%$ .

$$\langle u_f \rangle_n = -0.0022\Delta p_n^2 + 0.0976\Delta p_n + 8.0123 \quad (44)$$

While doing this interpolation we are well-aware that three points does not lead to a robust statistical data fitting. At the same time we are conscious of the importance to know the mean flow speed for each test with which recalibrate the experimental data. For this reason the mean snow flux and the snow mass gathered by the cylinders are recalibrated. Moreover when the speed of the flow  $u_f$  decreases during a test day, the relative velocity between the speed of the snow flux and the speed of particles injected by the snow gun can vary. One can suppose that this variation affects also the snow flux deviation. To deepen this aspect a series of concentration measurements with five collectors in a row have been performed as a function of the wind speed. The placement of the snow collectors follows the one seen in Figure 43. The figure beneath shows how the mass collected inside the five collectors remains almost constant changing the wind speed  $u_f$ .

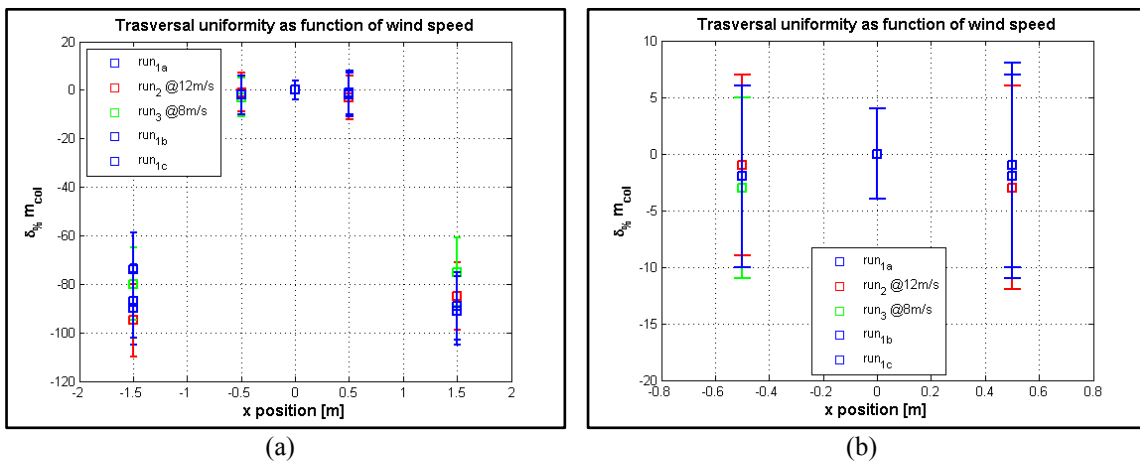


Figure 68. (a) Transversal flow uniformity. (b) Transversal flow uniformity – center zoom.

Moreover, analyzing Figure 68, one can suppose that the changing of  $u_f$  has an influence on the snow gathered by the collectors which can be considered negligible. Therefore in this work it has been supposed that the decrease of the wind speed does not influence the snow flow distribution that impacts the cylinder at the center and the snow collectors on the sides.

Finally, during the development of the analysis, it has been supposed that the recalibration here proposed can compensate the reduction of the wind velocity due to the blockage effect of the thermal exchanger. With all the data recalibrated it is now possible to proceed with the analysis of the accretion data obtained during the experimental campaign.

### **3.5.3 Wet snow accretions quantification: coefficient $\beta$**

To analyze the accretion on the test structure a dimensionless coefficient  $\beta_{exp}$  (45) is proposed as the ratio of the normalized flux of the snow developed on the cylinder  $\psi_a$  to the mean snow flux  $\langle\varphi_s\rangle$  (Figure 69). Once again, it is remembered how the mean snow flux  $\langle\varphi_s\rangle$  is evaluated aside the test structure and how the value it has been recalibrated by the coefficient  $k_s = 1.85$  explained before. This parameter  $\beta_{exp}$  allows to quantify the accretion on the cylinder with respect to the mean incoming snow flow, and it takes into account the three aspects of accretion: aerodynamic, mechanical and thermal. The extreme values of the parameter are one and zero. One in case that all the incoming snow flux sticks and forms the accretion on the cylinder, zero in case of no accretion.

$$\beta_{exp} = \frac{\psi_a}{\langle\varphi_s\rangle} \quad (45)$$

$\psi_a$  is defined as the snow accretion on the cylinder  $m_{cyl}$  divided by the effective section  $A_e$  and by the test duration  $t$  (46). The definition of the mean snow flux  $\langle\varphi_s\rangle$  has been given in paragraph 3.3.2.

$$\psi_a = \frac{m_{cyl}}{(A_e \cdot t)} = \frac{kg}{m^2 \cdot s} \quad (46)$$

where  $A_e$  is equal to  $(d_{cyl} \cdot l_{cyl})$  where  $d_{cyl}$  is the cylinder diameter and  $l_{cyl}$  the central portion of the cylinder equal to  $0.7m$ .

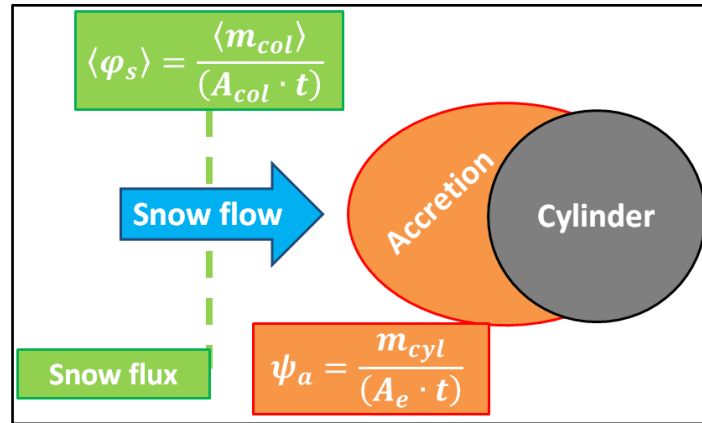


Figure 69. The mean snow flux and the normalized accretion on the cylinder, a later view.

The snow is taken from the central part of the cylinder. This approach ensures that the snow sample weighted had an uniform profile excluding not-uniform side portions of accretion (Figure 70). One can suppose that these non-uniformities of the side portions are related to perturbations sideways of the cylinder and, as seen before, to the non-uniformity of the impacting snow flow.

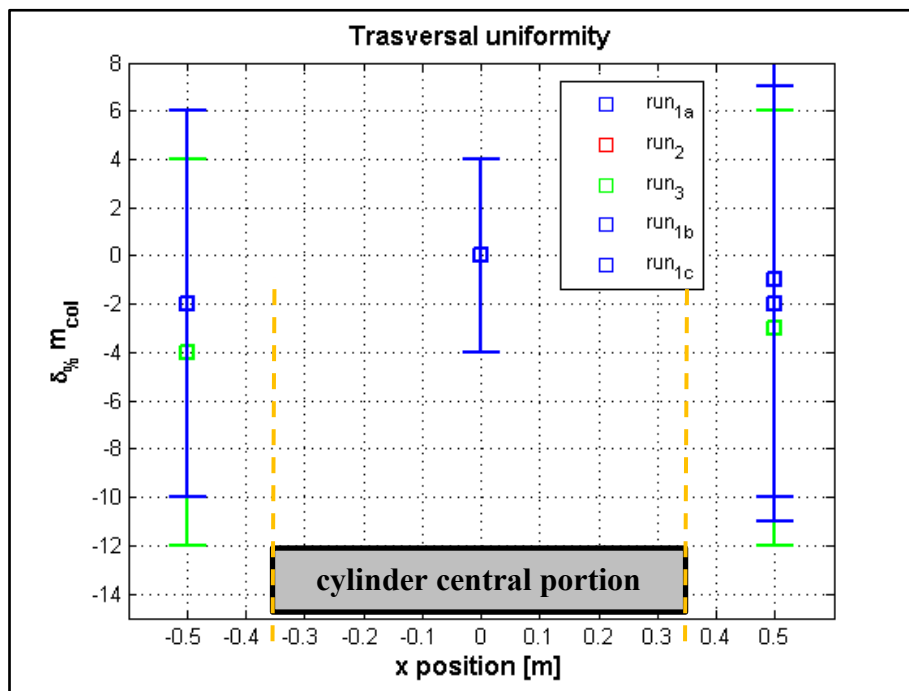


Figure 70. Impacting flow uniformity on the cylinder central portion.

### 3.5.4 Experimental analysis of the *LWC* role of wet snow accretion through the coefficient $\beta$ .

As seen before, one of the objectives of the experimental campaign is to study the influence of the particles *LWC* on the accretion. By adjusting the ambient temperature it is possible to modify the particle *LWC* through the particle freezing process. In Figure 71 the coefficient  $\beta_{exp}$  is reported as a function of the ambient temperature for the cylinder with a diameter of 50mm. Taking into account only one

cylinder, the aerodynamic influence on the coefficient  $\beta_{exp}$  is the same for all the temperatures.

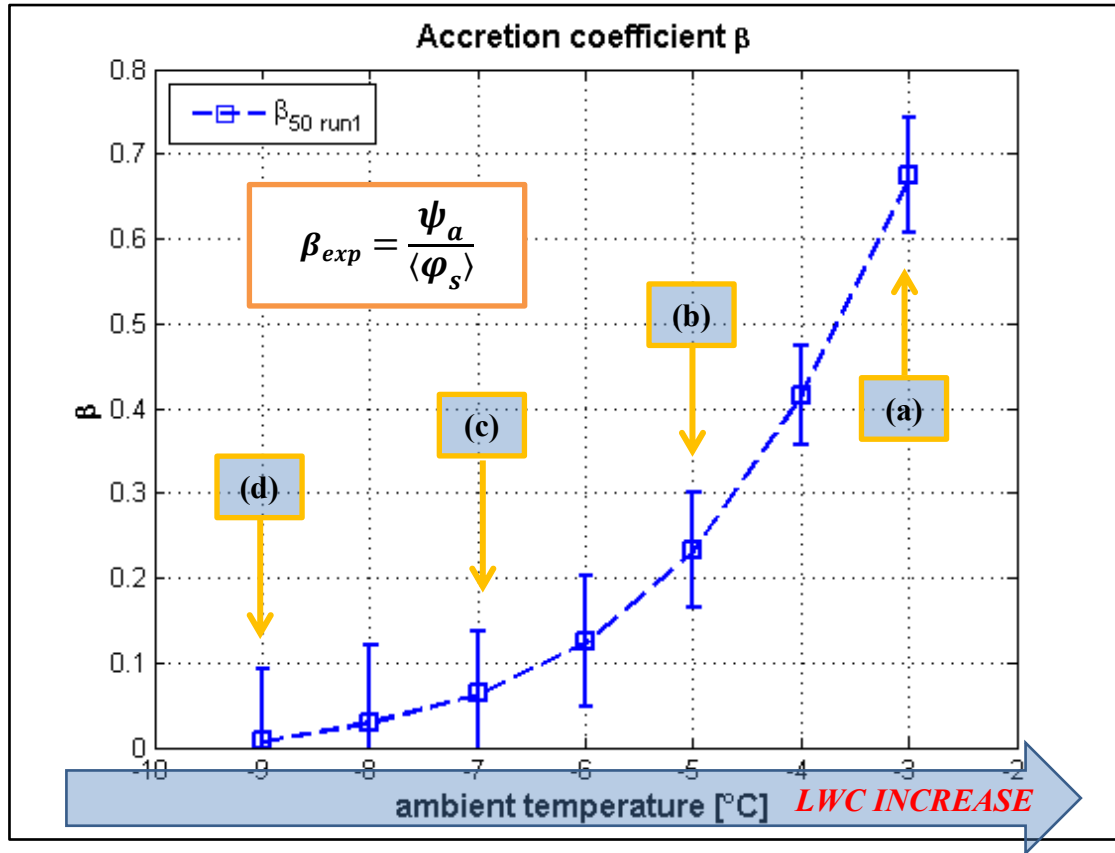


Figure 71. The coefficient  $\beta$  as a function of the ambient temperature.

The graph reported above shows how the coefficient  $\beta$  decreases while lowering the ambient temperature. Following the particle freezing process theory this means that a decrease of the ambient temperature leads to a decrease of particles *LWC*. As a consequence the snow mass accreted decreases while lowering the particles *LWC*. These values of  $\beta_{exp}$  will be linked to the snow flow *LWC* in the chapter five when will be exposed the accretion model.

Through the analysis of the accretion images in Figure 72 it can be observed qualitatively how the augmentation of the temperature leads to larger accretions. Through a close observation of the accretions during experiments it has been noted also how in case of high temperature the accretion was more humid.

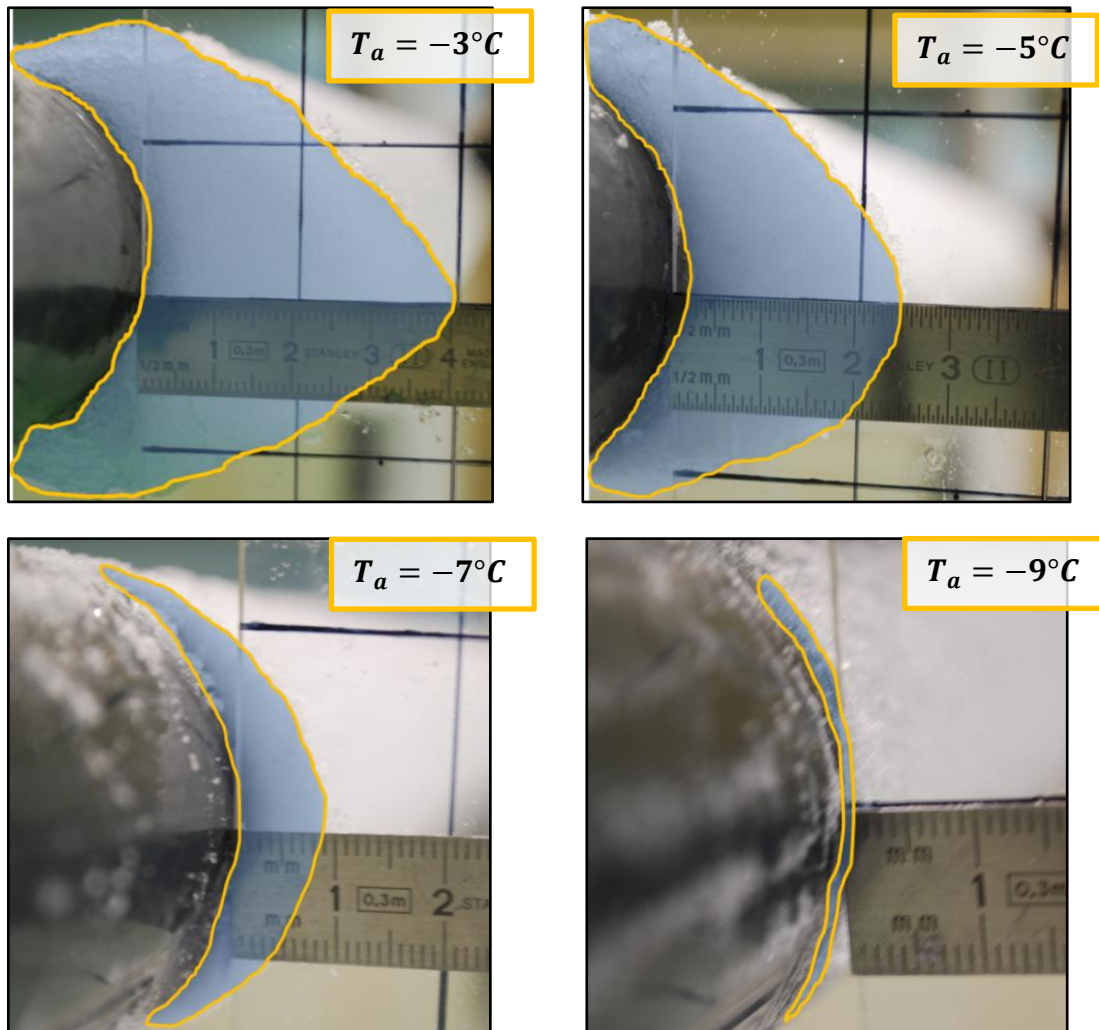


Figure 72. Four side views of the accretion on the cylinder  $d_{50}$ .

Focusing on Figure 73 it can be noted how the accretion (the red arrow) has grown more than the diameter of the cylinder (the yellow arrow) which leads to an effective section  $A_e$  bigger than its standard values ( $d_{cyl} \cdot l_{cyl}$ ). This image is related to the cylinder  $d_{50}$  at an ambient temperature  $T_a = -3^\circ C$ . Analyzing the image, one can suppose that the area augmentation leads to overestimate the coefficient  $\beta_{exp}$ . As a consequence the value of  $\beta_{exp}$  in this case have to be taken with care.

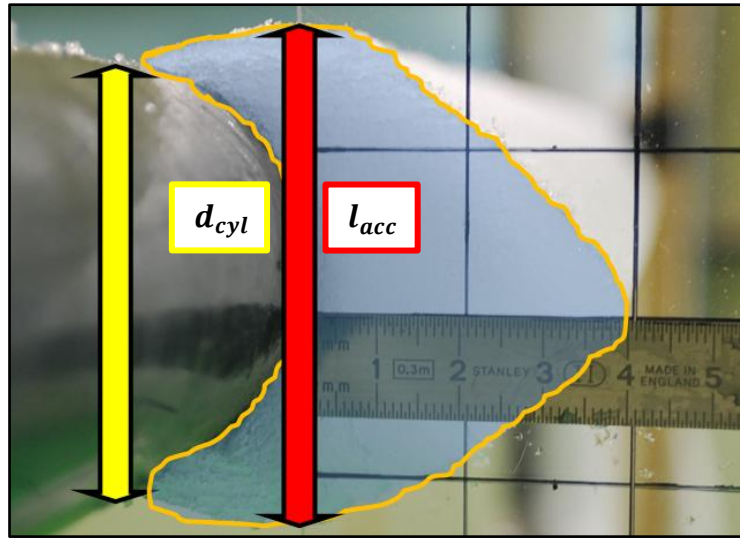
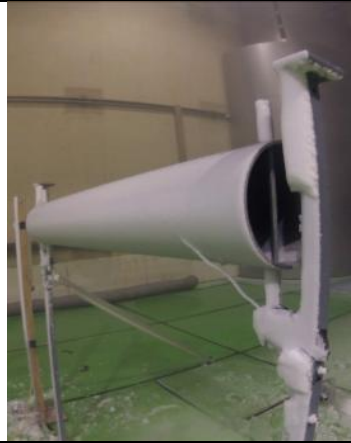


Figure 73. Augmentation of the effective section for  $\beta$  at  $T_a = -3^\circ C$ .

A preliminary evaluation of the effective area augmentation leads to a qualitative evaluation of this increase around 20%. One can preliminary suppose that this area augmentation could be due to an important runback of water, due to the high temperature, which freezes later on the cylinder surface. In accordance with the literature review, the runback is the liquid part of the particle which does not freeze on the surface and flows along the cylinder surface.

Here after a sequence of photos taken with the GoPro camera at different test moments is presented. The photos are referred to the snow accretions on the three cylinders for an ambient temperature  $T_a = -4^\circ C$  (Table 3). With a qualitative visual analysis one can see how the ratio of the accretion seems to be the same for all the three cylinders.

Table 3. Screens of snow accretions at the same ambient temperature  $T_a = -4^\circ\text{C}$ .

| $t_{screen} = 3min$   | $t_{screen} = 6min$   | $t_{screen} = 9min$   |
|---|---|---|
| $d_{cyl} = 50mm$  |   |   |
|    |    |    |
| $d_{cyl} = 200mm$   |   |   |
|   |   |   |
| $d_{cyl} = 315mm$   |   |   |
|  |  |  |

Moreover the same qualitative analysis can be done taking a sequences of images for the cylinder of  $d_{cyl} = 315mm$  for different ambient temperatures. In this case the influence of the temperature on the accretion is well evident from the images.

At low temperature, which it supposed to mean low  $LWC$ , the accretions was very thin which correspond a low coefficient  $\beta_{exp}$ .

Table 4. Screens of snow accretions for the same cylinder.

| $t_{screen} = 3min$   | $t_{screen} = 6min$   | $t_{screen} = 9min$   |
|---|---|---|
| $T_a = -4^{\circ}C$   |   |   |
|    |    |    |
| $T_a = -6^{\circ}C$   |   |   |
|   |   |   |
| $T_a = -9^{\circ}C$   |   |   |
|  |  |  |

### 3.5.5 Experimental analysis of the thermal aspect of wet snow accretions: temperature profiles

An additionally analysis can be performed by studying the temperature data for the four same cases shown above: ambient temperature of  $-3^{\circ}\text{C}$ ,  $-5^{\circ}\text{C}$ ,  $-7^{\circ}\text{C}$  and  $-9^{\circ}\text{C}$  for the  $d_{50}$  cylinder. Figure 74 reports the temperature on the wall inlet, the average temperature of the climatic chamber and the temperature on the cylinder. The temperature on the wall inlet is referred to a contact thermocouple placed in the climatic chamber inlet as shown in Figure 50. The average temperature of the climatic chamber is evaluated as a mean between the two thermocouples placed on both sides of the structure. The temperature of the cylinder surface is referred to a contact thermocouple on the external surface of the cylinder placed on the right, face to the snow flux, to avoid perturbations on the accretion.

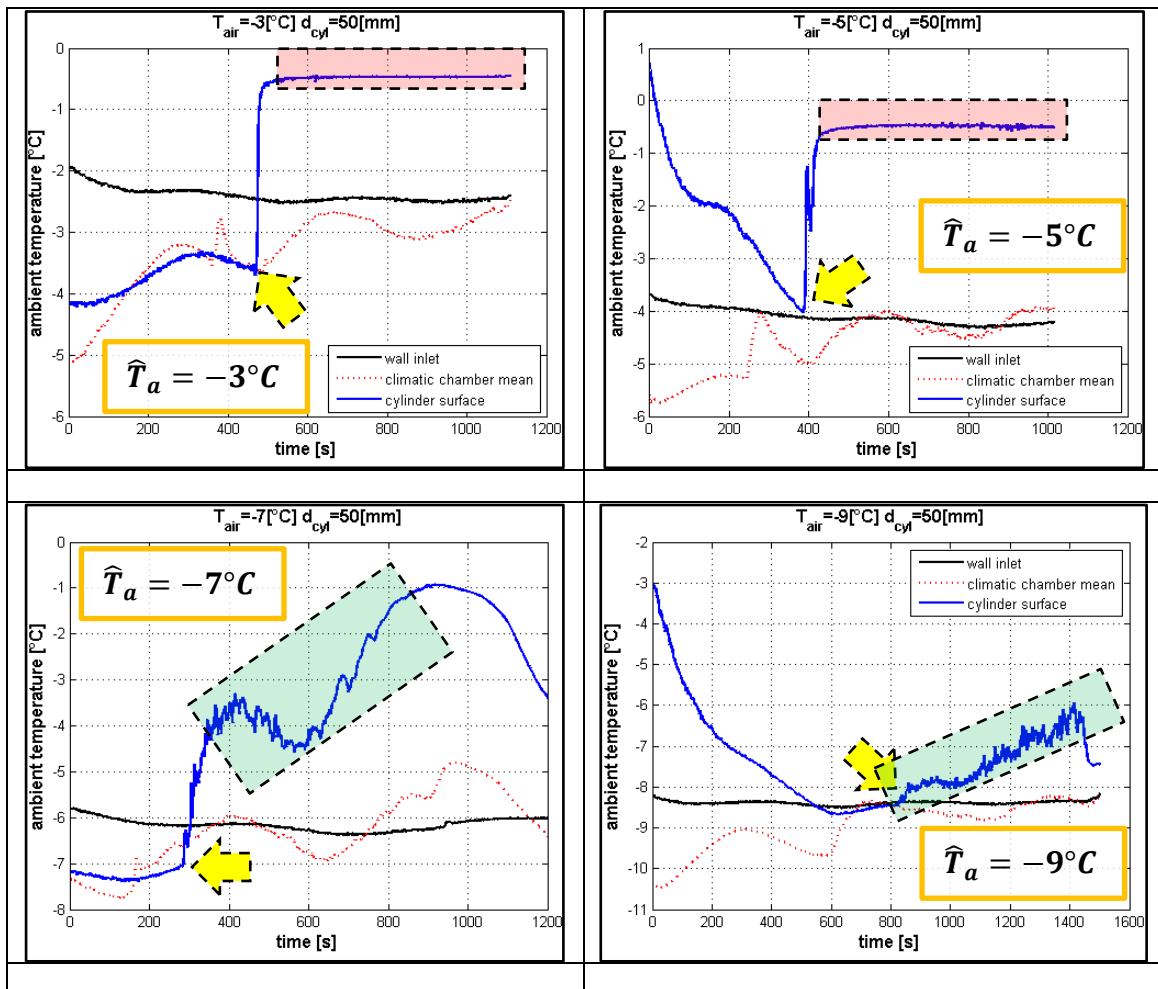


Figure 74. Temperature profiles for the same cylinder  $d_{50}$  at four ambient temperatures.

It is important to notice how all the profiles of Figure 74 show an augmentation of the temperature on the surface cylinder when the snow flow impacts the surface (yellow arrow). Nevertheless this augmentation is totally different in cases of high temperature: (a) and (b) or low temperature cases: (c) and (d). Taking in consideration the first two cases, supposed to be characterized with high  $LWC$ , it can be observed how after snow impact the temperature rise-up close to zero degrees. As seen in chapter 2 this condition is characterized by the presence of a water runback and it is called glaze

ice. During the accretion process in this case the temperature on the cylinder surface remains constant all time long as shown by the red square in Figure 74.

Analyzing the others two cases (c) and (d) supposed to be characterized by a low *LWC*, it can be noted how the temperature surface trend of the cylinder is completely different from the previous two. After the impact of the snow flow the temperature rises up but less rapidly than for the (a) and (b) cases and its value is far from zero degrees. When surface temperature is not close to zero the accretion is called rime.

### 3.5.6 Experimental analysis of the aerodynamic aspect of wet snow accretions: cylinders role through a Stokes number and coefficient $\beta_{exp}$ .

To study the aerodynamic aspect of the accretion three cylinders of different diameter are employed. The test procedure is repeated for all the cylinders for the whole range of temperatures as well as the evaluation of the coefficients  $\beta_{exp}$  (Figure 75).

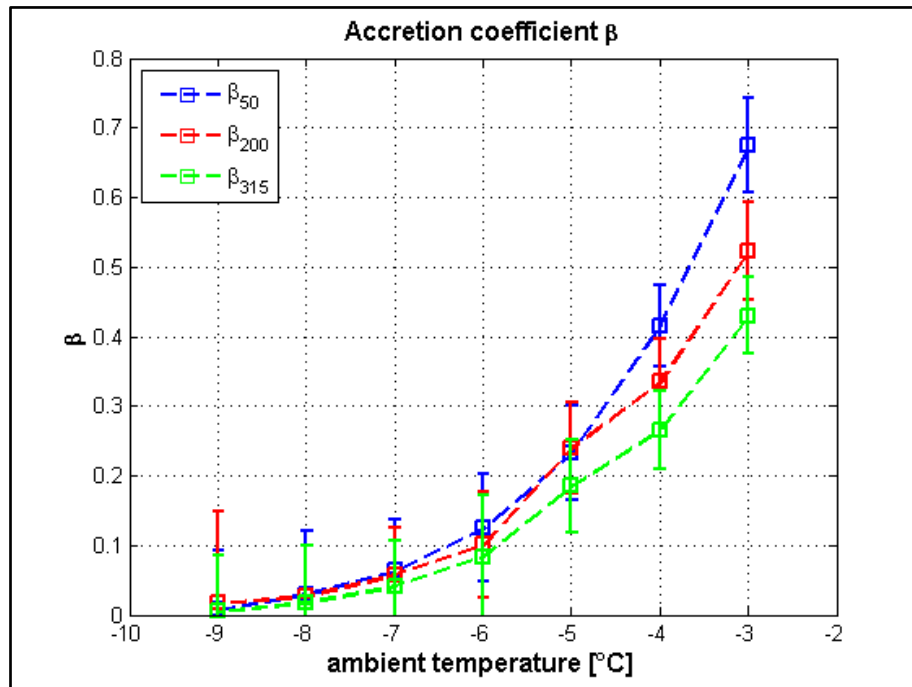


Figure 75. The  $\beta_{exp}$  coefficient for all the three cylinders as a function of the ambient temperature.

As shown in Figure 75 performing an aerodynamic analysis directly on the  $\beta_{exp}$  coefficient for all the three cylinders is not so evident. To better understand how aerodynamic influences the accretion, the  $\beta_{exp}$  coefficient is split in three contributions (47)

$$\beta_{exp}^{123} = \eta_1 \cdot \eta_2 \cdot \eta_3 \quad (47)$$

Where the three  $\eta$  follow the same definitions proposed in the literature review: the first one represents the aerodynamic contribution, the second one the mechanical contribution, and the last one represents the thermal contributions. To bring in evidence the aerodynamic aspect of the accretion, a ratio between the  $\beta_{exp}$  coefficients is proposed. Let us consider  $d_{50}$  and  $d_{200}$  the  $\beta_{exp}$  ratio means (48)

$$\frac{\beta_{\text{exp } 50}}{\beta_{\text{exp } 200}} = \frac{(\eta_1)_{50}}{(\eta_1)_{200}} \cdot \frac{(\eta_2 \cdot \eta_3)_{50}}{(\eta_2 \cdot \eta_3)_{200}} \quad (48)$$

Doing this it has been supposed as a first approach, that the contribution  $\eta_2 \cdot \eta_3$  is the same for two cylinders. As a consequence, the ratio is only a function of the aerodynamic aspect:  $\frac{\beta_{\text{exp } 50}}{\beta_{\text{exp } 200}} = \frac{(\eta_1)_{50}}{(\eta_1)_{200}}$ . Doing the ratios between the  $\beta_{\text{exp}}$  coefficients for all the cylinders leads to Figure 76.

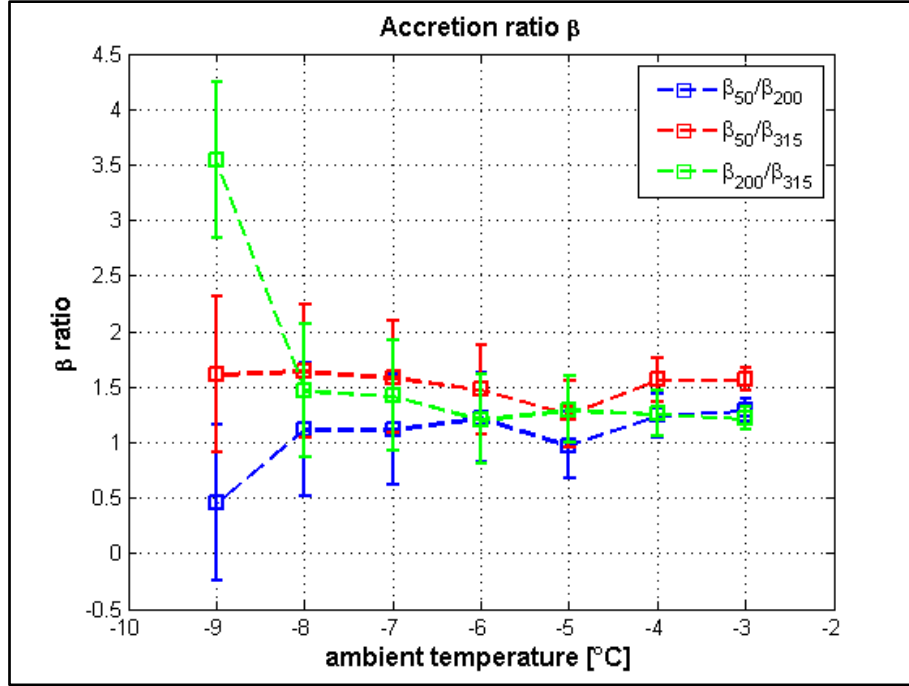


Figure 76. The accretion ratio for the three cylinders.

Figure 76 shows how the aerodynamic aspect is more favorable to the accretion for the cylinder  $d_{50}$ , this is why the ratios between  $\beta_{\text{exp } 50}$  and  $\beta_{\text{exp } 200}$  or  $\beta_{\text{exp } 50}$  and  $\beta_{\text{exp } 315}$  are greater than one with the exception of  $\frac{\beta_{\text{exp } 50}}{\beta_{\text{exp } 200}}$  at  $-9^\circ\text{C}$ . Analyzing the error bar in this last case the value of the ratio less than 1 can be imputable to the errors committed during the measurements. The same considerations can be done while studying the ratio  $\frac{\beta_{\text{exp } 200}}{\beta_{\text{exp } 315}}$ , where also in this case the smallest cylinder between the two, is more favorable to the accretion. The values at  $T_a = -9^\circ\text{C}$  are to take with precautions considering the error bars.

As explained in section 3.4.2, in a first approach, the aerodynamic aspect of the accretion can be investigated with the aid of a Stokes number:  $St_{\text{cyl}} = \frac{\tau_p}{\tau_{\text{cyl}}}$ .

The time scale of the cylinders  $\tau_{\text{cyl}} = \frac{d_{\text{cyl}}}{\langle u_f \rangle}$  is found supposing a  $\langle u_f \rangle = 9\text{m/s}$  which correspond to the mean flow velocity evaluated with the ultrasonic anemometer. So one can now evaluate the  $St_{\text{cyl}}$  (Table 5). It is important to remind how an higher value of  $St_{\text{cyl}}$  means a more inertial behavior of particles while approaching the cylinder.

Table 5. Values of  $St_{cyl}$

|            | $d_{cyl} = 50mm$ | $d_{cyl} = 200mm$ | $d_{cyl} = 315mm$ |
|------------|------------------|-------------------|-------------------|
| $St_{cyl}$ | $\approx 18$     | $\approx 4.5$     | $\approx 3$       |

The  $St_{cyl}$  show how particles are more subjected to impact when the cylinder is little. Hence particles which are approaching the cylinder of  $d_{cyl} = 50mm$  have more inertial behavior than in case of  $d_{cyl} = 200mm$  or  $d_{cyl} = 315mm$ . This inertial behavior can justify why the ratios  $\frac{\beta_{exp 50}}{\beta_{exp 200}}$ ,  $\frac{\beta_{exp 50}}{\beta_{exp 315}}$  and also  $\frac{\beta_{exp 200}}{\beta_{exp 315}}$  are greater than one analyzing Figure 76.

As a conclusion of the analysis of  $St_{cyl}$ , more the cylinder is little, more the accretion is favorable due to the more inertial behavior of particles upstream the cylinder.

The aerodynamic aspect with the evaluation of  $\eta_1$  will be deeply investigated in chapter five thanks to numerical simulations of particles dispersion close to the cylinders. Moreover the numerical simulations will give a confirmation of the loop sketched in Figure 52 to evaluate the relaxation time.

### 3.6 Physical measurements approached

To model we snow accretions, in chapter five will be proposed a numerical modeling. Hence, a set of boundary conditions must be measured. This set includes the particle distribution close to the cylinder with the associated  $LWC$  of particles.

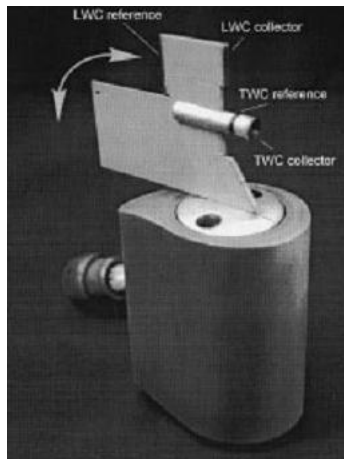
To evaluate the particle distribution close to the structure a numerical model has been developed. The development of this numerical model has been necessary seen the difficulties to acquire physically the information. An optical system, as for example, a MALVERN Spraytec was not possible to rent. Moreover, seen the high concentration of particles in the analysis area, the measurement obtained was certainly affected by important errors. Some tests have been also performed with two systems available at C.S.T.B.. The OTT Parsivel and the Campbell Scientific Presence Weather Sensor PWS100 have shown how the particle concentration was too high to measure the particle distribution.



Figure 77. (a) OTT Parsivel. (b) Campbell Scientific Presence Weather Sensor PWS100.

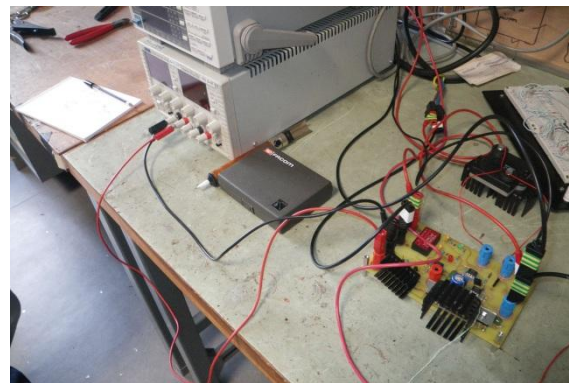
As a consequence of the difficulties to acquire the particle distribution via physical measurements a particle stochastic model has been set up to estimate this distribution. This numerical approach will be explained in the next chapter.

To study the *LWC* of particle close to structure some instruments are available, as for example the Nevzorov probe. This probe is based on the principle of an hot wire probe. The sensor is heated continuously, when a particle hits the sensor the temperature sensor decreases. At this point, to reestablish the predefined temperature, more current is supplied to the sensor. Through this supply of current, the sensor detect the *LWC* of a particle and, in case of a Nevzorov probe, also the particle solid part can be detected.



(a) (b)  
Figure 78. (a) TWC and LWC probe. (b) SEA probe.

Due to the high level of components implemented in this type of probe, the rent price was prohibitive. To obviate this drawback a first development of this kind of probe has been undertaken at C.S.T.B. (Figure 79)



(a) (b)  
Figure 79.: (a) Experimental probe sensor head. (b) Control system set up.

Unfortunately the electrical regulation system was not fast enough to adapt the current to the temperature decrease. Future modifications are planned to improve the response rapidity to a temperature decrease.

Seen the difficulties encountered to evaluate the particle *LWC* through physical measurements a numerical model has been setup to overcome this matter. This numerical model is coupled with the stochastic dispersion model mentioned before. The

numerical model for the evaluation of the particle *LWC* is based on the particle freezing theory and will be exposed in the next chapter.

### **3.7 Conclusions**

This chapter has presented our experimental approach to study the wet-snow accretion process. The results have been synthesized by a dimensionless coefficient  $\beta_{exp}$ . This coefficient takes into account the three factors which characterize wet snow accretion:  $\eta_1$ ,  $\eta_2$  and  $\eta_3$ . Test reproducibility has been also evaluated.

As seen, lowering the particles *LWC* by lowering the ambient temperature, results in an accretion decrease ( $\beta_{exp}$  decreases). In the next chapter, thanks to a particle freezing process model, the values of temperature will be related to the particles *LWC*. Moreover increasing the cylinder diameter at the same ambient temperature has shown a decreased accretion ( $\beta_{exp}$  decreases). This result, dependent on the particle-structure interaction, will be investigated again in the next chapter.

The analysis of the temperature profiles has shown how the ambient condition as well as the particles *LWC* can lead to rime or glaze accretion type.

A mean flow speed of  $9m/s$ , a turbulent intensity of 8% and integral length scale of  $\approx 0.9$  have been evaluated as a boundary condition of the stochastic dispersion model explained in next chapter. The data acquired on the mass and form of the accretions have given a database with which will be validated the accretion model presented in chapter five.

## Bibliography

- [1] S. Boisson-Kouznetzoff, "Qualification de la neige produite dans la soufflerie climatique Jules Verne: mise au point du dispositif expérimental et modélisation numérique du procédé," Docteur, Dynamique des Fluides et des Transerts, Ecole Doctorale Sciences Pour l'ingénieur De Nantes, Nantes, 1997.
- [2] P. Delpech, "Proces Verbal d'essais - CONFIDENTIEL," 2007.
- [3] D. Font, M. Mases, and J. M. Vilaplana, "Experimental mass-flux measurements: a comparison of different gauges with estimated theoretical data," *Annals of Glaciology*, vol. 26, pp. 225-230, 1998.
- [4] V. Chritin, R. Bolognesi, and H. Gubler, "FlowCapt: a new acoustic sensor to measure snowdrift and wind velocity for avalanche forecasting," *Cold Regions Science and Technology*, vol. 30, pp. 125-133, 1999.
- [5] M. Lehning, F. Naaim-Bouvet, M. Naaim, B. Brabec, J. Doorschot, G. Durand, G. Guyomarc'h, J.-L. Michaux, and M. Zimmerli, "Snow drift: acoustic sensors for avalanche warning and research," *Natural Hazards and Earth System Sciences*, vol. 2, pp. 121-128, 2002.
- [6] F.-X. Cierco, F. Naaim-Bouvet, and H. Bellot, "Acoustic sensors for snowdrift measurements: How should they be used for research purposes?," *Cold Regions Science and Technology*, vol. 49, pp. 74-87, 2007.
- [7] B. Oesterlé, *Écoulements multiphasiques*. Paris: Lavoisier, 2006.
- [8] C. Crowe, M. Sommerfeld, and Y. Tsuji, *Multiphase Flows with Droplets and Particles*: CRC Press, 1998.



# Chapter 4 Physical models for the determination of the boundary conditions

|       |   |     |
|-------|---|-----|
| 4.1   | MODEL IMPLEMENTATION: ESTIMATION OF PARTICLE <i>LWC</i> AT THE INSTANT OF IMPACT COUPLED WITH FLOW-PARTICLES INTERACTION..... | 86  |
| 4.1.1 | <i>Equations implementation in the coupled model: thermal and dynamic equations.</i> .....                                    | 87  |
| 4.1.2 | <i>Hypothesis introduced to represent the experimental conditions.</i> .....  | 93  |
| 4.1.3 | <i>Implementation in the model of the experimental conditions: thermal and flow parameters.</i> .....                         | 95  |
| 4.1.4 | <i>Resolution procedure of the coupled model.</i> .....   | 97  |
| 4.1.5 | <i>Model implementation conclusions</i> .....   | 100 |
| 4.2   | MODELS RESULTS DISCUSSION .....   | 101 |
| 4.2.1 | <i>Boundary condition estimation: particle distribution “on” the cylinders.</i> .....   | 101 |
| 4.2.2 | <i>Particle size distribution on the cylinder</i> .....   | 104 |
| 4.2.3 | <i>The role of the gravity on particle distribution</i> .....   | 107 |
| 4.2.4 | <i>Particles <i>LWC</i> “on” the cylinder surface as a function of the ambient temperature.</i> .....                         | 111 |
| 4.2.5 | <i>Physical parameters which can drive the particle <i>LWC</i>.</i> .....   | 119 |
| 4.2.6 | <i>Boundary condition estimation: <i>LWC</i> of the whole snow particle flow.</i> .....                                       | 122 |
| 4.3   | CONCLUSION.....   | 123 |
|       | BIBLIOGRAPHY .....  | 125 |

The goal of this work is to model wet snow accretions on structures. As seen in previous chapter, a series of experimental tests have been conducted to investigate the aerodynamic the mechanical and the thermal aspect of the wet snow accretions. The result, synthesized by an empirical parameter  $\beta_{exp}$ , has shown how the three aspects play a crucial role for the accretion process. These three aspects will be considered in chapter five.

A physical model able to model the experimental results requires to identify the boundary conditions. The two fundamental boundary conditions are: the particle distribution upstream the cylinder surface and the associated *LWC*. A series of tests to acquire the boundary conditions have been undertaken during the experimental campaign without success. These trials were based on physical measurements of particle distribution (with OTT Parsivel and the Campbell Scientific PWS) and particles *LWC* (with a prototype of a Nevzorov probe).

Due to the fact that physical measurements were not satisfactory to acquire the boundary conditions for the accretion model, a physical model has therefore been built in order to estimate the boundary conditions and their sensitivity to the characteristics of the air stream in the wind tunnel. This model is the main subject of this chapter. The

model is based on the particle freezing process to estimate the  $LWC$  coupled with a stochastic particles tracking model to estimate the particle distribution. The choice of a stochastic approach will allow to take in account flow-particles interactions.

Moreover the current chapter explains the procedure undertaken during the experimental campaign. It will be shown that the ambient temperature drives principally the particle liquid water content:  $LWC = \mathcal{F}(T_a)$ .

#### 4.1 Model implementation: estimation of particle $LWC$ at the instant of impact coupled with flow-particles interaction.

The goal of this section is to present the implementation of the particle freezing model coupled with the stochastic particle tracking model. The first model allows to estimate particles  $LWC$  at the instant of impact on the cylinder surface, while the second model the particle distribution “on” the cylinder. “On the cylinder” means here that, we take into account the statistical properties of the particles having a trajectory that crosses a point of the cylinder upstream surface in the absence of the cylinder. The role of the flow around the cylinder will be considered in chapter 5. The particles  $LWC$  and distribution are the boundary conditions of the accretion model presented in chapter five. The setup of the model is intended to mimic the experimental campaign (Figure 80).

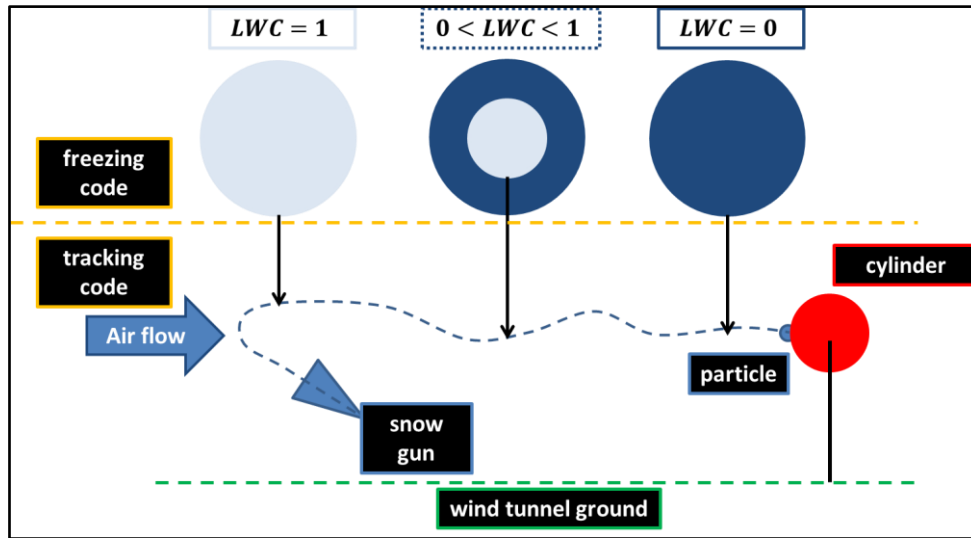


Figure 80. Coupling between freezing and tracking code

As presented during the literature review, wet snow particles are composed of a mix phase. Moreover, literature review and chapter three, has shown that the liquid water content ( $LWC$  – relation (1)) can be considered a crucial parameter for wet snow accretions.

$$LWC = \frac{m_p^l}{m_p} \quad (49)$$

Where  $m_p^l$  is the liquid mass of the particle and  $m_p$  the mass of the particle. As seen in literature review, the particle  $LWC$  can be estimated by developing the particle

freezing process (Strub et al. [1], Hindmarsh et al. [2]). This freezing process allows to tune the  $LWC$  by adjusting the ambient temperature  $T_a$ , that is one of the physical parameters of the experimental campaign:  $LWC = \mathcal{F}(T_a)$ .

The particle trajectory is evaluated by implementing a stochastic tracking model. This model allows to take in account the particle-flow interactions. Taking as a reference the particle diameter  $d_p = 290\mu m$ , in previous chapter we have evaluated that the relaxation time  $\tau_p$  of this particle is almost  $\tau_p \approx 0.1s$ . A characteristic time of turbulence can be defined as  $\tau_f = l / \sqrt{\langle u_f'^2 \rangle} \approx 1.2s$ . Where the integral length scale

estimated in previous chapter is  $l \approx 0.86m$  and the root mean square of the fluctuating velocity  $\sqrt{\langle u_f'^2 \rangle} = I_{v_0} \langle u_f \rangle = 0.72m/s$ . Hence a Stokes number can be evaluated as  $St = \tau_p / \tau_f \approx 0.1$  which indicates that the turbulence strongly affects the particles

behavior in the flow. For this reason, the model tracking the particles trajectories must include a stochastic feature.

#### 4.1.1 Equations implementation in the coupled model: thermal and dynamic equations.

The freezing process of a particle can be characterized by four different steps. The first one is the supercooling stage in which particle temperature  $T_p$  decreases till the nucleation temperature  $T_{nuc}$ . This one is the temperature at which crystals start to growth inside the particle (recalescence stage). In practice, it is not possible to accurately measure the particle temperature to characterize this stage of the particle freezing process. Moreover, one can assume that, due to the highly turbulent flow, the recalescence stage is very short or may not exist at all. As a consequence, this stage was neglected in the analysis. The same hypothesis was made in previous work [3]. The third step (freezing stage) is characterized by the freezing of the liquid part of particle at  $T_p = 0^\circ C$ . In the last step (tempering stage), the particle temperature decreases till reach the ambient temperature  $T_a$ . A scheme is reported in Figure 81.

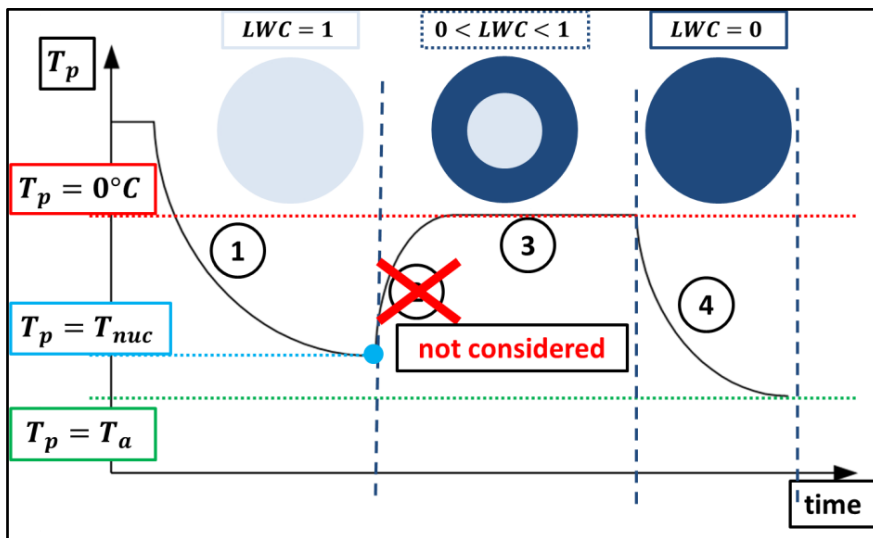


Figure 81. Particle freezing process scheme.

Neglecting the recalescence stage, the particle freezing process considered in the present work has three steps. Following the works of Strub et al. [1] and Hindmarsh et al. [2] the model is based on two hypothesis:

- the particle temperature is considered uniform.
- the particle remains spherical along the freezing process.

The first hypothesis allows to neglect heat conduction inside the particle. Hence, the thermodynamic state of the particle is assessed by a thermal balance including the heat sinks and sources  $\sum q_p$  and the internal energy of the particle  $U_p$ . The Biot number (50) allows to verified this first hypothesis.

$$Bi = \frac{h \cdot \frac{V_p}{S_p}}{\lambda_l} \quad (50)$$

Where  $h$  is the heat transfer coefficient,  $V_p$  the particle volume,  $S_p$  the particle surface and  $\lambda_l$  the thermal conductivity of water. Taking a particle of  $d_p = 290\mu m$ , the particle freezing model presented in this chapter quantifies a mean heat transfer coefficient  $\langle h \rangle = 562 \frac{W}{m^2K}$ . Hence,  $Bi = 0.06$ . When the Biot number is less than 0.1 the heat transfer inside the particle is neglected and the heat transfer is driven by the thermal gradient at the particle surface. As a consequence, particle temperature is considered uniform.

Thanks to the second hypothesis, the freezing process can be modeled as an isotropic process. The two hypothesis allow to present the freezing process as equation (51), the terms are expressed in [J].

$$U_p = \sum q_p \quad (51)$$

The assumption of uniform temperature is also reported by Hindmarsh et al. [2] as a common assumption to predict the freezing time of artificial snowmaking methods which corresponds to the context of this work.

As noted above, the particle freezing process is studied by resolving the equation  $U_p = \sum q_p$  for all the three stages. For the cooling stage and the tempering stage equation (52) is applied to evaluate the internal energy.

$$\frac{dU_p}{dt} = c\rho V_p \frac{dT_p}{dt} \quad (52)$$

where  $c$  is specific heat capacity of water  $c_p^l$  for the cooling state or of ice  $c_p^i$  for the tempering state.  $\rho$  is the density of the particle, i.e.  $\rho_l$  or  $\rho_i$  respectively in case of liquid or solid particle.

Several theories coexist to describe the freezing process. Inward or outward moving boundary models can be developed in the more detailed models that consider the spatial progression of the solidification front. The former supposes an external solid shell which grows toward the center of the particle. For the latter, the particle core is supposed to be solid growing towards the particle surface.

A third approach allows to model the freezing process through a heat balance. In this case, there is no hypothesis regarding the freezing spatial evolution. The freezing process is supposed to occur at constant and uniform temperature ..

Hindmarsh et al. [2] has shown that the three approaches are equivalent. The Figure 82.a shows the results of Hindmarsh et al. using the three approaches. The error made by the models for the estimate of the freezing time, with respect the experimental value for a particle of  $d_p = 40\mu m$  is shown. As one can note, the heat balance model and the Outward model provide the best results. Moreover, Figure 82.b shows how the heat balance mode represents well the particle temperature temporal evolution compared to the experimental measurement.

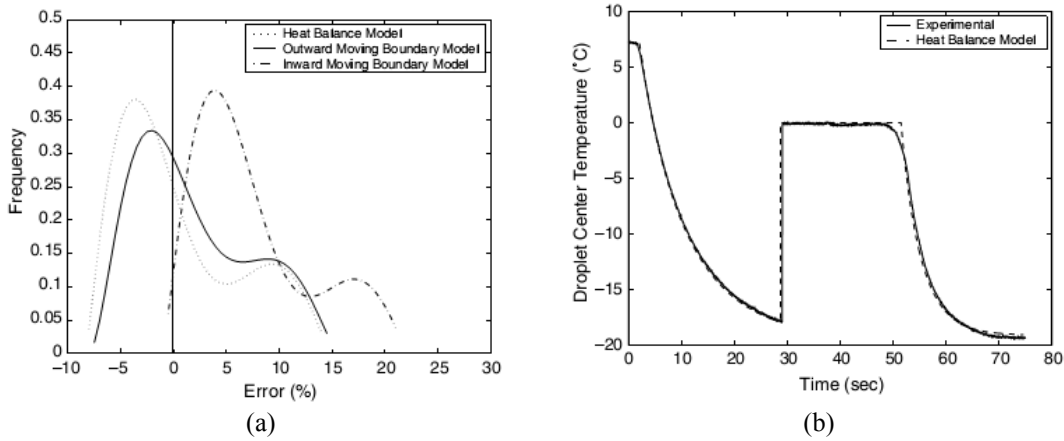


Figure 82. Freezing stage modeling [2]: (a) Assessment of the models regarding the freezing duration (the model outputs are compared to experimental results expressed in term of frequency of occurrence), (b) Temporal evolution of particle temperature according to the heat balance model superimposed to the experimental measurement.

A heat balance model is chosen in this work (53). This model is the fastest in term of computational time. The heat balance model is resolved by a finite-difference scheme while the moving boundary model requires implicit methods to resolve the space-time coupling.

$$\frac{dU_p}{dt} = L_f \rho_i \frac{dV_p^i}{dt} \quad (53)$$

where  $L_f$  is the latent heat of fusion/solidification and  $V_p^i$  is the ice volume of the particle.

As explained before, the particle internal energy  $U_p$  is balanced by the heat sinks from the particle. These heat fluxes are the convective heat flux  $q_h$ , the heat flux  $q_m$  due to the convective mass transfer and the heat flux  $q_r$  due to thermal radiation. All the heat transfers are expressed in [J]. The convective heat flux is expressed by equation (54).

$$q_h = hS_p(T_p - T_a) \quad (54)$$

Where  $h$  is the heat transfer coefficient and  $S_p$  is the particle external surface. The heat transfer coefficient  $h$  is assessed by using a correlation which relates the heat transfer coefficient and the Nusselt number  $Nu$ . Hughmark [4] proposes a correlation to

evaluate a mean Nusselt number for a wide range of Reynolds particle number  $Re_p$  and the Prandtl number of air  $Pr$  (55). These correlations are valid for forced convection around a sphere as in our cases.

$$\begin{aligned} Nu &= 2 + 0.6Re_p^{0.5}Pr^{0.33} & 0 \leq Re_p < 776.06 & \quad 0 \leq Pr < 250 \\ Nu &= 2 + 0.27Re_p^{0.62}Pr^{0.33} & 776.06 \leq Re_p & \quad 0 \leq Pr < 250 \end{aligned} \quad (55)$$

Where  $Pr = \nu_f / \alpha_f \approx 0.7$  with  $\nu_f$  the kinematic viscosity of the air and  $\alpha_f$  the thermal diffusivity. The Nusselt number is related to  $h$  through equation (56) in which  $k_f$  represents the thermal conductivity.

$$Nu = \frac{hd_p}{k_f} \quad (56)$$

The second heat transfer involved in the particle freezing process is the heat transfer due to the convective mass transfer  $q_m$  (57)

$$q_m = Lh_m S_p (C_p - C_a) \quad (57)$$

Where  $L$  represents the latent heat of evaporation. For the cooling stage the heat transfer  $L_e$  is related to evaporation, while when the particle is frozen, heat of sublimation must be considered:  $L_s$ . The heat mass transfer coefficient  $h_m$  is associated to the Sherwood number as (58)

$$Sh = \frac{h_m d_p}{D_{w/f}} \quad (58)$$

Here  $D_{w/f} = 2.2 \cdot 10^{-5} \cdot \left[ \frac{273+T_p}{273} \right]^{1.853}$  represents the water vapour diffusion in the air evaluated in  $\frac{m^2}{s}$ .

Moreover the Sherwood number is related to the Schmidt number  $Sc_f = \frac{\mu_f}{\rho_f D_{w/f}}$  an Reynolds number  $Re_p$  as (59).

$$\begin{aligned} Sh &= 2 + 0.6Re_p^{0.5}Sc^{0.33} & Re_p < 2 & \quad 0 \leq Sc < 250 \\ Sh &= 2 + 0.552Re_p^{0.5}Sc^{0.33} & 2 \leq Re_p < 12000 & \quad 0.6 \leq Sc < 2.7 \end{aligned} \quad (59)$$

In equation (57) the convective heat mass transfer  $q_m$  is also related to the water vapour concentration difference between the particle-air interface  $C_p$  and in the air  $C_a$ . This difference can be expressed through equation (60) [1] and it is evaluated in  $\frac{kg}{m^3}$ . The hypothesis applied to obtain equation (60) is to consider the air as ideal gas.

$$(C_p - C_a) = \frac{1}{R_v} \left( \frac{P_p^{SAT}(T_p)}{T_p} - RH \frac{P_p^{SAT}(T_a)}{T_a} \right) \quad (60)$$

$R_v$  is the ratio between the gas constant and the water molar mass,  $RH$  is the relative humidity of the airstream taken equal to 99% as monitored during the experimental campaign.

$P_p^{SAT}$  represents the saturated water pressure at the particle/air interface  $P_p^{SAT}(T_p)$  and in the air  $P_p^{SAT}(T_a)$ . Both values can be evaluated by empirical formulations (61). Moreover two different formulations are used for  $P_p^{SAT}(T_p)$  in case of liquid particle at  $T_p^l$  or frozen particle at  $T_p^i$  (61).

$$P_p^{SAT}(T_a) = 610.78e^{\left(\frac{T_a}{T_a+238.3}\right)^{17.2694}} \quad T > -70^\circ\text{C}$$

$$P_p^{SAT}(T_p^s) = e^{\left(\frac{-6140.4}{T_p^s+273}\right)^{+28.916}} \quad T_p^s > -100^\circ\text{C}$$
(61)

Where  $T$  in the first equation in (61) represents  $T_a$  for the saturated water pressure in air or  $T_p^l$  at the particle/air interface.

The last heat transfer involved in the particle freezing process is the heat transfer due to thermal radiation  $q_m$  (62).

$$q_r = \sigma \hat{\varepsilon} S_p (T_p^4 - T_a^4)$$
(62)

Where  $\sigma$  is the Stefan-Boltzmann constant and  $\hat{\varepsilon}$  the ice emissivity taken as 0.97.

As one can note from equation (55) and (59) the heat transfer coefficient  $h$  and the heat transfer due to convective mass transfer  $h_m$  are linked to the Reynolds number of particles  $Re_p$ , which is defined as (63). The Reynolds number is evaluated thanks to the stochastic tracking model discussed in what follows.

$$Re_p = \frac{d_p |u_r|}{\nu_f}$$
(63)

Where  $d_p$  is the particle diameter,  $\nu_f$  the kinematic viscosity of the air and  $|u_r|$  the relative speed between the particles  $u_p$  and the flow  $u_f$ , hence  $u_r = u_p - u_f$ . At this point of the model the coupling between the thermal code and the stochastic tracking code takes place. The speed of a turbulent flow can be modeled via a stochastic way as  $u_f = \langle u_f \rangle + u_f'$  where  $\langle u_f \rangle$  is the mean flow speed and  $u_f'$  is the fluctuating speed. At the beginning of the chapter we have shown that a stochastic model is necessary due to the turbulence influence on particle trajectories. Hence, the results of the thermal model are directly linked to the turbulent flow modeling. Later in the chapter, the effects of the turbulence modeling on the thermal part of the model will be investigated.

As seen in the literature review, two  $u_f'$  models have been presented: Eddy-Interaction-Model (EIM) or the Langevin approach. Both models have been implemented.

The EIM model expresses the fluctuating velocity  $u'_f$  as (64)

$$u'_f = \xi \sqrt{\frac{2}{3}} k \quad (64)$$

Where  $\xi$  represents a random variable following a Gauss normal distribution. The mean of  $\xi$  is zero and its variance is equal to one:  $\xi \sim \mathcal{N}(0,1)$ .  $k$  is defined as the turbulent kinetic energy equal to  $k = \frac{3}{2} (\langle u_f \rangle I_{90})^2$ .

For the Langevin approach, the fluctuating velocity  $u'_f$  is defined as

$$u'_f(t + \Delta t) = u'_f(t) - u'_f(t) \frac{\Delta t}{T_{f@p}^*(t)} + \sqrt{\frac{2\langle u_f^2 \rangle \Delta t(t)}{T_{f@p}^*(t)}} \xi(t + \Delta t) \quad (65)$$

Where  $\Delta t$  is the time step,  $T_{f@p}^*$  is the integral time scales of the fluid seen by the particles with the Csanady correction. This correction, as explained in chapter two, allows to take in account the inertia effect and the Crossing Trajectories Effect. The choice of the time step  $\Delta t$  will be presented later in the chapter.

The estimate of the particle size and velocity distribution “on” the cylinder is obtained by using a stochastic particle tracking model. The trajectories of the particles injected by the snow gun are tracked till they reach the cylinder. This tracking is performed using a lagrangian approach, following equation (66).

$$\sum_i \vec{F}_i = m_p \cdot \vec{a}_p \quad (66)$$

Here  $F_i$  represents the external forces acting on the particle,  $m_p$  the particle mass and  $a_p$  the particle acceleration. Particles are here considered as spherical smooth objects which can exchange with the fluid phase: mass, momentum and energy. Moreover, if particles can be considered, as in this case as points, the heat and mass exchanges can be modeled as a function of the local fluid properties. As discussed in chapter two a series of forces can be considered acting on a particle dispersed in a fluid phase. In case of small solid particles having a density much larger than the carrying fluid (as in our case  $\rho_p \gg \rho_f$ ), the drag  $F_d$  and the gravitational force  $F_g$  (67) are the two most significant forces acting on the particles [5].

$$F_d = \frac{1}{2} \rho_f A_p u_r^2 C_d \quad (67)$$

$$F_g = m_p g$$

Where  $A_p$  indicates the particle reference area and the coefficient of drag  $C_d$  is evaluated as (68):

$$\begin{aligned}
 Re_p &\ll 1 & C_d &\approx 24/Re_p \\
 1 < Re_p < 1000 & & C_d &\approx \frac{24}{Re_p} (1 + 0.15Re_p^{0.687}) \\
 1000 < Re_p & & C_d &\approx 0.44
 \end{aligned}
 \tag{68}$$

This leads to the resolution of the differential equation (66) as presented in (69).

$$\frac{\pi d_p^2}{8} \rho_f u_r^2 C_d + m_p g = m_p \cdot \frac{du_p}{dt}
 \tag{69}$$

This equation is resolved by a finite-difference scheme to evaluate the particle position at each time step  $\Delta t$ . This time step is not fixed a-priori and varies along the trajectories computation. As said before, it will be investigated in this chapter when comparing a series of characteristic times of the dispersion and thermal models.

A scheme to synthesize the coupling between the dynamic model and the thermal model is presented in Figure 83.

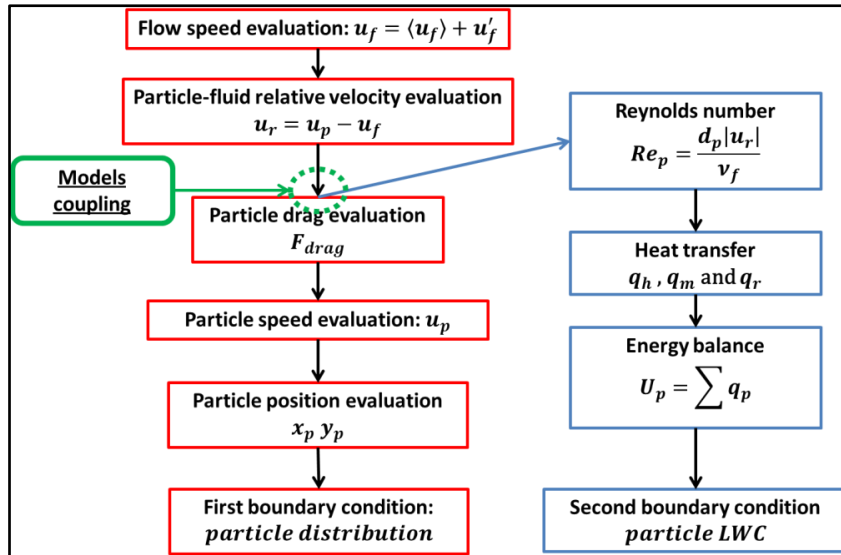


Figure 83. Dynamic and thermal coupling model

#### 4.1.2 Hypothesis introduced to represent the experimental conditions.

To apply the model presented above to the experimental framework, a series of hypothesis have been introduced.

As seen in previous chapter, the experimental analysis of the accretion has been conducted on a central portion of the cylinder. This central portion was characterized by a uniform transversal shape (Figure 84.a). Moreover the analysis of the spatial uniformity of the snow flux in the central portion of the cylinder, has shown a fair transversal homogeneity (Figure 84.b). As a consequence, the particle distribution has been supposed uniform along the central part of the cylinder. Hence, the model to evaluate the particle size distribution has been developed in two-dimensions.

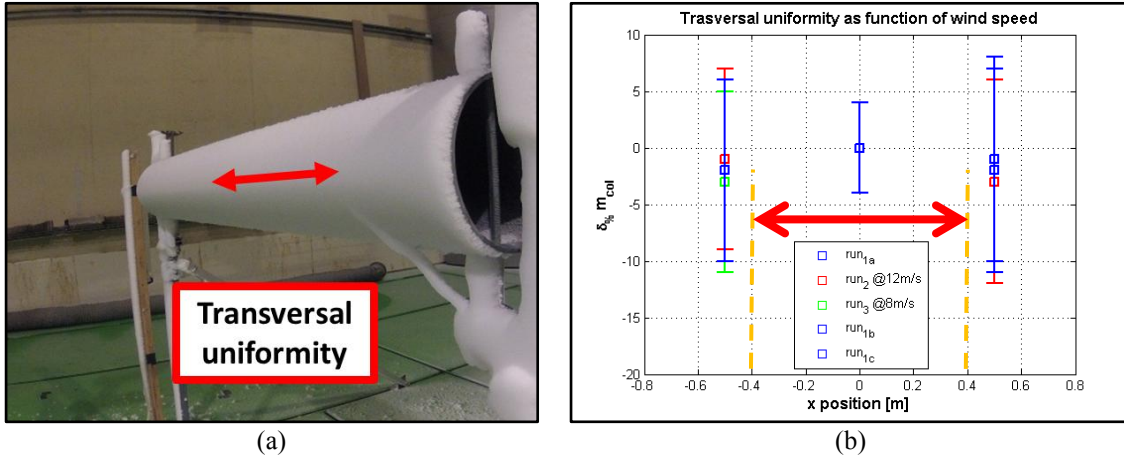


Figure 84. (a) accretion uniformity, (b) snow flux uniformity:  $\delta_{err} \%$  represents the percentage difference between the snow flux measured at  $x = 0$  and  $x = 0.5m$  or  $x = -0.5m$ .

Moreover, as seen during the experimental campaign, interactions between particles have been excluded as a consequence of  $\alpha_p = \frac{\dot{V}_p}{\dot{V}_{air}} \approx 9 \cdot 10^{-6}$ , where  $\alpha_p$  represents the particle concentration in the flow,  $\dot{V}_p$  the particle concentration and  $\dot{V}_{air}$  the air concentration. Therefore the assumption of mono-dispersed phase is taken during the development of the dispersion model for each particle size class. The interactions between particles, as for example particle coalescence, are also not taken in account for both models.

Another important hypothesis is made on the modeling of counter-current jet of the snow gun. During the evaluation of the particles path, due to the difficulties to estimate the influence of the air jet of the snow gun on the air stream, this aspect is not taken in account by the model. This leads to assume that water particles are injected in the counter-current air stream without considering the air jet of the snow gun. Doing this in our computations, one is aware of the introduction of an important simplification in the physical model.

As seen in previous chapter, the crucial parameter of the experimental campaign has been the ambient temperature  $T_a$  used to tune the particle liquid water content  $LWC$ . Additionally, the flow characteristics are kept unchanged along all the tests. Thus, one may consider that the experimental results are more correlated to the physical parameters of the freezing process than to varying characteristics of the air flow. As a consequence, it has been opted for a detailed modeling of the particle freezing process and a simplified model for the turbulent flow.

During the modeling of the turbulent flow, the turbulence has been assumed constant along the computational domain. As a consequence, the turbulent intensity  $I_0\%$  has been assumed constant and equal along the two dimensions as well as the integral length scale  $l$ . We are aware that this simplified model does not correctly represent the physic of the turbulent flow in the wind tunnel. However, we have supposed that this simple physical modeling allows to estimate reasonably well the particle distribution “on” the cylinders.

Regarding the frozen process, a constant ambient temperature and hygrometry is supposed for all the computational time. As will be shown later, the heat loss due to radiation can be neglected when compared to the convective heat loss and the mass

convective heat loss. The same hypothesis has been formulated by Strub et al. [1]. Moreover, the mass lost due to evaporation on the total mass of the particle has been considered negligible. Taking as a reference a particle diameter  $d_p = 290\mu m$ , the particle volume is  $V_p \approx 9 \cdot 10^{-12} m^3$ . The freezing code estimates a volume lost due to evaporation as  $V_p^{evap} = -2 \cdot 10^{-15} m^3$ . As a consequence the particle volume lost due to evaporation has been neglected.

It is well known from literature that some physical constant can be estimated as a function of the ambient temperature. Latent heat of fusion, sublimation, evaporation as well as, the heat capacity of water and ice or the dynamic viscosity of the air can be evaluated, through empirical formulations, as a function of the ambient temperature. Previous works of Leroy [6], Presteau [7] or Hindmarsh et al. [2] have adopted this principle. To examine if this kind of approach is needed in this work, a synthesis of the liquid water content evaluated with or without empirical formulation is presented in Table 6. The reference particle diameter is  $d_p = 290\mu m$ .

Table 6. Influence on particle *LWC*, of the evaluation method for the thermophysical proprieties.

| $T_a$        | <i>LWC</i> "empirical" | <i>LWC</i> "not empirical" |
|--------------|------------------------|----------------------------|
| $-3^\circ C$ | 0.82                   | 0.84                       |
| $-6^\circ C$ | 0.65                   | 0.66                       |
| $-9^\circ C$ | 0.47                   | 0.49                       |

Table 6 shows that the results in term of liquid water content are only slightly different. To simplify the task, an ambient temperature of reference  $T_a = -6^\circ C$  has been chosen to compute the values of the physical constants that can be expressed through empirical formulations.  $T_a = -6^\circ C$  represents the mean ambient temperature in the temperature range of the experimental campaign.

#### 4.1.3 Implementation in the model of the experimental conditions: thermal and flow parameters.

Regarding the stochastic tracking model, chapter three has permitted to measure three fundamental parameters: the mean flow speed  $\langle u_f \rangle \approx 9 m/s$ , the turbulence intensity  $I_0 \approx 8\%$  and the integral length scale  $l \approx 0.86 m$  at a distance of  $0.5 m$  upstream the cylinders. These last two parameters, are kept constant during the simulations as a consequence of the hypothesis exposed above (paragraph 4.1.2). Through these parameters the fluctuating kinetic energy  $k$  and the dissipation rate  $\varepsilon$  are as follow (70)

$$k = \frac{3}{2} (\langle u_f' \rangle)^2 \approx 0.78 \frac{m^2}{s^2}$$

$$\varepsilon = \frac{0.09^{3/4} \cdot k^{3/2}}{l} \approx 0.13 \frac{m^2}{s^3}$$
(70)

The Lagrangian integral time scale of the fluid  $T_f^L$ , employed in both the approach to model  $u_f'$  can be estimated as  $T_f^L = C \frac{k}{\varepsilon}$ . The value of  $C$  is characterized by a great uncertainty as reported by Oesterlé [5]:  $0.09 \leq C \leq 0.635$ . In our case is adopted  $C = 0.2$  (71) proposed by Oesterlé [5].

$$T_f^L \approx 0.2 \frac{k}{\varepsilon} \approx 1s \quad (71)$$

The Langevin approach is used to model the fluctuating velocity of flow  $\sqrt{\langle u_f'^2 \rangle}$ . In the Langevin approach, the time scale seen by particles  $T_{f@p}^*$  follows a formulation (72) proposed by Wang and Stokes [8].

$$T_{f@p}^* = T_f^E [1 - (1 - \Xi)(1 + \Xi St_p)^{-0.4(1+0.01\Xi St_p)}] \quad (72)$$

One can note that the relation above depends on the eulerian time scale  $T_f^E$  of the fluid.  $T_f^E$  is the turbulence time scale detected by an observer moving at the mean fluid velocity. The eulerian time scale is related to  $T_f^L$  by the  $\Xi = \frac{T_f^L}{T_f^E}$  coefficient as seen in chapter two. Once again, a great uncertainty concerns the value of  $\Xi$ . Oesterlé [5] proposes a value of  $\Xi \approx 0.55$  which leads to an Eulerian time scale (73).

$$T_f^E \approx \frac{T_f^L}{0.55} \approx 0.9s \quad (73)$$

Presuming a  $\Xi \approx 0.55$  leads to an eulerian time scale  $T_f^E$  bigger than the lagrangian time scale  $T_f^L$ . This is in agreement with the theory as reported by Oesterlé [5].

In equation (72) the Stokes number is:  $St_p = \frac{\tau_p}{T_{f@p}^*}$ . The Stokes number is estimated with respect to the integral time scale of the fluid seen by the particles  $T_{f@p}^*$ .

One of the most important hypothesis of the coupled model regards the snow gun. Due to the difficulties to model the effect of the counter current jet on the air, the particles are injected in the air flow without taking in account the jet influence. Particle injection is placed in the same configuration of the snow gun: 0.6m above ground with an inclination of  $\theta_{sg} = 20^\circ$ . As reported by Boisson-Kouznietzoff [3] the initial speed of particle is  $u_p \approx 100m/s$ . As shown in Figure 85 the particles are injected into the air stream with an angle  $\theta_{exit}$  which is related to the cone of injection.

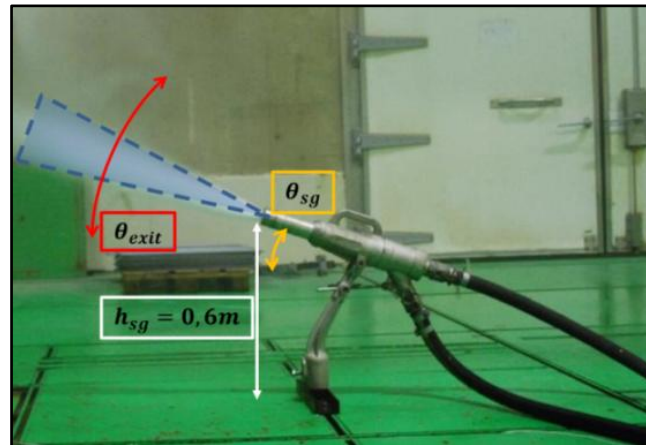


Figure 85. Particle injection scheme.

To take in account this aspect each particle is injected with a random angle  $\theta_{exit}$  which can vary between  $-10^\circ$  and  $+10^\circ$ . This assumption is extrapolated from a visual analysis of the snow gun jet from a side view. This estimation is also adopted by Boisson-Kouznetzoff [3]. As a consequence, the global injection angle is  $\theta = \theta_{sg} + \theta_{exit}$ . One is aware that modeling the snow gun jet in this way does not represent the physic involved in snow particles atomization. Moreover, taking as a reference diameter  $d_p = 290\mu m$  one can evaluate the Weber number to provide an estimation of the particles breakup (74). This non dimensional number concerns particles that, under aerodynamic forces, can break in smaller particles.

$$We = \frac{\rho_f u_r^2 d_p}{\gamma} \quad (74)$$

Where  $\gamma$  is the surface tension. Oesterlé [5] reports a limit  $We = 12$  above which a particle breaks in smaller particles. In our case, at the first instant of injection  $t \approx 0.01s$ , the Weber number exceeds 12. As a consequence, a particle break up arises. Anyhow, the stochastic tracking code does not include particle breakup. The choice can be justified with the fact that our analysis is focused on the experimental structure which is far away from the snow gun. As example, a particles  $d_p = 290\mu m$  reaches the experimental structure with a relative velocity close to  $u_r \approx 0.5m/s$  which means  $We \approx 10^{-4}$ . Hence, close to the cylinder, particle break up does not arise. Additionally, the particle distribution estimated with the tracking code will be weighted by the distribution measured by a MALVERN [9] as presented in chapter 3. The distribution measured can be assumed as the particles distribution downstream the complex series of events taking place at the snow gun exit. As a consequence, in this work, we suppose that the MALVERN distribution takes into account the particle break up.

Concerning the freezing process model, the particle temperature at the exit of the snow gun is one of the boundary condition to set-up. During this work, the initial temperature of the particle, is taken equal to the water temperature of the tank which contains the water used for the snow gun  $T_p(0) = 0.5^\circ C$ . Moreover, the relative humidity of the air, has been set as  $HR = 99\%$  as reported during the experimental campaign. The last boundary condition is the ambient temperature  $T_a$ , which varies according to the different configurations modeled and will be the main parameter of the liquid water content estimation.

#### 4.1.4 Resolution procedure of the coupled model.

The code modeling the particle freezing process is coupled with the stochastic tracking model. This means that, coupled with the particle trajectory evaluation, the particle temperature profile is also evaluated as well as the particle frozen mass. Especially, the tracking particle model allows to evaluate the Reynolds number of a particle  $Re_p$  involved in the correlations used to calculate the heat and mass transfer coefficients  $h$  and  $h_m$ .

Once a particle is injected, its trajectory is evaluated by solving equation (75) with a finite-difference method.

$$\frac{\pi d_p^2}{8} \rho_f u_r^2 C_d + m_p g = m_p \cdot \frac{du_p}{dt} \quad (75)$$

Along the particle trajectory, the particle temperature is computed at each time step  $\Delta t$  for all the different stages of the freezing process. For the first stage and third stage, equation (76) is solved. We recall that the heat loss of radiation is neglected.

$$\frac{dU_p}{dt} = c\rho V_p \frac{dT_p}{dt} \quad (76)$$

The temperature profile of the first stage is solved as (77) till the particle temperature reaches  $T_p(t) = 0^\circ\text{C}$ .

$$T_p^l(t + \Delta t) = [-h(t)(T_p^l(t) - T_a) - L_v h_m(t)(C_p(t) - C_a)] \frac{S_p}{c_l \rho_l V_p} \Delta t + T_p^l(t) \quad (77)$$

When particle starts to freeze during the freezing stage, the particle temperature  $T_p(t)$  is left unchanged and equal to  $0^\circ\text{C}$ . Here, as seen before, the ice volume of the particle is evaluated with heat balance model (78):

$$\frac{dU_p}{dt} = L_f \rho_i \frac{dV_p^i}{dt} \quad (78)$$

which leads to evaluate the particle ice volume  $V_p^i$  as (79):

$$V_p^i(t + \Delta t) = [-h(t)(T_p^l(t) - T_a) - L_s h_m(t)(C_p(t) - C_a)] \frac{1}{L_f \rho_i} \Delta t + V_p^l(t) \quad (79)$$

While analyzing equation (79) the latent heat of sublimation is used in the evaluation of the convective heat due to mass transfer. This is a consequence of the hypothesis that particles in our case start to freeze from the outer surface. Therefore, the mass transfer happens by sublimation from a solid surface to the air.

When the particle is fully frozen the temperature profile during the tempering stage is evaluated as (80) till  $T_p^s = T_a$ .

$$T_p^s(t + \Delta t) = [-h(t)(T_p^s(t) - T_a) - L_s h_m(t)(C_p(t) - C_a)] \frac{S_p}{c_s \rho_s V_p} \Delta t + T_p^s(t) \quad (80)$$

Finally the particle liquid water content  $LWC$  is evaluated as (81):

$$LWC = \frac{m_p^l}{m_p} \quad (81)$$

The liquid mass of the particle  $m_p^l$  is derived from the particle frozen volume  $V_p^i$ . The particle trajectory evaluation ends when the particle (with the associated  $LWC$ ) reaches the virtual cylinder surface. An example of trajectory computation for three particle diameters is reported in Figure 86. Let us note how the trajectories in red:  $d_p = 40\mu\text{m}$  do not reliably represent the injection process. This is supposed to be linked to the very simple approach to model the snow gun injection. One can assume that, in the first instant of injection, the spray can be considered as “compact”. This means that particles have more inertia than considered by the model. As a consequence,

most particles should follow a trajectory similar to the blue or the green one before to reverse their trajectory. Due to the fact that the model does not consider particle interactions, particles with low inertia reverse immediately their trajectory.

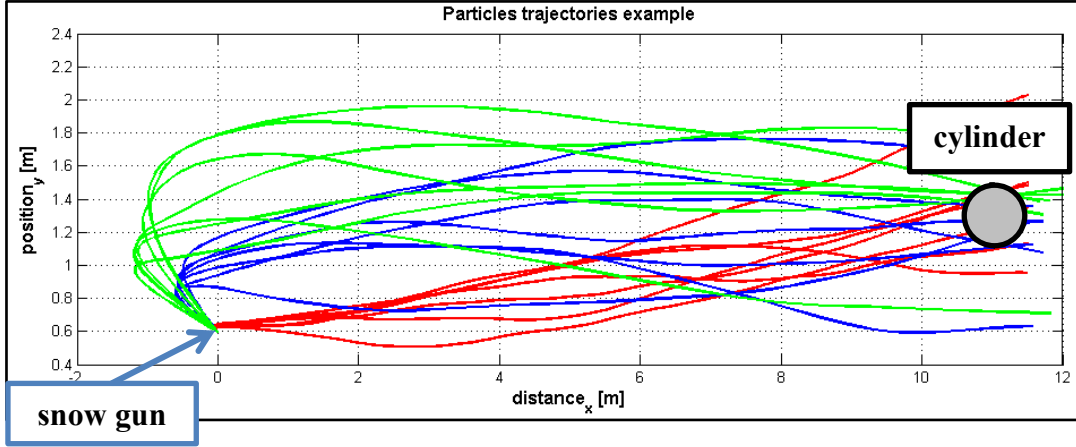


Figure 86. Particle trajectories example: red  $d_p = 40\mu\text{m}$ , blue  $d_p = 260\mu\text{m}$ , green  $d_p = 520\mu\text{m}$ .

As seen previously, the time step  $\Delta t$  has been evaluated by comparing the characteristic time of the tracking and freezing model. The characteristic time of the tracking code has been well defined before and is equal to  $\tau_p$ . The characteristic time of the freezing model has to be defined and computed.

As seen previously, the equation to solve for the particle temperature is (77).

$$T_p(t + \Delta t) = \left[ -h(t)(T_p(t) - T_a) - Lh_m(t)(C_p(t) - C_a) \right] \frac{S_p}{c\rho V_p} \Delta t + T_p(t) \quad (82)$$

which can be seen as (83):

$$\frac{dT_p}{dt} = AT_p + B \quad (83)$$

With  $A$  and  $B$  given by :

$$A = -\frac{h(t)S_p}{c\rho V_p}$$

$$B = \frac{h(t)T_a - Lh_m(t)C_p(t) + Lh_m(t)C_a}{c\rho V_p} S_p \quad (84)$$

If  $A$  and  $B$  are supposed constant (in fact they are not), the characteristic time of the cooling process  $\tau_t$  can be estimated as (85):

$$\tau_t = \frac{c\rho V_p}{h(t)S_p} \quad (85)$$

It characterizes the response time of a particle temperature to changes of the carrier fluid temperature. Values of density  $\rho$  and heat capacity  $c$  are taken in case of water particle state. The equation of  $\tau_T$  leads to suppose that particles characterized by

larger masses  $\rho V_p$  and larger heat capacities  $c$  are characterized by a slower thermal relaxation time.

In Table 7 is reported the estimation, for three particle diameters, of the mean  $\tau_p$  and  $\tau_T$ .

Table 7. Analysis of the characteristic times

| $d_p$            | $\langle \tau_p \rangle$ | $\langle \tau_t \rangle$ | $\langle \tau_t \rangle / \langle \tau_p \rangle$ |
|------------------|--------------------------|--------------------------|---|
| $d_p = 40\mu m$  | $\approx 0.005s$         | $\approx 0.02s$          | $\approx 4$                                       |
| $d_p = 260\mu m$ | $\approx 0.08s$          | $\approx 0.87s$          | $\approx 10$                                      |
| $d_p = 520\mu m$ | $\approx 0.14s$          | $\approx 2.44s$          | $\approx 17$                                      |

As one can note on the above table, the particle dispersion aspect involves smaller response times than the freezing aspect. Hence the time step of the coupled model will be based on the particle dispersion aspect as (86)

$$\Delta t = \alpha_t \cdot \tau_p(t) \tag{86}$$

The factor  $\alpha_t = 0.2$  is chosen so that the numerical models do not diverge. A similar approach can be found in Volkov [10]. Taking 100 particles of  $d_p = 260\mu m$ , Table 8 shows the number of particles which reach the cylinder as a function of  $\alpha_t$ . As one can note, a coefficient  $\alpha_t = 0.2$  ensures the convergence of the numerical model with a gain in computational time with respect to  $\alpha_t = 0.1$ .

Table 8. Analysis of  $\alpha_t$  influence

| $\alpha_t$ | $n$ strikes     |
|------------|-----------------|
| 10         | <i>diverged</i> |
| 1          | 27              |
| 0.5        | 24              |
| 0.2        | 29              |
| 0.1        | 29              |

#### 4.1.5 Model implementation conclusions

The first part of the chapters has dealt with the presentation of the coupled model. This model is based on a tracking lagrangian model, with which evaluate the particle trajectory coupled with a model of the particle freezing process. Moreover the influence of the turbulence is taken in account in both codes. This coupled model aims at the estimation of the boundary conditions for the numerical model on the accretion namely the particle distribution “on” the cylinder and the associated particle *LWC*..

The results of the model are presented below, discerning between the particle tracking model and the particle freezing model. We will then discuss the physical parameters which play an important role in the two models.

## 4.2 Models results discussion

### 4.2.1 Boundary condition estimation: particle distribution “on” the cylinders.

The first boundary condition needed for the accretion model of chapter five, is the particle distribution “on” the cylinder surface. Indeed, the particle distribution is directly linked to the mass of particle approaching the cylinder  $m_{inc}$ . Then, through the collision efficiency  $\eta_1$ , it will be possible to estimate the mass flux of particles impacting the cylinders as a function of the aerodynamic parameters. The collision efficiency  $\eta_1$  is defined as the ratio between the mass of particles which impact the cylinder and the incoming particle mass, both masses are normalized by a reference area. A detailed description of  $\eta_1$  will be given in chapter five.

The particle distribution is defined as  $PSD^v$ : particle size distribution based on the volume of particles (87). It allows to compare the volume of a class of particles with respect to the whole volume of particles. This kind of distribution will concern the definition of  $m_{inc}$  in the next chapter.

$$PSD^v = \frac{(d_p)_i^3 \cdot n_i}{\sum_i (d_p)_i^3 \cdot n_i} \quad (87)$$

The number of particles of each class  $i$  which reach the cylinder surface is  $n_i$ .  $d_{pi}$  is the particle diameter of the  $i$  class.

In a similar way, one can define the particle distribution  $PSD^n$ : particle size distribution based on the number of particles (88):

$$PSD^n = \frac{n_i}{\sum_i n_i} \quad (88)$$

Both particle size distributions will be used in the chapter to analyze the results. A simple table is proposed below to understand the difference between the distributions. As one can note in Table 9, the difference between  $PSD^n$  and  $PSD^v$  can be very large.

Table 9. Differences between  $PSD^v$  and  $PSD^n$

| $d_p$ [ $\mu m$ ] | $n_i$ | $PSD^n$         | $PSD^v$            |
|-------------------|-------|-----------------|--------------------|
| 1                 | 10000 | $\approx 90\%$  | $\approx 0.0002\%$ |
| 10                | 1000  | $\approx 9\%$   | $\approx 0.02\%$   |
| 100               | 100   | $\approx 0.9\%$ | $\approx 1.96\%$   |
| 1000              | 5     | $\approx 0.1\%$ | $\approx 98\%$     |

The estimation of  $PSD^v$  is made through a stochastic particle tracking model. The model tracks the particles injected by the snow gun and record particles reaching the cylinder, falling on the ground or exiting the domain. Then, by tracking which particles reach a control surface, the model estimates the  $PSD^v$ .

#### **Diameter range of particles adopted in the coupled model.**

One of the most important parameters of the particle dispersion model is the range of particle diameters used as initial condition to evaluate the volume particle size

distribution. The reason of its importance resides in the strict dependency between the volume  $PSD^v$  calculated by the model and the range of particle diameters used as initial condition. In this case the choice of the diameter range is based on the volume  $PSD^v$  evaluated during a precedent study with a MALVERN Spraytec [9]. As reported during the experimental campaign, this particle size distribution is here considered as the volume particle distribution at the “snow gun exit”.

This precedent test campaign has showed a particle range between  $d_p = 7.36\mu m$  and  $d_p = 1000\mu m$ . As will be shown below, the evaluation of the trajectory for small particles is computational costly due to the small time step needed for the trajectory evaluation ( $\Delta t = 10^{-5}s$ ). Indeed, as shown before, the time step  $\Delta t$  is linked to the relaxation time  $\tau_p$  which for  $d_p = 7.36\mu m$  is very small. For this reason a low cut-off on the diameter range, is applied in this work.

As example, the computational time of ten path of a particle with  $d_p = 7.36\mu m$  is  $t = 120s$ . This particle diameter has been taken as a reference in this estimation because it is the smallest one measured. As will be shown later, the number of trajectories chosen to obtain a correct statistical representation of all the incoming particles is 4000; this leads to a computational cost of  $\approx 13hours$ . Hence, to reduce the computational time a cut-off for small particles is performed.

The model has shown how the computational time becomes reasonable for particles with a diameter bigger than  $d_p = 40\mu m$  ( $\Delta t \approx 10^{-4}s$ ). For this particle size, the computational cost of 4000 trajectories is  $\approx 1hours$ .

Analyzing the volume distribution  $PSD^v$  of the snow gun, it can be demonstrated that, by choosing this low cut-off, only 1% of the whole particle volume injected is not taken in account by the model (Table 10)

Table 10. Analysis of low cut-off for particle diameter range [9]

| $d_p$ | <i>snow gun</i> $PSD^v$ | $\sum$ <i>snow gun</i> $PSD^v$ |
|-------|-------------------------|--------------------------------|
| ...   | 0                       | 0                              |
| 7.36  | 0.01                    | 0.01                           |
| 8.58  | 0.01                    | 0.02                           |
| ...   | ...                     | ...                            |
| 39.81 | 0.38                    | 1.02                           |
| 46.42 | 0.57                    | 1.60                           |

A preliminary simulation to establish if larger particles reach the cylinder has been performed. This to investigate if is necessary to take into account the whole particle range supposed to be injected by the snow gun. A simulation with 100 injections for each particle class has been performed. The result has shown that particles larger than  $d_p = 520\mu m$  do not reach the cylinder plane. It can be supposed that gravity plays a crucial role on larger particles which fall on the ground before reaching the cylinder. This high cut-off allows to reduce further the computational time. As a consequence of this preliminary analysis, the diameter range adopted in this work will be  $40\mu m < d_p < 600\mu m$ . The range has been discretized each  $40\mu m$ .

**Number of particles injected: convergence analysis.**

It is impossible, due to the computational cost, to simulate the trajectory of all the particles injected by the snow gun. To avoid this drawback it is imperative to choose a reduced number of injections for each class diameter which gives a correct statistical representation of all particles. The analysis is performed for one ambient temperature  $T_a$ . The number of injection chosen will be then extended to the whole range of ambient temperature.

The minimum number of particles to inject for the dispersion model has been chosen by a comparison between the  $PSD^v$  evaluated with different numbers of particles injected, and a  $PSD^v$  of reference. This last one has been assumed to be the one evaluated with 12000 injections for each particle class:  $PSD^v_{12000}$ . This one corresponds to the distribution evaluated with the maximum number of injections which keeps reasonable the computation cost evaluated as  $\approx 12hours$ .

The percentage difference  $\Delta PSD^v$  between the  $PSD^v$  for a given number of injections and the  $PSD^v_{12000}$  of reference is presented as (89).

$$\Delta PSD^v = \frac{(PSD^v - PSD^v_{12000})}{PSD^v_{12000}} \quad (89)$$

As example,  $PSD^v_{10}$  represents the particle distribution obtained with 10 injections for each class of diameter. The analysis is focused on a particle range between  $d_p = 160\mu m$  and  $d_p = 360\mu m$  which represents  $\approx 80\%$  of the particle volume which strike the control surface (Table 11).

Table 11. Analysis of number of particles to inject

| $d_p$ | $\Delta PSD^v_{10}$ | $\Delta PSD^v_{20}$ | $\Delta PSD^v_{100}$ | $\Delta PSD^v_{1000}$ | $\Delta PSD^v_{2000}$ | $\Delta PSD^v_{4000}$ |
|-------|---------------------|---------------------|----------------------|-----------------------|-----------------------|-----------------------|
| 160   | 68.23%              | -25.03%             | -19.14%              | 8.45%                 | -0.77%                | 2.66%                 |
| 200   | 373.01%             | 216.21%             | -24.22%              | -29.44%               | -8.04%                | -2.42%                |
| 240   | 100.00%             | 25.54%              | 40.59%               | -1.82%                | -4.83%                | -4.54%                |
| 280   | 100.00%             | 100.00%             | 100.00%              | 2.49%                 | -0.12%                | 0.19%                 |
| 320   | 100.00%             | 100.00%             | -34.39%              | -14.41%               | -5.76%                | 4.31%                 |
| 360   | 100.00%             | 100.00%             | 100.00%              | 34.54%                | 33.60%                | -3.22%                |

Considering Table 11, one can see that the percentage difference  $\Delta PSD^v$  for each class diameter, decreases with the increases of the number of particles injected. Moreover the computation begins to convergence starting from 1000 injections. With the analysis of Table 11, it has been considered acceptable to evaluate the particle size distribution with 4000 injections for each class diameter (see also Figure 87). This choice allows to keep the difference  $\Delta PSD^v_{4000}$  under 5%. As a consequence the choice of 4000 injections ensures a correct statistical convergence with also a gain in terms of computational time.

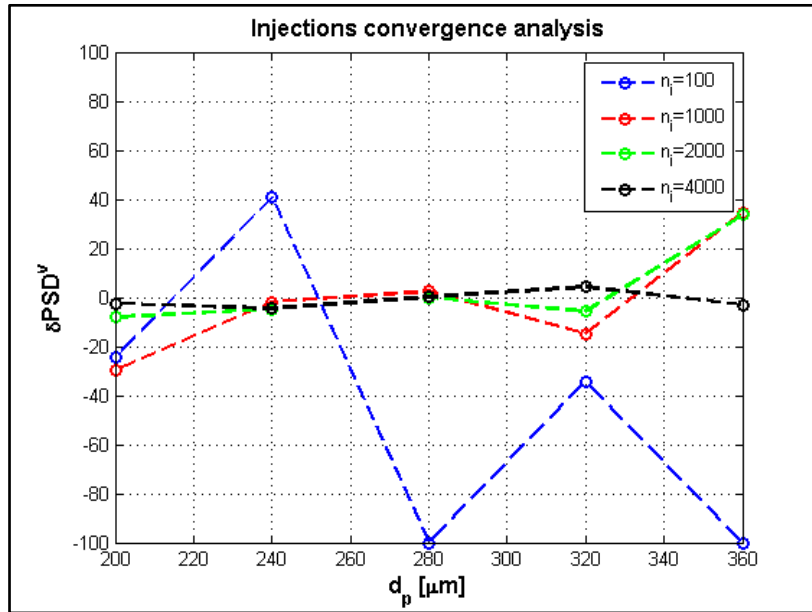


Figure 87. Injections number convergence

#### 4.2.2 Particle size distribution on the cylinder

For the particle range considered as well as the number of injections, the tracking model has been employed to estimate the volume particle size distribution reaching the surface of the cylinder. This one, must be weighted by the particle size distribution measured with the MALVERN Spraytec which is supposed to be the distribution at the snow gun exit (Figure 88).

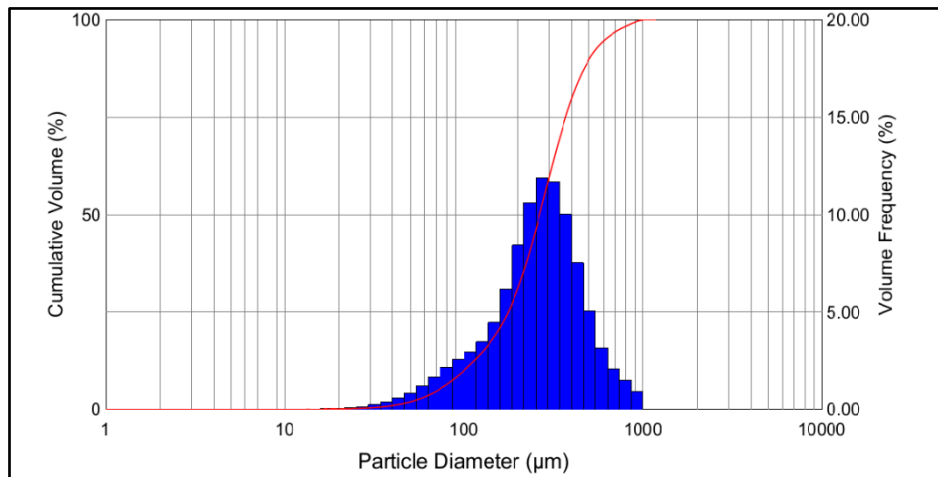


Figure 88. The PSD supposed at the exit of the snow gun [9]

The diameter class discretization of the MALVERN instrument distribution does not correspond to the one chosen for the tracking model. As a consequence, an interpolation with a third order polynomial has been performed to obtain the particle size distribution of the snow gun adapted to this work:  $PSD_{int}^v$  (Figure 89).

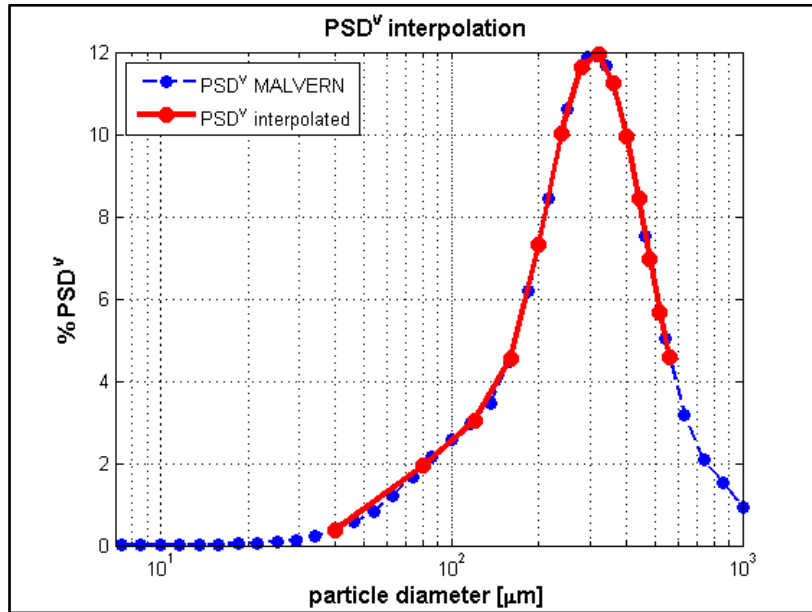


Figure 89. Snow gun particle size distribution interpolation.

With the particle size distribution of the snow gun calibrated on the particle class of the tracking model, it is now possible to evaluate the particle size distribution “on” the cylinder as (90). The particle distribution estimated is represented in Figure 91.

$$PSD_{Weighted}^v = PSD^v \cdot PSD_{int}^v \quad (90)$$

A schematic representation of the weighting process between particle distributions is presented in Figure 90.

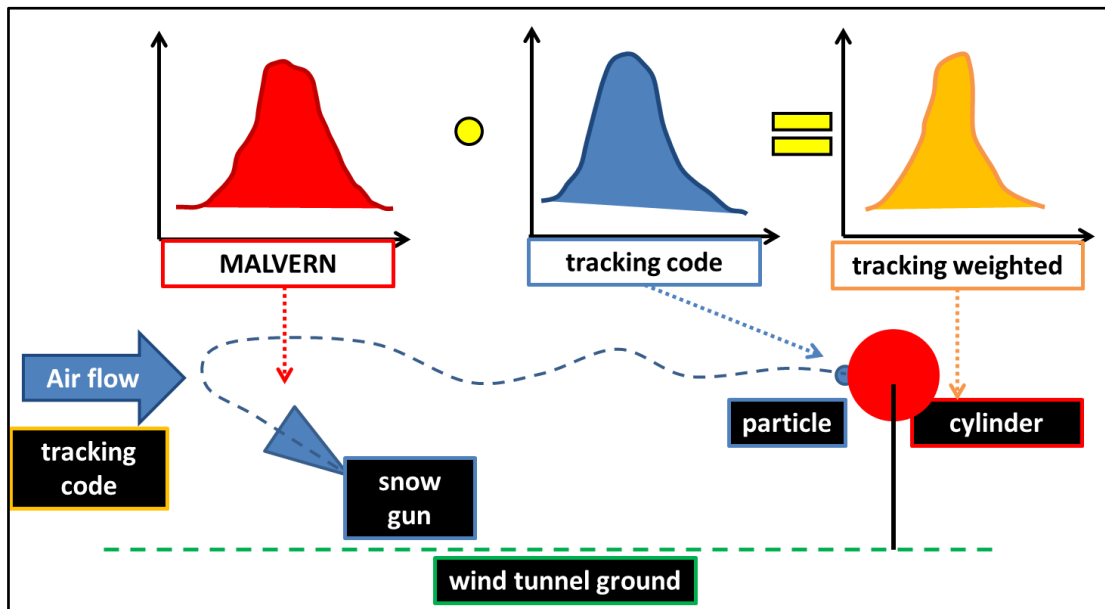


Figure 90. Particle size distribution weighting process.

The particle size distribution shown in Figure 91 is the first boundary conditions that will be used for the accretion analysis in the next chapter. As seen at the beginning of the paragraph, this particle distribution will be implemented to evaluate the mass of

particles which approach the cylinders. To simplify the reading,  $PSD_{Weighted}^v$  will be call  $PSD^v$  here after.

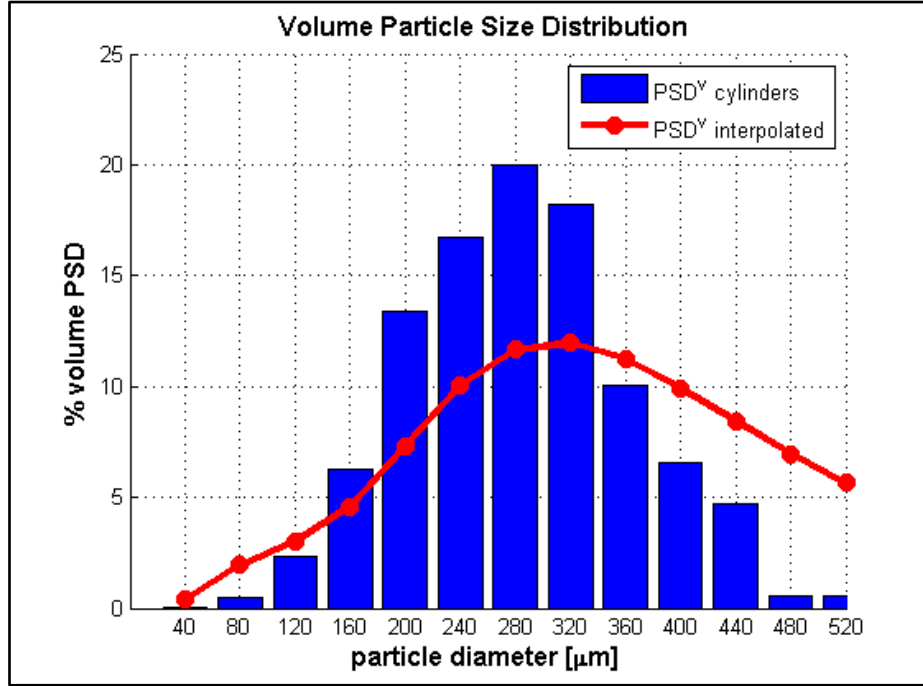


Figure 91. Particle size distribution “on” the cylinders.

To characterize the particle size distribution  $PSD^v$ , a series of characteristic diameters are here presented. The first one is the  $d_{32} = \frac{\sum d_p^3}{\sum d_p^2} \approx 220\mu m$  which is called the Sauter Mean Diameter, used to characterize the distribution in terms of particle surface. To characterize a particle size distribution in term of volume, the De Brouckere Mean Diameter is used often:  $d_{43} = \frac{\sum d_p^4}{\sum d_p^3} \approx 260\mu m$ . This is the typical diameter to characterize a particle distribution in terms of volume or mass and it is also called the mean volume diameter ( $M_{canVD}$ ).  $d_{43}$  will represent the reference diameter in what follows.

Taking  $d_{43} \approx 260\mu m$  is it possible to characterize the flow, which approaches the test structure, by a series of characteristic numbers. A mean particle relaxation time  $\langle \tau_p \rangle$  is evaluated through the model as  $\langle \tau_p \rangle \approx 80ms$ . Moreover the particle behavior with respect to the turbulent flow is characterized by a Stokes number which compares the mean relaxation time to a characteristic time of the flow:  $\tau_f = \frac{l}{\sqrt{\langle u_f'^2 \rangle}}$ . Where  $l$  is the

length of the eddy and  $\sqrt{\langle u_f'^2 \rangle}$  the root mean square of the fluctuating velocity. This leads to a Stokes number  $St_p = \frac{\langle \tau_p \rangle}{\tau_f} \approx 0.1$  which indicates how particles are subjected to turbulence influence. This analysis gives a confirmation of the hypothesis formed at the beginning of the chapter on the necessity of a stochastic approach.

Assuming a particle speed of  $u_p = 9m/s$ , a Froude number can be defined as equation (91). It represents the ratio between the inertial force and the gravity force.

$$Fr = \frac{u_p}{\sqrt{gL}} \quad (91)$$

Where  $g$  is the gravitational acceleration and  $L$  a characteristic length. In this case, assuming  $L = 11.5m$ , equal to the distance between the injection and the cylinder, the Froude number is  $Fr \approx 0.9$ . This indicates that gravity plays an important role on the particle along the path between the injection and the cylinders. As a consequence, to analyze this aspect, we propose an analysis of the role of gravity on the particle distribution “on” the cylinders and on the ground.

### 4.2.3 The role of the gravity on particle distribution

To understand well this part of the chapter, the results will be shown with a particle size distribution on number of particles defined as (92). Moreover the distribution will not be weighted with the particle distribution of the snow gun  $PSD_{int}^v$ .

$$PSD^n = \frac{n_i}{\sum_i n_i} \quad (92)$$

#### **Deposition of particles on the wind tunnel ground**

The computational domain has been divided in six sectors. Each sector is  $2m$  large. This allows to discretize the analysis along the domain and to better understand where deposition becomes important (Figure 92). The particle range is from  $d_p \approx 40\mu m$  to  $d_p \approx 1000\mu m$ .

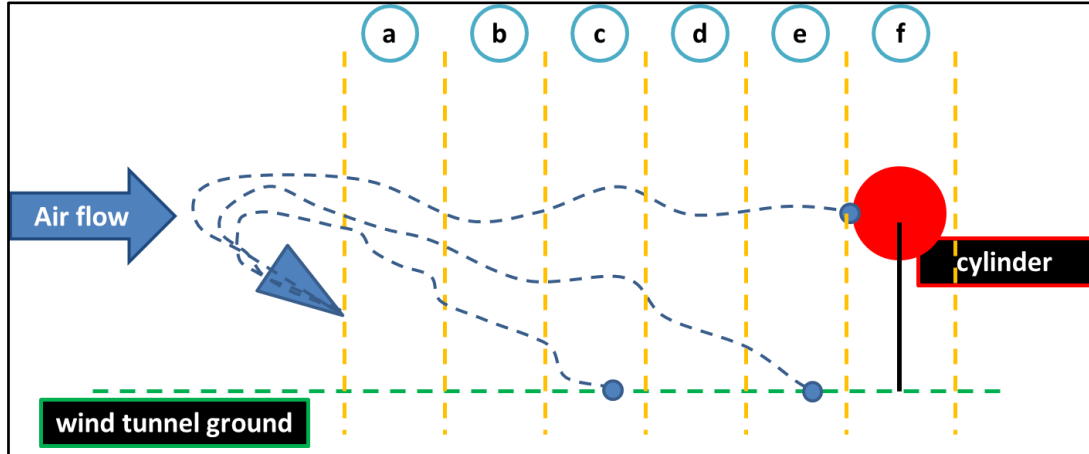


Figure 92. Wind tunnel ground discretization

The particle size distributions evaluated in number of particles are reported in Figure 93. Each bar represents the number of particles deposited as a percentage of the total number of particles deposited of each particle class. Analyzing the results, one can note how gravity plays a crucial role on the deposition of particles for the configuration chosen. It is possible to note that the deposition of larger particles takes place in the first six meters of the domain. Around 80% of particles larger than  $d_p \approx 720\mu m$  fall before six meters from the snow gun. Figure 93 also shows that small particles reach the ground further from the snow gun than larger particles. Moreover it is clear from Figure 93 that particle deposition on the ground follows a trend. Close to the cylinder, larger particles are more subjected to deposition (Figure 93.a and Figure 93.b). While

proceeding far from the snow gun, smaller particles are more and more subjected to deposition (Figure 93.c and Figure 93.d). A peak of deposition can be noted between 4 and 6 meters away from the snow gun (Figure 93.c). Close to cylinders, only smaller particles fall on the ground (Figure 93.e and Figure 93.f). In these last two cases, it is supposed that all the bigger particles have reached the ground before.

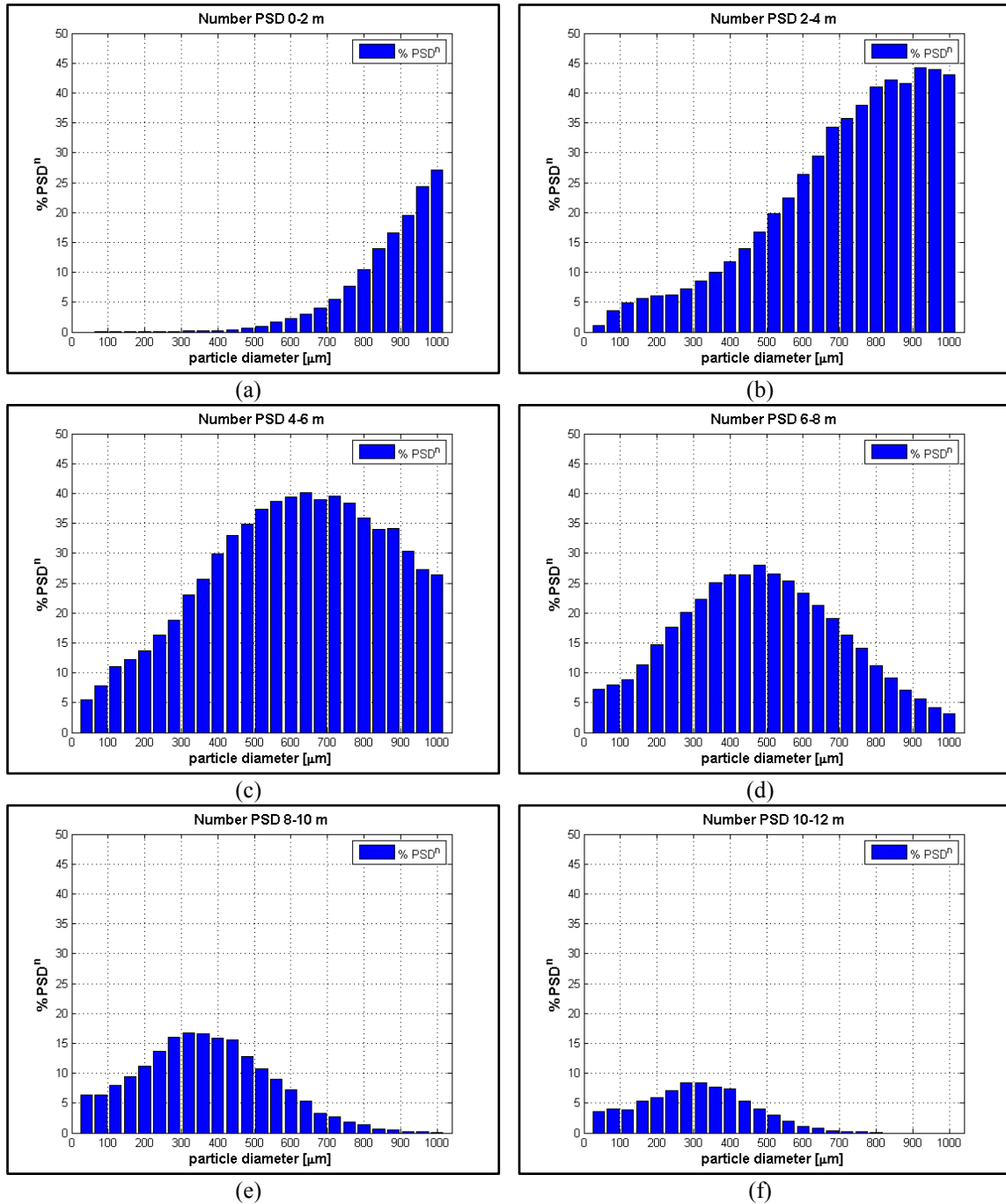


Figure 93. Deposition analysis: (a) 0 – 2m, (b) 2 – 4m, (c) 4 – 6m, (d) 6 – 8m, (e) 8–10m, (f) 10 – 12m.

Considering now the particle distribution in volume  $PSD^v$  evaluated on the ground weighted by the distribution of the snow gun  $PSD_{int}^v$ , we show in Figure 94 the result for a quantitative deposition estimation during the experimental campaign. One must be aware that the tracking code is based on important simplistic hypothesis which

cannot reproduce the physics of the turbulent flow as well as the physics of the snow gun. As a consequence, the analysis must be taken with care. Each bar corresponds to the diameter contribution in volume on the whole volume of snow deposited on the ground. A trend is clear: far from the snow gun the contribution of larger particles to the whole deposited volume of snow decreases.

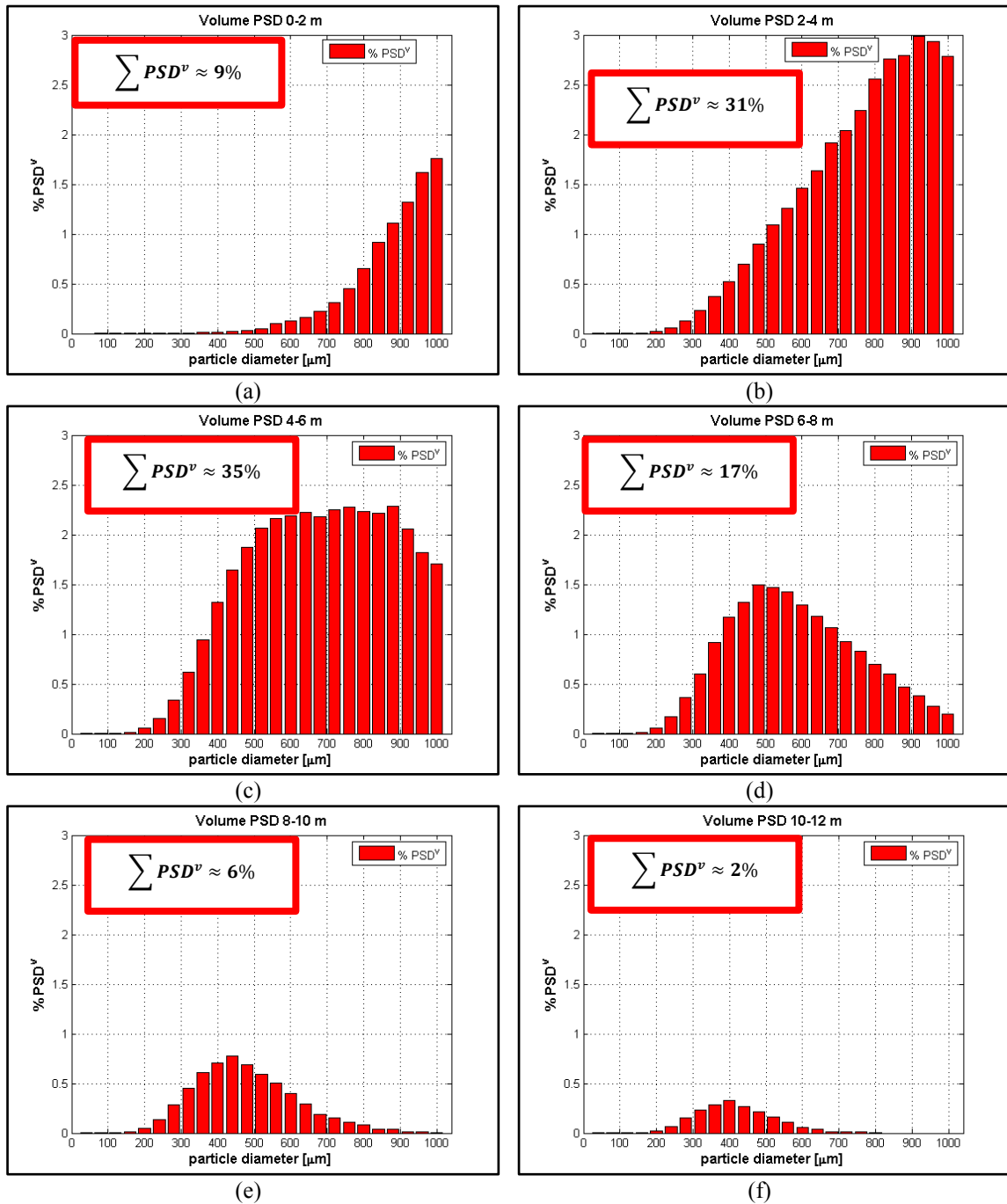


Figure 94. Deposition analysis: (a) 0 – 2m, (b) 2 – 4m, (c) 4 – 6m, (d) 6 – 8m, (e) 8–10m, (f) 10 – 12m.

Moreover, Figure 94 shows that more than half of the deposited snow reaches the ground between 2 and 6 meters from the snow gun. A schematic representation of the estimated snow distribution on the wind tunnel ground is proposed in Figure 95. Most part of deposition is far from the experimental structure. Hence, one can suppose

that the deposition does not affect so much the incoming flux of snow during the experimental campaign.

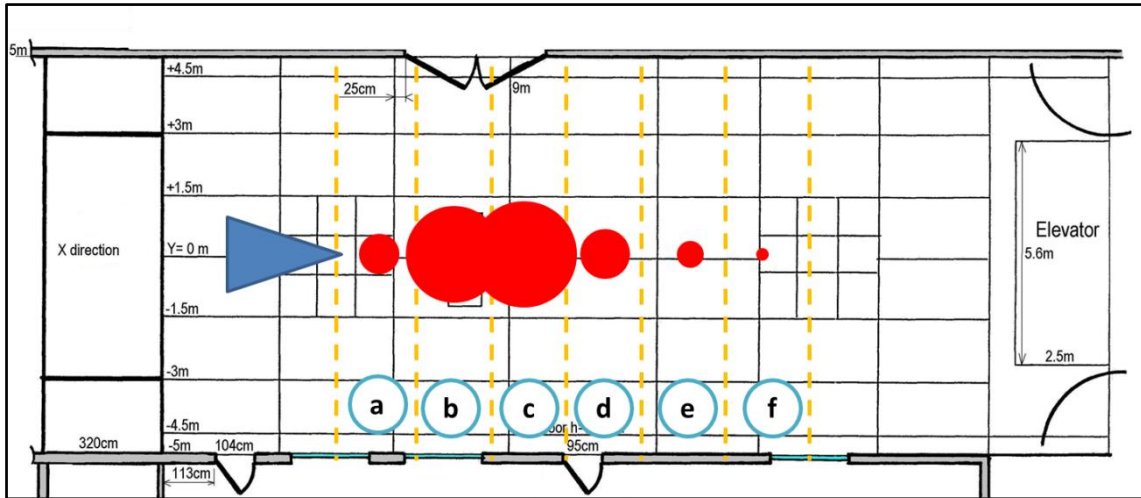


Figure 95. Snow deposition on wind tunnel ground.

This accumulation of snow on the central part of the wind tunnel has been observed during the experimental campaign.

**Gravity role on particle distribution “on” the cylinders.**

The gravity effect can be seen also analyzing the volume particle distribution “on” the cylinders. As one can note from Figure 96 gravity in this work plays a crucial role. The particle size distributions, with and without gravity effect, are completely different. Gravity moves the particle distribution center towards smaller particles (shown also by the vertical lines of the  $d_{43}$ ). This why gravity acts on larger particles that reach the ground before reaching the cylinder.

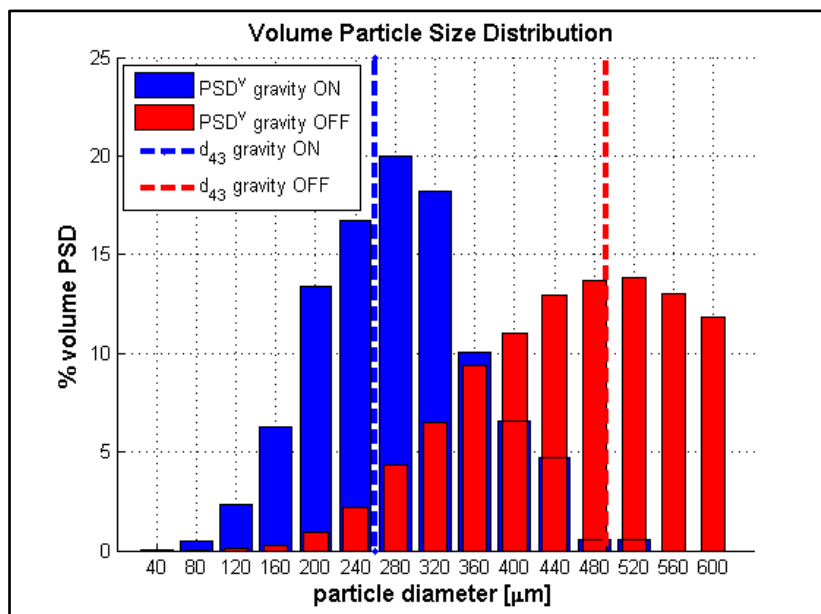


Figure 96. Gravity effect on  $PSD^v$ .

A similar analysis can be performed with the particle size distribution evaluated in number of particles:  $PSD^n$ . Figure 97 shows how without gravity (Figure 97 – red

bars), larger particles also reach the cylinder. This does not happen if one considers the gravity effect (Figure 97 – blue bars). This explains how, the volume particle size distribution seen in Figure 96 shows an important contribution of larger particles without taking in account gravity.

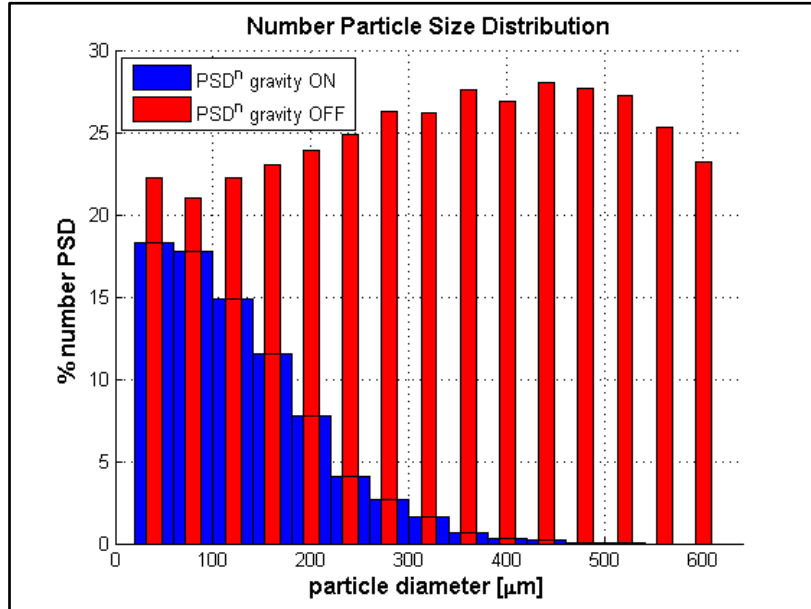


Figure 97. Gravity effect on  $PSD^n$ .

#### 4.2.4 Particles $LWC$ “on” the cylinder surface as a function of the ambient temperature.

The thermal model coupled with the tracking one has allowed to characterize the mixed phase of particle by applying the particle freezing theory. This model, for a given ambient temperature  $T_a$ , allows to estimate the  $LWC$  of the particles. This estimation has a capital importance for the accretion model in the next chapter. Indeed, to faithfully reproduce the experimental accretions, one has to know the liquid water content of particles which impact the cylinders. Moreover this part also offers an analysis on the strategy chosen during the experimental campaign to tune the particle  $LWC$ .

As seen before, interactions between particles are neglected owing to the particles concentration  $\alpha_p \approx 9 \cdot 10^{-6}$ .

#### *Influence of the fluctuating velocity models on the thermal aspect of the coupled model.*

Two approaches have been presented to model the fluctuating part  $u'_f$  of the flow velocity. The first one, called “Eddy Interaction Model”, models the fluctuating velocity through a series of discrete generations of  $u'_f$  along the particle path. The second approach, based on the Langevin equation, determines the fluctuating velocity continuously along the particle path.

To better understand what follows, a synthesis of the procedure leading to the heat transfer coefficient  $h$  and the heat coefficient due to mass transfer  $h_m$  is proposed (Figure 98).

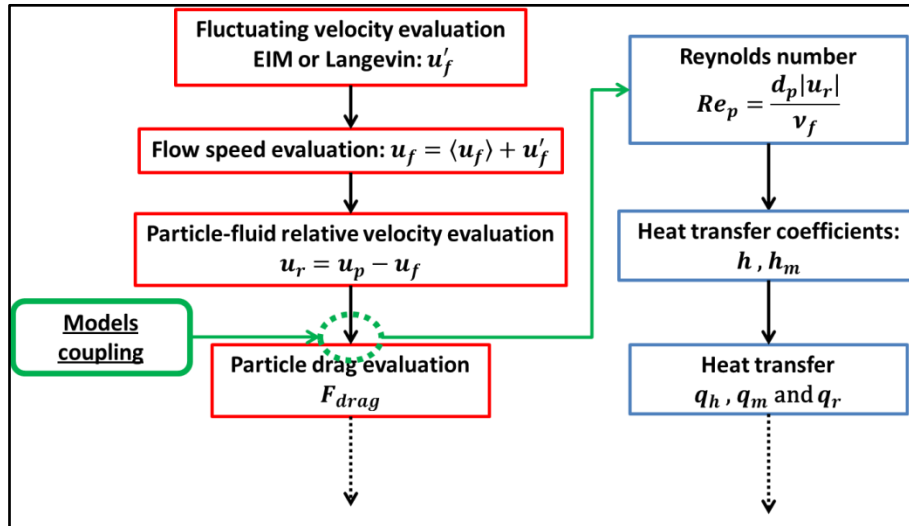


Figure 98. Stochastic and thermal coupling in the model

As one can note from Figure 98, the flow speed evaluated with the stochastic feature of the tracking model directly influences the particle Reynolds number. This last one is linked to the evaluation of the heat transfer coefficient  $h$ .

In Figure 99.a we show the coefficient  $h$  and the relative speed  $u_r$  as a function of the time for a particle  $d_p = 260\mu m$  which reaches the cylinders. On Figure 99.b is reported the fluctuating velocity  $u_f'$  evaluated through the EIM model. As one can note, the discontinuities of the fluctuating velocity are clearly reflected on the relative speed  $u_r$  (Figure 99.a – red line). These discontinuities of  $u_r$  are replicated on the heat coefficient  $h$  giving nonphysical jumps (Figure 99.a – blue line). Due to these anomalies in the coefficient  $h$ , a Langevin approach for  $u_f'$  has been implemented.

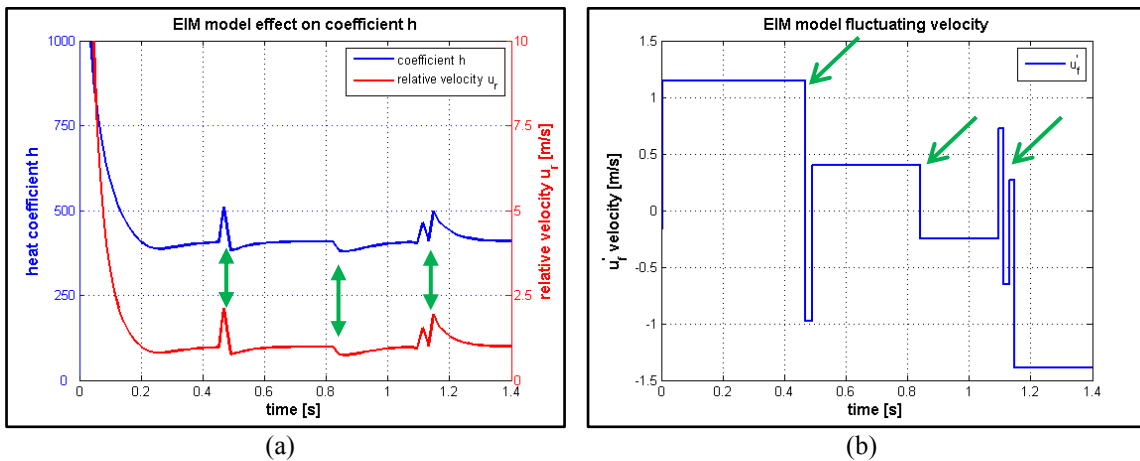


Figure 99. (a) Effects of EIM model on  $u_r$  and  $h$ , (b)  $u_f'$  example.

Figure 100.a shows the coefficient  $h$  and the relative velocity flow-particle  $u_r$  with a Langevin approach. As one can note, the coefficient  $h$  evolution does not show the discontinuities seen with the EIM approach. This way, the Langevin approach models  $u_f'$  in continuous way (Figure 100.b). Hence,  $u_f$  and  $u_r$  are continuous as well. As a consequence, the coefficient  $h$  is continuous.

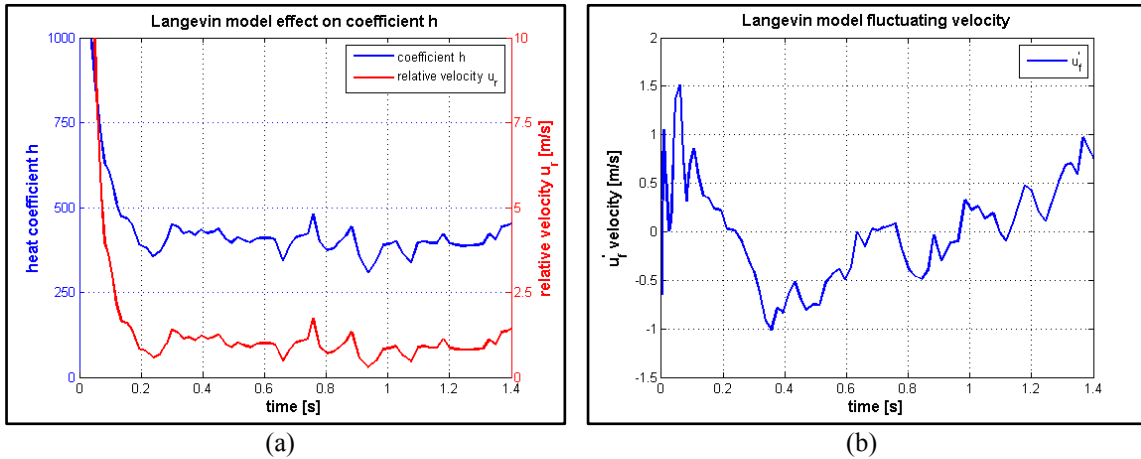


Figure 100. (a) Effects of Langevin model on  $u_r$  and  $h$ , (b)  $u_f'$  example.

Due to this analysis, the choice of a Langevin approach to model  $u_f'$  seems obvious. In case of a continuous  $u_f'$ , the heat transfer coefficient  $h$  is represented in a more physical way.

Taking as a reference particle  $d_p = 260\mu\text{m}$  and 50 injections for each fluctuating speed model, the  $LWC$  evaluated in case of EIM is  $LWC \approx 0.46$ . In case of a Langevin approach the particle liquid water content is  $LWC \approx 0.51$ . The percentage difference between the two  $LWC$  is around  $\approx 10\%$ . It is evident that a different  $u_f'$  modeling leads to a different  $LWC$ . Seen the fact that the  $LWC$  is the leading parameter of this work, the choice of a Langevin approach does not only influence the representation of  $h$  but, above all, the results of this work.

### **Heat transfer weight: radiation heat transfer**

As explained during the model presentation, the heat transfer due to thermal radiation has been neglected. With a particle reference diameter of  $d_p = 260\mu\text{m}$  and a temperature of reference  $T_a = -6^\circ\text{C}$ , which represents the median temperature in the range analyzed during the experimental campaign, two ratios are plotted in Figure 101. The analysis is based on the heat transfer of convection:  $q_m/q_h$  represents the ratio between the heat transfer due to convective mass transfer and the convective heat transfer.  $q_i/q_h$  represents the ratio between the heat transfer due to radiation and the convective heat transfer.

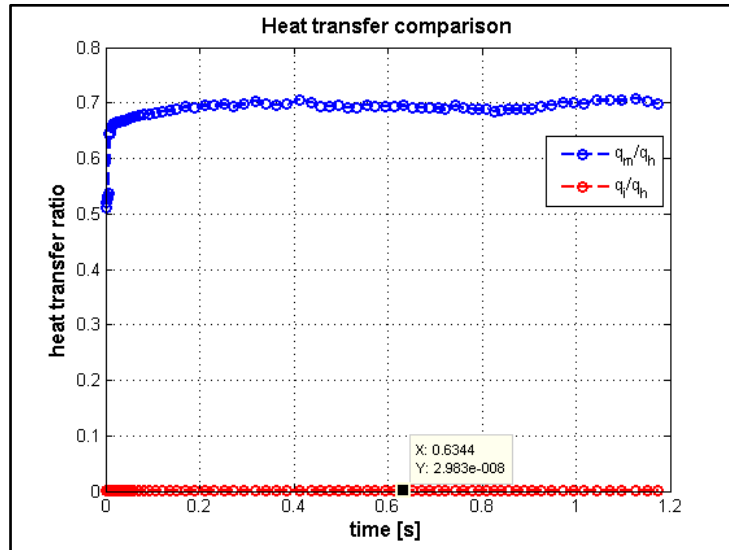


Figure 101. Heat transfers ratio

The ratios reported in Figure 101 shows that the two most important heat transfers are the convective one and the convective mass transfer one. As a consequence the heat transfer due to radiation has been neglected in the modeling.

**Physical parameters of the thermal model involved in experimental campaign: particle diameters and ambient temperature**

This part of the chapter is dedicated to the explanation of the effects of the particle diameter and the ambient temperature on the particle temperature. This analysis will lead to consider how the particle diameter and the ambient temperature play a role on the particle liquid water content *LWC*.

Taking as a reference the diameter  $d_p = 260\mu m$ , the temperature temporal evolution of a particle is investigated as a function of the ambient temperature. The temperature range chosen represents well the range of the experimental campaign:  $T_a = -3^\circ C$ ,  $T_a = -6^\circ C$  and  $T_a = -9^\circ C$ .

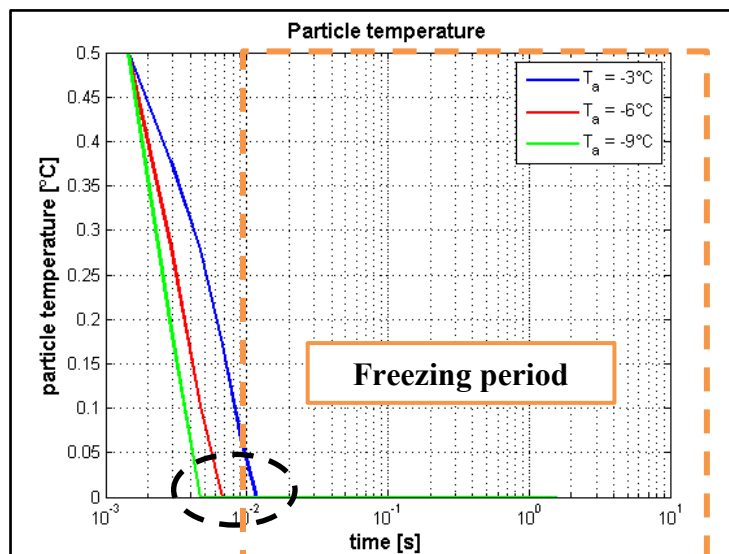


Figure 102. Particle temperature evolution as a function of  $T_a$

Figure 102 shows that, at the first instants of the injection, the particle reaches immediately the freezing stage and starts to freeze (Figure 102 – black circle). As one can see from Figure 102, the duration of the freezing period is dominant during the freezing process. One can suppose that this very short initial period is linked to the high relative speed of particles which induces a high heat coefficient  $h$ . The large  $h$  coefficient during the initial cooling phase leads the particle temperature to immediately fall to zero degree. Moreover the first part of Figure 102 corresponds to the part of particle injection. As seen before, the snow gun has been modeled through a very simple approach which does not at all represent the physics counterparty. Hence the first period of the particle temperature curve must be taken with care.

Figure 103 shows the temperature evolution of particles of different diameters ( $d_p = 40\mu m$ ,  $d_p = 260\mu m$  and  $d_p = 520\mu m$ ). The ambient temperature is fixed to  $T_a = -6^\circ C$ . As one can see from Figure 103 the particle diameter plays an important role in the freezing process. A small particle reaches the freezing point faster than a bigger particle. Moreover, the time needed to freeze completely is shorter in case of small particles (blue line in figure 24). Additionally in Figure 103, taking as a reference the blue line, one can confirm that the freezing stage is the longer among the three stages of the freezing process. Therefore, neglecting the nucleation temperature has certainly a very small influence on the final particle state.

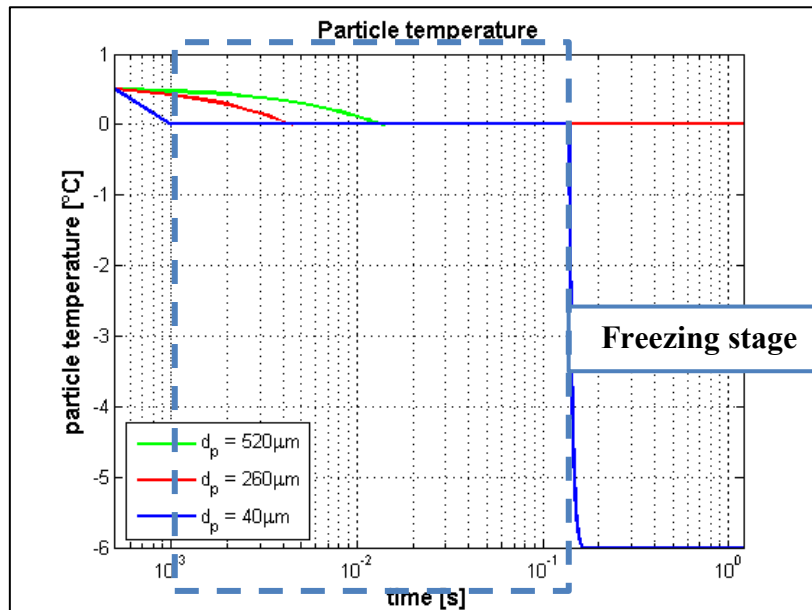


Figure 103. Particle temperature profile as a function of  $d_p$

**Estimation of particle LWC “on” the cylinder surface during the experimental campaign:  $LWC = \mathcal{F}(T_a)$ .**

We now know that the evolution of the particle temperature during its flight in the wind tunnel is very sensitive to the particle diameter and to the external temperature. Moreover, the freezing period, characterized by  $0 < LWC < 1$ , is the longest period. We now evaluate the particle LWC as a function of these physical characteristics. The particle LWC is evaluated as  $LWC = \frac{m_p^l}{m_p}$  which represents the ratio between the liquid mass and the total mass of the particle. The ambient temperature range reflects the one applied during the experimental campaign with also  $T_a = -2^\circ C$  and  $T_a = -10^\circ C$ .

As seen in chapter three, the *LWC* of particles during the experimental campaign is tuned by changing the ambient temperature of the wind tunnel  $T_a$ . To give an example of the ambient temperature influence on particle *LWC*, we show in Figure 104 the evolution of the liquid water content of a particle  $d_p = 260\mu\text{m}$  as a function of three ambient temperatures ( $T_a = -3^\circ\text{C}$ ,  $T_a = -6^\circ\text{C}$  and  $T_a = -9^\circ\text{C}$ ).

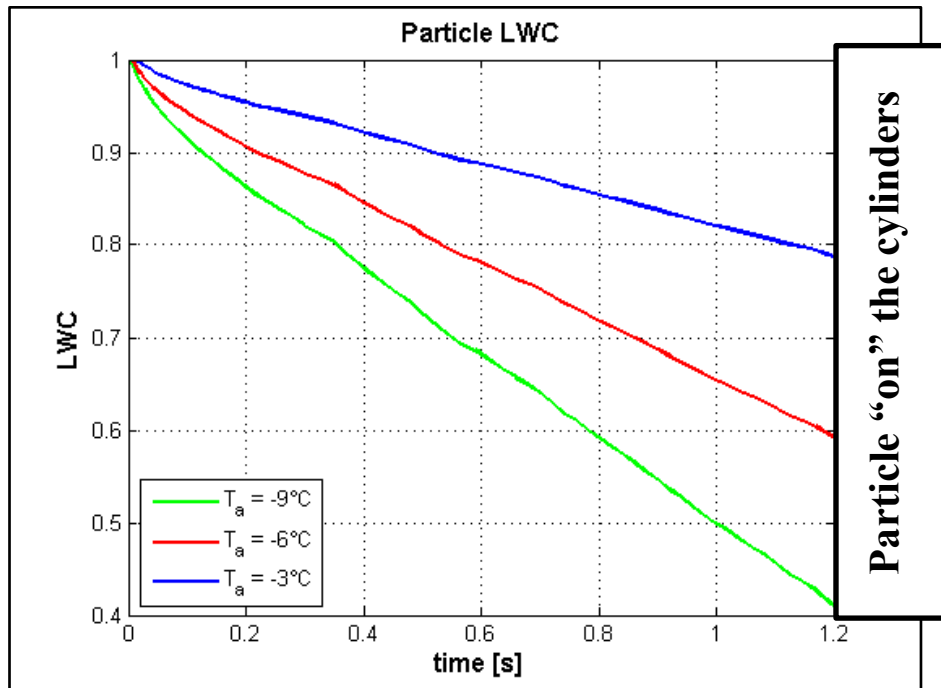


Figure 104. Particle LWC temporal evolution as a function of the ambient temperature  $T_a$ .

As can be noted from Figure 104, the liquid water content of a particle is very sensitive to the ambient temperature. For a temperature decrease, the *LWC* decreases as well and the solid part increases. Hence, one can consider that a slight variation of the ambient temperature during the experimental campaign leads to an important variation on the liquid water content. This liquid water content variation can be supposed directly reflected on the experimental accretions (Figure 105).

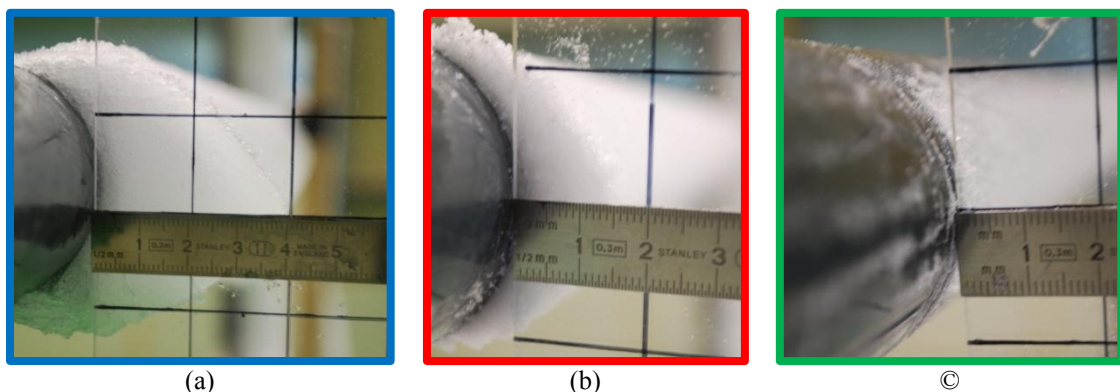


Figure 105.  $d_{cyl} = 50\text{mm}$  (a)  $T_a = -3^\circ\text{C}$ , (b)  $T_a = -6^\circ\text{C}$ , (c)  $T_a = -9^\circ\text{C}$

As seen before, the particle distribution which reaches the control surface is far from being a uniform distribution. To show how the *LWC* can vary as a function of the particle diameter, Figure 106 reports the *LWC* at an ambient temperature  $T_a = -6^\circ\text{C}$  for

three particles of different diameters:  $d_p = 40\mu\text{m}$ ,  $d_p = 260\mu\text{m}$  and  $d_p = 520\mu\text{m}$ . We see that small particles reach the cylinders completely frozen, on the other hand, large particles reach the cylinders almost completely liquid. Therefore, the LWC is also very sensitive to the diameter of the particles.

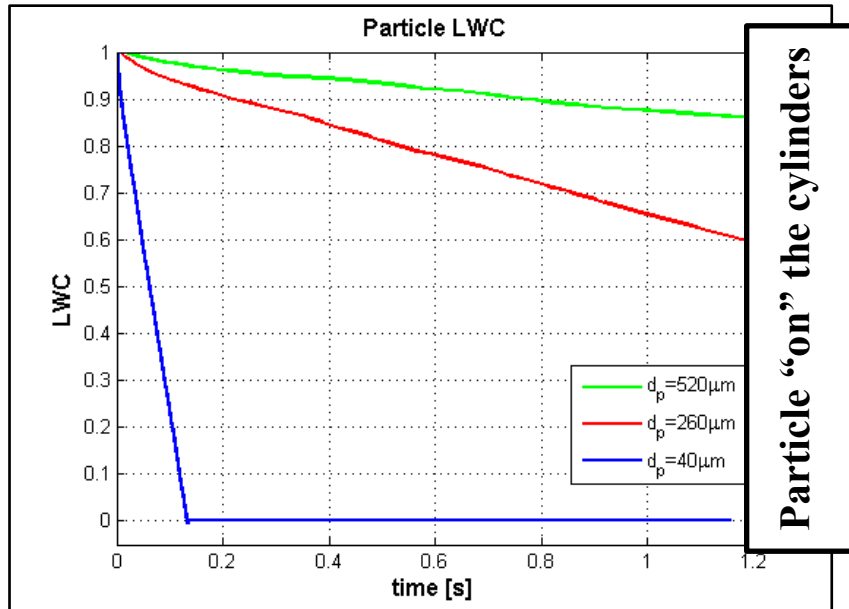


Figure 106. Particle LWC evolution as a function of the particle diameter.

Considering all the particle diameters involved in the stochastic tracking model as well as an ambient temperature range between  $-2^\circ\text{C}$  and  $-10^\circ\text{C}$ , the liquid water content estimated is reported in Figure 107.

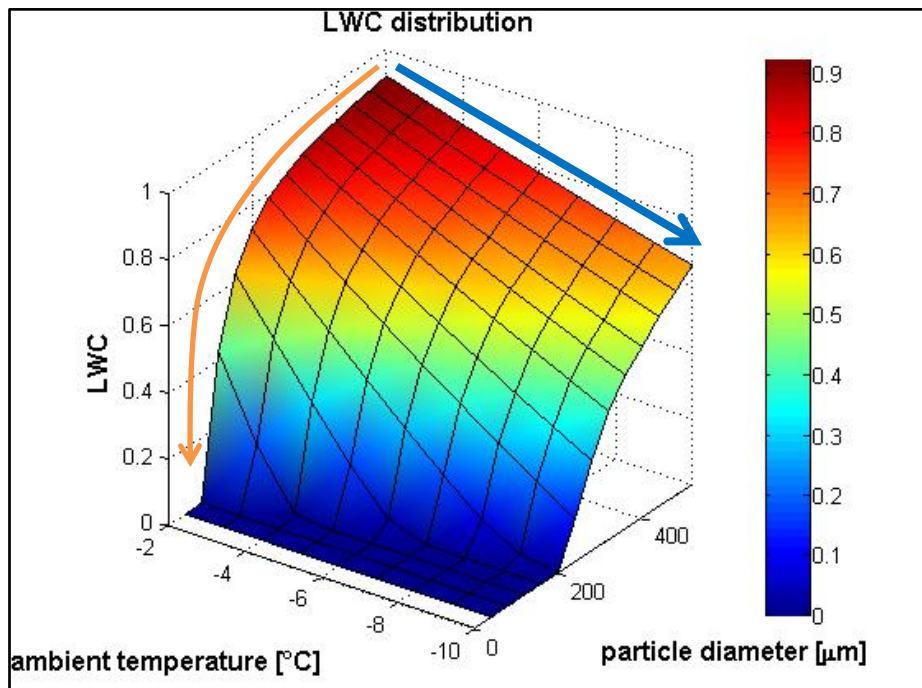


Figure 107. LWC of particles with respect to ambient temperature and particle diameter, 3D view.

The graph of Figure 107 gives the evolution of the particle liquid water content as a function of the ambient temperatures  $T_a$  and of the particle distribution “on” the cylinder surface. Fixing the diameter, when the ambient temperature  $T_a$  decreases, the particle  $LWC$  decreases as well (Figure 107 – blue arrow). In the same manner, for a fixed ambient temperature, when the particle diameter decreases, the liquid water content associated to that particle decreases as well (Figure 107 – orange arrow). The figure shows additionally as the sensibility of the  $LWC$  to a temperature change is a characteristic of all the particles class.

Figure 108 below represents in a more quantitative way the  $LWC$  associated to each class of diameter as a function of the ambient temperature. The particle class diameter which reaches the cylinders completely frozen, increase with the decrease of ambient temperature  $T_a$ . As example at  $T_a = -3^\circ\text{C}$  the particle that reach the cylinders completely frozen goes till  $d_p = 80\mu\text{m}$ . In case of  $T_a = -9^\circ\text{C}$  the particle completely frozen threshold diameter is  $d_p = 160\mu\text{m}$ .

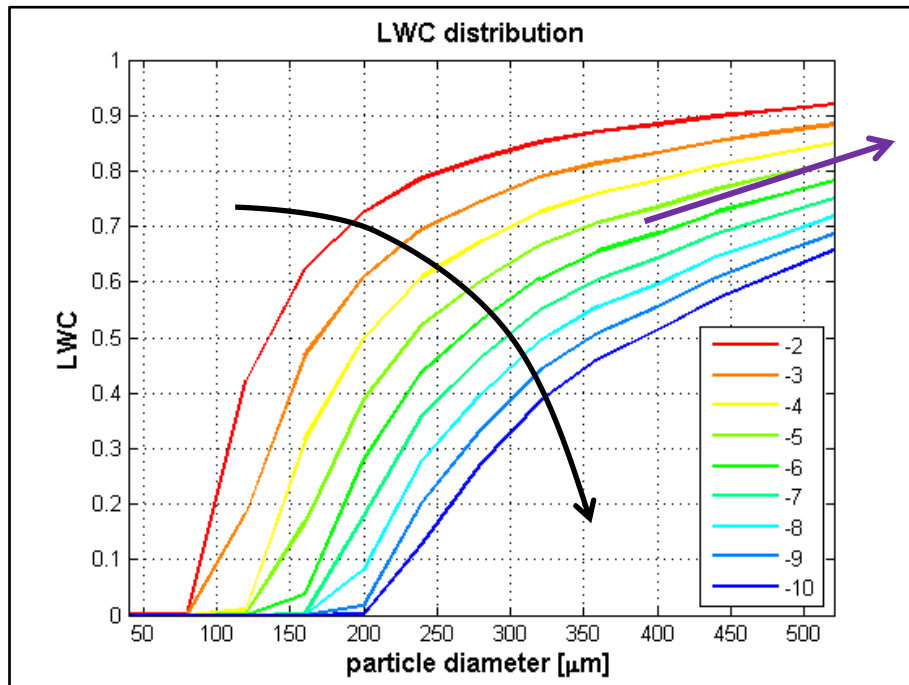


Figure 108. LWC of particles with respect to particle diameter for various ambient temperature , 2D view.

The results shown in Figure 107 and Figure 108 show that it is possible to evaluate a global liquid water content of the particle mass at the cylinder location.

**LWC as a function of  $T_a$  : conclusion.**

This part of the chapter has presented the results of the estimation of the liquid water content of particles that reach the cylinders location. A Langevin approach allows a better physical estimation of the heat transfer coefficient  $h$  compared to an EIM model. Above all, the paragraph has shown that the liquid water content is sensitive to the ambient temperature setting. Hence the approach undertaken in the experimental campaign has been validated: a change of the ambient temperature leads to an important change of the particle liquid water content:  $LWC = \mathcal{F}(T_a)$ .

We have also shown that the LWC varies significantly with the diameter of the particles generated by the snow gun. It was therefore very important to select a single working condition for the snow gun throughout all the experimental study.

The coupled model allows to investigate which are the other physical parameters influencing the particle liquid water content. An analysis of these parameters is proposed below.

#### 4.2.5 Physical parameters which can drive the particle LWC.

Thanks to the coupled model, we analyze the effect of the physical parameters on the particle LWC. These parameters could have been adjusted during the experimental campaign.

#### **Mean flow speed, turbulence intensity and cylinder-snow gun distance effect on particle LWC.**

The first analysis is based on a particle diameter of  $d_p = 260\mu\text{m}$  at an ambient temperature of  $T_a = -6^\circ\text{C}$ . Figure 109 shows the particle liquid water content as a function of the mean flow speed  $\langle u_f \rangle$ . The flow speed does not act on the evolution shape of the LWC: the four curves overlap. However, the larger is the flow speed, the faster particles will reach the cylinder. As a consequence, the freezing time is reduced. However, for a particle flying time divided by two, the particle liquid water content is reduced by only  $\approx 10\%$ . Doing this, one must be aware that with an increase of the wind speed, turbulence characteristics may change (turbulence intensity and integral length scale) inducing changes of the heat transfer coefficient. As a consequence, during our experimental campaign, to ensure the same turbulence characteristics and the same particle distribution on the cylinder, the mean flow speed has been kept fixed.

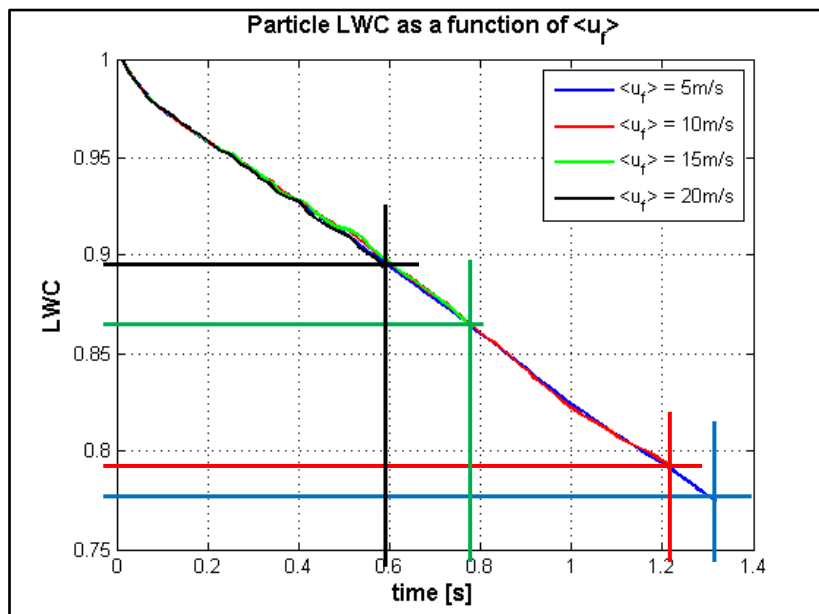


Figure 109. LWC tuning as a function of the mean flow speed  $\langle u_f \rangle$ .

Figure 110.a shows the liquid water content of a particle of  $d_p = 260\mu\text{m}$  at an ambient temperature of  $T_a = -3^\circ\text{C}$  as a function of the turbulence intensity. The turbulence intensity does not influence so much the final value of liquid water content. A slight reduction of LWC is only observed for the highest turbulence intensity because

this corresponds, for a given size class, to smaller Stokes numbers and to particles that respond less to changes in the fluctuating flow. One therefore expects larger values of the relative velocities and of the heat exchange coefficient.

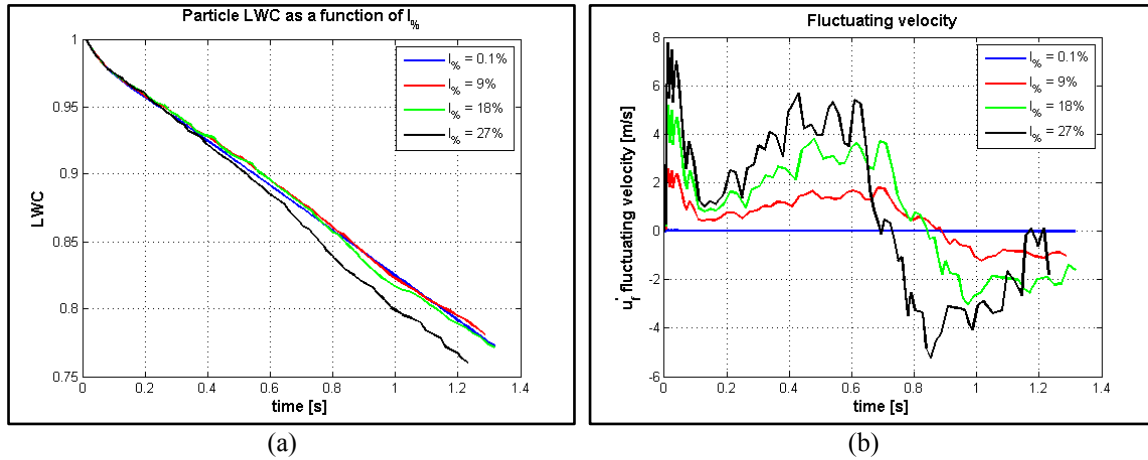


Figure 110. (a) LWC as a function of  $I_0\%$  (b)  $u'_f$  as a function of  $I_0\%$ .

The influence of the distance between the cylinders and the snow gun is investigated in Figure 111. Here the liquid water content of a particle  $d_p = 260\mu\text{m}$  at an ambient temperature  $T_a = -6^\circ\text{C}$  is reported. Obviously, when the time of flight (and the distance for a fixed mean velocity) is reduced, the LWC increases. However, changing the location of the experimental structure would be difficult in the wind tunnel. Moreover, this would lead to changes of the size distributions of particles flowing upstream the cylinders. Results would therefore be very complex to analyze.

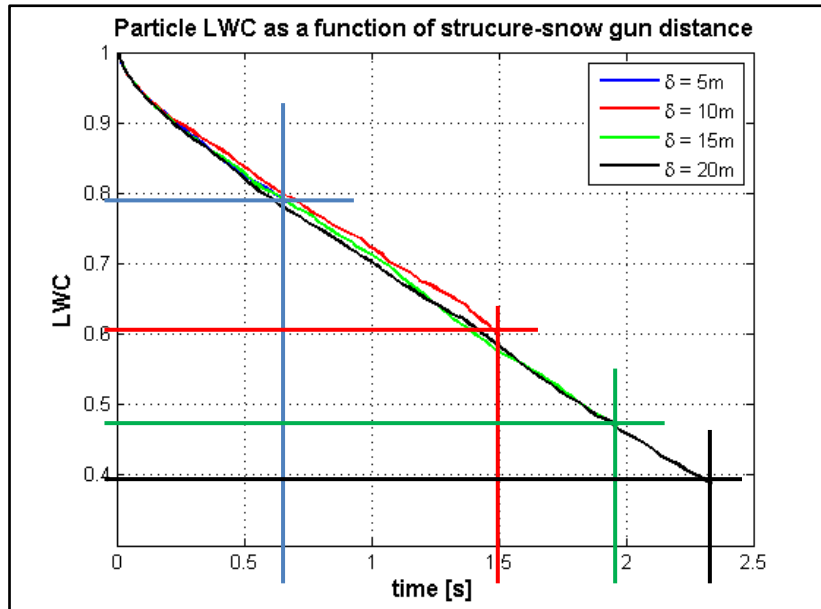


Figure 111. (a) LWC as a function of cylinder – snow gun distance:  $\delta$

### Particle initial temperature and hygrometry effect on particle LWC.

During the experimental campaign, the particle initial temperature has been supposed equal to the water in the tank which supplies water to the snow gun:  $T_p(0) = 0.5^\circ\text{C}$ . The influence of the initial particle temperature on the liquid water content is

considered here. The simulation condition is:  $d_p = 260\mu\text{m}$  and  $T_a = -6^\circ\text{C}$ . Figure 112 shows that the initial particle temperature does not influence so much the particle liquid water content. The percentage difference is kept in around  $\approx 6\%$  which can be considered small. This result is also interesting regarding the assumption made earlier about the initial cooling stage of the freezing process and the hypothetical supercooling of the particles. Hence, supercooling of water particle of a few degrees would have little influence on the resulting LWC of the particles at the cylinder location.

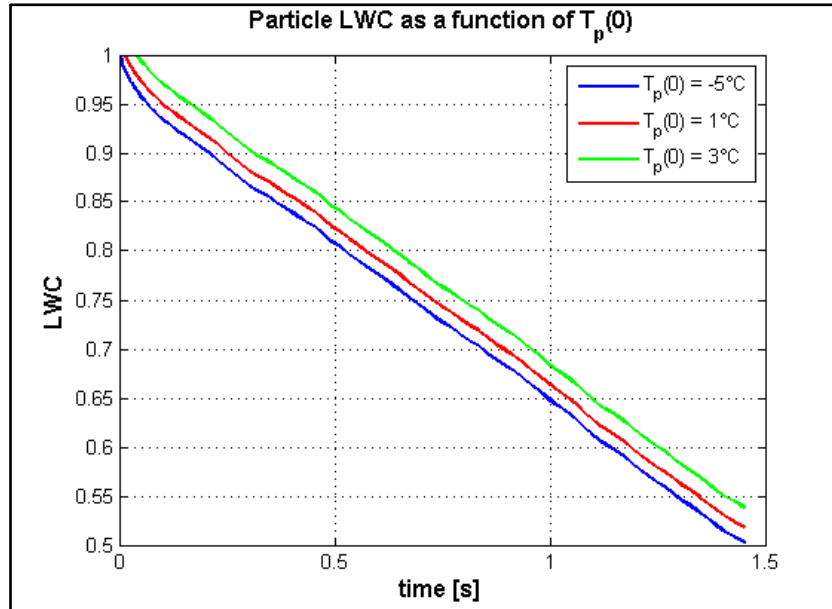


Figure 112. LWC as a function particle initial temperature.

Figure 113.a shows the liquid water content as a function of the hygrometry in the air. We observe that  $HR$  does not play an important role on the particle LWC. The liquid water content slightly increases with an increase of the hygrometry. The reason can be found in Figure 113.b where the heat transfer due to mass transfer is shown. This last one is the only heat transfer linked to the hygrometry. When the hygrometry increases,  $q_m$  decreases. Therefore, the global heat loss is lowered and the LWC slightly increases.

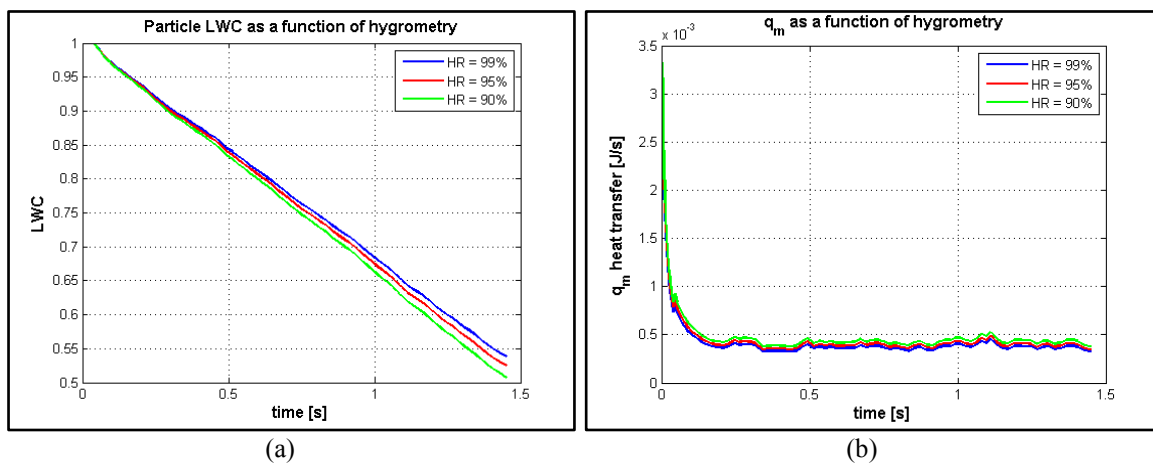


Figure 113. (a) LWC as a function of  $HR$  (b)  $q_m$  as a function of  $HR$ .

The hygrometry during the experimental campaign cannot be tuned due to the mixed nature of the flow (air and snow particles). The value of HR is systematically measured in the wind tunnel and shows that the ambiance is almost saturated.

#### 4.2.6 Boundary condition estimation: $LWC$ of the whole snow particle flow.

The goal of this last section is to compute the whole particle flux which reach the cylinder with a characteristic liquid water content as a function of the ambient temperature  $T_a$ . This means to weight the liquid water content of each diameter class  $i$  with the volume particle size distribution  $PSD^v$  obtained before. This allows to associate an unique value of liquid water content to the particle flow as a function of the ambient temperature. The estimation of the global  $LWC_g$  for all the ambient temperatures is made through the weighted mean (93).

$$LWC_g = \frac{\sum LWC_i \cdot (PSD^v)_i}{\sum (PSD^v)_i} \quad (93)$$

Table 8 provides all the information needed to compute the weighted liquid water content for three different temperatures.

Table 12.  $PSD^v$  with associated  $LWC$  for  $LWC_g$  evaluation

| $d_p$      | $PSD^v$ % | $LWC T_a = -3^\circ C$ | $LWC T_a = -6^\circ C$ | $LWC T_a = -9^\circ C$ |
|------------|-----------|------------------------|------------------------|------------------------|
| $40\mu m$  | 0.0132    | $\approx 0$            | $\approx 0$            | $\approx 0$            |
| $80\mu m$  | 0.5167    | $\approx 0$            | $\approx 0$            | $\approx 0$            |
| $120\mu m$ | 2.3022    | $\approx 0.1820$       | $\approx 0$            | $\approx 0$            |
| $160\mu m$ | 6.3024    | $\approx 0.4673$       | $\approx 0.0390$       | $\approx 0$            |
| $200\mu m$ | 13.3658   | $\approx 0.6084$       | $\approx 0.2803$       | $\approx 9e^{-4}$      |
| $240\mu m$ | 16.7608   | $\approx 0.6965$       | $\approx 0.4392$       | $\approx 0.1284$       |
| $280\mu m$ | 20.0197   | $\approx 0.7463$       | $\approx 0.5312$       | $\approx 0.2710$       |
| $320\mu m$ | 18.1918   | $\approx 0.7881$       | $\approx 0.6065$       | $\approx 0.3858$       |
| $360\mu m$ | 10.0858   | $\approx 0.8142$       | $\approx 0.6552$       | $\approx 0.4617$       |
| $400\mu m$ | 6.5442    | $\approx 0.8327$       | $\approx 0.6882$       | $\approx 0.5130$       |
| $440\mu m$ | 4.7477    | $\approx 0.8532$       | $\approx 0.7264$       | $\approx 0.5714$       |
| $480\mu m$ | 0.5665    | $\approx 0.8687$       | $\approx 0.7542$       | $\approx 0.6148$       |
| $520\mu m$ | 0.5834    | $\approx 0.8843$       | $\approx 0.7823$       | $\approx 0.6587$       |
| <hr/>      |           |                        |                        |                        |
| $Tot$      | 100       |                        |                        |                        |
| $LWC_g$    |           | $\approx 0.7117$       | $\approx 0.4847$       | $\approx 0.3071$       |

Figure 114 shows the global weighted liquid water content  $LWC_g$ . This evaluation has been performed as a function of the ambient temperature  $T_a$ . This last one represents the physical parameters through which the liquid water content has been tuned during the experimental campaign:  $LWC = \mathcal{F}(T_a)$ . An example of the results obtained during the experimental campaign is reported in Figure 105. A decrease of the ambient temperature induces a decrease of the accretion mass.

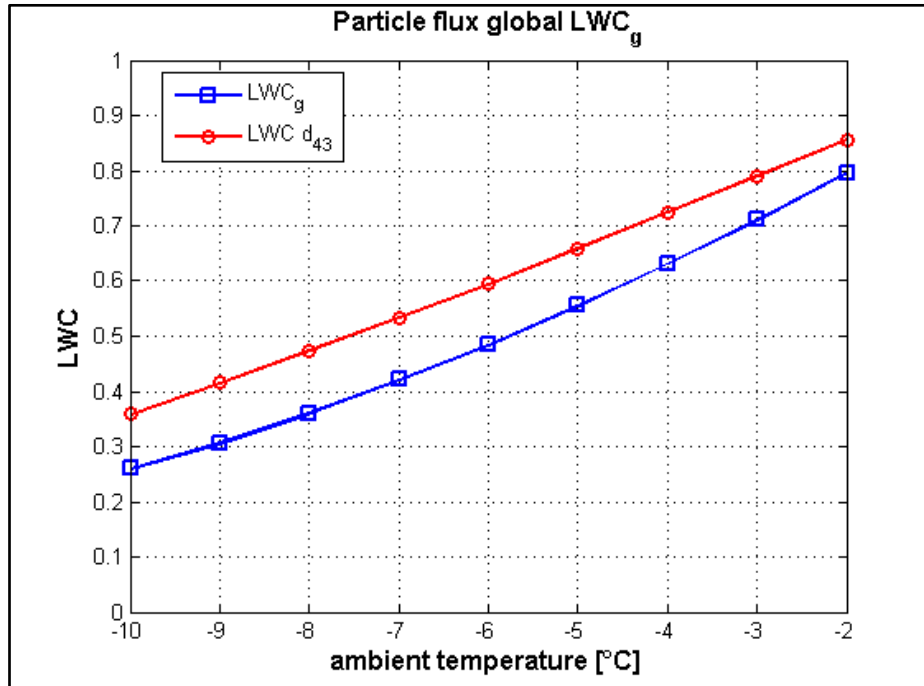


Figure 114. The LWC of the whole particle flux.

One can note that taking a  $LWC$  of the mean volume diameter  $d_{43}$  does not correspond to the global liquid water content. As a consequence, one has to take the whole particle distribution to obtain a robust result for the global particle liquid water content. This global liquid water content will be weighted in chapter five by the size distribution of particles which impact the cylinder. This will allow to evaluate the  $LWC_g$  of the particles which impact the cylinders.

### 4.3 Conclusion

In this chapter, we have estimated the boundary conditions for the accretion analysis of chapter five. It was not possible to measure these boundary conditions during the experimental campaign. Therefore, a model has been built.

This physical model presents two codes which are coupled together. The first code is a stochastic tracking dispersion code used to estimate the volume particle size distribution “on” the cylinders. This distribution corresponds to the first boundary condition sought:  $PSD^v$ . The distribution will be employed to estimate the collision efficiency in next chapter.

The second part of the model is based on the particle freezing process. Coupled with the tracking model, it allows to estimate the liquid water content of particles which reach the cylinder position. Then, the global liquid water content  $LWC_g$  of the whole particle flow has been evaluated as a function of the ambient temperature:  $LWC_g$ . This parameter represents the second boundary condition of the analysis presented in chapter five. The  $LWC_g$  evaluated in this chapter, will be weighted in chapter five by the size distribution of particles on the cylinder. This provides the assessment of the liquid water mass of the particle which impacts the cylinders.

The chapter has shown that the ambient temperature represents a physical parameter that can be used to tune the particle liquid water content. This justifies the approach chosen during the experimental campaign. Moreover we have shown that the liquid water content is very sensitive to a temperature variation:  $LWC = \mathcal{F}(T_a)$ .

## Bibliography

- [1] M. Strub, O. Jabbour, F. Strub, and J. P. Bédécarrats, "Experimental study and modelling of the crystallization of a water droplet," *International Journal of Refrigeration*, vol. 26, pp. 59-68, 2003.
- [2] J. P. Hindmarsh, A. B. Russell, and X. D. Chen, "Experimental and numerical analysis of the temperature transition of a suspended freezing water droplet," *International Journal of Heat and Mass Transfer*, vol. 46, pp. 1199-1213, 2003.
- [3] S. Boisson-Kouznietzoff, "Qualification de la neige produite dans la soufflerie climatique Jules Verne: mise au point du dispositif expérimental et modélisation numérique du procédé," Docteur, Dynamique des Fluids et des Transerts, Ecole Doctorale Sciences Pour l'ingénieur De Nantes, Nantes, 1997.
- [4] G. A. Hughmark, "Heat and Mass Transfer for Spherical Particles in a Fluid Field," *Industrial & Engineering Chemistry Fundamentals*, vol. 19, pp. 198-201, 1980/05/01 1980.
- [5] B. Oesterlé, *Écoulements multiphasiques*. Paris: Lavoisier, 2006.
- [6] A. Leroy, "Étude expérimentale et numérique des dépôts de givre discontinus sur les voilures en flèche d'aéronefs," Docteur d'université, Physique de l'Atmosphère, Blaise Pascal, 2004.
- [7] X. Presteau, "Modélisation Microphysique Tridimensionnelle des Dépôts de Givre: Application au Givre en Queue de Homard sur des Cylindres en Flèche," Docteur d'Université, Ecole Doctorale Des Sciences Fondamentales, Université Blaise Pascal, 2009.
- [8] L.-P. Wang and D. E. Stock, "Dispersion of Heavy Particles by Turbulent Motion," *Journal of the Atmospheric Sciences*, vol. 50, pp. 1897-1913, 1993/07/01 1993.
- [9] P. Delpech, "Procès Verbal d'essais - CONFIDENTIEL," 2007.
- [10] K. N. Volkov, "Internal Turbulent Two-Phase Flows Formed by Wall Injection of Fluid and Particles," presented at the V European Conference on Computational Fluid Dynamics, Lisbon, Portugal, 14-17 June 2010, 2010.



## Chapter 5 Estimation of the parameters to model wet snow accretions

|       |   |     |
|-------|---|-----|
| 5.1   | DETERMINATION OF THE AERODYNAMIC CONTRIBUTION TO WET SNOW ACCRETIONS: COLLISION EFFICIENCY. ....          | 128 |
| 5.1.1 | <i>Numerical modeling of the flowstream around the cylinders: setup</i> .....                             | 129 |
| 5.1.2 | <i>Numerical modeling of the flowstream around the cylinders: results</i> .....                           | 132 |
| 5.1.3 | <i>Lagrangian simulations of particle dispersion around the cylinders: setup</i> .....                    | 134 |
| 5.1.4 | <i>Flowstream and lagrangian modeling setting up conclusions</i> . ....                                   | 137 |
| 5.2   | COLLISION EFFICIENCY EVALUATION OF THE EXPERIMENTAL CYLINDERS.....  | 137 |
| 5.2.1 | <i>Relation between Stokes number and collision efficiency</i> . ....                                     | 138 |
| 5.2.2 | <i>Particle size distribution on the cylinders and the resulting liquid water content</i> .....           | 141 |
| 5.2.3 | <i>Collision efficiency evaluation: conclusions</i> . ....  | 143 |
| 5.3   | QUANTIFICATION OF THE COLLISION EFFICIENCY IMPACT ON THE EXPERIMENTAL COEFFICIENT $\beta_{exp}$ .....     | 143 |
| 5.4   | QUANTIFICATION OF MODELED ACCRETION SHAPES.....   | 146 |
| 5.5   | STICKING EFFICIENCY AS A FUNCTION OF THE PARTICLE-SURFACE ANGLE OF IMPACT .....                           | 150 |
| 5.5.1 | <i>Theoretical implementation of the angle criterion and application to the experimental cases</i> . 150  |     |
| 5.5.2 | <i>Accretion shape obtained with a threshold angle <math>\alpha_t = 45^\circ</math></i> . ....            | 152 |
| 5.5.3 | <i>Accretion shape influence on the global collision efficiency <math>\eta_1</math></i> . ....            | 153 |
| 5.5.4 | <i>Sticking efficiency evaluation for the experimental cases</i> .....                                    | 155 |
| 5.6   | ANALYSIS OF THE STICKING COEFFICIENT $\eta_2 = \mathcal{F}(\alpha_{imp})$ ON THE EXPERIMENTAL CASES. .... | 158 |
| 5.6.1 | <i>Sticking efficiency analysis: conclusions</i> . ....   | 161 |
| 5.7   | CONCLUSION.....   | 161 |
|       | BIBLIOGRAPHY .....  | 164 |

This chapter aims at presenting the procedure undertaken in this work to model wet snow accretions and the associated results. The test campaign and the literature review have shown how the accretion process is characterized by three aspects: aerodynamic, mechanic and thermal. These aspects are analyzed by three dimensionless coefficients. During the experimental campaign was not possible to analyze separately each aspect. As a consequence, a numerical approach is undertaken to estimate each aspect, and analyze the role of each aspect on the accretion process.

The first part of the chapter explains the numerical approach undertaken to study the influence of the cylinders on the incoming particle behavior. It is considered as the aerodynamic aspect of the accretion. This analysis is performed by analyzing the collision efficiency  $\eta_1$ . This coefficient allows to estimate the mass flux of snow which impacts the cylinder with respect to the mass flux which approaches the cylinders.

The second part of the chapter proposes an analysis of the sticking efficiency  $\eta_2$ . This coefficient is defined as the ratio between the sticking mass flux of particle and the impacting mass flux of particle. It will be investigated how the sticking efficiency can be a function of the liquid water content and of the angle of impact to the accretion surface.

The investigation in both parts, will be performed assuming an accretion efficiency  $\eta_3 = 1$ . This coefficient represents the ratio between the accretion mass flux and the sticking mass flux. This hypothesis means that the mass of wet snow lays on the cylinder surface once it has stuck on it.

## 5.1 Determination of the aerodynamic contribution to wet snow accretions: collision efficiency.

The main purpose of this part is to quantify the aerodynamic aspect of the experimental accretions by a numerical approach. The goal is to discern from the experimental coefficient  $\beta_{exp}$ , the aerodynamic influence.

Therefore, the first step of the analysis is setting up a numerical model to study the particle behavior close to the cylinders. The model will be set up to represent the conditions of the experimental campaign.

The analysis is focused on the collision efficiency  $\eta_1$ . This coefficient is defined as (94)

$$\eta_1 = \frac{\dot{m}_{imp}}{\dot{m}_{inc}} \quad (94)$$

The incoming mass flux  $\dot{m}_{inc}$  is evaluated as the ratio between the mass of particles which passes through a reference surface and the area of this reference surface. The ratio is evaluated per unit time. The reference area is evaluated as  $A_{ref} = d_{cyl} \cdot l_{cyl}$  where  $d_{cyl}$  is the cylinder diameter and  $l_{cyl}$  a reference length. The reference length is taken equal to the central portion of the cylinder as explained in chapter three:  $l_{cyl} = 0.7m$ . The impacting mass flux  $\dot{m}_{imp}$  is evaluated by normalizing the mass of particles which have impacted on the cylinder by the reference area  $A_{ref}$  (Figure 115) per unit time. The position of the reference area will be explained during the presentation of the model set up.

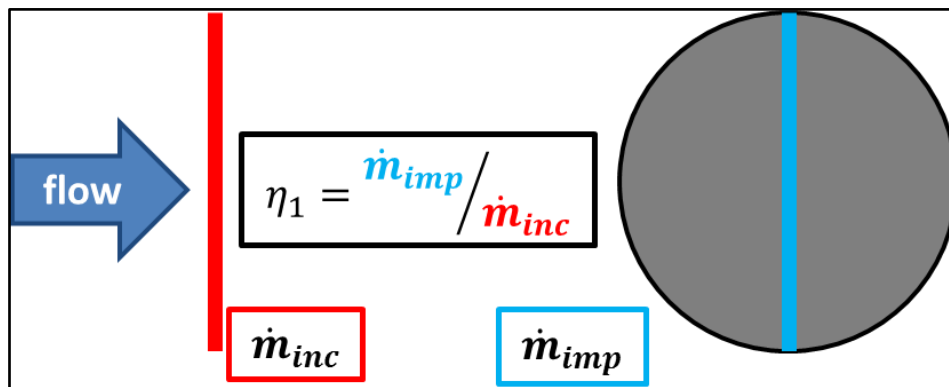


Figure 115. A representation of the collision coefficient  $\eta_1$

Let us consider a particle diameter equals to the MVD of the particle distribution evaluated in chapter four:  $d_{MVD} = 260\mu m$ . In Table 13 is presented a Stokes number  $St_{cyl} = \frac{\tau_p}{\tau_{cyl}}$  evaluated as the ratio between the relaxation time  $\tau_p$  and a characteristic

time of the flow around the cylinder  $\tau_{cyl} = \frac{d_{cyl}}{\langle u_f \rangle}$ . For the particle  $d_{MVD}$  the relaxation time is  $\tau_p \approx 0.1s$ . To evaluate  $\tau_{cyl}$  the mean flow speed  $\langle u_f \rangle$  is taken equal to  $9m/s$ .

Table 13.  $St_{cyl}$  as a function of the cylinder diameter

| $d_{cyl}$ | $St_{cyl}$    |
|-----------|---------------|
| 50        | $\approx 18$  |
| 200       | $\approx 4.5$ |
| 315       | $\approx 3$   |

The Stokes numbers proposed in In Table 13 vary noticeably as a function of the cylinder for the same particle diameter. As a consequence, one needs a numerical approach capable to model the flow nearby the cylinders and its interaction with the particles.

For the flow modeling, the RANS approach has been chosen. It is supposed that the framework of the study does not require to model turbulence by a more complex approach. The model integrates the lagrangian stochastic feature to model the particle-flow interaction. Let us consider the Stokes number  $St_{turb} = \frac{\tau_p}{\tau_{turb}}$  with  $\tau_p$  based on the particle types considered before. The characteristic time of the flow, based on the turbulence, is  $\tau_f = \frac{l}{\sqrt{\langle u_f'^2 \rangle}}$ . Where  $l$  is the integral length scale of the snow flow equal to

$l = 0.86m$  as seen in the experimental chapter. An approximation of  $\sqrt{\langle u_f'^2 \rangle}$  is

evaluated as  $\sqrt{\langle u_f'^2 \rangle} = I_{\%} \langle u_f \rangle \approx 0.72m/s$ . Therefore  $St_{turb} \approx 0.1$ . Hence,  $St_{turb}$  indicates that the turbulence plays a crucial role on the particle trajectory. As a consequence, a stochastic feature must be introduced in the numerical model to take into account the interaction of particles with the turbulence.

This stochastic feature is implemented in a different way from previous chapter. Here, an EIM (Eddy-Interaction-model) approach will be used for the task. As seen in chapter two, this model takes also in account the crossing trajectory effect and it is faster than a Langevin approach.

As seen in chapter three the influence of the particles on the carrier phase can be neglected. As a consequence, one can perform two distinct computations to establish the flowstream around the cylinder and to compute the particle dispersion on the cylinder with the flowstream previously evaluated.

Due to the spatial uniformity of the snow accretions obtained on the cylinders during the experimental campaign, the numerical models will be two-dimensional.

### 5.1.1 Numerical modeling of the flowstream around the cylinders: setup.

The numerical model for the airflow around the cylinder is based on the RANS approach to model the turbulence. With the RANS approach one solves the time-averaged version of the Navier-Stokes equations. In this work two turbulence models are employed.

The first one is the  $k - \varepsilon$  model.  $k \left[ \frac{m^2}{s^2} \right]$  represents the turbulent kinetic energy and  $\varepsilon \left[ \frac{m^2}{s^3} \right]$  the dissipation rate of  $k$ . The second model employed is the  $k - \omega$  with its SST variant. For this model  $\omega [Hz]$  represents the specific dissipation which determines the frequency scale of the turbulence. The choice of these two models is not trivial. The first one is the most common used and easy to implement. However, it presents a well-known anomaly on the evaluation of  $k$  at the stagnation point. The second one  $k - \omega$  SST, allows on the other hand, a good prediction of  $k$  where  $k - \varepsilon$  fails. Therefore, a comparison between the collision efficiency evaluated with both turbulence models will be proposed. The purpose is to investigate if the anomaly of the  $k - \varepsilon$  model influences or not the collision efficiency.

The initial conditions of the flow have been acquired during the experimental campaign. With a mean flow speed  $\langle u_f \rangle = 9m/s$ , a turbulence intensity of  $I_0 = 8\%$  and the integral length scale  $l \approx 0.86m$  it is possible to evaluate the initial conditions of the turbulence models.

For the  $k - \varepsilon$  model:  $k = \frac{3}{2} \langle u_f' \rangle^2 \approx 0.78 \frac{m^2}{s^2}$  and  $\varepsilon = \frac{0.09^{3/4} \cdot k^{3/2}}{l} \approx 0.13 \frac{m^2}{s^3}$ . For the  $k - \omega$  SST will be taken as  $\omega = \frac{k^{1/2}}{0.09^{1/4} \cdot l} \approx 1.85Hz$ . The flow speed is supposed to be uniform in the inlet. On the lower and upper bound, a condition of  $u_f = 0m/s$  has been imposed.

The computational domain is  $14m$  long and  $4m$  high (Figure 116). One can suppose that with a ratio between the height of the domain and the cylinder diameter larger than 10, the blockage effect is avoided (Table 14).

Table 14. Estimation of the blockage effect

| $d_{cyl}$ | $h_{domain}/d_{cyl}$ |
|-----------|----------------------|
| 50        | 80                   |
| 200       | 20                   |
| 315       | 13                   |

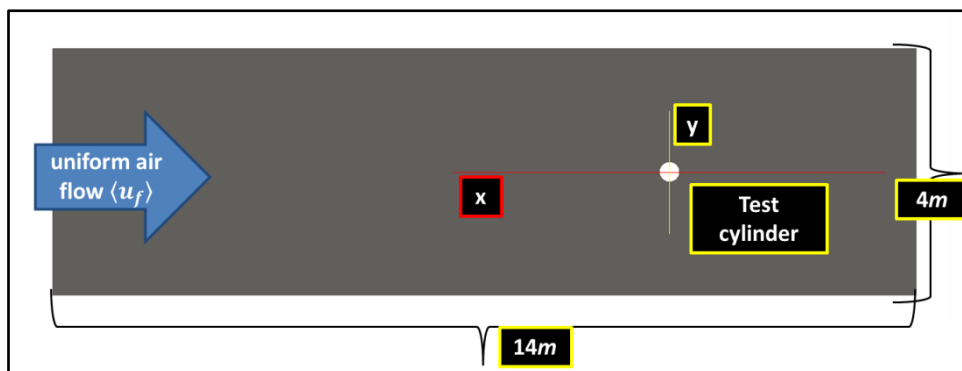


Figure 116. Computational domain for  $d_{cyl} = 50mm$ .

The mesh is refined close to cylinder to ensure an improved characterization of the flow close to the surface. This will lead to a better evaluation of the particle

trajectory. As a consequence of the different diameter of the cylinders, the number of cells is different for each computational domain. This is also why, the refinement close to the cylinder needs more cells when the cylinder diameter increases.

The quality of the meshes has been analyzed with the Skewness parameter. This one allows to measure the flatness of a cell through its area  $A_{cell}$  with respect to the reference one  $A_{ref}$  (95).

$$Skew = \frac{A_{ref} - A_{cell}}{A_{ref}} \quad (95)$$

In Figure 117.a is reported an image of the mesh refinement close to the cylinder with a scheme to illustrate what Skewness is (Figure 117.b).

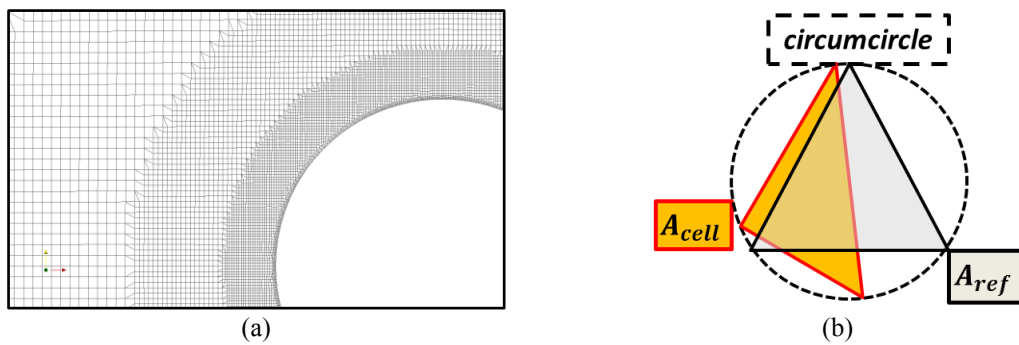


Figure 117. (a) mesh refinement evolution, (b) skewness concept.

The three meshes have a maximum skewness below 0.6. This skewness value is commonly considered acceptable for 2D meshes.

The mean wall distance  $y^+$  of the first grid (96) for the three cylinders is close to  $y^+ \approx 30$ . Without entering into the details this parameter allows to apply a boundary condition close to the cylinder surface. Seen the  $y^+$  value in our case, the law of the wall is used. It is based on a relation between the velocity and the friction at the wall, in the log region of a boundary layer.

$$y^+ = \frac{u_\tau \cdot y}{\nu_f} \quad (96)$$

Where  $u_\tau$  is the friction velocity,  $y$  is the distance from the cylinder surface to the center of the first cell mesh and  $\nu_f$  is the kinematic viscosity of air.

In Table 15 is proposed a synthesis of the characteristic parameters of the meshes developed.

Table 15. The analysis of the meshes.

| $Mesh d_{cyl}$ | $n_{celles}$ | $Skew$         | $\langle y^+ \rangle$ |
|----------------|--------------|----------------|-----------------------|
| 50             | 23922        | $\approx 0.40$ | $\approx 30$          |
| 200            | 31875        | $\approx 0.36$ | $\approx 36$          |
| 315            | 38144        | $\approx 0.35$ | $\approx 40$          |

The simulation is solved with an incompressible steady solver. The flow is considered incompressible because the Mach number  $Ma = \frac{\langle u_f \rangle}{u_{sound}} < 0.3$ . As a consequence, the density of the air  $\rho_f = 1.316 \frac{kg}{m^3}$  is fixed. One hundred iterations ensure the solution convergence. Figure 118 reports the convergence analysis based on the residual of the numerical simulation. The residuals can be synthesized as the difference between the exact and approximated solution. When the residuals reach a constant value the simulation is considered converged.

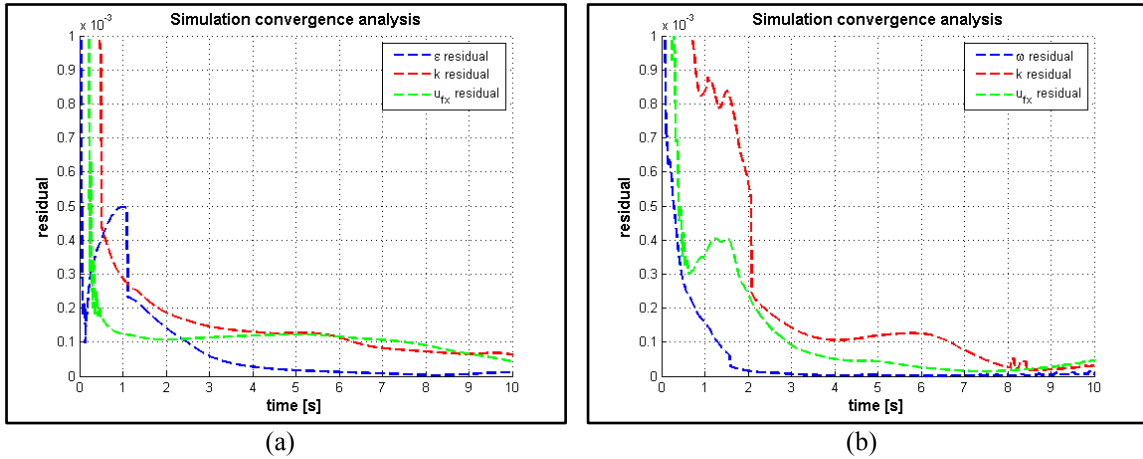


Figure 118. Convergence analysis (a)  $k - \epsilon$  model. (b)  $k - \omega$  SST model.

### 5.1.2 Numerical modeling of the flowstream around the cylinders: results.

To validate the fluid model, here after are reported a series of results. In particular, the attention is focused on the pressure coefficients define as  $C_p = \frac{p - P_a}{0.5 \rho_f u_f^2}$ . Where  $p$  the local pressure on the surface and  $P_a$  the ambient pressure. In Figure 119, one can see that the flow separates at  $\varphi \approx 60 - 80^\circ$  for the  $k - \omega$  SST model, while flow separation only occurs at  $\varphi \approx 80 - 100^\circ$  for  $k - \epsilon$  simulation.  $k - \omega$  SST model results in accordance with Zdravkovich [1] while  $k - \epsilon$  model results in a delayed flow separation. Both models fail in reproducing the pressure coefficient reported by Zdravkovich in the wake. One can see a difference on the pressure coefficient close to the separation point. The one calculated for  $d_{cyl} = 200mm$  seems to be the most in accordance with the experimental data found in literature.

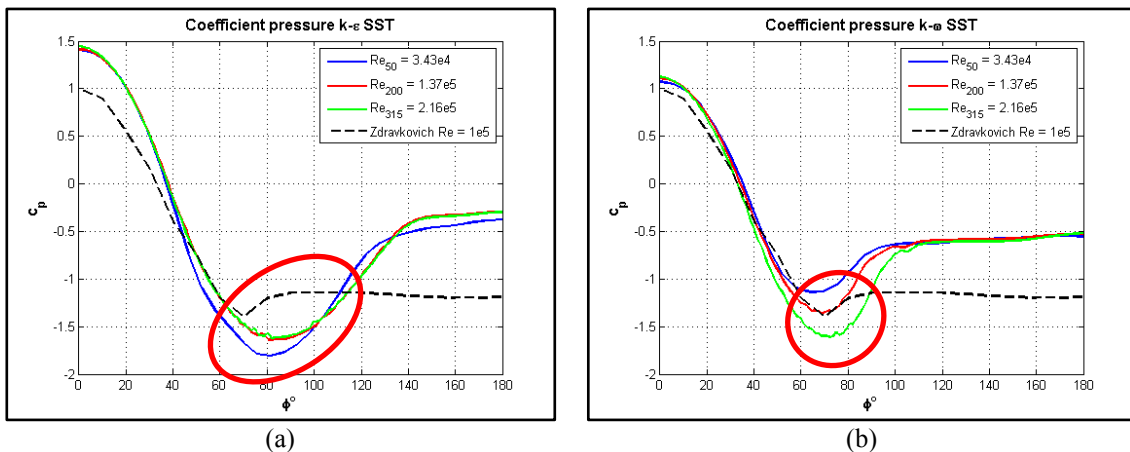


Figure 119. Pressure coefficient (a)  $k - \epsilon$  model. (b)  $k - \omega$  SST model.

Figure 120, shows the normalized turbulent kinetic energy computed by the  $k - \varepsilon$  and the  $k - \omega SST$  models. It clearly shows the overproduction of  $k$  by the  $k - \varepsilon$  model. This overproduction, then contaminates the boundary layer and results in a delayed separation for the  $k - \varepsilon$  model (Figure 119.a).

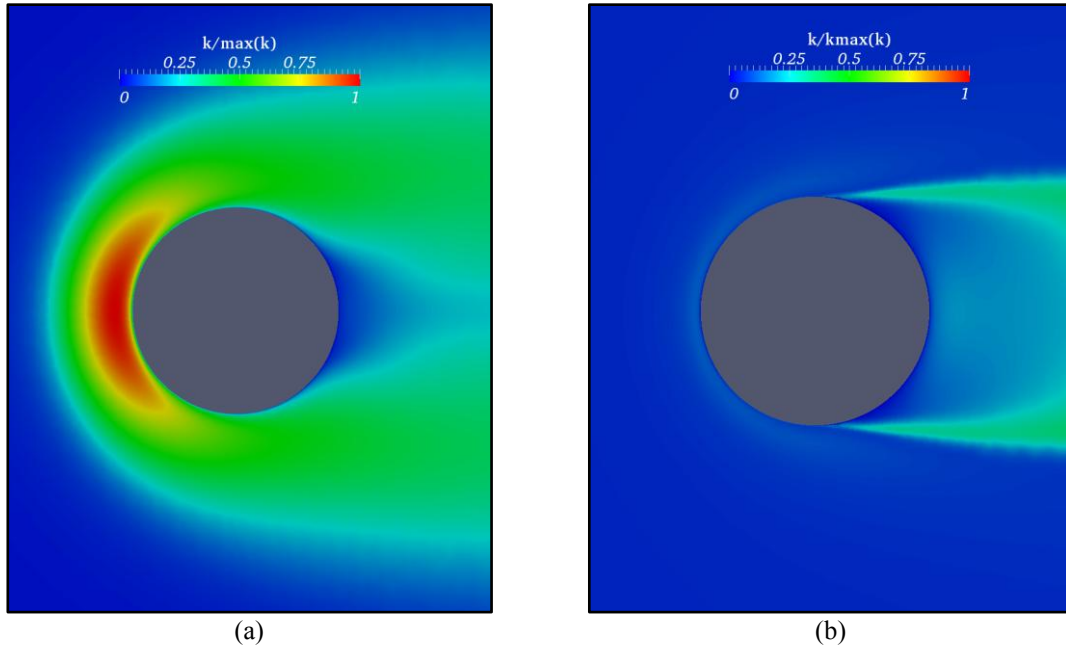
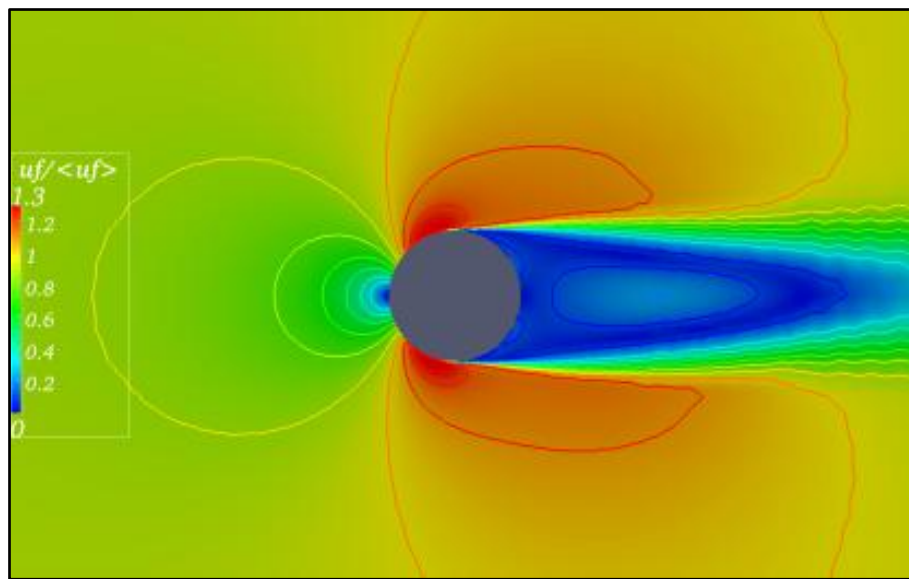


Figure 120. Overproduction of  $k$  (a)  $k - \varepsilon$  model. (b)  $k - \omega SST$  model.

Using the  $k - \omega SST$  model, one is now able to estimate the flow around the three cylinders tested during the experimental campaign. The analysis presented in this paragraph is not a detailed description of the flowstream around a cylinder (Figure 121). However, it allows to present a numerical simulation of the flow around the cylinders which is suitable for the lagrangian tracking of particles and hence, a good evaluation of the collision efficiency  $\eta_1$ .



$$d_{cyl} = 315\text{mm}$$

Figure 121.  $k - \omega SST$  flowstream computational results.

### 5.1.3 Lagrangian simulations of particle dispersion around the cylinders: setup

The dispersion model takes as a flow field the ones calculated in the first step (Figure 121). The particle distribution evaluated in chapter four (Figure 122) is used here as initial condition for particle injection.

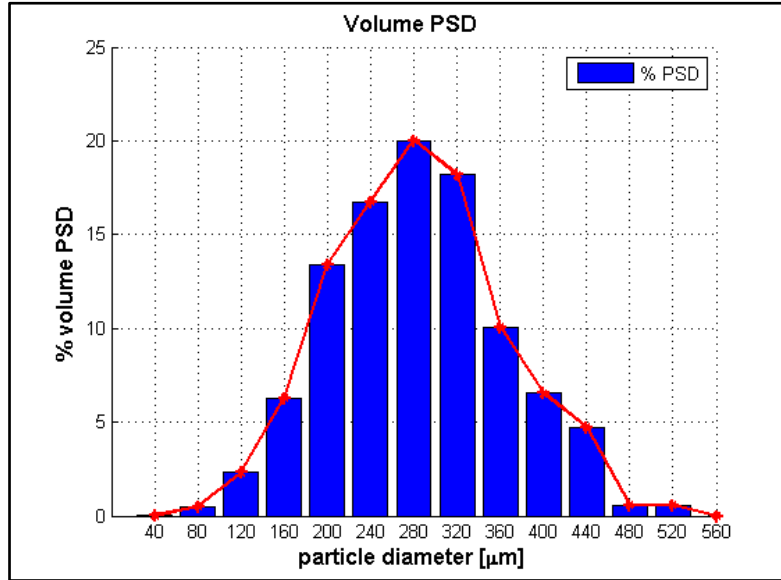


Figure 122. Volume PSD at the cylinder location.

The injection point is placed in a zone of the computational domain where the fluid velocity is constant (Figure 123.a) along all the vertical direction. This contributes to a uniform particles injection. The point of injection is placed at  $6m$  to the inlet and  $d_{inj} = 4m$  to the cylinders (Figure 123.b).

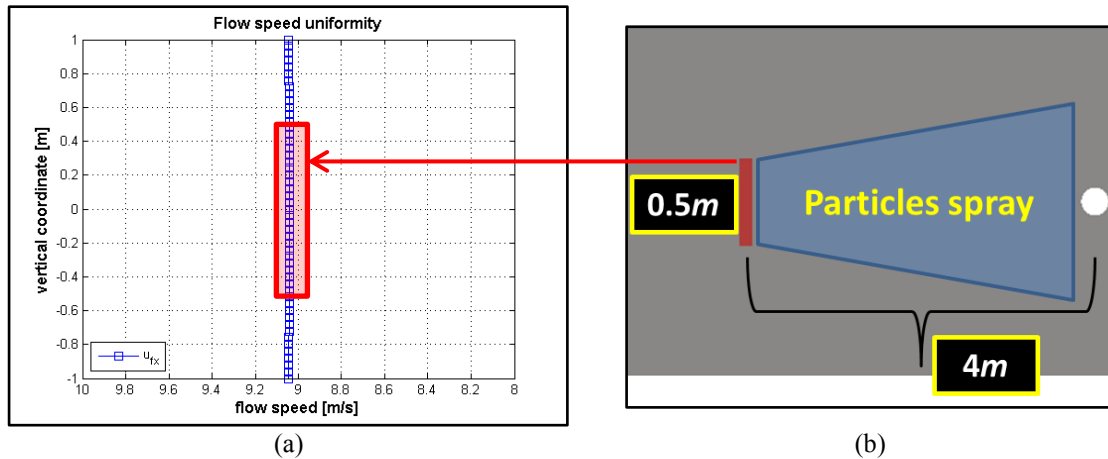


Figure 123. (a) flow speed uniformity at injection point. (b) Injection point location.

Moreover, it is supposed that the injection-cylinder distance is long enough to “stabilize” the particles in the flow. To ensure this hypothesis, a Stokes number  $St_{inj} = \frac{\tau_p}{\tau_{inj}}$  is proposed. Where the particle flying time is  $\tau_{inj} = \frac{d_{inj}}{\langle u_f \rangle} \approx 0.44$ , the mean flow speed is taken equal to  $\langle u_f \rangle = 9m/s$ . The particle reference is  $d_{MVD} = 260\mu m$  characterized by a mean relaxation time  $\tau_p \approx 0.1s$ .

As one can note  $St_{inj} \approx 0.2$  is smaller than unity. This means that the flying time of particle  $\tau_{inj}$  is 5 times longer than the response time  $\tau_p$ . Therefore, one can suppose that the distance of  $4m$ , between the injection point and the cylinders, is adequate to “stabilize” the particles with respect to the flow.

Particles are introduced in the computational domain from an injection line which is  $0.5m$  high and it is characterized by five hundred injection points. The vertical extension of the particle source ensures a full coverage of the cylinders by the particle flow. It is supposed that particles reach the cylinder at the same velocity of the flow. As a consequence particles are injected at the instant  $t = 0$  with velocity:  $u_p(0) = 9m/s$ . The particle injection is performed at each time step. A total of  $\approx 600000$  particles are injected for each simulation. In Figure 124 a representation of the injection in the whole computational domain.

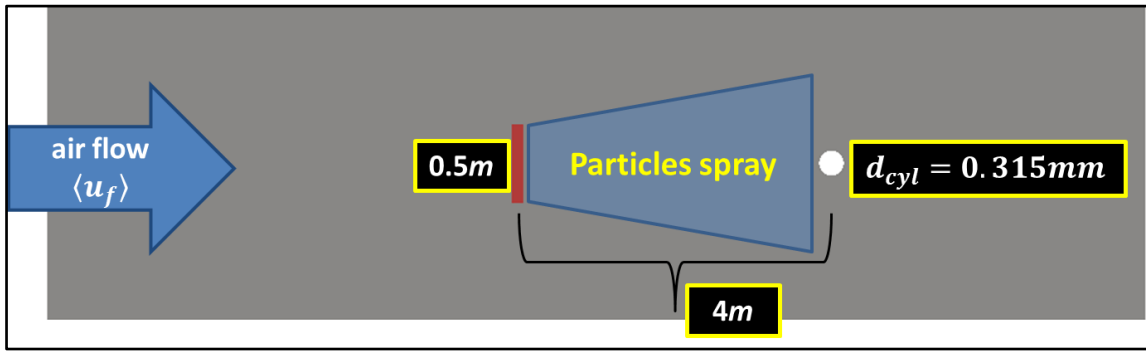
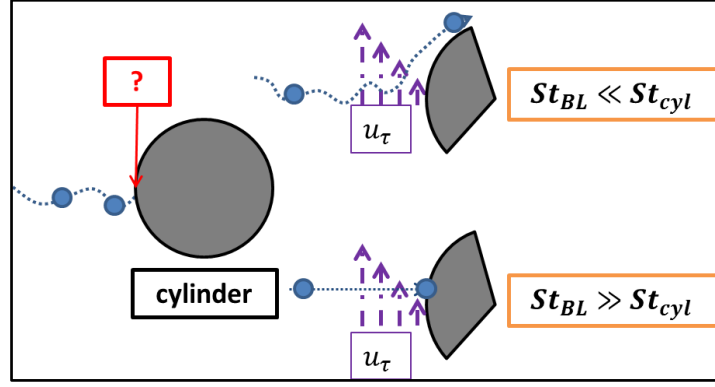


Figure 124. Particles injection point in the computational domain

Close to the cylinders, taking a particle  $d_{MVD} = 260\mu m$  characterized by  $\tau_p \approx 0.1s$  with a mean velocity  $\langle u_p \rangle = 9m/s$ , the Froude number is  $Fr = \frac{\langle u_p \rangle}{\tau_p g} \approx 9$ . This shows that the gravity will not influence significantly the motion of particles in the cylinder region. As a consequence, gravity effect has been neglected during these simulations.

Additionally, the numerical model has been setup under the hypothesis that particles are not interacting with the boundary layer turbulence. Indeed, particles responding to the mean wall turbulence can be “trapped” in the boundary layer flow, without impacting the wall (Aguinaga [2]).

To validate this hypothesis here follow an estimation of a Stokes number  $St_{BL} = \frac{\tau_p}{\tau_{BL}}$  based on the particle relaxation time  $\tau_p$  and a characteristic time of the mean wall turbulence  $\tau_{BL}$ . If this analysis shows:  $St_{BL} \gg St_{cyl}$  with  $St_{cyl} = \frac{\tau_p}{\tau_{cyl}}$ , one can exclude particles/wall turbulence interactions. As a consequence particle will hit in an inertial way the cylinder. Figure 125 represents a scheme to better understand the following analysis.


 Figure 125. Particle behavior in the boundary layer,  $St_{BL}$  meaning.

As seen before the value of  $y^+$  is around 35 which means that the boundary layer is treated with the log law. As a consequence, the characteristic time of the turbulence in this region can be approximated as  $\tau_{BL} = \frac{\kappa y}{u_{\tau}}$ . Where  $\kappa$  is the Von-Karman constant,  $u_{\tau}$  the friction velocity. As a consequence  $St_{BL}$  can be expressed as (97) (where  $u_{\tau} = 0.05\langle u_f \rangle$  has been chosen as a crude estimation).

$$St_{BL} = \frac{\tau_p}{\tau_{BL}} = \frac{\tau_p}{\kappa \cdot y} \cdot u_{\tau} = \frac{0.05}{\kappa \cdot \left(\frac{y}{d_{cyl}}\right)} \cdot \frac{\tau_p}{d_{cyl} / \langle u_f \rangle} = \frac{0.05 \cdot d_{cyl}}{\kappa \cdot y} \cdot St_{cyl} \quad (97)$$

Which leads to  $St_{BL} = \frac{0.05}{\kappa \cdot \left(\frac{y}{d_{cyl}}\right)} \cdot St_{cyl}$ . With  $y^+ = \frac{u_{\tau} y}{\nu_f}$ , we obtain (98)

$$St_{BL} = \frac{0.05^2}{\kappa \cdot y^+} \cdot \frac{\langle u_f \rangle \cdot d_{cyl}}{\nu_f} \cdot St_{cyl} = \frac{0.05^2}{\kappa \cdot y^+} \cdot Re_{cyl} \cdot St_{cyl} \quad (98)$$

Estimating a mean Reynolds number of the three cylinder  $Re_{cyl} \approx 1.3 \cdot 10^5$  and the constant  $\frac{0.05^2}{\kappa \cdot y^+} \approx 1.74 \cdot 10^{-4}$ , the Stokes number for the boundary layer is  $St_{BL} \approx 10St_{cyl}$ . As a consequence, it is possible to setup the model without taking into account particle/turbulence interaction in the mean wall flow.

The dispersion solver considers the fluid as incompressible, the time step  $\Delta_t$  is tuned as a function of the Courant number  $CFL$  (99) where  $\Delta_x$  is the length of the turbulent eddy.

$$CFL = \frac{u_f \Delta_t}{\Delta_x} \quad (99)$$

Due to the fact that interactions between particles are neglected, particle trajectories are independent from one to another. As a consequence, the duration of the numerical simulation has no importance. It is however necessary to check that enough particles have reached the cylinders to ensures a good statistical representation of the collision efficiency.

### 5.1.4 Flowstream and lagrangian modeling setting up conclusions.

The modeling setup presented will allow to evaluate the collision efficiency for the three experimental cylinders. To resume, the approach undertaken is divided in two steps. The former one concerns the modeling of the flowstream around the three cylinders. The modeling is based on a RANS approach with two turbulence models:  $k - \varepsilon$  and  $k - \omega SST$ . This last one has been chosen as a reference model. The latter part concerns the modeling of particles dispersion on the cylinders. The model uses as initial conditions the particle size distribution evaluated in chapter four and the flowstream evaluated in the first part.

## 5.2 Collision efficiency evaluation of the experimental cylinders.

The collision efficiency is evaluated through the second part of the numerical approach. This coefficient allows to estimate the particle flux which strikes the cylinders  $\dot{m}_{imp}$  with respect to the incoming particle flux  $\dot{m}_{inc}$  as reported in equation (100). The coefficient will allow to discern the aerodynamic effect on the experimental coefficient  $\beta_{exp}$  to analyze the accretion process as a function of  $\eta_2$  and  $\eta_3$ .

$$\eta_1 = \frac{\dot{m}_{imp}}{\dot{m}_{inc}} \quad (100)$$

The incoming particle flux  $\dot{m}_{inc} = \frac{m_{inc}}{A_{ref} \cdot t}$  is defined as the particle mass  $m_{inc}$  which flows through a control surface divided by the surface area  $A_{ref}$  and the simulation time  $t$ . The impacting mass flux  $\dot{m}_{imp} = \frac{m_{imp}}{A_{ref} \cdot t}$  is evaluated as the mass  $m_{imp}$  which impacts the cylinder divided by the reference area and the simulation time (Figure 126).

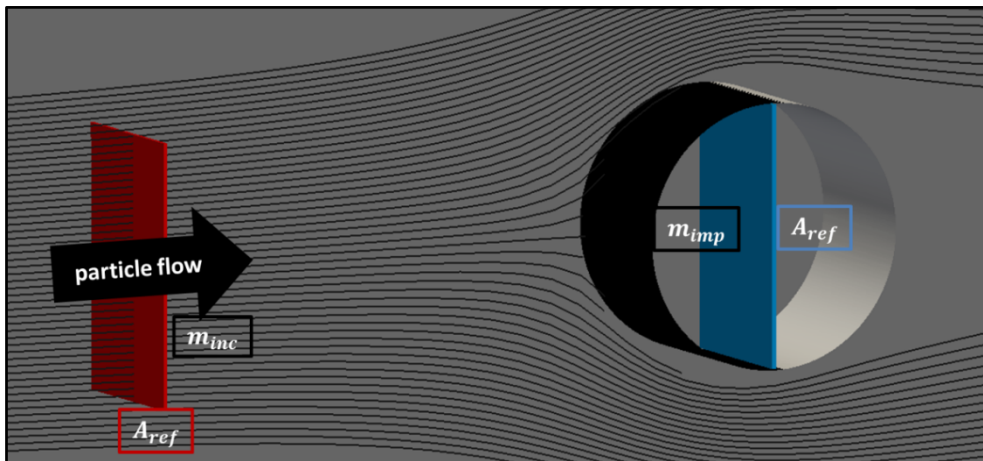


Figure 126. Scheme of the  $\eta_1$  evaluation.

The control surface for the incoming mass is placed at a distance of  $2 \cdot d_{cyl}$  from the stagnation point, where the flow velocity is uniform (Figure 127). Moreover, black streamlines show how the air flow is not deflected by the cylinder.

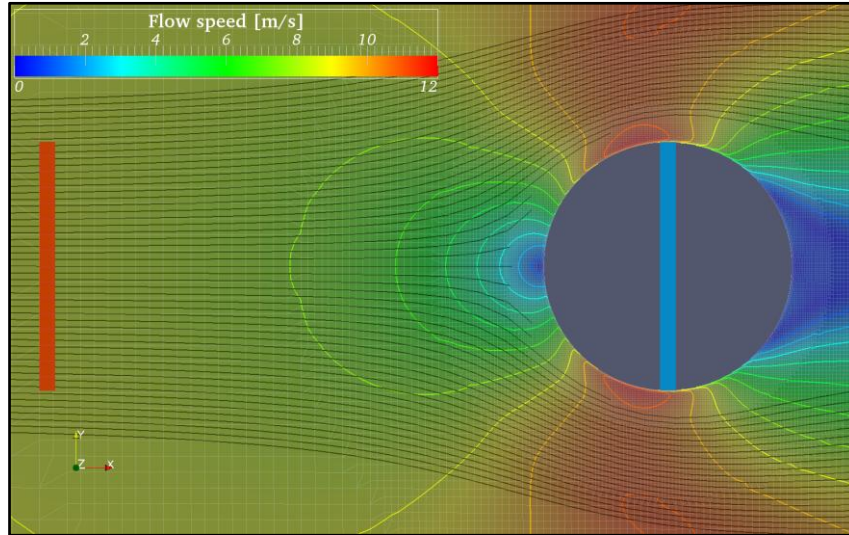


Figure 127. Location of the control surface,  $d_{cyl} = 315mm$ .

Table 16 reports the simulation results obtained for the three cylinders tested during the experimental campaign. To ensure the validity of the dispersion numerical model, the results are compared with the ISO standard formulation [3]. Table 16 confirms the accuracy of the setup: the results are in accordance. Moreover, this shows that the  $k - \varepsilon$  anomaly on the turbulence production  $k$  does not influence the collision efficiency.

Table 16. Collision efficiency

| $d_{cyl} [mm]$ | $\eta_1 k - \varepsilon$ | $\eta_1 k - \omega SST$ | $\eta_1 ISO$   |
|----------------|--------------------------|-------------------------|----------------|
| 50             | $\approx 0.93$           | $\approx 0.94$          | $\approx 0.94$ |
| 200            | $\approx 0.81$           | $\approx 0.82$          | $\approx 0.81$ |
| 315            | $\approx 0.73$           | $\approx 0.74$          | $\approx 0.74$ |

Table 16 shows that for a larger cylinder, the collision efficiency decreases. A large cylinder is less subjected to collect incoming particles. As a consequence, the interaction between particles and the flow surrounding the cylinders plays a role on the accretion process. Generally speaking, this analysis also justifies the necessity of a numerical approach which model the flow around a structure, in order to assess the collision efficiency for any kind of structure.

This part of the chapter has presented the method to assess the collision efficiency for the three cylinders tested in the experimental campaign. The results obtained with the numerical approach will allow to study the experimental accretions, through the coefficient  $\beta_{exp}$ , independently from the influence of the flow around the cylinders on the particles. To analyze how the flow surrounding a cylinder acts on a particle, here after is presented an analysis of the collision efficiency linked to the Stokes number.

### 5.2.1 Relation between Stokes number and collision efficiency.

As supposed in chapter three and confirmed in this chapter, the collision efficiency is linked to the particle behavior close to the cylinders. In this work, it has

been proposed a Stokes number to estimate how particles behave close to the cylinders (48). The reference particle diameter is  $d_p = 260\mu m$ .

$$St_{cyl} = \frac{\tau_p}{\tau_{cyl}} \quad (101)$$

Where  $\tau_p \approx 0.1s$  is the particle relaxation time and  $\tau_{cyl} = \frac{d_{cyl}}{\langle u_f \rangle}$  the characteristic time of the flow with respect to the cylinder.  $\tau_{cyl}$  is evaluated as the ratio between the cylinder diameter  $d_{cyl}$  and the mean flow velocity  $\langle u_f \rangle = 9m/s$ . In Table 17 is reported the particle  $St_{cyl}$  associated to the cylinders with the corresponding collision efficiency  $\eta_1$ .

Table 17. The evaluation of  $St_{cyl}$  and the associated  $\eta_1$ .

| $d_{cyl}$ [mm] | $St_{cyl}$    | $\eta_1$ k - $\omega$ SST |
|----------------|---------------|---------------------------|
| 50             | $\approx 18$  | $\approx 0.94$            |
| 200            | $\approx 4.5$ | $\approx 0.82$            |
| 315            | $\approx 3$   | $\approx 0.74$            |

When the  $St_{cyl}$  increases, the collision efficiency increases as well. At the same time, an increase of  $St_{cyl}$  means that a particle of the same diameter has a larger inertial behavior facing a smaller cylinder. Hence, a large collision efficiency is the consequence of a larger inertial behavior of particles facing a smaller cylinder. In this case, the particles have more chance to reach the cylinders.

In Figure 128 is proposed a scheme to illustrate the relation between  $St_{cyl}$  and the collision efficiency  $\eta_1$ . The reference particle diameter is the  $d_p = 260\mu m$ .

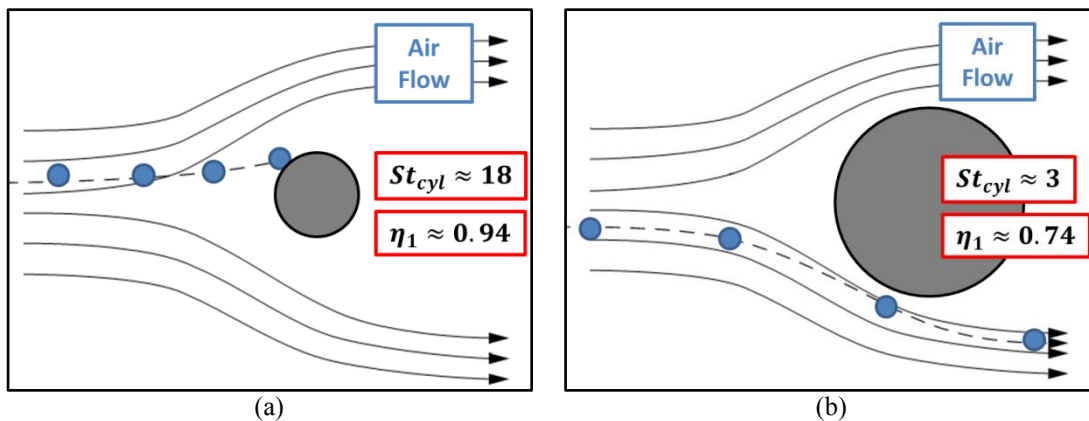


Figure 128.  $St_{cyl}$  concept (a) high  $St_{cyl}$ , (b) low  $St_{cyl}$ .

To study the relation between  $St_{cyl}$  and the collision efficiency  $\eta_1$ , the Stokes number  $St_{cyl}$  has been evaluated for each class diameter, of the particle size distribution injected. This evaluation has been performed for the three cylinder diameters. A focus of the result is presented in Figure 129.

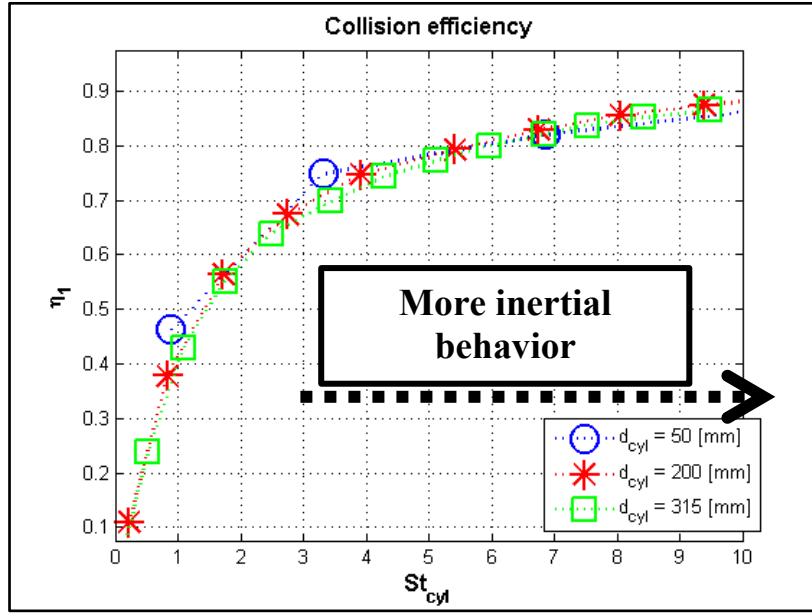


Figure 129. Collision efficiency  $\eta_1$  as a function of  $St_{cyl}$ .

One can see in Figure 129 that the curves calculated for each cylinder collapse in one single “universal” curve. It is possible to evaluate the collision efficiency of the cylinder starting from this curve. One has to integrate the curve, weighting the collision efficiency by the particle size distribution injected as following (102):

$$\eta_1 = \int_{d_p \min}^{d_p \max} \eta_1(St_{cyl}) \cdot PSD^v(d_p) \cdot dd_p \quad (102)$$

Let us consider the values of  $\eta_1(St_{cyl})$  for the smaller cylinder. In Table 18 is reported the evaluation of  $\eta_1$  according to equation (102).

Table 18. Collision efficiency evaluation with equation (102).

| $d_p$ [mm]            | $St_{cyl}$ | $\eta_1(St_{cyl})$ | $PSD^v(d_p)$    |
|-----------------------|------------|--------------------|-----------------|
| 40                    | 0.9        | $\approx 0.46$     | $\approx 0.013$ |
| 80                    | 3.3        | $\approx 0.75$     | $\approx 0.522$ |
| ...                   | ...        | ...                | ...             |
| 480                   | 53         | $\approx 0.96$     | $\approx 0.567$ |
| 520                   | 60         | $\approx 0.95$     | $\approx 0.583$ |
| $\eta_1 \approx 0.94$ |            |                    |                 |

Considering a large span of  $St_{cyl}$  values corresponding to a large distribution of particle size, an approximate methodology would be, to use the generic curve of Figure 129 together with a particle distribution of size, in order to compute the collision efficiency  $\eta_1$  without need to perform a numerical simulation.

The numerical simulations have also allowed to evaluate the particle size distribution  $PSD^v$  of the snow flux which has reached the three cylinders. Moreover, the

global liquid water content  $LWC_g$  associated to that snow mass can be estimated by the  $PSD^v$ . The evaluation of  $LWC_g$  allows to analyze the experimental results, via the coefficient  $\beta_{exp}$ , as a function of the liquid water content. The evaluation of  $PSD^v$  and  $LWC_g$  is presented below.

### 5.2.2 Particle size distribution on the cylinders and the resulting liquid water content

The particle distributions on size are evaluated as seen in previous chapter (103). The distribution is evaluated in volume of particles.

$$(PSD^v)_i = \frac{(d_p)_i^3 \cdot n_i}{\sum_i (d_p)_i^3 \cdot n_i} \quad (103)$$

Where  $d_p$  is the particle diameter of the  $i$  class and  $n_i$  is the number of particles which have impacted the cylinder. In Figure 130 is reported a comparison between the  $PSD^v$  injected and the  $PSD^v$  of particle which have impacted the three cylinders. As seen before, the small particles have a small inertia and they are more likely to be deviated by the air stream away from the cylinders.

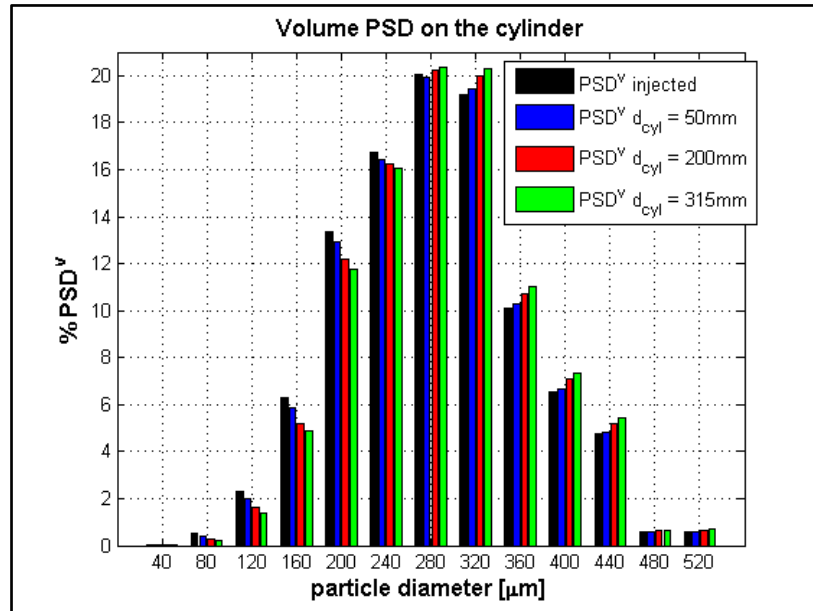


Figure 130.  $PSD^v$  comparison

The numerical model presented in chapter four has provided the liquid water content of each particle class:  $LWC_i = \mathcal{F}(T_a)$  at the cylinders location. To evaluate the global liquid water content of the particle mass on the cylinder surface, the  $LWC_i$  of each particle class is weighed by the particle size distributions on size evaluated above (93)

$$LWC_g = \frac{\sum LWC_i \cdot (PSD^v)_i}{\sum (PSD^v)_i} \quad (104)$$

Let us consider as example (Table 19), the values of  $PSD^v$  of particles which have respectively impacted the cylinder  $d_{cyl} = 50mm$  and  $d_{cyl} = 315mm$ . The  $LWC_i$  for an ambient temperature  $T_a = -9^\circ C$  for each particles diameter class is also reported.

Table 19. Example of  $PSD^v$  and  $LWC_i$  used for  $LWC_g$  evaluation.

| $d_p$      | $\%PSD^v d_{cyl} = 50mm$ | $\%PSD^v d_{cyl} = 315mm$ | $LWC T_a = -9^\circ C$ |
|------------|--------------------------|---------------------------|------------------------|
| $40\mu m$  | 0.0630                   | $9.6e^{-4}$               | $\approx 0$            |
| $80\mu m$  | 0.3959                   | 0.1940                    | $\approx 0$            |
| $120\mu m$ | 2.0215                   | 1.4056                    | $\approx 0$            |
| $160\mu m$ | 5.8840                   | 4.8524                    | $\approx 0$            |
| $200\mu m$ | 12.8951                  | 11.7569                   | $\approx 9e^{-4}$      |
| $240\mu m$ | 16.4433                  | 16.0525                   | $\approx 0.1284$       |
| $280\mu m$ | 19.9497                  | 20.3292                   | $\approx 0.2710$       |
| $320\mu m$ | 19.4534                  | 20.3160                   | $\approx 0.3858$       |
| $360\mu m$ | 10.2710                  | 11.0159                   | $\approx 0.4617$       |
| $400\mu m$ | 6.6674                   | 7.3218                    | $\approx 0.5130$       |
| $440\mu m$ | 4.8374                   | 5.4118                    | $\approx 0.5714$       |
| $480\mu m$ | 0.5772                   | 0.6557                    | $\approx 0.6148$       |
| $520\mu m$ | 0.5977                   | 0.6873                    | $\approx 0.6587$       |
| $Tot \%$   | 100                      | 100                       |                        |
| $LWC_g$    | $\approx 0.31$           | $\approx 0.33$            |                        |

Figure 131 shows the global liquid water content of particle mass for the three cylinders, as a function of the ambient temperature. As one can observe, the global liquid water content for a smaller cylinder, is always lower than the one for a larger cylinder. For a smaller cylinder, small particles (characterized by a low  $LWC$ ) are more subjected to reach its surface. As a consequence, small particles which have a very small  $LWC$  have contribute more to the global liquid water content. This leads to a lower  $LWC_g$ .

Additionally, Figure 131 shows the global liquid water content curve evaluated in chapter four (black curve - Figure 131). This  $LWC_g$  is evaluated for a particle mass which reaches the cylinder location without being influenced by the cylinder flow. As one can see, this curve is underneath the three others due to the fact that, no particle is deviated by the flow around the cylinders.

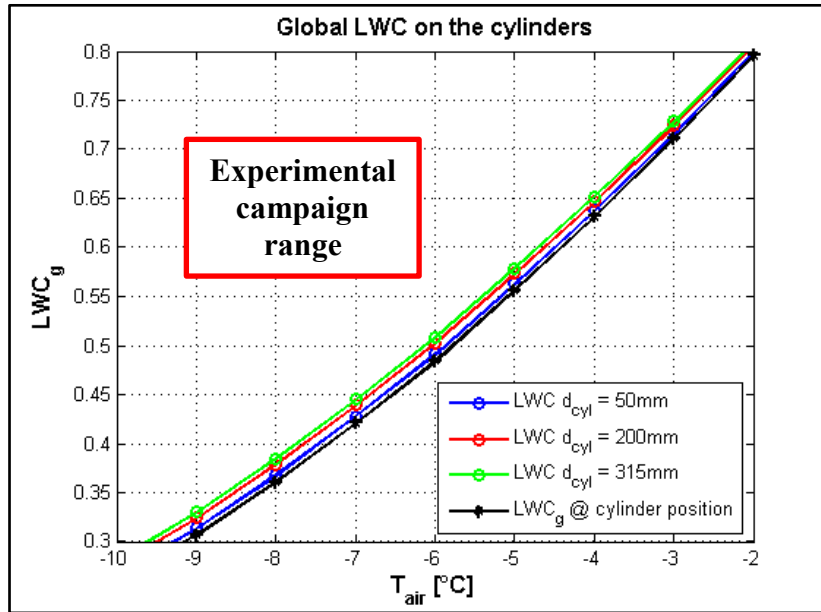


Figure 131.  $LWC_g$  for the three cylinders: a comparison.

The evaluation of a global liquid water content for the three cylinders, will be used in the next paragraph to analyze the experimental coefficient  $\beta_{exp}$ .

### 5.2.3 Collision efficiency evaluation: conclusions.

This part of the chapter has concerned the evaluation of the collision efficiency  $\eta_1$  and the global liquid water content of the mass impacting the cylinders. The collision efficiency increases when the Stokes number based on the cylinder diameter increases. The collision efficiency allows here after, to study the experimental coefficient  $\beta_{exp}$  without taking into account the effect of the flow around the cylinders on particle deposition. The analysis will be undertaken as a function of the global liquid water content.

Moreover, the procedure proposed, can be applied to evaluate the collision efficiency for objects of different forms. For the simple shapes of cylinders, the simplified approach proposed in the literature is accurate enough.

## 5.3 Quantification of the collision efficiency impact on the experimental coefficient $\beta_{exp}$ .

The dimensionless parameter  $\beta_{exp}$ , proposed in chapter three, takes in account the three aspects of the accretion process (aerodynamic, mechanical and thermal) (105).

$$\beta_{exp}^{123} = \eta_1 \cdot \eta_2 \cdot \eta_3 = \mathcal{F}(d_{cyl}, LWC_g) \quad (105)$$

Where  $\eta_1$  represent the collision efficiency,  $\eta_2$  the sticking efficiency and  $\eta_3$  the accretion efficiency. The first coefficient is related to the influence of the flow around the cylinder on the incoming particles. In Table 20 are reported the three coefficients  $\eta_1$  for the cylinders.

Table 20. Collision efficiency

| $d_{cyl}$ [mm] | $\eta_1 k - \omega SST$ |
|----------------|-------------------------|
| 50             | $\approx 0.94$          |
| 200            | $\approx 0.82$          |
| 315            | $\approx 0.74$          |

Through the collision efficiency  $\eta_1 = \mathcal{F}(d_{cyl})$ , evaluated numerically, it is possible to discern the aerodynamic aspect from the coefficients  $\beta_{exp}$  evaluated during the experimental campaign (106).

$$\beta_{exp}^{23} = \eta_2 \cdot \eta_3 = \frac{\beta_{exp}^{123}}{\eta_1} = \mathcal{F}(LWC_g) \quad (106)$$

The accretion efficiency  $\eta_3$  is defined as the ratio of the global mass flux of the accretion to the global mass flux of particles which reach and stick on the cylinder. If all particles which stick on the cylinder contribute to the accretion, the coefficient  $\eta_3$  will be equal to one (Figure 132.a). When the accretion efficiency is lower than one, a part of the particles which stick on the cylinder, does not contribute to the accretion.

Following previous accretion models (Messinger [4], Guffond [5], Makkonen [6] or the ISO 12494 standard [3]), in case of  $\eta_3 < 1$  the liquid part of the particles stuck on the cylinder, does not freeze completely. Then, the liquid part not frozen, is supposed to flow along the cylinder surface and finally drips away. These assumptions are commonly made in case of icing phenomena (Figure 132.b), where the solid part of particles is not taken into account. A first attempt of modelisation has been made in this work to take into account this phenomenon. It was based on a model developed at ONERA (Guffond [5]) for liquid droplets impacting airfoils. As the particles in the present work presented a mixed phase, a decomposition for  $\eta_3$  between the liquid and solid part was applied.  $\eta_3$  for solid part was assumed equal to one, while  $\eta_3$  for liquid part was computed using the ONERA model. The results led to a very different results from the ones observed during the experimental campaign.

For wet snow accretion (characterized by a mixture of ice and water), the behavior estimation of the liquid part not frozen is quite difficult (Makkonen [6]). Due to the porosity of the snow accretion, the liquid part can be soaked by the accretion, instead of drip or flow away (Figure 132.c). If all the liquid part is soaked, it contributes to the accretion even though it is not frozen. In this case, the global accretion efficiency  $\eta_3$  is equal to one.

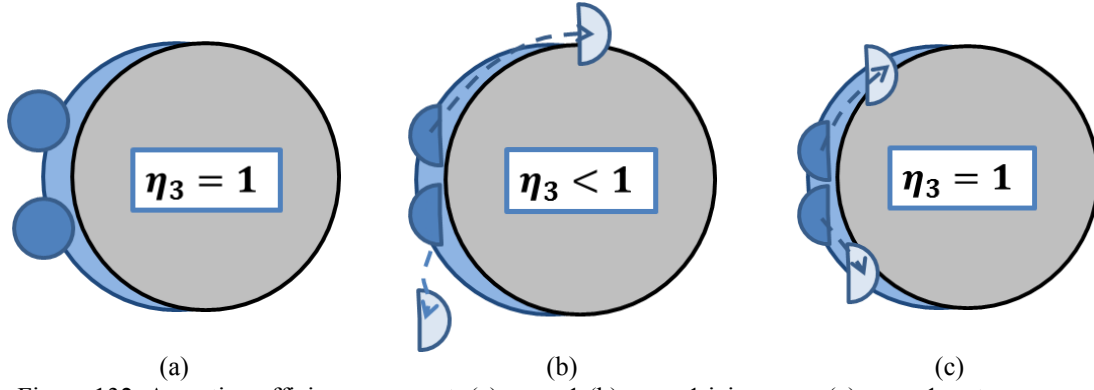


Figure 132. Accretion efficiency concept: (a)  $\eta_3 = 1$  (b)  $\eta_3 < 1$  icing case, (c)  $\eta_3 = 1$  wet snow case.

During the experimental campaign, we did not observe any noticeable drip or shed of water from the cylinders. Moreover, observing the accretions obtained, it has been noticed a certain amount of water trapped into accretions (Figure 133).

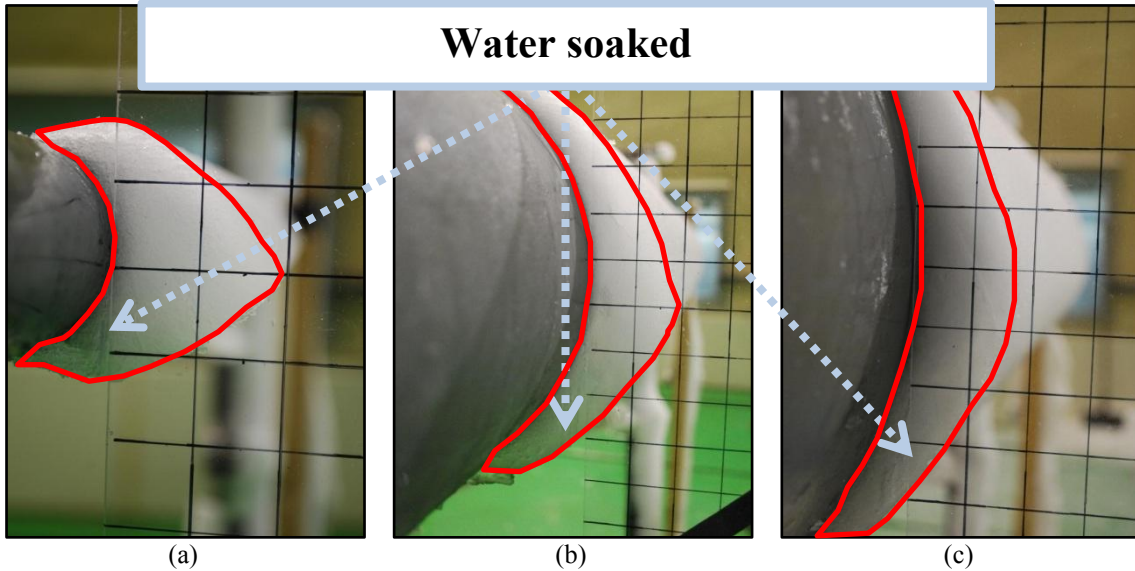


Figure 133. Accretions at  $T_a = -3^\circ\text{C}$ : (a)  $d_{cyl} = 50\text{mm}$  (b)  $d_{cyl} = 200\text{mm}$  , (c)  $d_{cyl} = 315\text{mm}$  .

As a consequence, it seems that to model the wet accretion, the modelisation efforts have to be focused on the sticking efficiency  $\eta_2$  rather than  $\eta_3$ . As a first attempt it is here proposed to take as hypothesis  $\eta_3 = 1$  in accordance with the experimental observations. It is then proposed to deduce a coefficient  $\beta_{exp}^{23}$  from the experimental measurements and the numerical assessment of  $\eta_1$ :(107)

$$\beta_{exp}^2 = \eta_2 = \frac{\beta_{exp}^{123}}{\eta_1} = \mathcal{F}(LWC_g) \quad (107)$$

As reported in Figure 134, the sticking coefficient increases with the increase of the liquid water content of particles that reach the cylinders. This means that particles are more likely to stick on the cylinders in case of high  $LWC_g$ . One can see from Figure 134 that the sticking efficiency  $\eta_2$  is close to  $\approx 0$  when the global liquid water content is almost 0.3. The maximum  $\eta_2$  measured during the experimental campaign corresponds to  $LWC_g \approx 0.7$ . Moreover, Figure 134 shows also that the differences

between the sticking efficiency of the three cylinders increase with the increase of the global liquid water content.

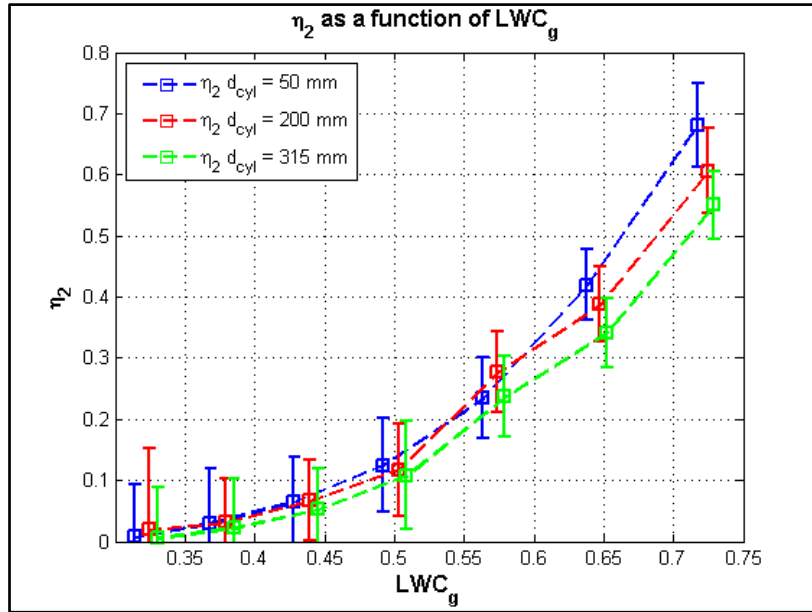


Figure 134.  $\eta_2 = \mathcal{F}(LWC_g)$ .

The three curves  $\eta_2 = \mathcal{F}(LWC_g)$  cannot be considered as a unique curve. If one can suppose that the differences is related to experimental errors which influence  $\beta_{exp}^{123}$ , on the other hand, one can assume that the sticking efficiency is not only a function of the global liquid water content. Hence, the aerodynamic impact on the accretion is not only related to the collision efficiency, but also to the sticking efficiency.

#### 5.4 Quantification of modeled accretion shapes

The numerical simulations which have been performed to compute the global collision efficiency  $\eta_1$  also allows to evaluate the shapes of the accretions. The accretion shape is first evaluated by considering that all the impacting mass sticks on the cylinder surface ( $\eta_2 = 1$ ).

The accretion shape estimation is based on the evaluation of the local collision efficiency. This coefficient is defined by equation (100) applied to each cylinder sector.

The local collision efficiency is defined as the ratio between the mass flux impacting a sector of the cylinder:  $\dot{m}_{imp\ local}$  and the incoming mass flux upstream the cylinder:  $\dot{m}_{inc}$  (Figure 135). This last one is evaluated as seen before, while  $\dot{m}_{imp\ local}$  follows equation (108).

$$\dot{m}_{imp\ local} = \frac{\dot{m}_{imp\ local}}{A_{ref\ local} \cdot t} \quad (108)$$

Hence the local collision efficiency can be estimated as (109).

$$\eta_1^{local}(\varphi) = \frac{\dot{m}_{imp}(\varphi)}{\dot{m}_{inc}} \quad (109)$$

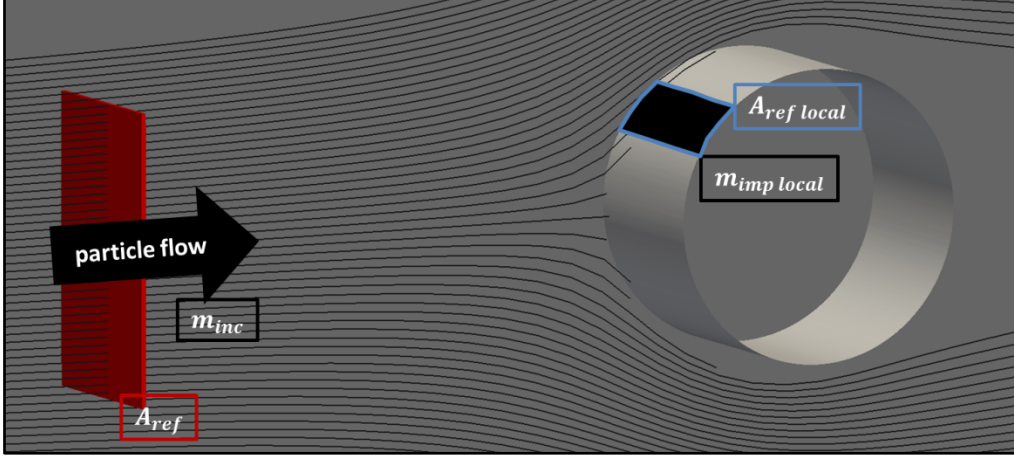


Figure 135. Scheme of the  $\eta_1$  local evaluation.

An accretion shape  $acc_{shape}(\varphi)$  is evaluated with the local collision efficiency. It represents the displacement of the cylinder surface due to the accretion. The displacement of the accretion surface is assumed normal to the cylinder surface ( $\vec{n}$ ). Thus  $acc_{shape}(\varphi)$  can be written as:

$$acc_{shape}(\varphi) = \eta_1^{local}(\varphi) \cdot \delta_{acc} \cdot \vec{n} \quad (110)$$

Where  $\delta_{acc}$  is a coefficient used to tune the accretion growth. If one wants to calculate the exact accretion shape, then  $\delta_{acc} = \frac{\dot{m}_{imp}(\varphi)}{\rho_{snow}} \cdot t$  where  $\rho_{snow}$  is the accretion density in  $\frac{kg}{m^3}$ . If one considers steady simulations for the flow and lagrangian calculations,  $\delta_{acc}$  can be chosen independently from any time consideration. However, if  $\delta_{acc}$  is too large it can lead to an overestimated growth of the accretion and hence induce the instability of the loop. As a consequence,  $\delta_{acc}$  has to be chosen to produce a representative growth for each step of the loop without compromising the stability of the coupling.

Let us consider the upper part of the cylinder  $d_{cyl} = 50mm$ . In Figure 136 is reported an example of the approach undertaken to evaluate the accretion shape. Figure 136.b reports only five angles, while the computation has been almost performed every five degrees. The number of elements along the cylinder surface is linked to the mesh obtained in the numerical simulations. The example concerns the first step of modeling.

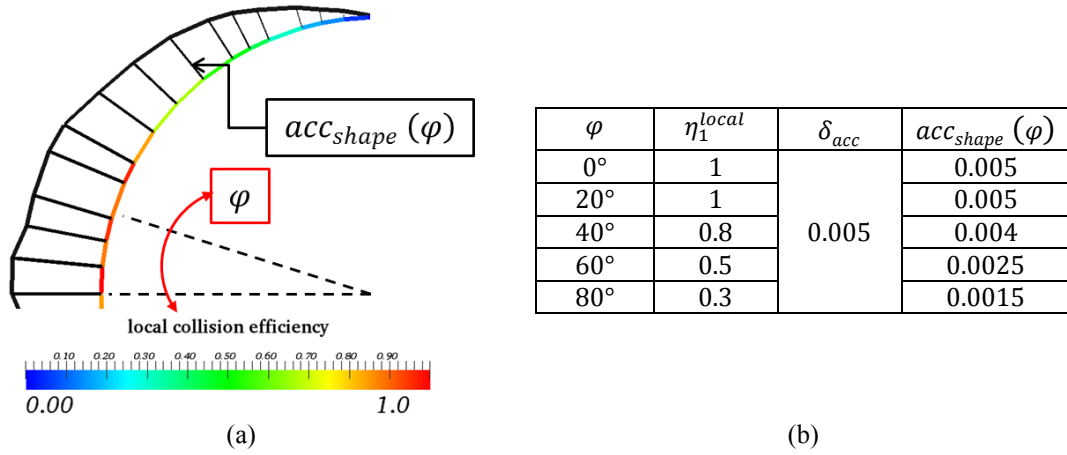


Figure 136.  $acc_{shape}(\varphi)$  concept (a) a scheme, (b) an evaluation example.

Figure 137 shows the result for the three cylinders. As one can see this approach leads to the same shape for the three cylinders.

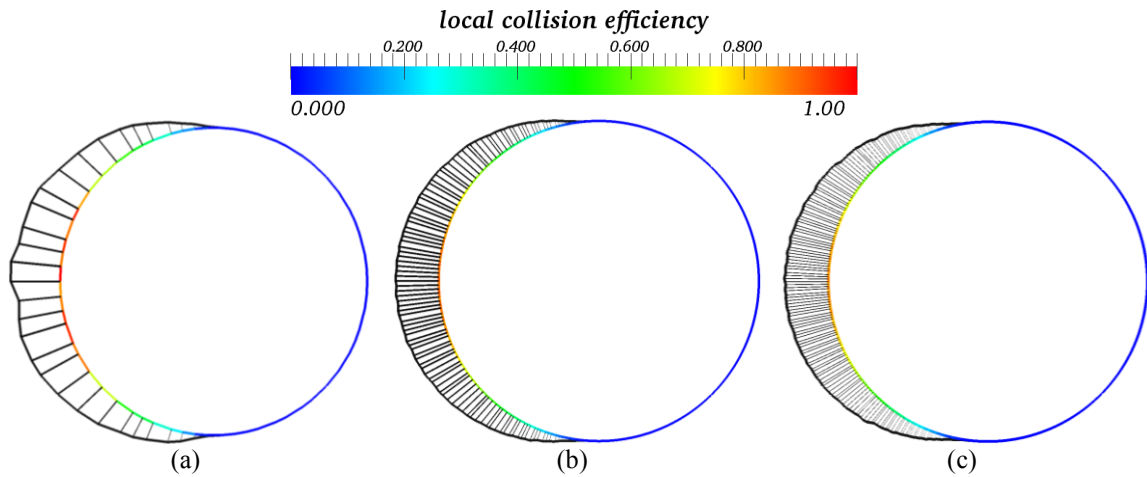


Figure 137. Accretion shapes: (a)  $d_{cyl} = 50mm$  (b)  $d_{cyl} = 200mm$  , (c)  $d_{cyl} = 315mm$ .

With the accretion shape obtained, a new numerical computation of the flow around each cylinder has been performed. The methodology for the numerical computation is exactly the same as the one presented previously. Once the aerodynamic computation has reached convergence, the particles are injected to obtain a new local collision efficiency (Figure 138).

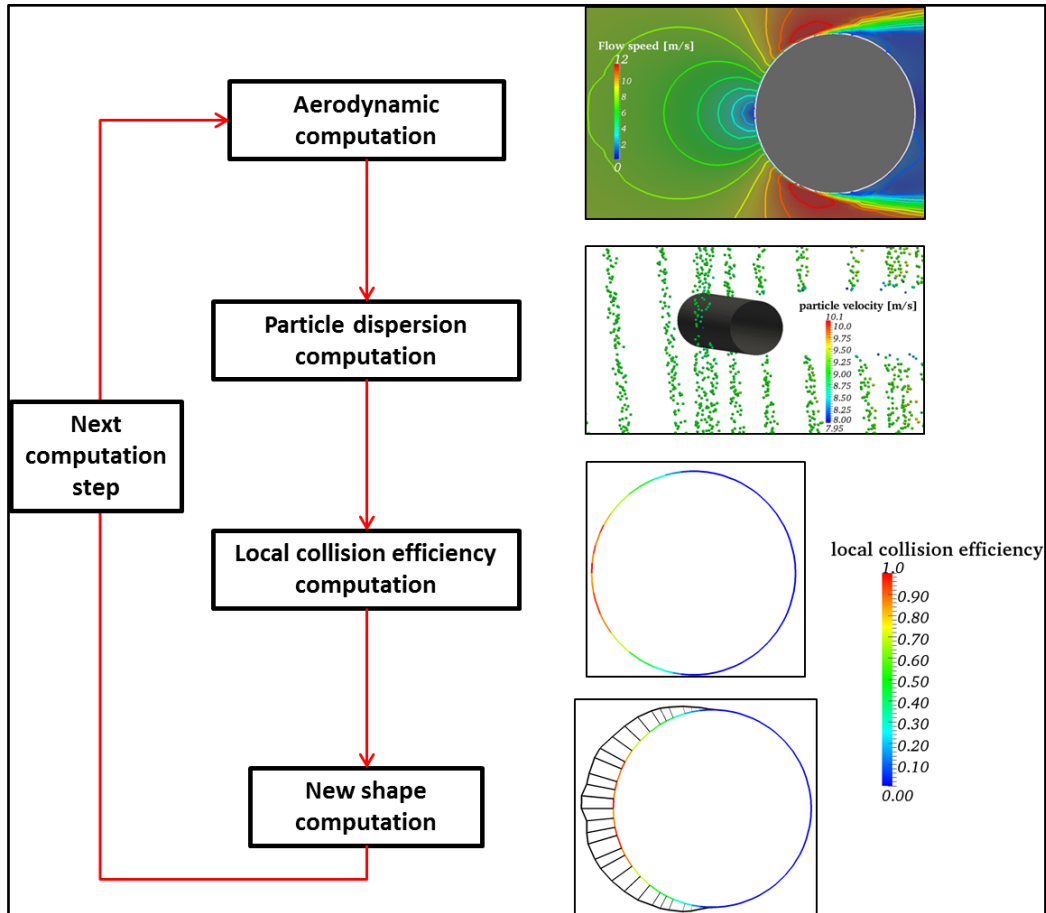


Figure 138. Loop undertaken to compute the accretion shape.

As one can see from Figure 138 the computation procedure associates the aerodynamic evaluation of the flow around the cylinder and the lagrangian particle dispersion model. The result of the aerodynamic computation influences the particle dispersion result which determines the accretion shape. The new shape is then used to perform an updated aerodynamic computation. The present coupling considers a “steady” approach for both the flow and the lagrangian computation. As a consequence, there is no real duration associated to each loop. Thus the accretion coefficient  $\delta_{acc}$  has been kept constant for each step and chosen to obtain a significant growth without compromising the stability of the coupling.

Let us consider the cylinder of diameter  $d_{cyl} = 50mm$ . As one can see from Figure 139, the shape of accretion obtained after three computational steps does not correspond to the one obtained during the experimental campaign.

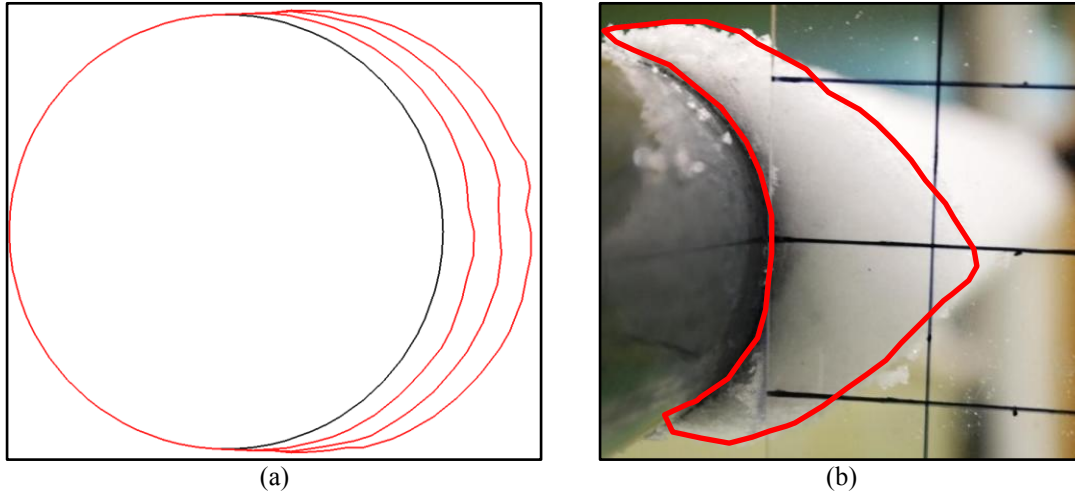


Figure 139. Accretion shape (a) model result, (b) experimental result.

The approach proposed does not reproduce correctly the ogival shape of the experimental accretion. Focusing on the sticking coefficient one can see that the hypothesis of  $\eta_2 = 1$  is not applicable to wet snow accretions. The literature review reports an approach to model the sticking efficiency  $\eta_2$  as a function of the angle of impact between the particle and the surface. This approach, proposed by Trenker et al. [7, 8], is applied to our case in the next paragraph. The Trenker approach takes also into account the friction velocity of particles when impacting the surface. In the analysis here after presented, this condition is not considered.

## 5.5 Sticking efficiency as a function of the particle-surface angle of impact

This part of the chapter aims at investigating how a sticking coefficient based on the particle-surface angle of impact can correctly reproduce the experimental accretion shapes. The first part of the paragraph explains the theoretical approach, while the second part exposes the results obtained.

### 5.5.1 Theoretical implementation of the angle criterion and application to the experimental cases.

The Trenker sticking criterion is based on two assumptions. A particle sticks on the surface only if the angle between the surface normal and the particle trajectory direction is lower than a threshold angle. This angle in the works of Trenker is assumed equal to  $45^\circ$ . This condition is coupled with a friction velocity  $u_\tau$  on the surface which must be lower than  $0.21m/s$ .

When the particle does not stick on the surface, it bounces away with an energy loss. The particle momentum is reduced to one percent along the normal direction  $M_p^{\perp'}$  and 20% along the tangential direction  $M_p^{\parallel'}$ . Owing to the momentum reduction induced by the impact, the particles would more likely creep along the surface instead of being deviated away from the surface as the result of an elastic bounce.

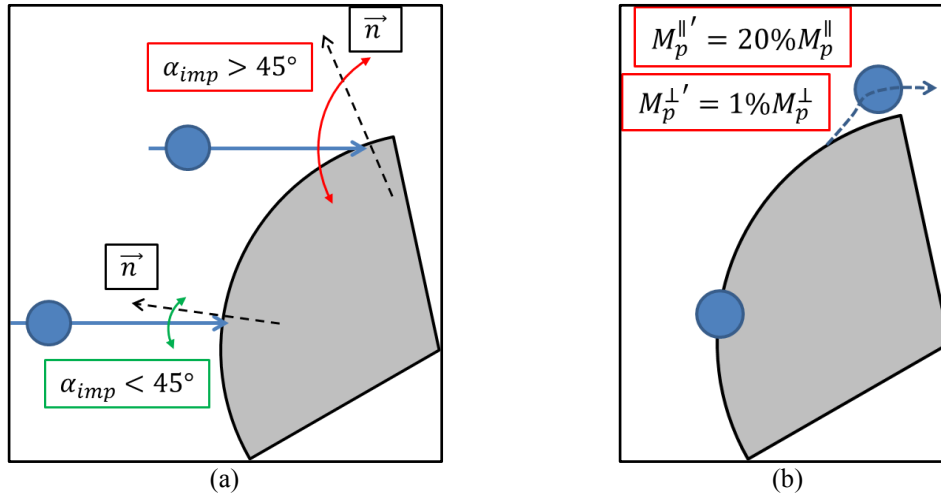


Figure 140. Trenker principle (a) angle of impact constraint, (b) particle behavior after impact.

The approach proposed by Trenker and implemented in this work is based on the angle of impact between the particle and the surface. No information were found in the literature to explain why the threshold angle was set to  $\alpha_t = 45^\circ$ . Hence, before applying the angle proposed by Trenker, a series of simulations for different  $\alpha_t$  have been performed. This allows to identify the best threshold angle in our case, to obtain an accretion shapes similar to the experimental one (Figure 141). The simulations of Figure 141 concern the cylinder of  $d_{cyl} = 50\text{mm}$ .

The simulations setup follows the same procedure seen before (Figure 140). The analysis is performed after 26 iterations which ensure a good representation of the accretion shape.

Figure 141 shows how the angle of impact between the particle and the surface strongly influence the accretion shape. The larger is the threshold angle, the larger is the accretion. Moreover, one can note that the simulation made with the angles  $\alpha_t = 20^\circ$  and  $\alpha_t = 30^\circ$  do not induce accretion shapes similar to the one observed in the experimental campaign. As a consequence, it is considered here after, a threshold angle:  $\alpha_t = 45^\circ$ .

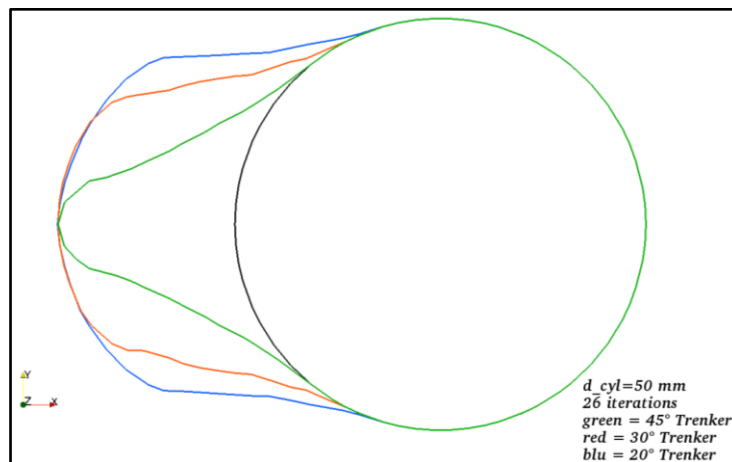


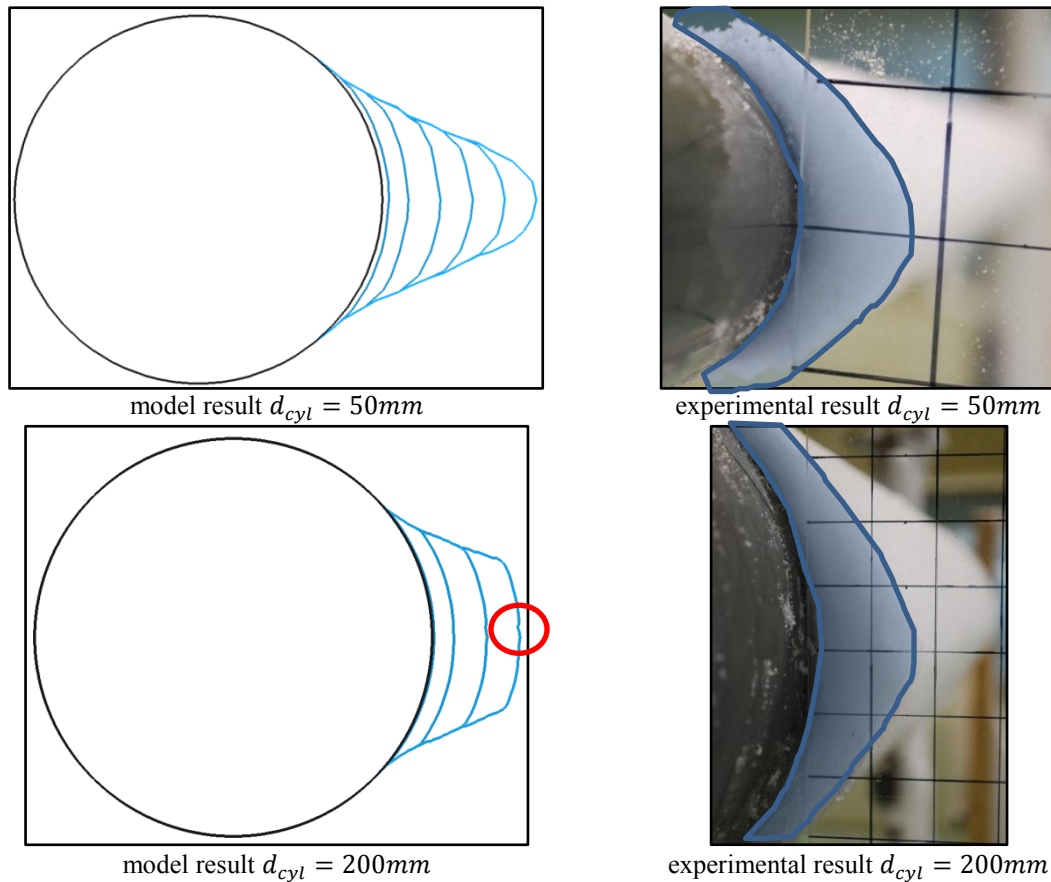
Figure 141. Accretion shapes at different threshold angles  $\alpha_t$ .

Figure 141 shows that a threshold angle  $\alpha_t = 45^\circ$  seems well adapted to our case, when a cylindrical object is tested. Anyhow, the literature does not offer any information about the suitability of  $\alpha_t = 45^\circ$  with other object shapes. One of the perspective of this work could be to test different object forms at different orientation with respect to the incoming snow flow. This will allow to validate if the threshold angle of  $\alpha_t = 45^\circ$  can be applied as one of the factor which influence the sticking efficiency.

### 5.5.2 Accretion shape obtained with a threshold angle $\alpha_t = 45^\circ$ .

Figure 142 shows the result of the approach undertaken to estimate the accretion shapes for the three cylinders. One can note that, the sticking efficiency linked to the particle-surface angle of impact induces an accretion shape more similar to the experimental one than the one obtained by imposing  $\eta_2 = 1$ . All the accretion shapes obtained are characterized by an ogival form in their central part. This characteristic has been observed for the experimental accretions for all the liquid water content tested.

The modeled accretions for the cylinder  $d_{cyl} = 200mm$  and  $d_{cyl} = 315mm$  does not reach a clear ogival shape. This is due to problems encountered while meshing the last shape obtained. For both the cases the last mesh was too coarse to perform the airflow computation. With red rounds, in Figure 142 are highlighted the point where meshing was impossible. Reducing the accretion coefficient  $\delta_{acc}$  did not solved the problem.



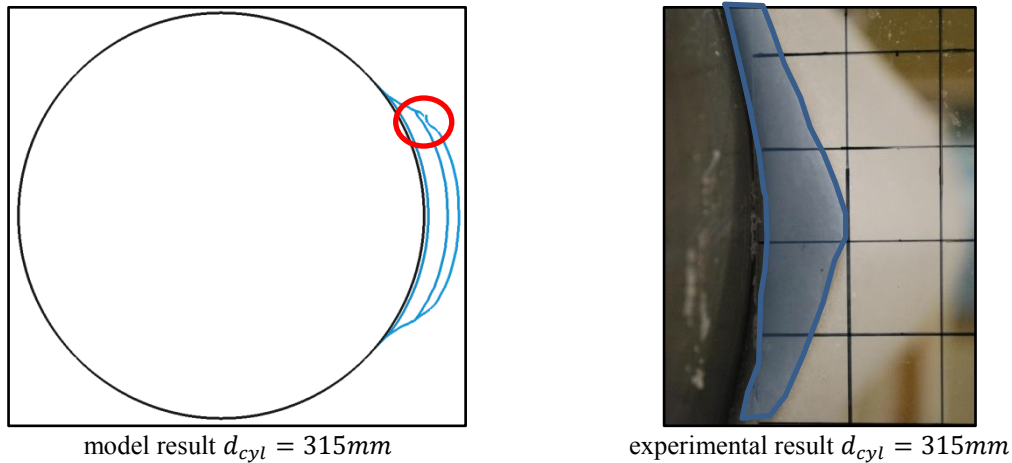
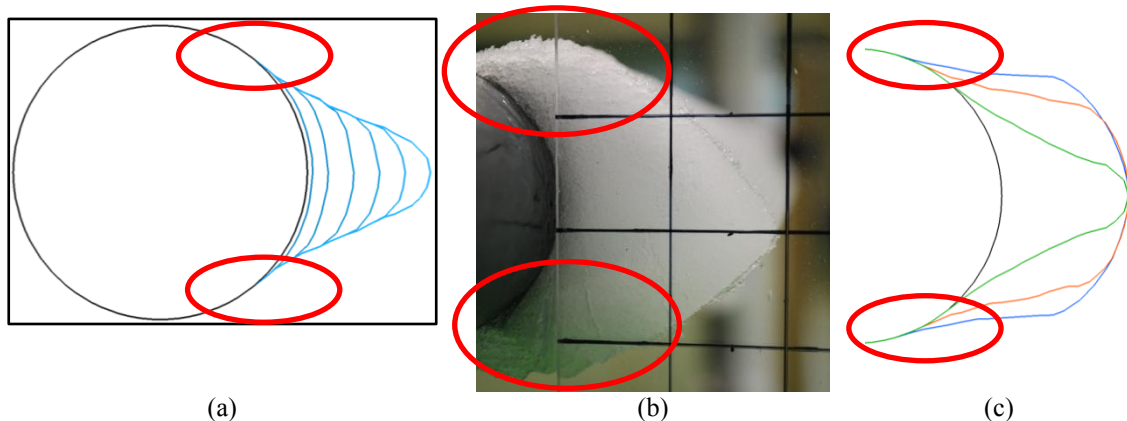


Figure 142. Accretion shapes obtained.

The angle criterion has improved the shape modeling, especially on the central part, but it fails on the upper and lower part of the cylinders. None of the threshold angles tested (Figure 143.c) is able to reproduce exactly these accretion parts. As a consequence, models only based on the angle criterion might not be sufficient to reproduce the accretion shape.

Figure 143. Accretion analysis of the upper and lower part of the cylinder  $d_{cyl} = 50mm$ : (a) numerical simulation  $\alpha_t = 45^\circ$  (b) experimental result, (c)  $\alpha_t = 20^\circ, 30^\circ$  and  $45^\circ$ .

As seen before, the loop used to model the accretion shape has three principal steps. The first one concerns the computation of the flow around the accretion. The second part concerns the lagrangian particle dispersion computation and the third part concerns the accretion evaluation. For each loop, a new dispersion computation is performed with a new accretion shape. As a consequence, for each loop, a new global collision efficiency is calculated which takes into account the new shape.

The next paragraph aims at the quantification of global collision efficiency evolution during the accretion process.

### 5.5.3 Accretion shape influence on the global collision efficiency $\eta_1$ .

A shape change means that the flow around the accretion is modified with respect to the one of a “clean” cylinder. In Figure 144 a comparison between the flow field around the cylinder  $d_{cyl} = 50mm$  (Figure 144.a) and the flow field for the last accretion step (Figure 144.b) is proposed. As one can note, the most important

differences concern the flow at the stagnation point. Due to the differences of the flow fields, particles are supposed to act differently whether they are close to the cylinder or the accretion.

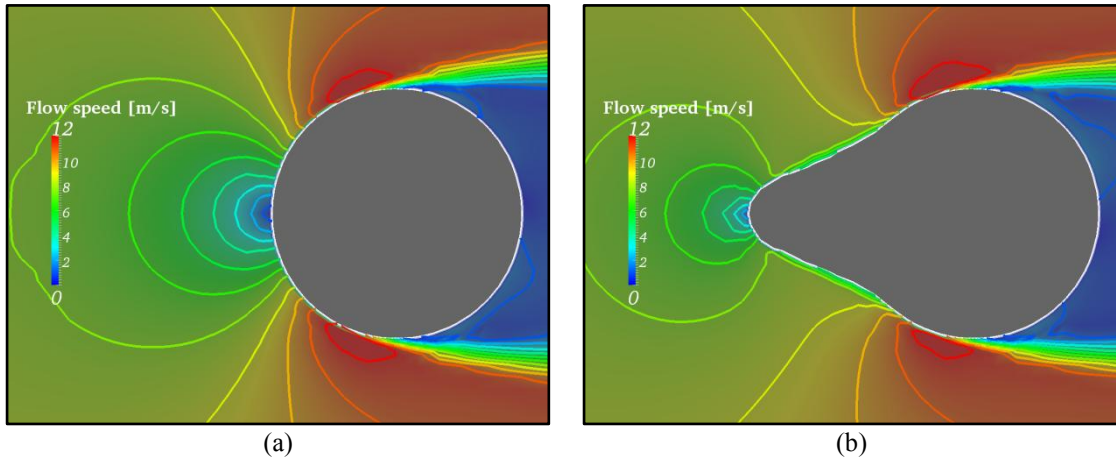


Figure 144. Flow fields (a) cylinder shape (b) accretion shape.

Figure 145.a shows the global collision efficiency evolution during the computational steps for the three cylinders. The coefficient definition is exposed in paragraph 5.3 (111).  $\dot{m}_{imp}$  represents the mass flux which impacts the accretion and  $\dot{m}_{inc}$  the incoming mass flux.

$$\eta_1 = \frac{\dot{m}_{imp}}{\dot{m}_{inc}} \quad (111)$$

As one can see, the coefficient shows a decrease for the three cases. The decrease is more evident for cylinder  $d_{cyl} = 50mm$  and  $d_{cyl} = 315mm$ . In Figure 145.b is reported the slope of  $\eta_1$  for the cylinder  $d_{cyl} = 50mm$ .

This decrease is due to the fact that the flow field around the accretion changes along the computational steps. The coefficient decreases because an ogival shape, is more streamlined and the particles are more likely to follow the flow instead of impact on the accretion surface.

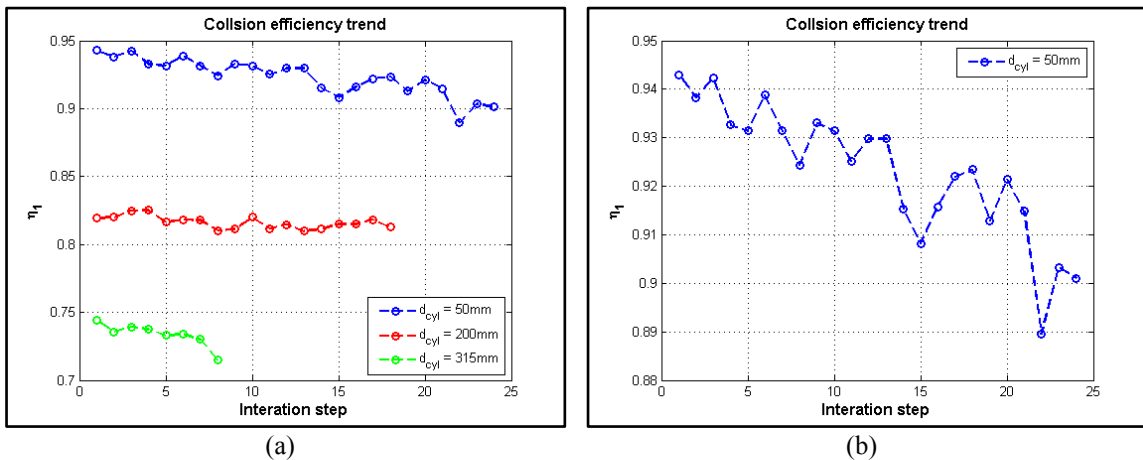


Figure 145. Global collision efficiency evolution (a) for the three cylinders, (b)  $d_{cyl} = 50mm$  zoom.

#### 5.5.4 Sticking efficiency evaluation for the experimental cases

The numerical simulations seems to confirm that the accretion shape depends on the angle between the particle path and the normal at the accretion surface. For each calculation loop, the mass flux of particles stuck on the surface  $\dot{m}_{stick}$  can be quantified as the ratio between the mass stuck per unit time and the reference area. The reference area  $A_{ref}$  follows the same definition seen for the impacting mass flux (Figure 126). This allow to evaluate the global sticking efficiency  $\eta_2$  during the accretion evolution (112).

$$\eta_2 = \frac{\dot{m}_{stick}}{\dot{m}_{imp}} \quad (112)$$

In Figure 146.a is reported in blue the mass which impacts the cylinder while in Figure 146.b is reported the mass which sticks applying the angle criterion. The figure below shows that the angle criterion reduces the mass stuck with respect to the impacting one. Anyhow, this reduction is too large with respect to what observed during the experimental campaign.

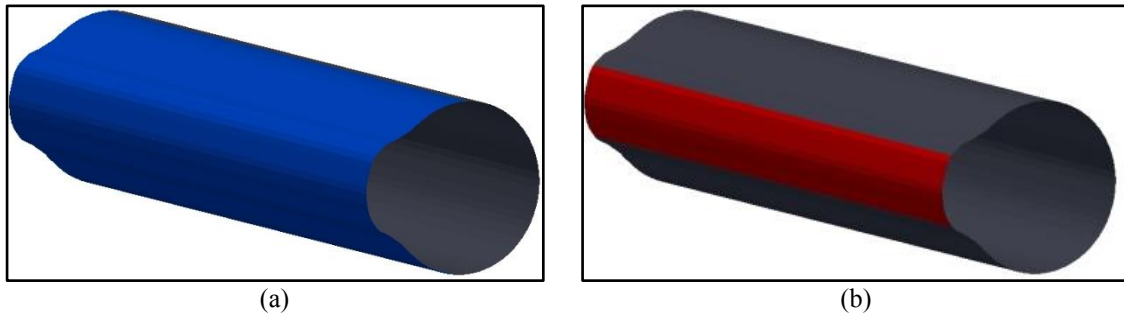


Figure 146. (a) impacted mass, (b) stuck mass

In Figure 147 is reported the sticking efficiency coefficient evaluated for the three cylinders at each loop of the computation. The curves end at the last step computed: due to the bad mesh quality, no other steps could be performed. One can note from Figure 147 that the coefficient seems to not depend on the cylinder diameter. The three curves presented seems to collapse to a single one. This is thus not linked to the cylinder diameter. It might however change if one considers a different object (means something else than a cylinder).

Figure 147 also shows a large decrease of the global sticking efficiency. This means that with the accretion growth, the mass which sticks on the accretion is lower and lower.

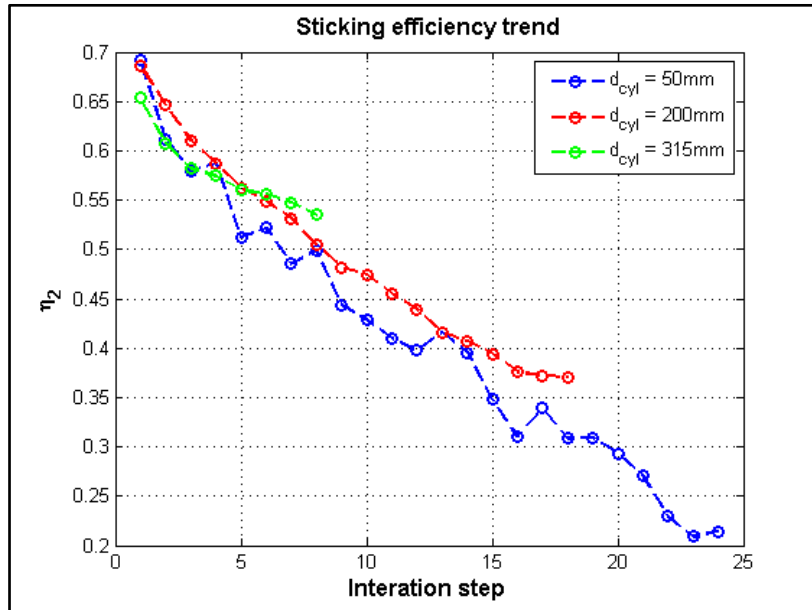
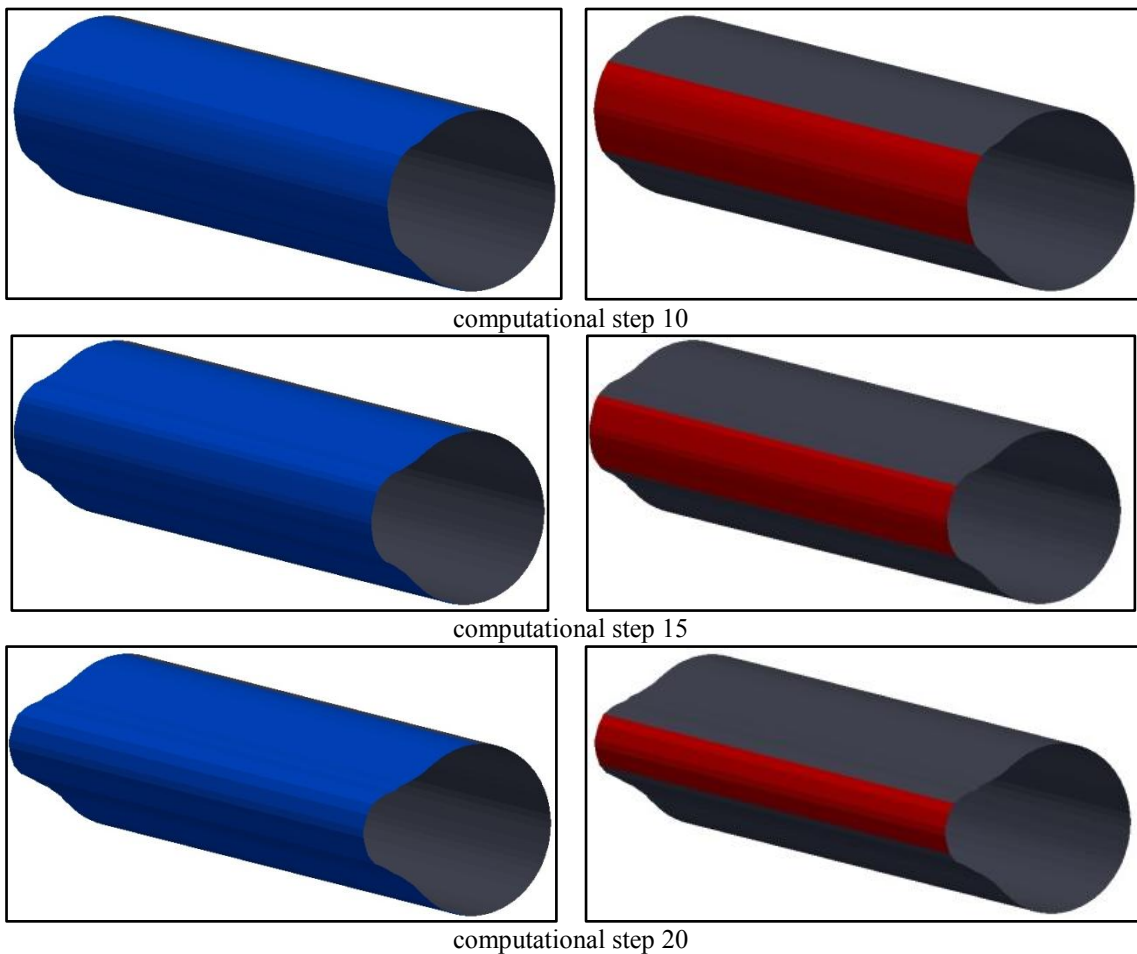


Figure 147. Sticking efficiency evolution at each loop

To study the decrease of the stuck mass, in Figure 148 is reported with the blue color the impacted mass and in red the mass which sticks on the surface for four steps of computation. The reference cylinder is  $d_{cyl} = 50\text{mm}$ . While the accretion shape becomes more ogival, less and less particles stick to it.



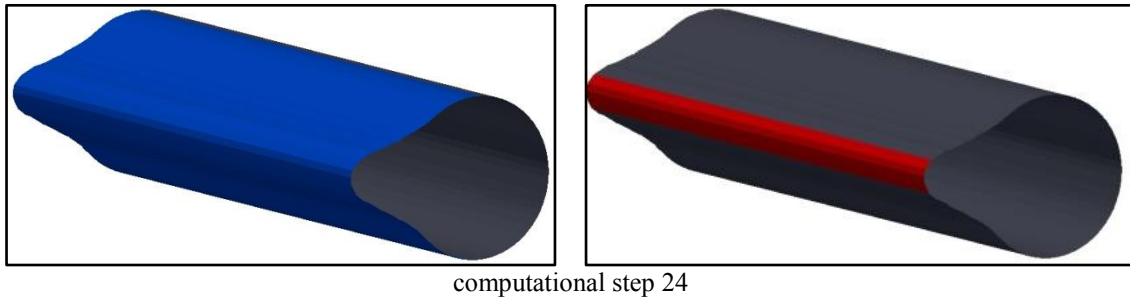


Figure 148. sticking analysis (left) impacted mass, (right) stuck mass.

The more the accretion develops, the more the angle of impact between a particle and the accretion surface increases. This means that, while the accretion grows, a larger number of particles impact on the accretion with an angle larger than the threshold angle  $\alpha_t = 45^\circ$ . As a consequence, fewer particles contribute to the accretion.

Let us consider two particles approaching the accretion at step 10 and 24 (Figure 149). The two particles have the same trajectory in both cases. For the step 10 the two particles impact the accretion with an angle lower than  $\alpha_t = 45^\circ$  (Figure 149 square 1 and 2). For the step 24 only one particle sticks on the accretion according to the angle criterion (Figure 149 square 4). The other one bounces away (Figure 149 square 3). This explains how the mass which sticks on the surface decreases with the accretion growth. When the accretion progresses its shape becomes sharpened. As a consequence, the number of particles which satisfy the angle criterion decreases with the accretion progress.

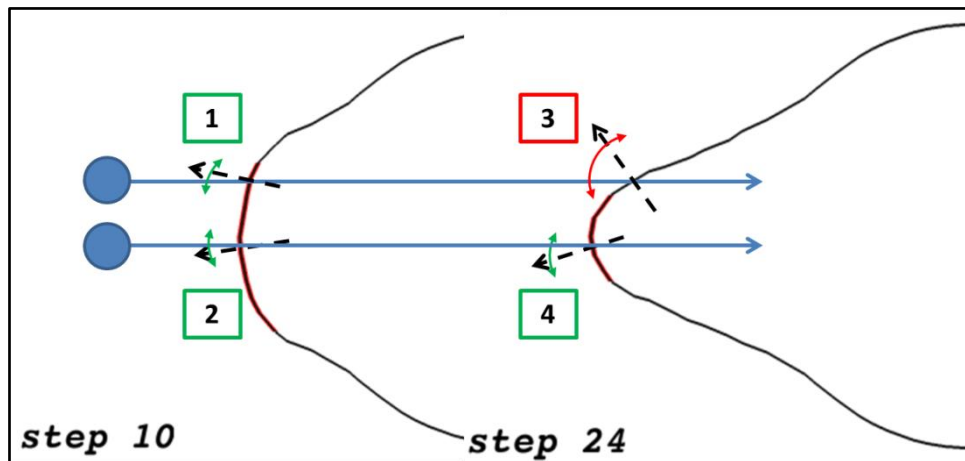


Figure 149. Accretion shape evolution linked to the angle criterion.

One can suppose that with this approach, the accretion evolution reaches a limiting stage when no more particles contribute to the accretion process. This hypothesis was not confirmed by the simulation, due to the problems encountered with the mesh quality for the highest steps. A perspective for this work is to enhance the mesh quality after the accretion calculation.

### ***Collision and sticking efficiency role on the accretion evaluation***

As seen in paragraph 5.5.3 and 5.5.4 both the collision and sticking efficiency have a role in the accretion process. The first one concerns the evaluation of the particle mass which impacts the cylinder, while the second one quantifies the particle mass

which sticks on the accretion surface. Moreover, both coefficients decrease as the accretion grows. Let us consider the cylinder  $d_{cyl} = 50mm$ . Table 21 reports the difference on percentage between the first and the last step for the collision and the sticking efficiency:  $\Delta\eta = \frac{(\eta_{step1} - \eta_{step24})}{\eta_{step24}}$ .

Table 21.  $\Delta\eta_1$  and  $\Delta\eta_2$  evaluation

|                |                 |
|----------------|-----------------|
| $\Delta\eta_1$ | $\Delta\eta_2$  |
| $\approx 4\%$  | $\approx 230\%$ |

As one can note, in our work, the difference between the first and the last step of computation are more important for the sticking coefficient. Therefore, for the simulation cases presented, the sticking efficiency influence more the accretion progress than the collision efficiency. Hence one can assume that the evolution of a wet snow accretion, is more sensitive to the sticking efficiency decrease than the collision efficiency one.

## 5.6 Analysis of the sticking coefficient $\eta_2 = \mathcal{F}(\alpha_{imp})$ on the experimental cases.

The analysis presented in paragraph 5.5 has described an approach to model the sticking efficiency as a function of the impact angle between the particle and the normal at the accretion surface. This approach gives accretion shapes more similar to the experimental one than in case of  $\eta_2 = 1$ . Moreover, the sticking efficiency  $\eta_2 = \mathcal{F}(\alpha_{imp})$  constantly decreases for each loop of the calculation. In order to study how the numerical results are related to the experimental ones a mean sticking efficiency is evaluated as (113).

$$\langle \eta_2 \rangle = \int_{step\ min}^{step\ max} \eta_2(i) dstep \tag{113}$$

Figure 147 has shown that the decrease of  $\eta_2$  can be considered equal for the three cylinders. Moreover,  $d_{cyl} = 50mm$  is the cylinder diameter which leads to the largest number of calculation loops before experiencing meshing issues. As a consequence, it has been assumed as the most accurate to estimate the mean sticking efficiency. Taking  $\eta_2(i)$  of  $d_{cyl} = 50mm$ , equation (113) leads to  $\langle \eta_2 \rangle = 0.41$ .

Figure 150 shows the sticking efficiency as a function of the global liquid water content as presented in paragraph 5.3. The sticking efficiency has been obtained thanks to the experimental measurements and the numerical evaluation of  $\eta_1$ . As one can note, the sticking efficiency of 0.41 corresponds in the curve Figure 150 to the ones measured for a global  $LWC_g = 0.64$ . As a conclusion, the proposed modelisation based on the impact angle might corresponds to the behavior of particle with a global  $LWC_g = 0.64$ .

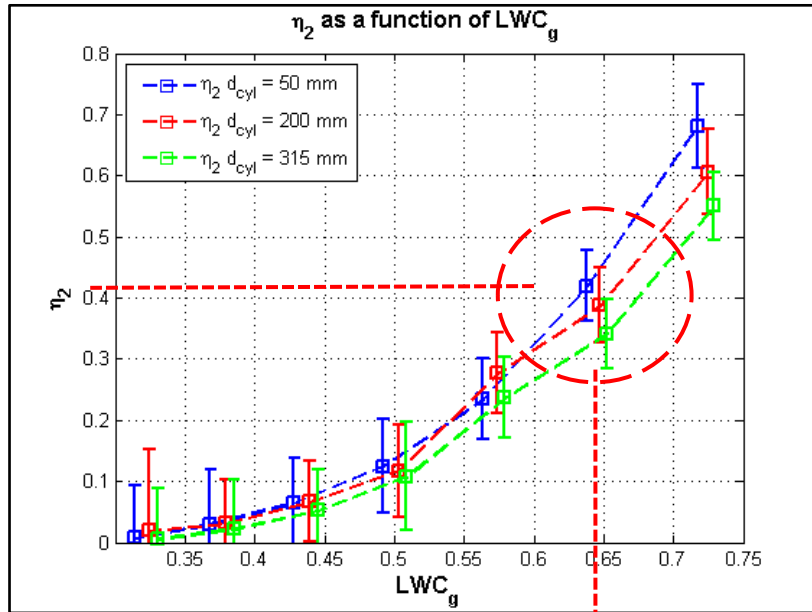


Figure 150. Relation between  $\langle \eta_2 \rangle$  and  $LWC_g$ .

Let us consider the three cylinders. Figure 151 shows a comparison between the accretion shapes obtained numerically and the experimental one obtained for a  $LWC_g \approx 0.64$ . One can note that the numerical shapes present a similar trend compared to the ones obtained during the experimental campaign. Anyhow the accretion on the upper and lower part of the cylinders is not well predicted.

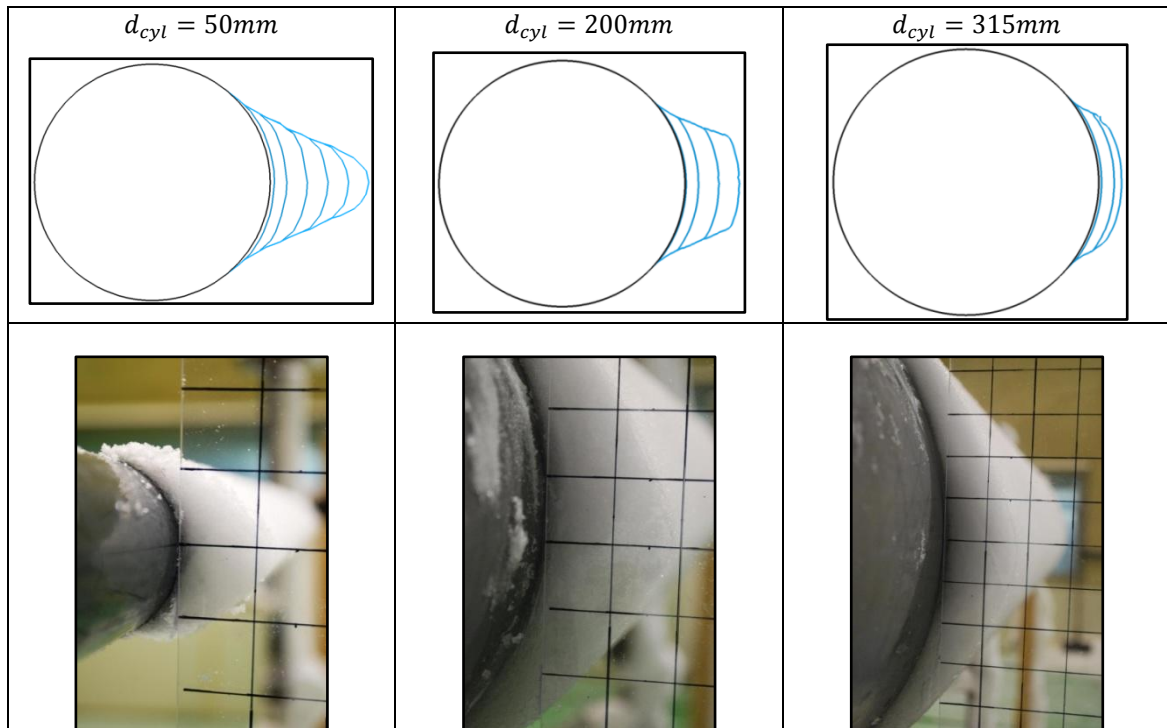


Figure 151. Accretion shapes: (a)  $d_{cyl} = 50mm$  (b)  $d_{cyl} = 200mm$  , (c)  $d_{cyl} = 315mm$ .

As a conclusion, the model based on the impact angle criterion evaluated with a loop between the aerodynamic calculation and the lagrangian calculation leads to a

better prediction of the accretion shapes. However, these models cannot reproduce many of the features observed during the experimental tests.

First, the accretion shape is not exactly similar to the one observed in the wind tunnel especially on the lower and upper parts of the accretions. This means that the impact angle is not sufficient to predict the accretion in those parts. Other parameters might be necessary to better predict the accretion shape.

Makkonen (also reported in the ISO standard 12494), suggests a modelisation deduced from experimental observations of sticking efficiency following  $\eta_2 = \frac{1}{\langle u_f \rangle}$  where  $\langle u_f \rangle$  is the mean wind speed. One is aware that this formulation is not relevant, since  $\eta_2$  is not dimensionless. Hence, it cannot be applied in our studied cases. Anyhow, it suggests that the sticking efficiency is linked to the velocity of the particles. Figure 152 shows the impact velocity of particles calculated during the lagrangian simulations for the three cylinders as a function of the particles diameters.

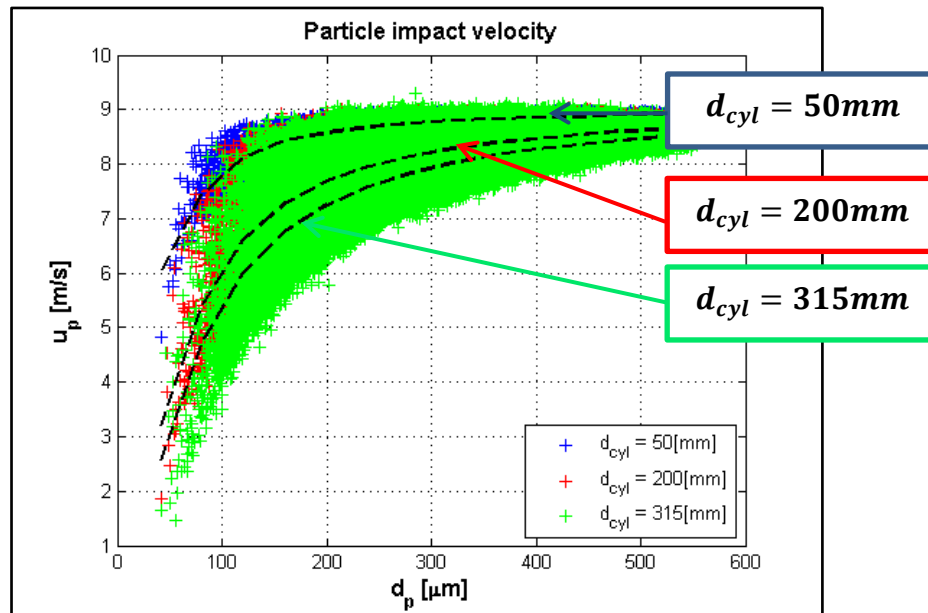


Figure 152. Particles impact speed.

One can see that there is a difference for the three diameters. This trend can be explained in the same way as the one for the collision efficiency  $\eta_1$  using the Stokes number based on the cylinder. The differences between the impact speeds for each cylinder could be linked to the ones of the coefficient  $\beta_{exp}^2$  shown in Figure 150. One can suppose that an improved modelisation which also takes into account the impact speed of particle would be able to explain the differences observed in Figure 150 between the three cylinders.

Finally, the model for  $\eta_2$  proposed in this work does not take into account the liquid water content of the particles. As a consequence, the evolution of  $\beta_{exp}^2$  as a function of  $LWC_g$  cannot be reproduced. The model as it is proposed seems to lead to a reproduction of the accretion observed for a  $LWC_g = 0.64$ .

It is not clear how the liquid water content of particles impacts on the sticking efficiency. There is likely a mechanical aspect: the liquid water part could help in the

sticking process of the particle to the surface. Additionally, the thermal aspect might also be considered by a local heat and mass balance of the particle liquid part at the impact on the surface.

Moreover, for very high  $LWC_g$  it has been observed on "over-accretion" bigger than the diameter of the cylinder. One can assume that this "over-accretion" might be linked to the runback of the liquid part of the accretion. As a consequence a most accurate modelisation of  $\eta_3$ , different from the one proposed in the aeronautic models for the liquid droplet model, has to be considered.

As a conclusion, one is aware that the modelisation of accretion coefficients  $\eta_3$  and  $\eta_2$  is very complex and involves aerodynamic, mechanic and thermal models. Specific experimental tests and the development of physical models have to be undertaken to better understand the local interaction of the particles on the accretion at the impact.

### 5.6.1 Sticking efficiency analysis: conclusions.

This last part of the chapter has analyzed separately, the sticking efficiency as a function of the global liquid water content  $LWC_g$  and as a function of the angle of impact between the particle and the surface  $\alpha_{imp}$ . The analysis of  $\eta_2 = \mathcal{F}(LWC_g)$  has shown that the sticking efficiency increases when the  $LWC_g$  increases as well. It has been assumed that the liquid part of particles acts as an "adhesive".

A first attempt to model the accretion shape was done by assuming  $\eta_2 = 1$ . The accretion shapes obtained did not correspond to the experimental ones. To obtain a more realistic shape, literature review has provided an approach to model the sticking efficiency as a function of the particle-surface angle of impact  $\eta_2 = \mathcal{F}(\alpha_{imp})$ . With this approach, the accretion shapes obtained were more similar to the experimental ones with respect to the hypothesis  $\eta_2 = 1$ . Anyhow, with this second approach, the global liquid water content is not taken into account. Moreover, the numerical results have shown that  $\eta_2 = \mathcal{F}(\alpha_{imp})$  fails in predicting the accretion on the upper and lower part of the cylinder. A conclusion of the comparisons between the model results and the wind tunnel measurements show that the proposed model for  $\eta_2$  is clearly not sufficient.

## 5.7 Conclusion

In this chapter a procedure to estimate the model parameters of wet snow accretions has been presented. As presented in this work, wet snow accretion has been modeled by three coefficients:  $\eta_1$ ,  $\eta_2$  and  $\eta_3$ . The framework of reference has been the experimental campaign.

The aerodynamic aspect of the accretion is investigated through the collision efficiency  $\eta_1$ . This coefficient has been evaluated for the experimental cylinders with a numerical dispersion model. The lagrangian tracking model, presented in chapter four, and the experimental campaign have supplied the initial conditions for this dispersion model. The results show that collision efficiency varies as a function of the particle inertia quantify by Stokes number. The more is the particle inertia, the larger is the collision efficiency.

The second part of the chapter has been focused on the modelisation of the sticking coefficient  $\eta_2$ . Considering the experimental results the accretion efficiency  $\eta_3$  has been assumed equal to one. A first attempt to quantify  $\eta_3$  involving a complex model from ONERA used for liquid water droplet failed in reproducing the trends observed during the experimental campaign.

In this part, it has been investigated the sticking efficiency as a function of the global liquid water content  $\eta_2 = \mathcal{F}(LWC_g)$ . One can assume that the liquid part of the snow particles acts as an “adhesive”. As a consequence, to high values of  $LWC_g$  correspond high values of  $\eta_2$ .

The chapter has also proposed an approach based on the works of Trenker [7, 8] to estimate the shape of the accretions. This approach takes into account the angle between the particle path at the impact with the surface and the normal to the surface. If this angle  $\alpha_{imp}$  is lower than a threshold angle  $\alpha_t = 45^\circ$  the particle sticks on the surface. The approach has allowed to obtain accretion shapes closer to the experimental ones than in case of  $\eta_2 = 1$ . However it fails to predict accretion on the upper and lower part of the cylinder. Moreover, this models is not able to reproduce the evolution of the accretion with the LWC content.

Some propositions have been made to improve the models. It seems that more complex models have to be developed in order to take into account the aerodynamic, mechanical and thermal aspect of the coefficient  $\eta_2$ . Moreover, for very high liquid water content the hypothesis of  $\eta_3 = 1$  might not be valid any longer. Hence, models inspired from the one used for aeronautic purposes might be developed.

The present work as shown how a reliable experimental databases is helpful in assessing the models. An extended database for wet snow accretions in wind tunnel could be interesting. It would involve objects with different shapes and with different angles of orientation relative to the wind. The present work has shown how to setup such experiments to provide accurate results.

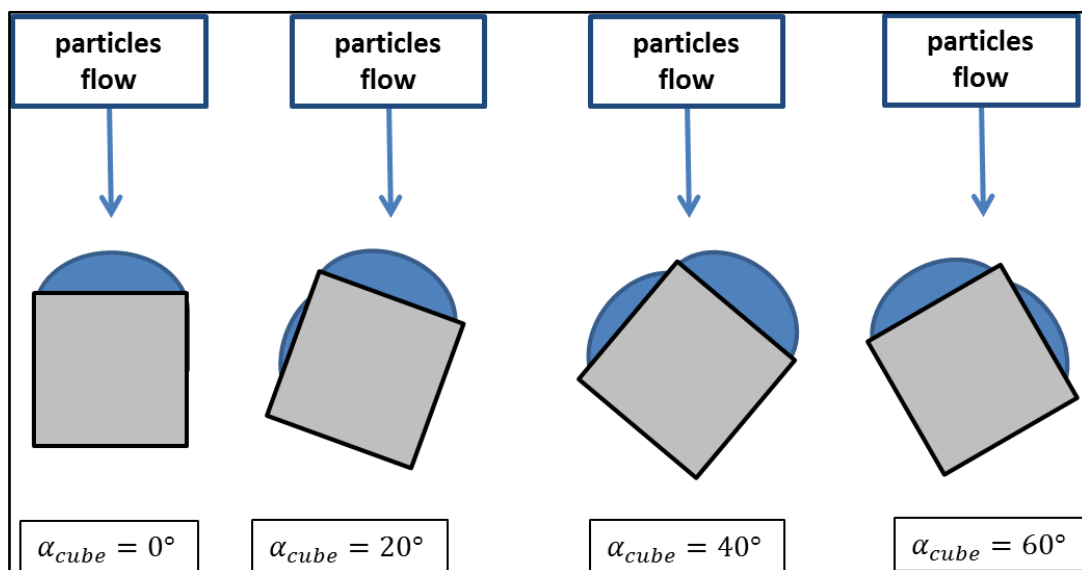


Figure 153. Experimental setup proposed.

Performing these experimental tests in conjunction with a tuning of the physical parameter global liquid water content during the tests, it could be possible to generate a database of results to establish a relationship that includes the angle of impact  $\alpha_{imp}$  and the global liquid water content  $LWC_g$ :  $\eta_2 = \mathcal{F}(\alpha_{imp}, LWC_g)$ .

## **Bibliography**

- [1] M. M. Zdravkovich, *Flow Around Circular Cylinders* vol. 1: Fundamentals. Oxford: Oxford Science Publications, 1997.
- [2] S. Aguinaga, "Dispersion turbulente et déposition de gouttes d'eau ; expérimentation et modélisation numérique," 2008.
- [3] ISO, "Atmospheric icing of structure," vol. 12494, ed. Geneva: ISO copyright office, 2001, p. 58.
- [4] B. L. Messinger, "Equilibrium temperature of an unheated icing surface as a function of air speed," *Journal of Aeronautical Science*, vol. 20, pp. 91-104, 1953.
- [5] D. Guffond, "Aspects Thermiques du givre atmosphérique des aéronefs," O.N.E.R.A., Meudon.
- [6] L. Makkonen, "Models for the growth of rime, glaze, icicles and wet snow on structures," *Philosophical Transactions: Mathematical, Physical and Engineering Sciences*, vol. 358, pp. 2913-2939, 2000.
- [7] M. Trenker, W. Payer, C. Krenn, G. Haider, and M. Mann, "Numerical Simulation of Snow Entrainment with Application to Train Undercarriage Design," presented at the NAFEMS, World Congress, Malta, 2005.
- [8] M. Trenker and W. Payer, "Investigation of snow particle transportation and accretion on vehicles," presented at the 24th Applied Aerodynamics Conference, San Francisco, 2006.

## Chapter 6 Conclusion

In this work we have studied the wet snow accretion phenomenon. This kind of accretion can be considered as a part of the atmospheric icing phenomena. Wet snow accretions may concern several fields of engineering. Regarding buildings and civil engineering, wet snow accretions to structures can cause important damages and severe risks for people. Particles which generate wet snow accretion are characterized by a mixed phase. The water/solid ratio of particles has been synthesized in this work by the liquid water content:  $LWC$ . This dimensionless parameter represents the ratio of the liquid mass of the particle to the total mass of the particle:  $LWC = \frac{m_l}{m_p}$ .

To analyze wet snow accretions this work has presented an approach based on three dimensionless coefficients. The coefficient  $\eta_1$  concerns the efficiency of particles to reach the structure. The coefficient  $\eta_2$  concerns the efficiency to collect particles which have reached the structure. The third coefficient  $\eta_3$ , concerns the accretion efficiency. The three coefficient have been synthesized with the coefficient  $\beta^{123} = \eta_1\eta_2\eta_3 = \frac{\dot{m}_{acc}}{\dot{m}_{inc}}$ , considered in the experimental part of this work.

To study wet snow accretions, an experimental campaign has been undertaken in a climatic wind tunnel facility. The experimental tests were focused on the role of the liquid water content on the accretions. Three cylinders were tested ( $d_{cyl} = 50mm$ ,  $d_{cyl} = 200mm$ ,  $d_{cyl} = 315mm$ ). The choice of three different cylinders has allowed to investigate the influence of the object dimension on the accretions. Wet snow particles were produced by a snow gun. The particle  $LWC$  was tuned as a function of the ambient temperature  $T_a$  of the wind tunnel:  $LWC = \mathcal{F}(T_a)$ . The experimental campaign has shown that wet snow accretion is influenced by the particle inertia facing a structure. Moreover, wet snow accretion are strongly influenced by the particle liquid water content. Anyhow, the analysis of the role of each coefficients on the accretion was hard, as well as, the quantification of the boundary conditions for the numerical model ( $PSD^v$  and  $LWC_g$ ).

To overcome the matter of boundary conditions quantification, a physical model has been developed. This model quantifies the  $PSD^v$  and  $LWC_g$  by coupling two numerical codes. The first code concerns the dispersion of particles injected by the snow gun. This part is based on the lagrangian approach to evaluate the particle trajectories and it integrates a stochastic feature to model the turbulent characteristic of the flow. The analysis performed with the particle dispersion code has shown that a Langevin approach leads to a more physical evaluation of the heat transfer coefficient  $h$ . As a consequence, the Langevin approach has been assumed as the reference in the coupled model. The second code is based on the particle freezing process and is used to quantify the particle  $LWC$ . It has shown that the heat transfers due to convection and mass transfer are the main heat sinks driving the freezing process. It has also allowed to justify the experimental procedure.

Due to the fact that discerning the role of each coefficient during the experimental campaign, a numerical approach has been undertaken. It was based on

RANS turbulence model and it integrated a stochastic feature to model the particle characteristic of the flow.

The evaluation of the collision efficiency has allowed to analyze the experimental coefficient  $\beta_{exp}^{123}$  independently from the efficiency of particles to reach the cylinders:  $\beta_{exp}^{23} = \frac{\beta_{exp}^{123}}{\eta_1}$ . Moreover, if  $\eta_1$  can be evaluated with a simplified approach (ISO 12494 Standard) our work has proposed a procedure to evaluate the collision efficiency for any kind of engineering structures. To study the sticking efficiency  $\eta_2$ , following the work of Makkonen and the experimental results, it has been assumed an accretion efficiency  $\eta_3 = 1$ . This means that all the sticking mass contributes to the accretion. The results have shown that the sticking efficiency  $\eta_2$  is strongly driven by the  $LWC_g$ . When the liquid water content increases,  $\eta_2$  increases as well. It has been supposed that the liquid part of the particles acts as an “adhesive” for the particles.

To model the accretion forms it has been assumed as a first attempt a sticking efficiency  $\eta_2 = 1$ . The accretion forms obtained did not correspond to the experimental ones. Then, a second approach has been proposed. It has been based on the angle of impact  $\alpha_{imp}$  between the particle path and the surface normal. If the angle of impact was less than a threshold angle, the particle stuck on the surface. The threshold angle has been fixed to  $45^\circ$  after a series of optimization tests. This approach has led to an accretion forms more similar to the experimental ones.

Anyhow, with the approach based on the only angle of impact, it is not possible to explain the accretion on the higher and lower parts of the cylinder, especially for the higher values of liquid water content. Additionally the model  $\langle \eta_2 \rangle = \mathcal{F}(\alpha_{imp})$  did not take into account the liquid water content which this study has shown to play a crucial role in wet snow accretion.

As a future perspective it is suggested to study the accretion on different simple forms. This will allow to apply the method developed in this work to other object forms. Additionally, changing the liquid water content as well as the object orientation facing the flow may allow to acquire a series of experimental data. These results might lead to a more comprehensive model to take into account both the particle liquid water content and the angle of impact that this work has identified as the two crucial aspects involved in wet snow accretion process.

It is also very important to design academic experiments allowing to characterize the behavior of impacting snow particles on different types of surfaces (dry or covered with snow of varying properties). Such approach is typically encountered for the model of liquid particles interacting with walls and is used in the aeronautical industry. The presence of mixed phases for snow particles makes progress more difficult and information are very rare in the literature. However, such model experiments, supported when possible by theoretical analysis based on physical principles, would be of great help in the computation of accretion of snow on structures.

---

---



---

*Résumé de chaque chapitre en français*

**Le deuxième chapitre** présente l'état de l'art et une synthèse bibliographique concernant les accrétions de neige collante. La première partie du chapitre présente les effets de ce type d'accrétion sur différentes structures. Les particules qui sont à l'origine des accrétions de neige collante sont caractérisées par un mélange liquide solide. Le ratio entre la partie liquide et la masse totale de la particule est quantifié par un coefficient adimensionnel TEL: teneur en eau liquide. Dans le cadre de ce travail, la TEL est défini comme étant le ratio de la masse liquide d'eau sur la masse totale de la neige. Bien que la Teneur en Eau Liquide soit traduite par "Liquid Water Content" (LWC), cette grandeur est différente de celle communément utilisée dans le domaine du givrage aéronautique, où LWC désigne la concentration d'eau dans l'air. Le chapitre présente la modélisation thermique de la congélation d'une goutte d'eau. La modélisation conforte l'approche expérimentale d'ajustement de la TEL des particules en fonction de la température ambiante. Le chapitre présente les trois phénomènes physiques qui interviennent dans le processus d'accrétion des particules de neige sur une structure. Le premier phénomène concerne la tendance d'une particule à impacter une structure. Il est quantifié par le coefficient de collision  $\eta_1$ . Le deuxième phénomène est lié à la capacité d'une particule à "coller" sur la surface de la structure après avoir impacté la structure. Il est quantifié par le coefficient de collage  $\eta_2$ . Le troisième phénomène prend en compte la faculté des particules "collées" à la surface à contribuer à l'accrétion. Il est quantifié par le coefficient d'accrétion  $\eta_3$  (Figure 17).

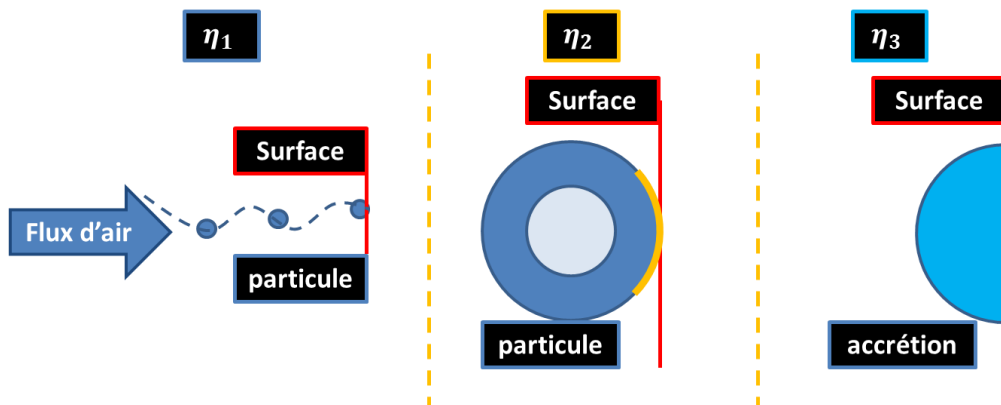


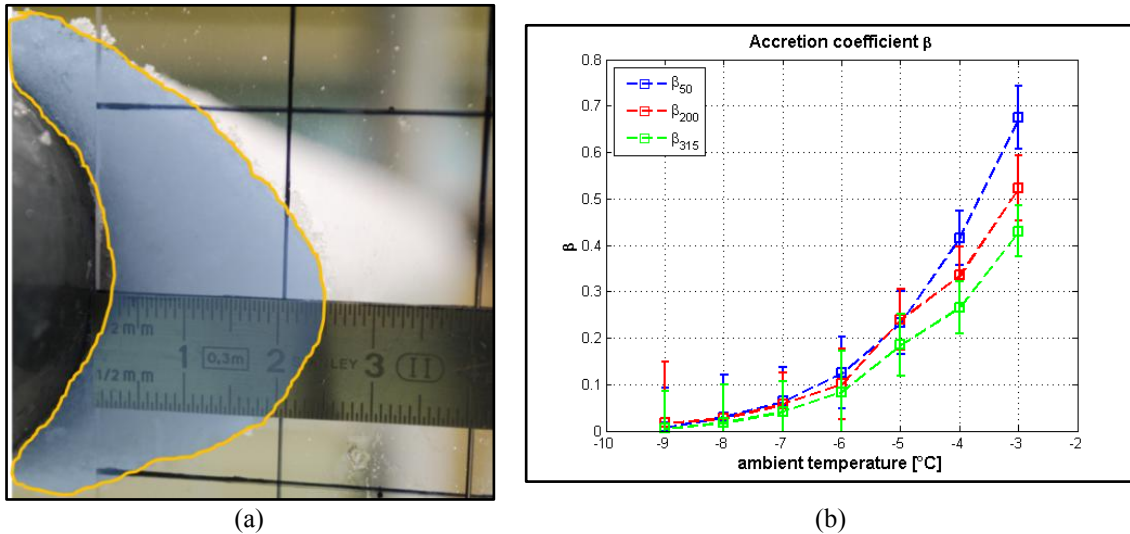
Figure 154. Les trois phénomènes physiques analysés.

La nature diphasique du problème nécessite, la modélisation des interactions particule-turbulence. Les modèles Eddy Life Time et Langevin sont expliqués. Les deux approches ont été implémentées dans la modélisation numérique.

**Le troisième chapitre** présente la procédure expérimentale développée pour reproduire les accrétions de neige collante. Deux aspects ont été étudiés: l'effet de la TEL sur les accrétions ainsi que l'influence de la dimension de la structure sur l'accrétion. Le premier aspect a été analysé en modifiant la TEL des particules par ajustement de la température ambiante. Le deuxième aspect a été étudié en mesurant l'accrétion sur trois cylindres de différents diamètres (Figure 155 - a). Les particules de neige qui forment les accrétions ont été produites en utilisant un canon à neige. Le spray formé par le mélange d'eau et d'air sous pression permet la production des particules givrantes. La quantité de la partie liquide a été ajustée en variant la température ambiante. Les accrétions obtenues, en fonction de la température ambiante, ont été évaluées par à un

---

coefficient expérimental  $\beta_{exp} = \eta_1\eta_2\eta_3$  qui intègre les contributions des trois aspects physiques décrits dans le chapitre deux (Figure 155 - b). Le coefficient  $\beta_{exp}$  a été défini comme le ratio entre le flux massique d'accrétion sur le flux massique incidente.



La partie expérimentale a permis une caractérisation de l'écoulement chargé en neige pour la modélisation numérique des chapitres quatre et cinq. L'écoulement a été caractérisé en termes de vitesse moyenne, longueur d'échelle intégrale et intensité de turbulence. Compte tenu des difficultés rencontrées pour caractériser l'écoulement amont des cylindres en termes de répartition granulométrique et teneur en eau liquide, un modèle simple pour estimer ces deux caractéristiques a été développé dans le chapitre quatre.

**Le quatrième chapitre** présente le modèle physique développé pour estimer la distribution granulométrique (partie dynamique du modèle) à l'amont des cylindres avec la teneur en eau liquide associée (partie thermique du modèle). Le modèle évalue les deux caractéristiques en même temps: l'évaluation de la teneur en eau liquide est couplée à l'estimation de la distribution granulométrique. Ces deux conditions sont utilisées dans le chapitre cinq pour analyser les trois aspects de l'accrétion. Un modèle lagrangien a été développé pour estimer la distribution des particules à l'amont des cylindres (Figure 156 - a). Une approche stochastique est mise en œuvre pour modéliser les effets de la turbulence sur les particules. Les deux modèles implémentés sont: Eddy Life Time et Langevin. L'approche Langevin, mieux adaptée au problème physique, a été retenue. La teneur en eau liquide des particules à l'amont des cylindres (Figure 156 - b) a été estimée en implémentant un modèle thermique de congélation d'une goutte d'eau dans la partie dynamique du modèle.

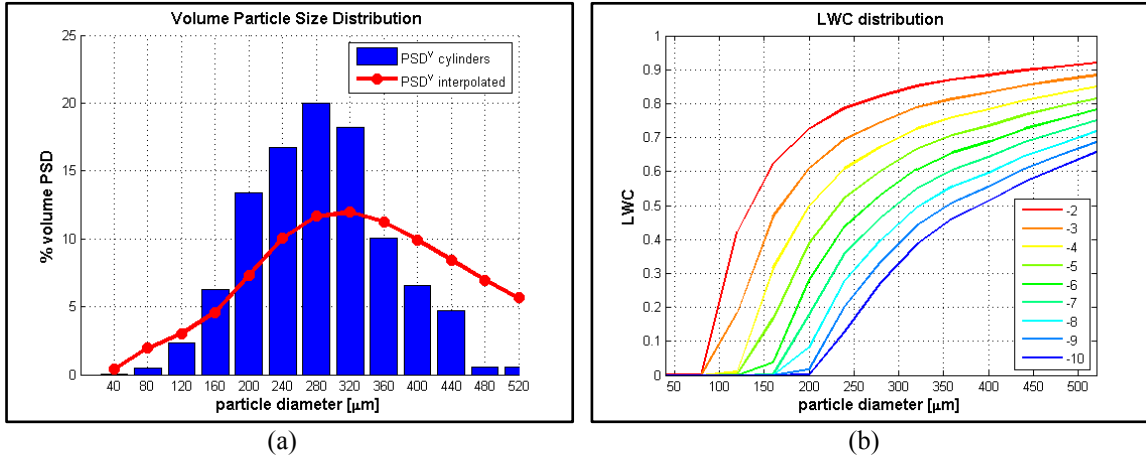


Figure 156. (a) distribution granulométrique . (b) teneur en eau liquide des particules.

Le modèle a montré, entre autres, l'influence importante de la gravité sur la distribution granulométrique des particules qui impactent la structure ainsi que la sensibilité élevée de la teneur en eau liquide à la température ambiante et au diamètre des particules.

**Le chapitre cinq** présente l'analyse des trois aspects physiques à la base des accrétions de neige collante. La partie expérimentale présentée dans le chapitre trois et le modèle physique présenté dans le chapitre quatre ont donné les conditions aux limites pour développer l'analyse du chapitre cinq. La première partie du chapitre expose l'analyse de la tendance des particules à impacter le cylindre. Cette tendance est quantifiée par le coefficient de collision  $\eta_1$ . Une simulation numérique RANS avec dispersion des particules a été développée pour l'estimation du coefficient  $\eta_1$ . Les résultats ont montré l'augmentation de la tendance des particules à impacter le cylindre alors que le diamètre du cylindre diminue. Cette tendance a été reliée au nombre de Stokes ( $St_{cyl}$ ) qui quantifie l'inertie des particules vis-à-vis des forces induites par l'écoulement de contournement des cylindres. Plus l'inertie est importante plus les particules ont tendance à impacter le cylindre (Table 17).

Table 22. Le lien entre  $St_{cyl}$  et le coefficient de collision  $\eta_1$ .

| $d_{cyl}$ [mm] | $St_{cyl}$    | $\eta_1$ $k - \omega$ SST |
|----------------|---------------|---------------------------|
| 50             | $\approx 18$  | $\approx 0.94$            |
| 200            | $\approx 4.5$ | $\approx 0.82$            |
| 315            | $\approx 3$   | $\approx 0.74$            |

La deuxième partie du chapitre est dédiée à l'analyse de la tendance des particules à rester "collées" à la surface et sur la modélisation des formes expérimentales. Les observations expérimentales ont amenées à considérer que toutes les particules qui adhèrent à la surface contribuent à l'accrétion. En conséquence, le coefficient d'accrétion  $\eta_3$  a été considéré égal à 1. Cette hypothèse a amené à étudier la tendance des particules à "coller" en fonction de la teneur en eau liquide des particules:  $\eta_2 = \mathcal{F}(TEL)$  (Figure 157 – a). Les résultats de l'étude expérimentale ont montrés que plus la teneur en eau liquide d'une particule est élevée plus celle-ci adhère à la surface. La modélisation numérique des formes d'accrétion a considéré deux critères mécaniques: en supposant que toutes les particules adhèrent à la surface:  $\eta_2 = 1$  et en fonction de l'angle d'impact:  $\eta_2 = \mathcal{F}(\alpha_{imp})$ . Les résultats des simulations ont montré que le critère

d'angle , génère les formes d'accrétion les plus proches des formes obtenues expérimentalement (Figure 157 - b).

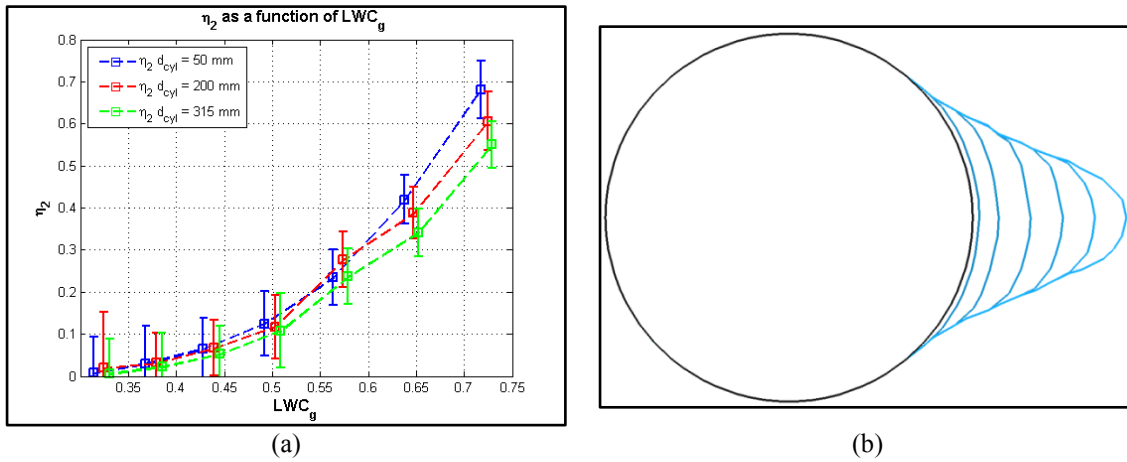


Figure 157. (a)  $\eta_2 = \mathcal{F}(TEL)$  . (b) forme d'accrétion modélisée.

**Le chapitre six** présente les conclusions et les perspectives du travail de recherche. La construction d'une base des données expérimentale permettrait d'affiner le critère d'angle qui détermine la forme de l'accrétion en fonction de la TEL. La modélisation de ce processus serait précisée. En parallèle, une analyse locale des effets de ruissèlement induits par les contraintes de cisaillement pourrait améliorer la compréhension des phénomènes physiques à la base des accrétions par neige collante.

---

---

---

## *Abstract*

The present work aims at studying the atmospheric phenomenon of wet-snow accretion to structures. This phenomenon may induce severe damages to structures. Freezing particles which generate wet-snow accretions are characterized by a mixed phase ice/water. The particle state in this framework is quantified by a dimensionless parameter: the liquid water content *LWC* defined as the ratio of the particle liquid mass to the whole particle mass. This *LWC* definition is different from the aeronautical one. In this work, wet snow is produced with an ambient temperature below 0°C. Both experimental and numerical approaches are undertaken to investigate the subject. The experimental approach, undertaken in a climatic wind tunnel, is based on the *LWC* effect on the accretions obtained on a test structure. The particle *LWC* is tuned by adjusting the ambient temperature of the test chamber. The results are synthesized by a coefficient  $\beta$  defined as the ratio of the accretion mass flux to the snow mass flux. A first numerical model assesses the boundary conditions of the accretion model, i.e. the particle size distribution upstream the structure and the associated *LWC*. The first part of accretion model concerns the study of the particle behavior close to the structure which is quantified with a Stokes number. The efficiency of particles to impact the structure is synthesized by a dimensionless parameter  $\eta_1$ . The analysis of the experimental coefficient  $\beta$  according to  $\eta_1$  is developed. This allows to study the efficiency of particles to stick on the structure as a function of the *LWC*. The result is synthesized by the  $\eta_2$  coefficient. The second part concerns an attempt to model the accretion shape by the sticking efficiency  $\eta_2$  as a function of the particle-surface angle of impact. A series of perspectives are presented.

Keywords: *LWC*, atmospheric icing, particle mixed phase, climatic wind tunnel, numerical modeling, two-phase flow

## *Résumé*

Ce travail est consacré à l'étude du givrage atmosphérique des structures par accréation de neige collante qui peut conduire à des dommages sévères aux structures. Les particules à la base de ce type d'accréations sont caractérisées par un mélange d'eau et glace quantifié dans cette étude par un paramètre sans dimension: la teneur en eau liquide: *TEL* définie comme le ratio de la masse liquide sur la masse totale de la particule. La définition de la *TEL* considérée dans ce travail est différente de celle utilisée en aéronautique. Dans cette étude, la neige collante a été reproduite avec une températures ambiante négative. L'approche expérimentale, mise en œuvre dans une soufflerie climatique, est consacrée à l'étude de l'effet de la *TEL* sur l'accréation de neige sur une structure de test. La *TEL* est ajustée en modifiant la température ambiante. Les résultats sont synthétisés par le coefficient  $\beta$  défini comme le ratio entre le flux massique de l'accréation, et le flux massique de neige incidente. Un premier modèle numérique évalue les conditions aux limites pour le modèle d'accréation: c.à.d. la distribution en taille des particules à l'amont de la structure et la *TEL* associée. La première partie du modèle numérique d'accréation concerne l'analyse du comportement des particules à proximité de la structure expérimentale quantifié par le nombre de Stokes. La capacité des particules à impacter la structure est synthétisé par le coefficient de collision  $\eta_1$ . L'analyse du coefficient expérimental  $\beta$ , en fonction de  $\eta_1$  est développée. Ceci permet l'étude de la capacité des particules à s'accrocher à la surface en fonction de la *TEL*. Le résultat est évalué par le coefficient de collage  $\eta_2$ . La seconde partie expose une approche pour modéliser la forme d'accréation, par le coefficient de collage  $\eta_2$ , en s'appuyant sur l'angle d'impact entre la particule et la surface. Des perspectives sont proposées.

Mots clefs: *TEL*, givrage atmosphérique, particules en condition mixtes, soufflerie climatique, modélisation numérique, écoulement diphasique

---